CRYSTALLINE INORGANIC ION EXCHANGERS FOR SEPARATION OF CATIONS FROM NUCLEAR WASTE: DESIGN AND MECHANISTIC INVESTIGATIONS FROM STRUCTURE-PROPERTY CORRELATIONS

By

SAMATHA BEVARA

CHEM01201304033

Bhabha Atomic Research Centre, Mumbai

A thesis submitted to the Board of Studies in
Chemical Sciences

In partial fulfilment of requirements
for the Degree of
DOCTOR OF PHILOSOPHY

OF

HOMI BHABHA NATIONAL INSTITUTE

JULY, 2018

Homi Bhabha National Institute[1]

Recommendations of the Viva Voce Committee

As members of the Viva Voce Committee, we certify that we have read the dissertation prepared by **Ms. SAMATHA BEVARA** entitled **"Crystalline inorganic ion exchangers for separation of cations from nuclear waste: Design and mechanistic investigations from structure-property correlations"** and recommend that it may be accepted as fulfilling the thesis requirement for the award of Degree of Doctor of Philosophy.

Chairman : **Prof. C. P. Kaushik** **Date:** 11/12/18

Guide / Convener: **Prof. S. N. Achary** S. N. Achary **Date:** 11/12/2018

Co-guide - (if any) **Date:**

Examiner : **Prof. Anirban Chowdhury** **Date:** 11/12/18

Member : **Prof. A. K. Tyagi** **Date:** 11/12/2018

Member : **Prof. S. Kannan** **Date:** 11-12-2018

Invitee : **Date:**

Final approval and acceptance of this thesis is contingent upon the candidate's submission of the final copies of the thesis to HBNI.

I/We hereby certify that I/we have read this thesis prepared under my/our direction and recommend that it may be accepted as fulfilling the thesis requirement.

Date: Mod-Lab, BARC

Place: 11-12-2018

S. N. Achary

(Signature) 11-12-2018

Guide

---

[1] This page is to be included only for final submission after successful completion of viva voce.

Version approved during the meeting of Standing Committee of Deans held during 29-30 Nov 2013

STATEMENT BY AUTHOR

This dissertation has been submitted in partial fulfilment of requirements for an advanced degree at Homi Bhabha National Institute (HBNI) and is deposited in the library to be made available to borrowers under rules of the HBNI.

Brief quotations from this dissertation are allowable without special permission, provided that accurate acknowledgement of source is made. Requests for permission for extended quotation from or reproduction of this dissertation in whole or in part may be granted by the Competent Authority of HBNI when in his or her judgment the proposed use of the material is in the interests of scholarship. In all other instances, however, permission must be obtained from the author.

SAMATHA BEVARA

DECLARATION

I (Samatha Bevara), hereby declare that the investigation presented in the thesis has been carried out by me. The work is original and has not been submitted earlier as a whole or in part for a degree / diploma at this or any other Institution / University.

SAMATHA BEVARA

List of publications arising from the thesis

1. Preparation and crystal structure of $K_2Ce(PO_4)_2$: a new complex phosphate of Ce(IV) having structure with one-dimensional channels
B. Samatha, S. N. Achary, S. J. Patwe, A. K. Sinha, A. K. Tyagi
Dalton Trans, 2016, 45, 980-991.

2. Phase transformation, vibrational and electronic properties of $K_2Ce(PO_4)_2$: a combined experimental and theoretical study
B. Samatha, K. K. Mishra, S. J. Patwe, T. R. Ravindran, M. K. Gupta, R. Mittal, P. S. R. Krishna, A. K. Sinha, S. N. chary, A. K. Tyagi
Inorg. Chem, 2017, 56, 3335-3348.

3. Temperature dependent structural, vibrational and magnetic properties of $K_3Gd_5(PO_4)_6$
B. Samatha, S. N. Achary, K. K. Mishra, T. R. Ravindran, A. K.Sinha, P. U. Sastry, A. K Tyagi
Phys. Chem. Chem. Phys, 2017, 19, 6030-6041.

4. Recent progress on synthesis and structural aspects of rare-earth phosphates
S. N. Achary, **B. Samatha,** A. K. Tyagi
Coordination Chemistry Reviews, 2017, 340, 266-297.

5. Separation of ^{90}Sr from nuclear waste by ion exchangeable phosphates of Ce(IV) and Zr(IV)
B. Samatha, G. Prema, S. J. Patwe, S. N. Achary, R. K. Mishra, A. Kumar, A.K. Sinha, C P. Kaushik, A. K. Tyagi·
J. Env. Chem. Eng, 2018, 6, 2248-2261.

6. Pressure and temperature dependent structural studies on hollandite type ferrotitanate and crystal structure of a high pressure phase
B. Samatha, S. N. Achary, Abhishek Chitnis, Nandini Garg, P. U. Sastry, A. B. Shinde, P. S. R. Krishna and A. K. Tyagi
Inorg. Chem, 2018, 57, 2157-2168.

7. High pressure behavior of complex phosphate $K_2Ce(PO_4)_2$: Gruneisen parameter and anharmonicity properties
K. K. Mishra, **B. Samatha**, T. R Ravindran, S. J Patwe, M. K Gupta, R. Mittal, R V. Krishnan, S. N Achary, A. K Tyagi
Journal of Solid State Chemistry, 2018, 258, 845-853.

8. Birnessite: a new-generation and cost effective ion exchange material for separation of clinical-grade ^{90}Y from $^{90}Sr/^{90}Y$ mixture
R. Chakravarty, **B. Samatha**, J. Bahadur, S. Chakraborty, H. D. Sarma, S. N. Achary, A. Dash, A. K. Tyagi
ChemSelect, 2018, 3, 10670-10676.

9. Separation of ^{90}Sr from nuclear waste by synthetic birnessite minerals
B. Samatha, G. Prema, S. N. Achary, G. Bhallerao, R. K. Mishra, A. Kumar, C. P. Kaushik, A. K. Tyagi
J. Env. Chem. Eng, 2018, 6, 7200-7213.

10. Thermodynamic investigations on $K_3Ln_5(PO_4)_6$, Ln = Eu, Gd compounds
R. Dawar, **B. Samatha**, S. N. Achary, R. Mishra, A. K. Tyagi
J. Alloys and Compds, 2019, 771, 936-943.

11. Temperature dependent structural studies and phase transition behavior of $K_2Th(PO_4)_2$
Samatha Bevara, B. Rajeswari, S. J. Patwe, P. S. R. Krishna, A. B. Shinde, S. N. Achary, R. M. Kadam, A. K. Tyagi
J. Alloys and Compds, DOI: 10.1016/j.jallcom.2018.12.315.

Conferences

1. Preparation, thermal and magnetic properties of $Mn_5(HPO_4)_2(PO_4)_2.4H_2O$
B. Samatha, S. N. Achary, P. D. Babu, A. K. Tyagi
AIP Conference Proceedings, 1665, 030021 (2015), VIT, Vellore, India.

2. Sr^{2+} and Cs^{+} ion exchange properties of $KLn(PO_3)_4$: Ln = Ce and Eu
B. Samatha, S. N. Achary, J. Ram kumar, S. Chandramouleeswaran, A. K. Tyagi
ISMC Proceedings, 2014, BARC, Mumbai, India.

3. X-ray diffraction studies on $K_3Gd_5(PO_4)_6$ between 20 K to 1073 K
B. Samatha, S. N. Achary, A. K. Tyagi, A. K. Sinha, P. U. Sastry
COMPEC Proceedings, 2016, p.70-71, BARC, Mumbai, India.

4. Crystal structure and cation exchanging properties of a novel open framework phosphate of Ce (IV)
B. Samatha, S. N. Achary, S. J. Patwe, A. K. Sinha, R. K. Mishra, A. Kumar, C. P. Kaushik, A. K. Tyagi
AIP Conference Proceedings 1731, 140040 (2016), AMITY University, Delhi, India.

5. Crystal structure and Sr^{2+} ion exchange properties of $K_2M(PO_4)_2$, for M = Ce and Zr
B. Samatha, G. Prema, S. J. Patwe, S. N. Achary, R. K. Mishra, Amar Kumar, C. P. Kaushik, A. K. Tyagi
ISMC proceedings, 2016, 332 p, BARC, Mumbai, India.

6. $K_2Ce(PO_4)_2$: a new complex phosphate of Ce (IV)
B. Samatha, S. N. Achary, A. K. Tyagi
Acta Cryst, (2017), A73, C844, Hyderabad, India.

Oral presentations

1. Preparation, thermal and magnetic properties of $Mn_5(HPO_4)_2(PO_4)_2.4H_2O$
DAE-SSPS-2014, VIT, Vellore, India.

2. $K_2Ce(PO_4)_2$: A new complex phosphate of Ce (IV)
IUCr-2017, Hyderabad, India.

3. Crystalline inorganic ion exchangers for ^{90}Sr separation from nuclear waste, Research scholars meet, Mumbai, 2017.

Samatha Bevara

Dedicated to my Parents, Bharat and Mamatha whose love and support sustained me throughout

ACKNOWLEDGEMENTS

First and foremost I would like to acknowledge my supervisor, **Dr. S. N. Achary**, Nuclear and Energy Materials Section, Chemistry Division for his guidance and constant support throughout the tenure. I am deeply grateful and indebted for his supervision and support, which was indispensible. I am thankful to him forever for his enthusiasm, inspiration, teaching, sound advice and great efforts to explain things in simple ways. I wish to express my special thanks to **Dr. A. K. Tyagi**, Head, Nuclear and Energy Materials Section, Chemistry Division for his guidance, never-ending enthusiasm, very inspiring discussions and constant support over the years. I would like to express my deepest gratitude to his excellent suggestions, care, patience and providing me an excellent atmosphere for doing research.

I am thankful to **Dr. B. N. Jagtap**, Ex-Director, Chemistry Group, BARC and **Dr. P. D. Naik**, Associate director, Chemistry Group, BARC, for giving me an opportunity to carry out the research work in Chemistry Division. I would also like to thank **Dr. V. K. Jain**, Ex-Head, Chemistry Division, **Dr. K. I. Priyadarsini**, Head, Chemistry Division, BARC for their support and encouragement. I am also thankful to **Department of Atomic Energy** for the financial support. I express my profound gratitude to **Dr. C. P. Kaushik**, **Dr. Amar Kumar**, **Dr. R. Mishra** and **Ms. Prema Giri** for providing radioactive lab facilities, discussions and timely help while carrying out radioactive experiments. I express my sincere gratitude to **Dr. S. Kannan** and **Dr. Ratikant Mishra** for their positive comments and support during annual review meetings.

Many thanks to former Ph.D students from our group, **Dr. Farheen Sayed**, **Dr. Vasundhara Katari**, **Dr. Jerina Majeed**, **Dr. Pooja Sawant**, **Dr. P. Anita Kumari** for their help, caring and suggestions in the early stages of my research work. I would also like to express my heartfelt thanks to **Dr. S. J. Patwe**, **Dr. Rimpi Dawar**, **Ms. Kruti halankar**, **Dr. Dipa Dutta** who were around in any time of need and for emotional support. My thanks are due to cheering section members **Dr. Mainak Roy**, **Dr. Vinita G. Gupta**, **Dr. Balaji P. Mandal**, **Dr. Rakesh Shukla**, **Mr. Mohsin Jafar** and **Mrs. Aruna Ghadge** for their help, encouragement and for making our laboratory as a best place. I would also like to thank **Dr. A. Singhal**, **Dr. D. Dutta** and **Dr. O. D. Jaya kumar** for their good words which kept on encouraging me during the Ph.D tenure. The administrative staff of chemistry division are also thanked for their timely help.

I extend my thanks to training school friends **Dr. G. Somu Naidu**, **Mr. V. Srikanth**, **Mr. D. Sai Krishna**, **Dr. D. Srinivas**, **Ms. Priyanka Biswas**, **Ms. Rakhee Yadav**, **Mr. Ganesh K. Mourya**, **Mr. Tapas Das**, **Mr. Sheetaljit Sharma**, **Dr. Susma Rawool**, **Ms. Ramya Nair** and **Dr. Ashish Nadar** for providing exciting and fun filled environment during my research years. I extend my thanks to all friends, well-wishers who made my stay pleasant and memorable in BARC. I thank all of them, whose names might have not been appeared but whose assistance has helped in the progress of my research work.

Last but not the least, the most important persons in my life, my parents **Venkata Narayana** and **Subhashini**, husband **K. Bharat Kumar** and sister **Mamatha** for their unconditional love and constant moral support without which this thesis would not be possible. I am pleased to acknowledge my parent-in-laws **K. Prasada Rao** and **K. Lakshmi**, brother **Dr. K. Sarat Kumar** for their affection, encouragement, support and trust over me. Finally, I thank Almighty for everything.

Samatha Bevara

CONTENTS

SYNOPSIS

Rapid growth in human population, limited renewable energy sources raises the importance of non-conventional energy sources like nuclear energy. Because of increasing energy demands many countries around the world are currently going through energy transition. Many technological limitations hinder the expected contribution of renewable energy sources like solar, hydro and wind energies. Because of the complexity in designing an energy supply from renewable energy sources, the nuclear energy is being adopted as an innovative and efficient source of energy. In light of the closed nuclear fuel cycle adopted by India, spent nuclear fuel undergoes reprocessing for recovery of the fissile and fertile nuclides to bring them back to the fuel cycle operation. The spent fuel of a typical PHWR type reactor contains ~96% U, ~1% Pu, ~3% fission products like ^{137}Cs, ^{90}Sr, ^{106}Ru, ^{99}Tc etc. along with minor actinides ^{237}Np, ^{241}Am, ^{247}Cm and variety of rare earths [1]. Separation of fissile isotopes and long lived isotopes like ^{137}Cs, ^{90}Sr reduces the nuclear waste burden on environment significantly. In order to reduce the nuclear waste volume and cost of nuclear waste management, separation of fission products with high concentrations and long half lives such as ^{137}Cs, ^{90}Sr, ^{99}Tc, Am, ^{106}Ru, ^{144}Ce etc. is essential [2].

Inorganic ceramic materials have been considered as promising ion exchanging materials for selective separation of radionuclides from liquid nuclear wastes due to their higher chemical and radiation stabilities [3]. Due to the structural and crystal chemistry features, inorganic materials show high selectivity during ion exchange process. In view of this, many framework type phosphates have been studied for the selective separation of radionuclides from nuclear waste and for immobilization of long lived isotopes. The main objective of the present thesis is to develop crystalline inorganic ion exchangers for selective separation of radionuclides from nuclear waste and to investigate stable host matrices for the immobilization of long lived radionuclides. Special emphasis is given for the separation of ^{90}Sr from various nuclear waste streams using crystalline inorganic materials formed by framework connections of phosphates, titanates, manganates and their ion exchange properties. The ion exchanged materials were also characterized for possible stable immobilization matrix with the exchanged ions. This thesis has been divided into ten chapters elaborating the work carried out under the Ph.D theme crystalline inorganic ion exchangers for separation of radionuclides from nuclear waste. Brief outlines of the chapters are as follows.

Chapter 1: Introduction

This chapter deals with the introduction of nuclear energy and its importance to compensate the increasing energy demands followed by a brief mention on nuclear energy programme in India. Since India has adopted closed nuclear fuel cycle, spent nuclear fuel bears huge importance for the separation of fissile isotopes and fission products. This chapter also elaborates the technological as well as industrial applications of various fission products generated from a nuclear reactor. Conventional processes which are currently in practice for nuclear waste management are also discussed along with their advantages and disadvantages. Phosphates, titanates, silicates and tungstates as potential matrices for radionuclides separation and for immobilization have been discussed in the final section of this chapter.

Chapter 2: Experimental techniques

A concise description of methods used for the synthesis of various inorganic ion exchanging materials and characterization techniques used for the identification of the phase purity of synthesized materials have been discussed in this chapter. The general procedures adopted for the preparation of various ion exchange materials like solid state synthesis route and solution methods like co-precipitation followed by oxidation have been discussed in this chapter. Characterization of the prepared phosphates, titanates, manganates, silicates etc. have been carried out mainly by powder X-ray diffraction techniques (PXRD) using lab source as well as synchrotron sources. Other complimentary techniques like Fourier transform infrared spectroscopy (FTIR), Raman spectroscopy, X-ray florescence spectroscopy (XRF) and Thermogravimetry (TG) techniques were also used. Morphologies of the synthesized materials have been studied by using microscopic techniques like scanning electron microscopy (SEM) and transmission electron microscopy (TEM). Ion exchange characteristics of the synthesized materials have been investigated by radiometric analysis using radioactive tracer by investigating the kinetics of ion exchange and ion exchange capacity of the materials. The kinetics and isotherms of ion exchange have also been studied by various kinetic models like pseudo first order, first order, pseudo second order models and isotherm models like Langmuir, Freundlich and Hill adsorption isotherm models. Brief outline of the experimental methods and the theories of used models have been elaborated in this chapter.

Chapter 3: $K_2M(PO_4)_2$; M=Ce, Zr inorganic ion exchangers

This chapter explains the synthesis and ion exchange characteristics of novel framework phosphates of cerium and zirconium with potassium ions as exchangeable ions. $K_2Ce(PO_4)_2$ and $K_2Zr(PO_4)_2$ have been synthesized by solid state reactions of KPO_3 and CeO_2/ ZrO_2. The powder XRD patterns of the synthesized samples indicate that $K_2Ce(PO_4)_2$ crystallizes in monoclinic lattice with space group $P2_1/n$, whereas $K_2Zr(PO_4)_2$ crystallizes in rhombohedral lattice with space group P-3. Differences in the ionic radii of Ce^{4+} and Zr^{4+} govern the crystal structures. In case of $K_2Ce(PO_4)_2$, potassium ions are located in the tunnel generated by the 3-dimensional framework formed by $[Ce(PO_4)_2]^{2-}$ complex ions. However, for $K_2Zr(PO_4)_2$ potassium ions are located in between the layers generated by the sheet like arrangement of $[Zr(PO_4)_2]^{2-}$ ions. Both the materials are porous in nature potassium ions are selectively exchangeable with ^{90}Sr because of their similar ionic sizes and electropositivity. Ion exchange characteristics of the title materials have been investigated using radioactive ^{85}Sr tracer solution. High K_d ~ 30000 mL/g and 8000 mL/g have been observed for $K_2Zr(PO_4)_2$ and $K_2Ce(PO_4)_2$, respectively. The ion exchange capacity (q_e) increases with increasing Sr^{2+} ions concentration for both the materials and the typical values of q_e are ~ 521 μmol/g for $K_2Ce(PO_4)_2$ and ~ 603 μmol/g for $K_2Zr(PO_4)_2$. Correlation of structure and ion exchange properties indicated that the layered structure of $K_2Zr(PO_4)_2$ is the origin for its large K_d value. The studies on kinetics and exchange isotherms of both $K_2Ce(PO_4)_2$ and $K_2Zr(PO_4)_2$ suggested pseudo-second order favourable chemisorptions process is the plausible mechanism [4].

Chapter 4: High temperature studies on $K_2Ce(PO_4)_2$

In continuation to characterization of the prepared $K_2Ce(PO_4)_2$, investigations on structural stability and phase stability at high temperature are discussed in this chapter. *In-situ* and *ex-situ* temperature dependent XRD studies are carried out to investigate the possibility of the title material as immobilization lattice. The *in-situ* and *ex-situ* high temperature powder XRD studies on $K_2Ce(PO_4)_2$ indicated its decomposition at and above 900°C via decomposition reaction: $6K_2Ce(PO_4)_2 = 4K_3Ce(PO_4)_2 + 2CePO_4 + P_2O_5 + 1.5O_2$. The *in-situ* variable temperature XRD studies also revealed that the ambient temperature monoclinic ($P2_1/n$) phase reversibly transforms to a tetragonal ($I4_1/amd$) structure at higher temperature. Also from the experimental and theoretical calculations, the high temperature crystal chemistry of $K_2Ce(PO_4)_2$ is explained in this chapter [5].

Chapter 5: Synthetic Na and K-birnessite as inorganic ion exchangers

A concise description of ^{90}Sr removal from nuclear waste using synthetic birnessite mineral has been elaborated in this chapter. Birnessite is one of the common minerals of manganese oxide and has a structure formed by layers of MnO_6 octahedral units. K, Na-birnessite type materials have been synthesized by oxidation of $Mn(OH)_2$ in presence of NaOH or KOH in an oxygen purge rate of 24L/min [6]. Interlayer spacings of the synthesized materials are ~ 7 Å, which can accommodate cations like K^+, Na^+, Mg^{2+}, Ni^{2+} and Sr^{2+} etc. The large inter layer spacing renders sodium/potassium ions to exchange when they are in contact with other ions of similar size and charge.

Ion exchangeability of the title materials have been investigated radiometrically, using ^{85}Sr tracer solution. Na/K-birnessites have shown high distribution coefficient (K_d) for the uptake of ^{85}Sr compared to ^{137}Cs. Ion exchange studies have revealed stability of these materials in wide pH range. Maximum distribution coefficient (K_d) ~ 25000 mL/g in case of Na-birnessite and ~21526 mL/g in case of K-birnessite was observed within 2h of equilibration time. Ion exchange kinetics of both the materials followed pseudo second order kinetics. Observed ion exchange results could be successfully fitted with Langmuir adsorption model. The value of obtained ion exchange capacity for Na and K-birnessite samples are 2.56 mmol/g and 0.96 mmol/g, respectively. From the interferences studies with other ions like Na^+, Ca^{2+}, Al^{3+}, it is inferred that these materials are selective for ^{90}Sr even in presence of high concentrations of interfering ions. Ion exchange studies have also been carried out by equilibrating sample with inactive $Sr(NO_3)_2$ solutions to find variation of structure after ion exchange. Ion exchange characteristics for ^{90}Sr separation by both Na, K-birnessite materials were explained in detail in the titled chapter.

Chapter 6: Temperature dependent structure properties of $K_3Gd_5(PO_4)_6$

This chapter comprises of ion exchange and high temperature studies of complex phosphate $K_3Gd_5(PO_4)_6$. Title material has an open tunnel containing three dimensional structure built by periodic arrangements of $[Gd_5(PO_4)_6]^{3-}$ ions which in turn are formed by PO_4^{3-} tetrahedra and GdO_n (n = 8 and 9) polyhedra. The empty tunnels in the structure are occupied by K^+ ions to maintain charge neutrality in the lattice. The XRD patterns in the temperature range of study 20 K - 1073K indicated no change in the crystal structure which is also supported by differential thermal analysis and Raman spectroscopy. Evolution of unit cell parameters with temperature shows systematic increase with temperature. The average axial thermal expansion coefficients between 20 K and 1073 K are: $\alpha_a = 10.6 \times 10^{-6}\ K^{-1}$, $\alpha_b = 5.5 \times 10^{-6}\ K^{-1}$ and $\alpha_c = 16.4 \times 10^{-6}\ K^{-1}$. Temperature dependent Raman spectroscopic studies also indicated no change in the coordination number of any ions in the complex [7].

As seen from the structural features and temperature dependent structural evolutions, the K^+ ions provide charge neutrality to the anionic frame of unit cell. Thus it can be expected that the K^+ ions in $K_3Gd_5(PO_4)_6$ can be exchanged by other ions. To observe possible ion exchange properties in this compound, weighed quantity of the material was equilibrated with aqueous solution of radioactive Sr^{2+} ions (^{85}Sr) and the decrease in activity of filtered solution was analyzed radiometrically. The distribution constant (K_d) estimated from the initial and final activity was significantly low ($K_d \sim 5$). This suggests that the K^+ ions are not strictly exchangeable with Sr^{2+} ions. Ion exchange properties of this compound were studied by equilibrating with radioactive and stable Sr^{2+} ions, ICP-AES results of the supernatant solution after ion exchange revealed that though there is exchange between K^+ ions and Sr^{2+}, the extent of ion exchange is minimum. This might be due to stronger bonding of the K^+ ions with the anion frame or the wavy arrangement of K^+ ions in the tunnels where the motion of ions are restricted by the adjacent ions.

Chapter 7: Pressure and temperature dependent structure properties of $K_2Fe_2Ti_6O_{16}$

This chapter elaborates the temperature and pressure dependent structural properties of hollandite lattice for the nuclear back end applications. Hollandite type materials in particular, titanates possess significant structural stabilities under geological conditions and thus hollandite type manganite or titanates are observed in nature. In view of this, tetragonal hollandite type $K_2Fe_2Ti_6O_{16}$ is synthesized by solid state synthesis route using K_2CO_3, Fe_2O_3 and TiO_2 and characterized. A tetragonal lattice with space group I4/m is used to explain its structure. The structure has octahedral MO_6 (M = Ti/Fe) as building units. The typical inter atomic distances in the octahedral MO_6 (where M = 0.75Ti+0.25Fe) units are: M-O1 =1.948(5) Å, M-O1 = 1.927(3) Å x 2, M-O2 = 1.993(4) Å, M-O2 = 2.019(3) Å x2. From the dispersion of bond lengths, the distortion in the octahedral MO_6 unit is found to be 4.090 x 10^{-4} which suggests that a nearly regular octahedral is formed around the M^{n+} ion. The stability of $K_2Fe_2Ti_6O_{16}$ has been investigated with temperature by variable temperature powder neutron diffraction and XRD as well as with pressure using in situ high pressure XRD. The tetragonal phase is found to be stable in a wider range of temperature viz. 6 K to 1273 K while it reversibly transforms to a monoclinic (I2/m) structure at a moderate pressure, viz. 3.6 GPa. High temperature stability of the Na analogous composition shows stability at higher temperature. The pressure induced structural transition and high temperature stability of the hollandite type $K_2Fe_2Ti_6O_{16}$ have been explained in the titled chapter [8]. A similar composition with Cs^+ ions ($Cs_2Fe_2Ti_6O_{16}$) is found to have an orthorhombic lattice and remains stable up to 600°C.

Chapter 8: Na-birnessite for separation of clinical-grade ^{90}Y from ^{90}Sr/^{90}Y mixture

The widespread clinical utilization of ^{90}Y for preparation of target specific radiopharmaceuticals stipulates design of superior advanced materials for facile and cost effective separation of ^{90}Y. Birnessite type phyllomanganates can be used as potential materials for radiochemical separation of clinical grade ^{90}Y from ^{90}Sr/^{90}Y mixture. This chapter deals with the separation of ^{90}Sr from ^{90}Sr/^{90}Y mixture. Ion exchange experiments in presence of ^{90}Sr/^{90}Y equilibrium mixture confirmed the exceptionally high selectivity of synthetic sodium birnessite for ion exchange of Sr^{2+} ions and the conditions have been optimized to achieve radiochemically pure ^{90}Y (> 80 % separation yield) meeting all the pharmaceutical requirements for its clinical use [9]. The separated ^{90}Y has been used to prepare ^{90}Y radiolabeled 1,4,7,10-tetraazacyclododecane-1,4,7,10-tetraacetic acid coupled dimeric cyclic RGD peptide derivative [DOTA-E[c(RGDfK)]$_2$] and the biological efficacy of the radiotracer was established in C57/BL6 mice bearing melanoma tumors [10]. The results indicated highly target specific radiotherapy and hence a cost effective mode for radiochemical separation of ^{90}Y.

Chapter 9: Thermophysical properties of relevant phosphates

This chapter is comprised of three independent sections describing ion exchange properties, thermodynamic characteristics and magnetic properties of several other prepared phosphates for the aim of thesis. First part of the chapter deals with the synthesis and ion exchange properties of complex phosphates $KLn(PO_3)_4$, Ln=Ce, Eu with potassium ions as an exchangeable ions. Ion exchangeability with inactive caesium and strontium ions in $KCe(PO_3)_4$ and $KEu(PO_3)_4$ compounds have been discussed. Second part of the chapter comprises of thermodynamic properties of two complex phosphate as $K_3Ln_5(PO_4)_6$, where Ln = Eu and Gd. Comparison of measured standard molar enthalpy of formation and molar heat capacity of these compounds by high temperature calorimeter has been discussed in this chapter. Measured standard free energy of formation from standard molar enthalpy of formation and heat capacities are discussed in this section. Third part of this chapter deals with the preparation, crystal structure and magnetic properties of complex phosphate $Mn_5(HPO_4)_2(PO_4)_2.4H_2O$. This compound is found to be stable up to 300°C and show a ferromagnetic like sharp transition at 6K [11].

Chapter 10: Summary and future scope

The present thesis gives a brief account of the importance of nuclear waste management and significance of stable ceramic materials in the back end of nuclear fuel cycle. It describes the importance of inorganic ion exchangers over organic ion exchangers in harsh conditions of nuclear waste. Several tunnel and layered structured materials have been synthesized under the scope of PhD thesis title. Ion exchangeability of these materials has been investigated for separation of $^{90}Sr^{2+}$ in presence of large concentration of several interfering ions. Among all the synthesized materials, $K_2Ce(PO_4)_2$, $K_2Zr(PO_4)_2$, synthetic Na/K-birnessite minerals have shown stability in nuclear waste conditions and exhibited ion exchange properties with ^{90}Sr. Dual properties of crystalline inorganic ion exchangers as materials for ion exchangers and stable immobilization lattices are useful in nuclear waste management. Crystal structures of the materials have been used to explain and to envisage the ion exchange properties of the synthesized materials.

Based on the results and conclusions from the study, future research scope on the aim of the nuclear waste management has been mentioned in this chapter. Selective separation of the radionuclides can be carried out by varying the size of the exchangeable ions and porosity of the material by incorporating different ligands. The preparation of more porous inorganic ion exchange materials for better elution of the loaded radionuclides and regeneration of the ion exchange material need to be explored in future.

References

[1] International Atomic Energy Agency, Application of membrane technologies for liquid radioactive waste processing, IAEA Technical Reports Series No. 431, IAEA, Vienna, Austria, 2004.

[2] K. Raj, K. K. Prasad, N. K. Bansal, *Nucl. Eng. Des*. 2006, *236*, 914–930.

[3] R. O. A Rahman, H. A. Ibrahium, Y. T. Hung, *Water* 2011, *3*, 551–565.

[4] B. Samatha, G. Prema, S. J. Patwe, S. N. Achary, R. K. Mishra, A. Kumar, A. K. Sinha, C. P. Kaushik, A. K.Tyagi, *J. Env. Chem. Eng*. 2018, *6*, 2248–2261.

[5] B. Samatha, K. K. Mishra, S. J. Patwe, T. R. Ravindran, M. K. Gupta, R. Mittal, P. S. R. Krishna, A. K. Sinha, S. N. chary, A. K. Tyagi, *Inorg.Chem.* 2017, *56*, 3335–3348.

[6] B. Samatha *et al. J. Env. Chem. Eng*, 2018, *6*, 7200-7213.

[7] B. Samatha, S. N. Achary, K. K. Mishra, T. R. Ravindran, A. K.Sinha, P. U. Sastry, A. K Tyagi, *Phys. Chem. Chem. Phys.* 2017, *19*, 6030-6041.

[8] B. Samatha, S. N. Achary, Abhishek Chitnis, Nandini Garg, P. U. Sastry, A. B. Shinde, P. S. R. Krishna and A. K. Tyagi, *Inorg. Chem*. 2018, *57*, 2157−2168.

[9] R. Chakravarty *et al. ChemistrySelect.* 2018, *3*, 10670-10676.

[10] N L. Lopano Christina, J. Heaney Peter, E. Post Jeffrey, *Am. Mineral.* 2009, *94*, 816-826.

[11] Samatha Bevara, S. N. Achary, P. D. Babu, and A.K. Tyagi, *AIP Conf. Proc.* 2015, *1665*, 030021.

LIST OF FIGURES

LIST OF TABLES

LIST OF ABBREVIATIONS

BSE	Back Scattered Electrons
DTA	Differential Thermal Analysis
FC	Field Cooled
FT-IR	Fourier Transform Infrared
HLW	High Level Nuclear Waste
HPGe	High Pure Germanium
HT-XRD	High Temperature X Ray Diffraction
ICP-AES	Induction Coupled Plasma -Atomic Emission Spectroscopy
ILW	Intermediate Level Nuclear Waste
KCP	$K_2Ce(PO_4)_2$
K_d	Distribution Coefficient
KEuPO	$K_3Eu_5(PO_4)_6$
KGdPO	$K_3Gd_5(PO_4)_6$
KMO	K-birnessite
KZP	$K_2Zr(PO_4)_2$
LLW	Low Level Nuclear Waste
MnHPO	Hureaulite Mineral
NFC	Nuclear Fuel Cycle
NMO	Na-birnessite

PND	Powder Neutron Diffraction
SE	Secondary Electrons
SEM	Scanning Electron Microscopy
SQUID	Superconducting Quantum Interference Device
TEM	Transmission Electron Microscopy
TGA	Thermogravimetric Analysis
XANES	X-ray Absorption Near Edge Structure
XPS	X-Ray Photoelectron Spectroscopy
XRF	X-Ray Fluorescence
XRD	X-Ray Diffraction
ZFC	Zero Field Cooled

Chapter 1

Introduction

1.1. Introduction

"Man shapes himself through decisions that shape his environment"

-Rene Dubos.

Enhanced quality of human life relies on high consumption of energy which in turn has immensely affected the natural fossil energy sources. Due to limited availability and non-renewable nature, the current rate of usage of natural energy sources poses a serious concern for future generations. Thus alternates to fossil energy sources and renewable energy sources are gaining importance. Nuclear energy is considered as a promising alternate energy source as it is economical and eco-friendly with zero emission of green house gases. Thus varieties of strategies for utilization of nuclear energy have been adopted all over the world. India has adopted a three stage nuclear energy program which relies on its closed fuel cycle and limited resources of uranium [1]. The reprocessing of spent nuclear fuel not only brings back the materials that did not under gone fission but also recovers additional fissile materials and useful fission products for a sustainable nuclear energy program [2]. This reduces the nuclear waste burden over the environment and cost of the nuclear waste management [3]. However, the reprocessing of spent nuclear fuel is a challenging task from chemistry, engineering and safety aspects due to high radioactivity and extreme chemical environment. A variety of methods are available for separation of ions from solution, among them ion exchange is a simple, safe and reliable technique. Inorganic ion exchangers owe a great importance in this regard compared to organic ion exchangers because of their high radiation, thermal and chemical stabilities [4]. In this thesis, efforts have been made to synthesize some crystallographically flexible inorganic ion exchange materials in the aim of nuclear back end applications and the obtained results are explained in different chapters.

Chapter 1

This chapter deals with the introduction of nuclear energy and its importance to compensate the increasing energy demands followed by a brief mention on nuclear energy programme in India. This chapter also elaborates the technological as well as industrial applications of various fission products generated during the operation of nuclear reactor. Conventional processes which are currently in practice for nuclear waste management are discussed along with their advantages and disadvantages. The importance of ion exchange process and crystalline inorganic ion exchangers in nuclear waste management are mentioned in brief. Subsequently, various framework type phosphates, titanates, silicotitanates, manganates and tungstates as potential ion exchangers for radionuclides separation as well as host matrices for radionuclides immobilization have been discussed in this chapter [5].

1.2. Nuclear energy program

Growing energy demands around the world leads to an energy transition, many policies are mainly aimed to reduce the burden of green house gases and to maintain sufficient renewable energy resources for future generations owing to regimes [6]. Until now, fossil fuels such as coal/peat contributes maximum to the world power generation, followed by natural gases and petroleum products. Many technological limitations reduces the contribution of renewable energy sources like solar, hydro, wind energies and still remains underutilized [6].

Nuclear energy is considered as an innovative and efficient source of energy with zero carbon dioxide emission, more over high burn-up values can be achieved with safe and inexpensive operation conditions. According to nuclear fission technology, heavy nuclei like ^{233}U, ^{235}U, ^{239}Pu can shatter into lighter nucleus by the bombardment of thermal or fast neutrons and releases enormous energy per fission[7]. Also in the nuclear reactor, fertile heavy nuclei like ^{238}U and ^{232}Th can be transformed to fissile ^{239}Pu and ^{233}U, respectively which can be further utilized. According to present power scenario in India, ~ 6000MWe power has been generated by utilizing present operating nuclear power reactors by the fission of heavy nuclides [2a]. In India, a closed nuclear energy program is designed bearing in mind that optimum utilization of limited resources of uranium and large reserves of thorium for a sustainable long term energy source.

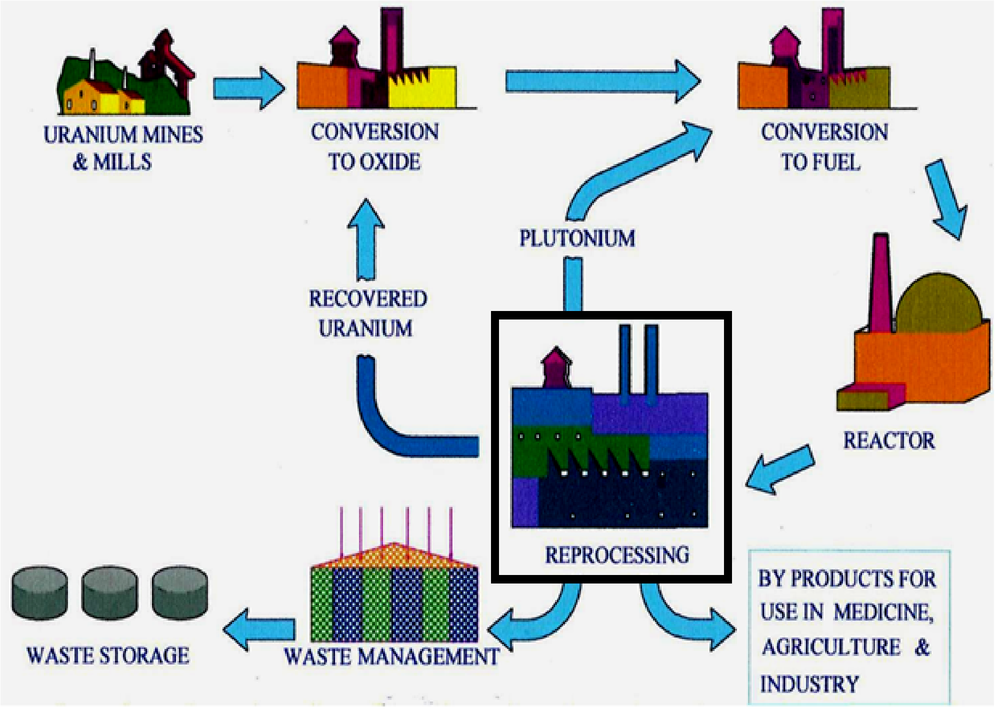

Fig.1.1: Schematic diagram representing closed nuclear fuel cycle

In light of the closed nuclear fuel cycle, spent nuclear fuel undergoes reprocessing for recovery of fissile and fertile nuclides for further utilization. The first generation nuclear reactor named Pressurized Heavy Water Reactor (PHWR) is the flagship reactor of the Indian nuclear energy program. PHWR works by the fission of natural uranium with heavy water as coolant and moderator [1]. Second stage of Indian nuclear energy program is the fast breeder reactor, where the fission of ^{239}Pu recovered from PHWR is used as energy source and also to produce ^{233}U from ^{232}Th. Huge reserves of thorium in India drives nuclear energy program towards third generation nuclear reactors like Advanced Heavy Water Reactor (AHWR) by using ^{233}U as nuclear fuel for fission and to produce more ^{233}U from ^{232}Th. Additionally, several innovative reactors like High Temperature Reactor (HTR), Molten Salt Breeder Reactor (MSBR) etc. are also aimed for future nuclear energy. Although, nuclear energy is a promising sustainable energy source, the waste generated from nuclear reactors is a concern and is being addressed worldwide by different policies, various research and development programs.

1.3. Nuclear waste

Many countries like France, Russia, Japan, India, China, etc. have adopted closed nuclear fuel cycle, whereas countries like USA, Canada, Finland, Sweden etc. have opted for direct disposal of spent nuclear fuel [8]. In closed nuclear fuel cycle, the spent nuclear fuel is allowed to cool under water deposits in order to allow the isotopes with short half-life to decay to permissible radioactive limits. The spent nuclear fuel for a typical PHWR type reactor contains ~96% U, ~1% Pu, ~3% fission products like ^{137}Cs, ^{90}Sr, ^{106}Ru, ^{99}Tc etc. along with variety of rare earths and minor actinides ^{237}Np, ^{241}Am, ^{245}Cm, ^{144}Ce. [9] Typical values of half lives of shorter and long lived isotopes present in spent nuclear fuel are given in Table 1.1. Reprocessing of spent nuclear fuel is carried out by PUREX process for PHWR type nuclear reactors in order to separate fissile uranium and plutonium elements from rest of the nuclear waste solution [10].

Table 1.1: Half-lives of radionuclides present in spent nuclear fuel

Short lived isotopes present in HLW		Long lived isotopes present in HLW	
Isotope	**Half life(Y)**	**Isotope**	**Half life (Y)**
^{90}Sr	28.8	^{99}Tc	2×10^{5}
^{106}Ru	1	^{129}I	1.7×10^{7}
^{137}Cs	30	^{237}Np	1.6×10^{6}
^{144}Ce	1.3	^{238}Pu	85.3
^{147}Pr	2.3	^{239}Pu	24360
^{244}Cm	17.4	^{240}Pu	6500
		^{241}Am	432.2
		^{242}Am	141
		^{245}Cm	8500

According to PUREX process, chopped spent nuclear fuel is dissolved in 3M concentrated nitric acid, stripping of the fissile uranium and plutonium isotopes has been carried out by taking advantage of variable oxidation states of uranium and plutonium. Mixture of 30% tributyl phosphate (TBP) in an organic medium like dodecane solution is added to the spent fuel acidic mixture in order to strip uranium, plutonium from rest of the radionuclides present. Uranium and plutonium in VI oxidation state form an organic soluble stable $U/PuO_2(NO_3)_2.2TBP$ complex and this complex migrates to organic phase from the aqueous phase. Organic phase containing both U^{6+} and Pu^{6+} is further processed to separate pure plutonium and uranium. Reduction of Pu^{6+} in organic phase to Pu^{4+} by uranous nitrate stabilized with hydrazine renders the migration of Pu^{4+} to aqueous phase and pure U^{6+} is trapped in organic phase, pure Pu^{4+} is isolated in aqueous phase.

Using PUREX process, pure uranium and plutonium can be extracted with high yields. Such solvent extraction process is not found suitable for separation of fission products selectively from nuclear waste because of generation of huge secondary waste volume and thus separation of fission products from nuclear waste using different methods has attracted huge research interest. Selective separation of long lived fission products from nuclear waste is carried out in such a way that the chosen process must reduce waste volume without generating huge secondary waste volume [4].

1.3.1. Types of nuclear waste

Classification of nuclear waste is crucial in view of reprocessing and for safe disposal of nuclear waste. Nuclear waste can be classified according to physical state, chemical, biological, radiological, mechanical properties and finally depending on the nature of waste origin. Various states of nuclear waste like solid, liquid and gaseous states have been generated at various stages of nuclear fuel cycle. Among these types of nuclear waste, liquid nuclear waste treatment needs more attention because of high volume and mobility. Solid nuclear waste arises from the insoluble spent fuel or clad material left in acid medium. Gaseous nuclear waste arises by the dust escaped from conveyer belts, crushers and high temperature reaction processes generating fumes etc. [11]

Highest volume of nuclear waste generated during reprocessing of spent fuel is in liquid state because of the dissolution of spent nuclear fuel. Concentration of the radioactivity in the nuclear waste varies from the source of generation. Depending on the amount of radioactivity, liquid nuclear waste can be classified as high level liquid nuclear waste (HLW), intermediate level liquid nuclear waste (ILW), low level liquid nuclear waste (LLW). Liquid nuclear waste containing concentration of radioactivity above 3.7×10^9 Bq/m^3 is treated as HLW. In case of ILW radioactivity vary in between 3.7×10^7 to 3.7×10^9 Bq/m^3 and for LLW radioactivity is in the range of 37 to 3.7×10^4 Bq/m^3. [7, 11b] Classification of the liquid nuclear waste with respect to radioactivity and the constituents of different categories of waste are given in Table 1.2.

Table 1.2: Classification of nuclear waste in accordance with radioactivity

Category	Solid Surface Dose (mGy/h)	Liquid Activity (Bq/m^3)	Gaseous Activity Level (Bq/ m^3)
Extreme Waste[3]	<2	$< 3.7\times10^4$	< 3.7
Low Level Waste[3]	2-20	3.7×10^4 to 3.7×10^7	3.7 to 3.7×10^4
Intermediate Level Waste[12]	>20	3.7×10^7 to 3.7×10^9	$> 3.7\times10^4$
High Level Waste[13]	Alpha Bearing	3.7×10^9 to 3.7×10^{14}	$> 3.7\times10^4$

1.3.1.1. Constituents of HLW

Major constituents of high level liquid nuclear waste are unprocessed uranium and neutron captured transuranic series elements, fission products, etc. [7] Though HLW constitutes only 3% of the total nuclear waste generated, it causes 95% of the total radioactivity of nuclear waste [14]. High level waste gives of large amounts of heat and radioactivity for several hundred of years due to α, β, and γ-decay of the radionuclides present. HLW with high radioactivity and actinides with long half lives cannot be stored in liquid form for several years to reduce the radioactivity to permissible limits. List of long lived radionuclides and their half lives are given in Table 1.1. Thus separation of fission products from HLW by suitable materials is a tedious process and several ceramic materials have been investigated for separation of radionuclides and for immobilization [4, 5c, 15]. Process of immobilization of radionuclides using borosilicate glasses is called as vitrification and the vitrified waste is buried into the deep geological repositories. Various process and materials for the reprocessing of the HLW and immobilization lattices have been discussed in the subsequent sections [2b, 3, 14b].

1.3.1.2. Constituents of ILW

Intermediate liquid nuclear waste comprises of radionuclides with long half lives and low concentration of α-emitting radionuclides along with β, γ-emitting radionuclides. Intermediate level nuclear waste is not stored directly, whereas converted into low level waste. Long lived radionuclides present in ILW are concentrated in order to convert the ILW to HLW. In order to separate long lived radioisotopes, many ceramic and polymer based materials have been reported and much research efforts were dedicated to investigate materials with high radiation stability and high decontamination factors [5d, 16]. Reprocessing of ILW using various organic, inorganic resins and polymer based materials has been explained in the subsequent sections.

1.3.1.3. Constituents of LLW

Low level liquid nuclear waste comprises 95% of the total nuclear waste volume generated in the nuclear fuel cycle but carries ~1% of total radioactivity of the nuclear waste.

LLW constitutes are mostly β and γ emitting radionuclides with shorter half lives [5d]. LLW arises not only from nuclear power reactors but also from hospitals, laboratories and industries using radioactive materials. Low level nuclear waste treatment is carried out by concentrating the waste and contained radionuclides are allowed to decay to the permissible radioactivity level and discharged into the environment. Indigenously developed materials like resorcinol formaldehyde resin (RF resin) and iminodiacetic acid (IDA) were used in industrial scale for selective separation, also can be regenerated for multi cycle applications[2]. Large quantity of LLW is being reprocessed using these materials.

1.4. Radionuclides separation and their importance

Currently many countries including India have launched long term program for the remediation of nuclear waste by separating high concentration fission products with long half lives such as ^{137}Cs, ^{90}Sr, ^{99}Tc, ^{245}Am, ^{106}Ru, ^{144}Ce etc. [8] Separation of these long lived radionuclides reduces volume of the nuclear waste significantly and hence reduces the nuclear burden on the environment and cost of nuclear management [5c, 9, 17]. Investigation of various materials for separation of radionuclides has been started since late forties; research in this area is a challenge due to extreme conditions of nuclear waste, safety and security issues. Besides, many fission products produced during the nuclear fuel cycle have vast technological, industrial as well as medicinal applications. Technological as well as medicinal relevances of some of the fission products are as follows.

1.4.1. Importance of ^{137}Cs

Among the wide spectrum of fission products generated during nuclear fission, ^{137}Cs is of great importance because of long half life (30.17y) as well as high energy γ-decay scheme. ^{137}Cs decays to ^{137m}Ba by emitting β^- of energy 0.512MeV (95%) and the metastable ^{137m}Ba converts to a stable ^{137}Ba by emitting 0.662 MeV γ-ray. ^{137}Cs directly converts to stable ^{137}Ba by emitting 1.17 MeV (5%) energy β-radiation. Typical radioactive decay scheme of ^{137}Cs is shown in Fig.1.2. ^{134}Cs and ^{137}Cs are the isotopes of Cs produced during reactor operation, with 7% combined yield of ^{133}Cs and ^{134}Cs. Fission yield of ^{137}Cs is ~6% of all the fission products generated. Recovered ^{137}Cs from nuclear waste can be used for sterilization of medical supplies, food items and also has many industrial applications like generating heat shrink plastic tubing. As a radiation source, ^{137}Cs possess many medicinal applications like brachytherapy and blood irradiation, etc. as well as hygienisation of sewage sludges [18].

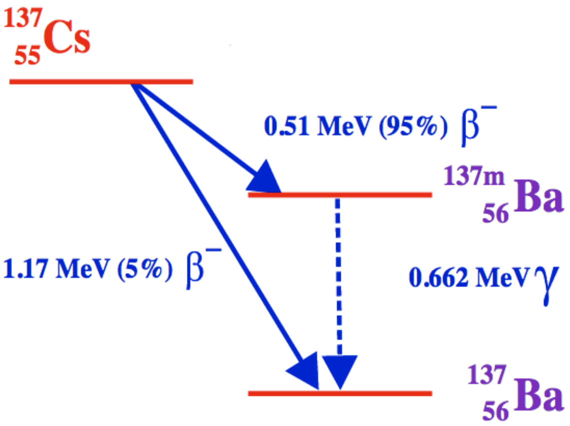

Fig.1.2: Decay scheme of ^{137}Cs

1.4.2. Importance of ^{90}Sr

^{90}Sr is another important long lived radio isotope with high fission yield. ^{90}Sr is a β-emitter with half life of 28.8y and having specific activity of 1.5×10^2 Ci/g. Nuclear reactors, radioactive laboratories, radiopharmaceutical laboratories, industries with radiation sources are the other sources of ^{90}Sr. Among the various radionuclides present in the nuclear waste, separation of ^{90}Sr is a major concern because of its high concentration and acidic nature of the medium. ^{90}Sr separated from nuclear waste can be utilized in thermoelectric generator in spacecrafts, works as radioactive tracer in agriculture and also utilized as a bone seeker in cancer therapy. ^{90}Sr converts to ^{90}Y by emitting a β-particle and ^{90}Y is also a β-emitter with decay energy of 2.28 MeV and half life of 64h. Typical radioactive decay scheme of ^{90}Sr is shown in Fig.1.3.

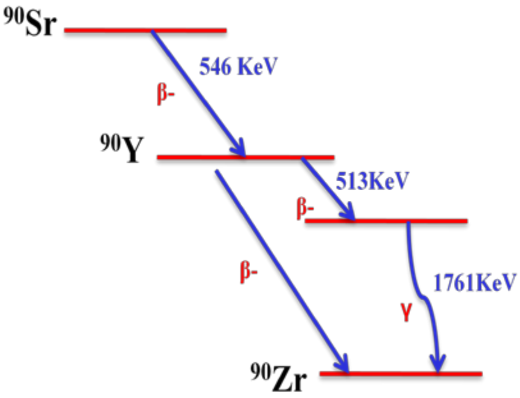

Fig.1.3: Decay scheme of ^{90}Sr

Both ^{90}Sr and ^{90}Y generates huge amount of heat in nuclear waste, while ^{90}Y plays a significant role in the treatment of hepatocellular carcinoma (HCC) and other liver cancers [19]. Selective separation and immobilization of ^{90}Sr thus plays an important role not only in the nuclear waste management but also for generation of affordable and pure ^{90}Y. Various technological as well as conventional approaches have been developed for separation and immobilization of ^{90}Sr, which has been discussed in other sections of this thesis.

1.4.3. Importance of ^{99}Tc

^{99}Tc is generated during nuclear fission of ^{235}U with a fission yield ~6%; possess significantly long half life (~211,000 y). ^{99}Tc converts to stable ^{99}Ru isotope by emitting beta particles. Long half life and high energy beta decay impart significance for the separation of

^{99}Tc from nuclear waste. ^{99}Tc forms a stable anionic complex with ^{129}I and generally escapes from the cationic ion exchangers [15, 20]. Impact of pertechnate on the environment is high because of its significantly long half life. ^{99m}Tc plays a significant role as cancer diagnostic isotope with half life of 6h and can be generated by the isomeric transition of ^{99}Mo, which is a widely used process for diagnosis of cancer.

1.4.4. Importance of ^{106}Ru

^{106}Ru is a fission product of ^{238}U with half life of 1year and converts to stable ^{106}Rh isotope by emitting β^- particles with decay energy of 3.54 MeV. During reprocessing of the spent fuel, dissolved ^{106}Ru forms a stable ruthenium nitrosyl complex, which can be separated by oxidation and distillation of RuO_4 [15]. Typical estimation of 1L of nuclear waste solution after reprocessing contains 500 GBq of ^{106}Ru even after 4 years of cooling [21]. Moreover, removal of isotopes like ^{106}Ru can reduce the nuclear waste burden significantly. However, chemically pure ^{106}Ru separated from nuclear waste solution is used in brachytherapy because of its high energy (3.54 MeV) β^-decay.

1.4.5. Importance of ^{241}Am

^{241}Am is not the direct decay product of ^{235}U but is the neutron capture product of ^{239}Pu generated by neutron capture of ^{238}U. ^{239}Pu decays to ^{241}Am by absorbing two neutrons and emitting one β^- particle. Though ^{241}Am is not produced in large quantities, separation of ^{241}Am is very tedious and hence expensive. ^{241}Am is utilized as ionizing smoke detector, as a neutron source and as parent element for generation of many other radioactive elements [22]. There are many such fission products with various applications in nuclear medicine and industries. Table 1.3 describes the uses of various fission products generated during reactor operation. Details of selective separation of radioisotopes have been described in subsequent chapters of the present thesis.

Table 1.3: Various applications of some of the fission products

S. No	Isotope	Relevance
1	^{137}Cs	• Radiation source in brachytherapy • Blood irradiation • Food irradiation • Hygienisation of sewage sludge
2	^{90}Sr	• ^{90}Y generator • Thermo electric generator in spacecrafts • Bone pain palliation
3	^{99}Tc	• Cancer diagnostic isotope
4	^{106}Ru	• Used in brachytherapy
5	^{241}Am	• Utilized as ionizing smoke detector • Neutron source
6	^{131}I	• Hyperthyroidism (solution and capsules) Thyroid carcinoma
7	^{125}I	• Used in brachytherapy
8	^{144}Ce	• Interstitial and intravascular brachy therapy
9	^{242}Cm	• Used in Curium batteries

1.5. Nuclear waste management

India as a developing country lies in the list of selected countries having an elaborated nuclear energy program. At present, India has experience in all stages of nuclear fuel cycle and specifically expertise in reprocessing and disposal of waste of heavy water reactor types

[2a, 23]. Typical figure indicating the steps involved in nuclear waste management is shown in Fig.1.4.

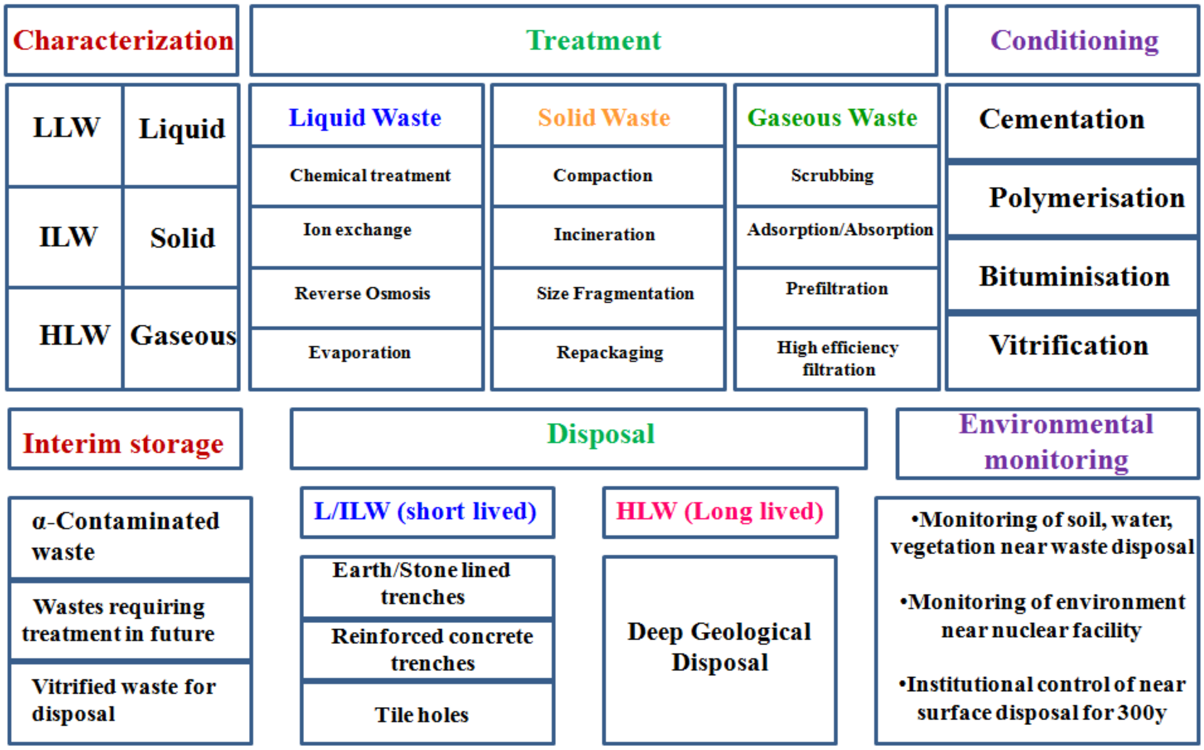

Fig.1.4: Typical figure indicating the steps involved in nuclear waste management

1.5.1. Management of HLW

Though reprocessing of spent nuclear fuel is the most accepted strategy for attaining closed nuclear fuel cycle, generation of high level liquid nuclear waste is of major concern [7, 14a, 24]. Most of the constituents of HLW are long lived isotopes with high decay energy. Significant research is being carried out currently to generate wealth form nuclear waste by investigating materials for selective separation of radionuclides from nuclear waste and for immobilization. Borosilicate glass is the promising material for immobilization because of its integrity for a span of thousands of years. Currently synroc based sodium silicate glass formulations are treated as worldwide acceptable immobilization lattices [5b, c, 7, 14a, 16, 21, 24], because of wide range of acceptable chemical compositions with minimum leachability and long durability. Ceramic lattices namely lead iron glass, titanate based glasses are widely reported as potential immobilization lattices [25]. Though vitrification of high level liquid waste is well developed on industrial scale in India, further reduction and elimination of radioactive inventory by other suitable means is an ongoing research process. Elimination of heat generating radionuclides like ^{137}Cs, ^{90}Sr is considered as pretreatment of the nuclear waste which significantly reduces the radioactive inventory in the waste to be disposed. The solvent comprising of 0.2M extractant N,N,N′,N′-tetra-2-ethylhexyl diglycolamide (TEHDGA), 30% TEHDGA+30% Isodecyl alcohol/n-dodecane developed on plant scale and specific for decontamination of rare earths and minor actinides in simulated high level waste conditions [26]. ^{241}Am was separated with decontamination factor ~ 3000 using TEHDGA as an extractant. Calix-[4]-arene-Crown-6 (Calix crown) derivatives in the 1,3-alternative conformations exhibits high specificity for ^{137}Cs separation from nuclear waste solution and separated ^{137}Cs is used for irradiation of blood.

1.5.2. Management of ILW

Intermediate level nuclear waste is generated mainly because of chemical decladding of spent fuel or by the waste evaporation cycle. ILW is mostly alkaline in nature with dissolved salts in it. Most of the radioactivity of the ILW is generated due to ^{137}Cs, ^{90}Sr, ^{106}Ru and low concentrated elements like ^{125}Sb, ^{144}Cs, ^{99}Tc [16, 17b, 24]. Major constituents of ILW and concentration of radionuclides before and after elution are given in Table 1.4. The earlier process considered for the disposal of ILW is cementization. Preconcentration of ILW using various inorganic ion exchange materials like ammonium molybdophospahte [27], layered zirconium phosphates [5c, 28], manganese oxides [29] has minimized the waste disposal volume with high decontamination factors. Resorcinol-formaldehyde resin is used for the separation of ^{137}Cs from ILW thus generating two streams of ILW one comprised of rich ^{137}Cs and the other is ion exchange effluent of the ILW. Resorcinol formaldehyde synthesized in plant scale at BARC, Trombay takes ^{137}Cs with distribution constant K_d~7000 mL/g, at an optimum flow rate of 3-4 bed volumes/h. [30]

Table 1.4: ILW constituents before and after resorcinol-formaldehyde treatment

Parameter	**ILW (mCi/L) (pH = 11-12)**	**Effluent (mCi/L) (pH = 8-10)**
Gross β	3.4-4.5	1×10^{-2} to 3×10^{-2}
^{137}Cs	2.98 to 3.95	1×10^{-3} to 4×10^{-3}
^{90}Sr	1.3×10^{-2} to1.5×10^{-2}	6×10^{-3} to 7×10^{-3}
^{125}Sb	1.6×10^{-3} to 9.89×10^{-3}	2×10^{-3} to 5×10^{-3}
^{106}Ru	1.5×10^{-3} to 9.89×10^{-3}	2×10^{-3} to 7×10^{-3}

1.5.3. Management of LLW

LLW is generated from many sources like hospitals and industries where radionuclides are used. Most of the low level nuclear waste generated is stored to disintegrate all the radionuclides to well below the permissible limits and then discharged into the environment.

1.5.4. Management of gaseous waste

In order to prevent the direct flow of radioactive inventory through air route, all the nuclear facilities are having an off-gas monitoring system. India has developed very efficient gas cleaning scrubs like venture, dust, packed bed, cyclone separators and high efficiency particulate air (HEPA) filters [31]. Choice of system depends on specific activity, type of radioactivity, density, size distribution, specific volatile contaminants and their concentrations. Minimization of radioactive inventory from the intermediate/high level nuclear waste can be achieved by practicing various chemical methods and by different inorganic/organic materials. Conventional methods currently in practice for nuclear waste treatment such as chemical methods, precipitation, evaporation, ion exchange, solvent extraction etc. are elaborated in the following sections.

1.6. Methods for nuclear waste treatment

In order to concentrate the intermediate and low level liquid waste, there are various chemical, physical and biological methods for the treatment of liquid nuclear waste.

1.6.1. Chemical methods

Chemical methods involve precipitation and co-precipitation using suitable precipitating agents, oxidation or reduction of elements using various oxidizing or reducing agents, absorption, adsorption, ion exchange and other chemical reactions which facilitate the separation of radionuclides from large quantities of liquid nuclear waste. Ion exchange materials play a major role in selective separation of radionuclides from waste solutions because of size, charge and ion selectivity. Solvent extraction is a promising process used for the separation of uranium and plutonium from large quantities of fission products.

Significance of process like solvent extraction, precipitation, ion exchange is explained in the following sections.

1.6.2. Physical methods

Physical methods for reprocessing of nuclear waste comprises of separation without any chemical change of nuclear waste constituents. Filtration, stripping, sedimentation, flotation, reverse osmosis etc. are the methods in use to concentrate the nuclear waste without changing the chemical state and composition of reprocessing solution.

1.6.3. Biological methods

Biological methods involve microorganisms for decontamination of nuclear waste. Bioremediation to radioactive nuclear waste offers an inexpensive and *in-situ* alternative to the commonly used physical and chemical methods. Bioprecipitaiton especially as metal phosphates by microbes offers a promising alternative to physicochemical process for precipitation of low concentrated heavy metals from large volumes of liquid nuclear wastes. Bacteria such as Citrobacter Spand recombinant Escherichia [32] are reported for the precipitation of heavy metals as metal phosphate from nuclear waste. Many other microbes also have been known for the biodegradation of radioactive materials into simple molecular units which can be separated in simpler ways.

Conventional process like chemical treatment, solvent extraction, filtration, evaporation, membrane filtration and ion exchange process are used for the preconcentration of nuclear waste. Processes which are currently in use for nuclear waste management with advantages and limitations were summarized in Table 1.5.

Table 1.5: Chemical methods for pre-concentration of nuclear waste along with advantages and disadvantages

Technology	Features	Limitations
Precipitation	• Suitable for large volumes and high salt content waste • Easy non-expensive operations	• Low DF • Efficiency depends on solid-liquid separation step
Ion exchange	• Good chemical, thermal and radiation stability • Large choice of products ensuring high selectivity	• Affected by high salt content • Regeneration and recycling often difficult employed
Evaporation	• DF > 10^4 to 10^6 • Well established technology • High volume reduction factor • Suitable for a variety of radionuclide	• Process limitations (scaling, foaming, corrosion, volatility of certain radionuclides) • High operation and capital costs
Reverse osmoses	• Removes dissolved salts • DF 10^2–10^3 • Economical • Established for large scale operations	• High pressure system, limited by osmotic pressure • Non-back washable, subject to fouling
Ultrafiltration	• Separation of dissolved salts from particulate and colloidal materials • Good chemical and radiation stability for inorganic membranes	• Fouling • Organic membranes subject to radiation damage
Microfiltration	• High recovery (99%) • Low fouling when air backwash	• Sensitive to impurities in waste stream
Solvent extraction	• Selectivity enables removal, recovery or recycle of actinides	• Generates aqueous and organic secondary waste

1.7. Conventional methods for nuclear waste treatment

1.7.1 Precipitation

Chemical precipitation is a well established method for treatment of low/intermediate level waste and is extensively used in nuclear waste processing plants as well as at fuel fabrication facilities. Precipitation methods are widely used for softening of water and current improvement in this process meets the requirement of specific radioactive element removal from nuclear waste. Precipitation methods are particularly more advantageous where large volume of waste contains relatively less concentration of radionuclides. High salt concentrations in nuclear waste solutions do not affect the precipitation of radionuclide and thus the process is cost effective compared to other alternative techniques. Removal of radionuclides by precipitation using a precipitating agent comprises of following steps;

a) Addition of suitable reagent

b) Flocculation of radionuclides

c) Sedimentation

d) Solid-Liquid separation

Efficiency of co-precipitation by chemical treatment is defined by two factors namely volume reduction factor (VRF) and decontamination factor (DF). Decontamination factor is the ratio between total activity in feed solution and total activity in effluent. (*Equation 1.1*)

$$\mathrm{DF} = \frac{\text{Total activtvy in feed } (a_f v_f)}{\text{Total activtvy in effluent } (a_e v_e)} \qquad (1.1)$$

Where a_f and v_f are the activity of feed solution and volume of the feed solution respectively, a_e and v_e are the activity and volume of the effluent. Higher decontamination factors confirm the separation efficiency of the material and technique used. Precipitation of radionuclides mainly depends on chemical properties of medium like pH, speciation, concentration of radionuclides present etc. It also depends on physical properties like electrical conductivity, turbidity, emulsifying ability, density and surface tension of the medium. Presence of organic liquids in the waste solution adversely effects emulsification and form colloidal suspensions thereby reducing DF [33].

Majority of the precipitation techniques use metal hydroxides to precipitate the heavy metal ions from the nuclear waste stream under neutral or alkaline medium. In this process, most of the radionuclides get hydrolyzed and get suspended either by co-precipitation or by sorption. Separation of rare earths and actinides by precipitating out actinides using lanthanide oxalates is achieved in slightly acidic medium [34].

Table 1.6: Various precipitating agents in use for separation of fission products

Element	Precipitating agent	pH
Pu, Am	Ferric hydroxide, Oxalates	7-12
^{137}Cs	Ferro cyanide, Ammonium molybdophosphate	6-10
^{106}Ru	$Fe(OH)_2$, Cobalt sulphide	1-8.5
^{90}Sr	$BaSO_4$, MnO_2	>8.5

Precipitation of alkaline earth metals and transition elements like Ni, Co, Zn, etc. can be achieved by complexing agents like EDTA (Ethylene diamine tetra acetate). Various precipitating agents are in use for the separation of various metals, details of the elements and precipitating agents are listed in Table 1.6. Precipitation allows the nuclear waste stream to divide into two streams having low and high radioactivity constituents. Disadvantage with this process is, achieving high decontamination factors in single step is tedious and requires high amount of precipitating agents resulting in large amounts of secondary waste volume. Achieving high decontamination factors in accordance with the disposal limit of nuclear waste into the environment is difficult to achieve using precipitation method.

1.7.2. Solvent extraction

Solvent extraction plays a major role in extraction of uranium from pitchblende (U_3O_8) ore [35]. Extraction of uranium from highly corrosive sulfuric acid and nitric acid containing dissolved pitchblende was carried out by di-(2-ethyl hexyl) phosphoric acid (DEHPA), mixture of trioctyl and tridecyl amines, and tributyl phosphate [36]. Partition of spent nuclear fuel into fissile isotopes, transuranic elements and fission products is carried out by solvent extraction process. Solvent extraction is widely used because of its simplicity, large scale applications, ease of separation and wider scope. Solvent extraction can be carried out with minimum instrumentation and in shorter time. Solvent extraction is the process of rapid transfer of one or more components of interest from the feed usually solid dispersed in liquid medium to a physically separable phase which is immiscible with the original solvent phase [37]. Removal of radionuclides in this technique is based on the solubilities of the radionuclides in aqueous stream solution to that of extractant containing organic medium. Some precious isotopes like ^{137}Cs, ^{90}Sr, ^{242}Am, ^{245}Cm etc. can be extracted using various organic extractants like calixarenes and crown ethers like dicyclohexo-18-crown-6 and dibenzo-18-crown-8. [34b]

Crown ethers are another class of organic compounds containing macro cyclic polyether compounds. Mc.Dowell *et al.* have reported that rigid benzo-crown ethers are having high tendency to extract monovalent ions, whereas cyclohexa-crown-ethers have high tendency to extract bivalent ions [38]. Though solvent extraction is well utilized technique to extract uranium and plutonium from spent nuclear fuel solution, it has serious limitation in extraction of fission products from the reprocessing solution because of large volume of secondary nuclear waste generation.

1.7.3. Solid-liquid extraction

In order to overcome the challenges like incomplete recovery of the radionuclides, large volume of secondary waste generation, disposal of large quantities of organic solvent into the environment etc. in the separation processes like precipitation and solvent extraction, solid-liquid extraction methods are preferred. This technique overcomes the disadvantages over the conventional separation process. Selective separation of radionuclides can be carried out by using various sorbents which makes the separation process more economical with more yields compared to other separation techniques. Solid liquid extraction is used in nuclear fuel cycle for the treatment of the nuclear waste generated at various stages using different sorbents and ion exchangers.

1.7.3.1. Sorption

Preconcentration of high level liquid nuclear waste can be carried out by selective separation of radionuclides using sorption of radionuclides of interest with different inorganic/organic materials having stability in nuclear waste conditions. Sorption is accumulation of solutes over a surface because of attraction between the solute particles and adsorbent surface. Unsaturated surface forces of the adsorbent can be balanced by the adsorption of the solute particles on its surface thus preferential concentration of the solute molecules occur near the proximity of the adsorbent. Both short range (repulsive forces) and long range (attractive forces) forces gets balanced because of accumulation of sorbate molecules on sorbent. Accumulation of solute concentration occurred only at the surface of sorbent is called as adsorption, whereas solute particles dispersed uniformly throughout the sorption material is called as absorption. Depending on the nature of bonding between adsorbate (solute molecules) and adsorbent, surface sorption can be divided into physisorption and chemisorption.

Physisorption: Adsorption is called physisorption if van-der-waal forces of attractions are responsible for adhering of solute particles over the adsorbent surface.

Chemisorption: Sorption of adsorbate molecules over the surface of adsorbent is called as chemisorption if it occurs due to formation of chemical bond.

1.7.3.2. Ion exchange

Ion exchange materials are the insoluble solids in liquid medium having either cations or anions bound to it in ionic fashion. Ion exchange is a charge compensation process, for every unit charge that migrates into the material, equal amount of charge migrates from the material to maintain the charge neutrality. Ion exchange process is different form physisorption and chemisorption. In these two processes, charge neutrality has been achieved by sorbing the ion but without a need to desorb or release of any ion. As no ion is released, material has to provide bonding at the surface either by physical or weak chemical forces. Since ion exchange is an equilibrium process, selectivity of an ion over another can be measured by an equilibrium constant called distribution coefficient (K_d) defined as distribution of ion of interest between solid and liquid phase at equilibrium and has a unit mL/g. Many factors like functionality of the active site, pore size, crystal structure of the material, size, charge and extent of hydration of the ion of interest, concentration and composition of the solution in contact with the ion exchange play important role on the values of distribution coefficients. The equilibrium constant can be calculated using (*equation 1.2*)

$$K_d = \frac{[A_i - A_f]}{A_f} \times \frac{V}{W}\left(\frac{mL}{g}\right) \qquad (1.2)$$

Where A_i = counts before equilibration, A_f = counts after equilibration, V= volume of solution in mL, W = mass of the sorbent in gram.

Ion exchange is an extensively used process for the separation of radionuclides from nuclear waste solutions because the process occurs depending on ionic radii and charge of the ions undergoing the process. Various amorphous and crystalline inorganic materials have shown potentials to separate radionuclides from nuclear waste conditions. Clearfield *et al.* have reported crystalline acid salts of zirconium exhibiting ion exchange with various radionuclides and successfully correlated the crystal structure with ion exchange property for the first time [28, 39]. Wide variety of inorganic ion exchange materials are currently in use, some of them are discussed in further sections of this chapter.

1.7.3.3. Inorganic materials for nuclear waste reprocessing

For the first time large scale nuclear waste treatments were carriedout using zeolites as inorgnaic ion exchangers, for over 25 years zeolites were in use for the separation of radionuclides. Owing to the ion exchange abilities of zeolities, many technological as well as industrial relevances such as water softeners in detergents etc. were observed. Zeolites are the crystalline aluminosilicates formed by the framework arrangement of tetrahedral $[SiO_4]^{4-}$ and $[AlO_4]^{5-}$ units via oxygen bridges [40]. Zeolites form porous structures with cavities and tunnels thus used as ion seives. Zeolites are commonly mesoporous in nature, large pore size results relatively lower selectivity thus not suitable for the radionuclides separation in presence of high to medium range salt concentrations. In addition to this, dissolution of Al^{3+} from the framework at extreme pH limits their usage to narrow pH range [41].

Ammonium molybdophosphate with chemical formula $(NH_4)_3PMo_{12}O_{40}$ has been extensively used for separation of ^{137}Cs from high level liquid nuclear waste. Ammonium ions present in the structure are exchangeable with ^{137}Cs because of comparable ionic radii and ease of exchangeability [27, 30]. Manganese oxide minerals with framework structures having exchangeable sodium and potassium ions are selective for separation of ^{90}Sr [24, 33a]. Calixarenes and crown ethers with different functional groups have shown high decontamination factors for radionuclides separation, for example diglycolamide functionalized calix [4] arene is used to separate ^{137}Cs and ^{90}Sr [7, 38].

A large number of materials with nanostructure, i.e. with larger surface to volume ratio have been considered as promising materials for such applications. Though the quantitative separation is excellent in such materials, the stability and reproducibility is yet to be established. The concepts of structural features have been used to develop new and efficient materials for separation of radionuclides [42]. Ceramic materials with structure similar to the rocks and minerals are the best host lattice for fixing of nuclear waste for longer period. These materials will overcome the drawback of the conventional glass compositions in regard of possible devitrification and following accelerated leaching of the radioactive ions to the environment. Thus ceramic materials have been considered to be the most promising due to their structural stability and inertness to harsh chemical and thermal conditions of nuclear waste. Several compositions in perovskite, zirconolite, pyrochlore, titanate, rutile, zircon and monazite structures have been considered for fixing different type of radionuclides [21, 43].

1.8. Inorganic ion exchangers

Materials to be used in nuclear back end applications should have high thermal, mechanical stability and need to be resistant to ionizing radiation. Although organic ion exchangers possess vast technological as well as industrial relevances, they lack stability in harsh nuclear waste conditions and thus more attention is being given to inorganic ion exchangers. Of these inorganic ion exchangers, framework connected phosphates, silicates, metal oxides like titanates, tungstates, molybdates, clays, hetero poly acid salts and layered double hydroxides (anion exchangers) offered superiority in separation of radionuclides from nuclear waste with advantage of high separation coefficients and selectivity [4, 44]. Synthesis of inorganic ion exchangers began with amorphous materials with variable compositions. Mechanisms of ion exchange as well as physical and chemical properties of materials were less explored due to lack of knowledge on their structure. Clearfield *et al*. have synthesized crystalline phase of zirconium phosphate as an inorganic ion exchanger and made possible attempts to explain the mechanisms relating with structure [28b, 39]. In the subsequent years, structural knowledge of the inorganic materials provided more in-depth information to correlate the crystal structure with their properties. From such structure property correlations, it becomes possible to tailor the property of the material developed through synthetic design instead of conventionally used “trial and error” synthesis method.

Three dimensional inorganic frameworks are resulted by the stable arrangement of polyhedra with central metal atom having high charge. Repultions between central metal atoms lead to the formation of free space around the polyhedra. In real crystals, the effective packing may restrict not only the nature of the polyhedra but also their angles. Such angled features resulting from the tilting of the polyhedra are commonly observed in real crystals. Growing number of open framework coordination compounds thus give an emphasis on ion exchange mechanism in frame work connected phosphates, titanates, manganates, tungstates etc. [5b, 43b, 44b, 45] Since the inspection of nuclear energy programme, ion exchange properties of insoluble framework architectured inorganic materials are known. However, these materials attract a huge research interest owing to several new effecient inorganic ion exchangers such as titanates, crystalline silicotitanates and hexacyanoferrate etc. Many inorganic ion exchangers are capable of separating radionuclides from high salt concentrations and brought to the market. Crystalline silicotitanates (CST) are the most promising ion exchange materials till date for the separation of radionuclides in presence of large interfering ion concentrations over broad pH range. Crystalline silicotitanates are very effective for the separation of ^{137}Cs and ^{90}Sr from nuclear waste. Among the titanates, layered sodium titanates such as $Na_4Ti_9O_{20}.nH_2O$ is known for selective separation of ^{90}Sr from high pH solutions even in presence of interfering sodium ions [46]. Exact crystal structure of $Na_4Ti_9O_{20}.nH_2O$ is not known due to poor crystalline nature, but the structure comprises of edge shared TiO_6 octahedra forming two-dimensional layers and the TiO_6 layers are connected with sodium ions located in between the layers by sharing epical oxygens of TiO_6 octahedra.

Sodium titanium oxide based ion exchanger, popularly known as Sr-Treat is commercially available and industrially used for separation of strontium from basic nuclear waste solutions, but not effective in acidic conditions [33a]. Co-treat and Cs-treat are the other well known commercially available inorganic ion exchangers currently in use for the separation of radionuclides. Cs-treat is potassium cobalt hexacyano ferrate, widely used for the separation of ^{137}Cs from high salt waste concentrations [47]. Co-treat is titanium oxide based inorganic ion exchanger successfully used for the removal of cobalt and other metal ions from radioactive solutions in optimum pH range. Prior to Co-treat, only activated charcoals are effective in separating Co^{2+} ions [48]. The reason for the complicated uptake of cobalt ions is due to the existence of these ions as complexes with iron colloids and rarely exists as divalent ions. The field of crystalline inorganic ion exchangers is vast, inorganic ion exchangers like zeolites and molecular solids are still attracting huge research interest and thus the discussion is limited to only some classes of framework connected phosphates, titanates, silicotitanates, manganates and tungstates.

1.8.1. Framework phosphates

Ion exchange properties of insoluble metal phosphates are of interest because of their structural stability towards ionizing radiations. Ion exchange property of these materials depends more on the crystal structure compared to the nature of the metal ion present. In the 1980’s Edith M. Flanigen of Union Carbide Corp. had introduced a new class of porous materials based on metal phosphates for the first time. Aluminophospahtes were formed by sharing corners only; charge neutrality in the molecule was achieved by joining alternative terminal atoms in aluminate and phosphate polyhedra. For such structures, foreign ions are not required for the charge balance reasons and generated channels can be evacuated completely thus results in the formation of ring size greater than 14 [5b, 35, 41, 49]. Clearfield *et al.* have reported the ion exchange properties of the layer structured crystalline zirconium phosphate and explained the structure as pillared hydroxyl groups are responsible for ion exchange and are promising materials for the separation of radionuclides from nuclear waste.

Table 1.7: Variation of interlayer distance with extent of hydration

Formula	Name of the phase	Inter layer distance (Å)
$Zr(HPO_4)_2.H_2O$	α-ZrP	7.56
$Zr(HPO_4)_2$	β-ZrP	9.4
$Zr(HPO4)_2.2H_2O$	γ-ZrP	12.2
$Zr(HPO_4)_2.1/2H_2O$	δ-ZrP	7.13
$Zr(HPO_4)_2$	ε-ZrP	5.59
$Zr(HPO_4)$	ζ-ZrP	7.41
$Zr(HPO_4)_2$	η-ZrP	7.37
$Zr(HPO_4)_2.8H_2O$	θ-ZrP	10.4

Crystalline phosphates other applications have been found in catalysis, proton conduction, water desalination, fuel cells and sensors etc. [50] Initial synthesis of metal phospahtes was carriedout as materials having readily hydrolysable acid groups. Refluxing of these amorphous products for long time results in the formation of crystalline phase, which are having more stability in ionizing radiations and better ion exchange capacities compared to amorphous phase because of increased order within the structure [51]. Zirconium phosphates can be synthesized in various stable phases depending on the extent of hydration and thus resulting different interlayer distances. Typical classification of zirconium phosphates with extent of hydration and respective interlayer distance is given in Table 1.7 [52]. All these forms of zirconium phosphates have been synthesized by similar method. Powder neutron diffraction reveals that orientation of water molecules present between the layers is different form structure to structure and thus rendering different inter layer spacing [53].

Table 1.8: Variation of interlayer spacing with central metal atom

Compound	Formula	Interlayer Spacing (Å)	Ion exchange capacity(meq H^+/g)
Titanium Phosphate	$Ti(HPO_4)_2.H_2O$	7.56	7.76
Zirconium Phosphate	$Zr(HPO_4)_2.H_2O$	7.56	6.64
Hafnium Phosphate	$Hf(HPO_4)_2.H_2O$	7.56	4.17
Germanium(IV) phosphate	$Ge(HPO_4)_2.H_2O$	7.60	7.08
Tin (IV) phosphate	$Sn(HPO_4)_2.H_2O$	7.76	6.08
Lead (IV) phosphate	$Pb(HPO_4)_2.H_2O$	7.80	4.79

Table 1.8 describes the variation of interlayer distance with the change in ionic radii of the central metal element. Germanium phosphates are known to be least stable phosphates among IV group elements and which possibly explains the less number of studies on them. Ion exchange characteristics of different rare earth phosphate are elaborated in the following chapters. Titanium phosphates are the second most abundant materials in this category; these materials are synthesized by refluxing solution of $TiCl_4$ in phosphoric acid medium. In a similar manner, various phosphates like $Ti(HPO_4)_2.H_2O$, $Hf(HPO_4)_2.H_2O$, $Ge(HPO_4)_2.H_2O$, $Sn(HPO_4)_2.H_2O$, $Pb(HPO_4)_2.H_2O$ have been reported [51b].

1.8.2. Framework titanates

Titanates are another class of materials having resistance to ionizing radiation, unlike zeolites, titanate based ion exchange materials are stable in alkaline solutions. Tests conducted at Sandia and Hanford showed that amorphous hydrous titanium oxide materials can be used for separation of ^{90}Sr and ^{239}Pu, ^{237}Np from both the acidic and alkaline nuclear waste solutions [43b, 46]. Amorphous sodium titanates show only 3.7% of the total theoretical ion exchange capacity in the reprocessing of high level nuclear waste. The reason for such value may be due to the formation of core-shell type structure formation around the surface of the material. Glass like interior of the sorption material is not exposed resulting in lower separation coefficients [54]. Many layered crystalline sodium titanates belong to either of the class of materials $Na_2Ti_nO_{2n+1}$ and $Na_2Ti_nO_{2n+2}$, where n=1 to 9. TiO_6 polyhedra are connected to each other by sharing edges and results in the formation of two dimensional sheets separated by sodium ions. These sodium ions are exchangeable with other ions of similar size and charge. Various reports are available on the ion exchange properties of amorphous hydrous titanium oxide and crystalline sodium titanates for ^{90}Sr removal from nuclear waste by exchanging the sodium ions present in between the layers.

1.8.2.1. Ion exchange properties of silicotitanates

Initial reports on hydrous silicotitanates indicated that sodium intercalated silicotitanates are superior to other inorganic and organic ion exchangers for separation of ^{137}Cs, ^{90}Sr from nuclear waste solutions. Aaron *et al*. have reported the extraordinary uptake of ^{137}Cs by crystalline silicotitanates (H-CST; $H_2Ti_2SiO_7 \cdot 1.5H_2O$) in extreme alkaline conditions ranging from 1 to 7M NaOH containing solutions [55]. Selectivity for ^{137}Cs at extreme pH conditions and stability in harsh nuclear conditions make these materials capable for nuclear waste treatment in large scale. Native $Na_2Ti_2SiO_7 \cdot 1.5H_2O$ (Na-CST) can be ion exchanged to form $H_2Ti_2SiO_7 \cdot 1.5H_2O$ (H-CST) and this material shows high selectivity for the separation of ^{137}Cs, ^{90}Sr from nuclear waste solutions [17a, 56]. Structural differences in H-

CST and Cs-CST are only subtle, eight membered elliptical ring openings were converted to eight membered circular ring openings by conformational changes in the framework and that plays a major role for selective capture of Cs^+ ions. TAM-5 (hydrous crystalline silico titanate) in this class of material has remarkable efficiency to selectively separate cesium ions present even in parts per million concentrations and thus becomes a promising material for the separation of ^{137}Cs from nuclear waste.

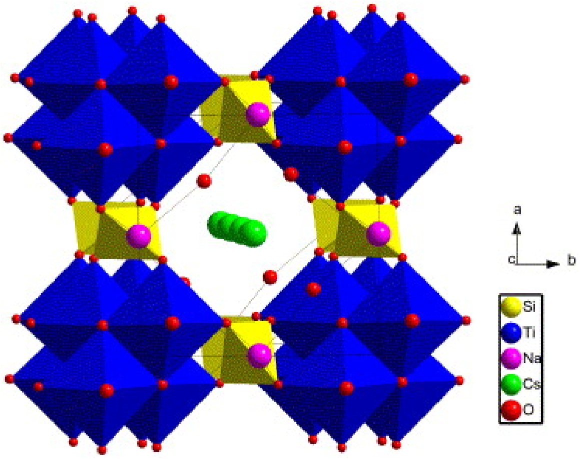

Fig.1.5: Crystal structure of silicotitanates [55]

Crystal structure of these materials is build by the TiO_4 cubane like molecular units connected by the tetrahedral SiO_4 units resulting in the formation of tunnels occupied by the charge balancing ions, thus making these materials as most promising materials for the selective separation of the ^{137}Cs and ^{90}Sr from nuclear waste. Chitra *et al.* have synthesized 'Nb' substituted CST, which has also shown high affinity to ion exchange with ^{137}Cs and ^{90}Sr [55]. In order to develop an efficient ion exchange material for ^{90}Sr separation, Ryu *et al.* have reported sodium titanate nanotubes and explained the ion exchange behaviour of Na^+ in fibre like titanate nanotubes with $^{90}Sr^{2+}$ ions from sea water.

1.8.3. Phyllomanganates

Layers of manganese oxide octahedra formed by sharing edges and these layers are stacked along one direction which are called as phyllomanganates [57]. Manganese oxides are highly reactive and high surface area particles, plays a major role in separation of trace elements, also stable in extreme nuclear waste conditions. Amorphous manganese oxides are well studied for the separation of heavy metal pollutants and for nuclear waste reprocessing [58]. Various hydrous manganese oxides were under investigation for separation of heavy metal pollutants and radioactive cations from aqueous media because they are cost effective and able to form a stable inner sphere complex with the foreign ions. Uptake of Co^{2+}, Ni^{2+}, Cu^{2+}, Zn^{2+} transition metal ions by amorphous δ-Manganese dioxide phase was reported by Bhusan *et al.* where the electrostatic interactions between adsorbate and adsorbent govern the sorption [59].

Birnessites are another class of crystalline phyllomanganate family extensively studied for the removal of various radionuclides as well as heavy metal ions. Birnessite is a natural existing mineral of manganese and its layered structure render capability for ion exchange. Many reports are available comparing the ion exchange characteristics of amorphous manganese oxide with crystalline birnessite mineral indicating that birnessite has shown faster sorption kinetics, higher adsorption capacities and high stability in the aqueous medium for various metal ions as compared to the amorphous manganese oxide [29a]. This may be due to specific surfaces are not available for adsorbate in amorphous phase compared to crystalline phases. Crystalline birnessite is stable in wide pH range and sorption capacity is not altered much with pH variations where as amorphous phase is sensitive with changes in pH.

1.8.4. Aluminosilicates

Silicates are known for the formation of long polymeric chains by sharing corners of SiO_4^{4-} tetrahedral units leading to the formation of various porous structures. Mica with AlO_4^{5-} and SiO_4^{4-} tetrahedral units as building blocks crystallizes in open framework structure resulting in the formation of three dimensional structures; hydrous aluminosilicates are the major components in clay minerals and can be utilized for the nuclear back end applications because of high resistance in nuclear conditions. Kaolinite group of minerals having chemical composition $Al_4(Si_4O_{10})(OH)_8$ are major components of clay minerals. Aluminosilicates have attracted huge research interest because of their molecular and ion sieving properties. Zeolites have been utilized extensively for gas adsorption and for catalysis [60]. Zeolites are the crystalline cross-linked polymeric aluminosilicates with basic units of the polymeric polyhedra composed of tetrahedral SiO_4^{4-} and AlO_4^{5-}. Each tetrahedron containing aluminum formally bears one unit of negative charge which is compensated by metal cations such as Na^+, K^+, Ca^{2+}, Mg^{2+}, Sr^{2+} etc. present in the tunnels generated by the aluminosilicate framework. These cations usually are mobile in nature and responsible for their ion exchange behavior [61]. Varieties of zeolites can be synthesized by varying Al^{3+} with Ge^{3+} and Cr^{3+}, Si^{4+} with Ge^{4+}, Be^{2+} and Mn^{4+} respectively. The structure of zeolite framework consists of a geometrical arrangement of linked $((Si, Al)O_4)$ tetrahedra forming secondary structural units including 4, 6, 8-membered rings of tetrahedra, double rings of tetrahedra, several types of chain, sheets and a variety of polyhedra [62]. The larger polyhedra have substantial intra polyhedral free volumes (called cages or cavities) in which guest molecules may reside and where also the mobile exchangeable cations are usually sited. Though zeolites are capable for removal of radionuclides, aluminum from the lattice leaches at lower pH thus minimizing the efficiency of the material, large pore size of these materials hamper the ion selectivity.

1.8.5. Tungstates

Tungstophosphates are the second most widely studied group of hetero polyacids. Mixed alkali metal salts of $H_3PW_{12}O_{40}$ such as Cs_2NaWP, Cs_2KWP, Cs_2RbWP, Cs_2LiWP, $(NH_4)_2CsWP$, $(NH_4)_2RbWP$ and K_2CsWP have been prepared by ion exchange method. Most of these materials exhibit strong exchange properties in basic medium. Tungstophosphates are highly specific towards Cs^+ ion separation in harsh nuclear conditions, selective for the separation of the monovalent ions compared to bi or trivalent elements [63].

Aluminotungstates are another class of materials with high radiation stability and high ion exchange capacity. These materials are well studied for the separation of alkaline earth metals as well as transition metal elements from nuclear waste and for removal of heavy metal ion contaminations [64]. Ti(IV) tungstates have also been studied for ion exchange applications because of the resistance of material in lower pH. Trivalent metal ions can be separated using Ti (IV) tungstates and more promising compared to zirconium tungstates. Different metal (IV) tungstates like stannic-tungstates, silico-tungstates and zirconium-tungstates are well studied for their ion exchange aspects.

1.9. Scope of present thesis

Scope of the present thesis with title “Crystalline inorganic ion exchangers for separation of cations from nuclear waste: Design and mechanistic investigations from structure-property correlations” is to investigate various crystalline inorganic ion exchange materials to correlate the structure with properties for nuclear back end applications. Various framework architecture phosphates, titanates, manganate systems have been synthesized and ion exchange characteristics of variety of systems have been studied. Synthesis and ion exchange characteristics of novel framework type phosphates of Ce(IV), Zr(IV) with composition $K_2M(PO_4)_2$; M=Ce, Zr have been investigated and the results are discussed in chapter 3. Inorganic ion exchangers after elution of the radionuclides can be converted into stable lattices for the immobilization directly. In view of this, high temperature behaviour of $K_2Ce(PO_4)_2$ is studied, monoclinic to tetragonal phase transition at temperature 550°C was obtained. Phase transition characteristics with theoretical calculations evidences have been elaborated in chapter 4. Apart from phosphates, layered manganates belonging to phyllomanganate family called birnessite minerals have been synthesized for selective separation of radionuclides from nuclear waste. Ion exchange characteristics of Na, K-birnessite minerals are discussed in chapter 5. Tunnel structured $K_3Gd_5(PO_4)_6$ with exchangeable potassium ions has been investigated and its high temperature stability and potential for use as immobilization matrix has been discussed in chapter 6. Synthesis and stability of hollandite type titanates with composition $K_2Fe_2Ti_6O_{16}$ are explained in chapter 7. Na-birnessite for separation of clinical-grade ^{90}Y from $^{90}Sr/^{90}Y$ mixture is discussed in chapter 8. Various other phosphate systems investigated for magnetic and thermodynamic properties have been explained in chapter 9. Finally ion exchange results obtained and conclusions made from various synthesized materials have been summarized in chapter 10.

Chapter 2

Experimental techniques

2.1. Introduction

Variety of inorganic ion exchange materials were synthesized and investigated for nuclear back end applications such as separation of radionuclides from nuclear waste and immobilization of radionuclides in stable matrices. This chapter of the thesis has been elaborated on the basis of theories behind synthesis methods used, followed by theory of characterization techniques used to confirm the phase purity of the synthesized material. Prepared materials were characterized by several analytical techniques like powder X-ray diffraction techniques (PXRD) using lab source as well as synchrotron sources and also other complimentary techniques like Fourier transform infrared spectroscopy (FTIR), Raman spectroscopy, X-ray florescence spectroscopy (XRF) and Thermogravimetry (TG) techniques. Morphologies of the synthesized materials have been studied by using microscopic techniques like scanning electron microscopy (SEM) and transmission electron microscopy (TEM). Ion exchange characteristics of materials have been investigated using various kinetic models like pseudo first order model, pseudo second order models. Mechanism of ion exchange was interpreted using various adsorption isotherm models like Langmuir adsorption isotherm model, Freundlich adsorption isotherm model and Hill adsorption isotherm model.

2.2. Synthesis methods

Inorganic ion exchangers with stoichiometric compositions were synthesized predominantly by solid state synthesis route and co-precipitation method. Preparation method is often selected on the basis of ease of reaction, nature of the desired product and functionality of the material. Each synthesis method possesses certain advantages and disadvantages. Novel synthesis method adopted to obtain required material depends on the physical and chemical nature of the desired product. Some of the general synthesis methods followed in this study is elaborated below.

2.2.1. Solid state synthesis route

Solid state synthesis route is the most commonly used economical and conventional method to synthesize stoichiometric crystalline materials using non-volatile solids. Initially, uniform mixture of solid reactants is obtained by mechanical mixing of reactants and allowed to react to form product phase by heating at elevated temperature generally for long duration. Reaction temperature is determined depending on the melting temperature of the reactants. Moreover, high temperature melting ceramic oxides are the common starting materials used in this method and hence solid state reactions at low temperature are extremely slow. Solid state synthesis proceeds through diffusion of ions, inherently a slow process. Thus solid state reaction is a diffusion controlled reaction. Rate of the diffusion controlled solid state reaction is given by Fick's law [65]

$$J = -D\left(\frac{dc}{dx}\right) \tag{2.1}$$

Where 'J' is diffusion flux, 'D' is diffusion coefficient, 'c' is concentration of the reactant, 'x' is the distance travelled by the reactant. Solid state reactions are intrinsically slow although mixing of reactants at atomic level is achieved by grinding for long time. Reaction mixture is somewhat inhomogeneous since no solvent medium is present to facilitate the reactants to expose each other. Solid state reactions proceed with high acceleration at the initial stage of the reaction and become sluggish with reaction time due to formation of product phase as barrier between the reactants. It can be mentioned here that intermittent grindings of the reaction mixture lead to the formation of uniform product phase by bringing unreacted reactants into contact. Solid state reactions are well affected by the particle size of the reacting solids, as the area of contact increases rate of the reaction. As the particle size of the reacting solids decreases, the surface area increases and hence increases the reactivity of the reacting solids. Particle size of the reactants can be reduced by crushing the reactants into fine powder [66]. Area of contact between the reactants can be increased by repeated grinding of the reaction mixture and by pressing into compact circular pellets after each interval of heat treatment. Repeated grindings, pelletization and heating are essential to complete the synthesis by bringing fresh reactant surfaces into contact. Though solid state reaction is very reliable in order to obtain stoichiometric composition products, consumes a lot of time and energy intensive. Sometimes high temperature reaction conditions even decompose the formed product phase. Many framework connected phosphates and titanates namely $K_2Ce(PO_4)_2$, $K_2Zr(PO_4)_2$, $K_3Gd_5(PO_4)_6$, $KCe(PO_3)_4$ and $K_2Fe_2Ti_6O_{16}$ were synthesized using solid state synthesis route and details of the synthesis are elaborated in further chapters.

2.2.2. Co-precipitation

The problem of reactant heterogeneity in solid state synthesis can be avoided in co-precipitation method because perfect atomic level homogeneity can be achieved in solution state. Co-precipitation employs a solvent medium in which crystalline product phase formed from the soluble precursors can be separated physically. Crystalline precipitate separating from the solution are not always pure contains imperfections from the mother liquor with foreign constituents. However it can be emphasized that three major phenomenon accounts for the incorporation of impurities in the precipitate are, formation of mixed crystals, occlusion and surface adsorption. Mixed crystals are formed by the incorporation of foreign ions in the crystal structure without changing the regular structure. In case of occlusion, impurities are not incorporated in the crystal lattice, but they are adsorbed during the growth of the crystals and give rise to the formation of imperfections in the crystal. Precipitation due to surface adsorption has practical importance only if the precipitate contains a large surface area [67]. Precipitation was used for the synthesis of layered birnessite mineral ($Na_{0.55}Mn_2O_4$ $1.5H_2O$) and complex phosphate based hureaulite mineral for ion exchange studies. Details of synthesis procedure are discussed in subsequent chapters [68].

2.3. Characterization techniques

Characterization of the inorganic ion exchangers was carried out by various commonly used techniques. Phase purity of the materials was verified by powder X-ray diffraction using lab source as well as synchrotron source, vibrational spectroscopic methods, and morphological details were investigated using scanning electron microscopic technique. Several supporting techniques, like X-ray photoelectron spectroscopy (XPS) and X-ray absorption near edge structure (XANES) have been used to understand the local structure and oxidation states of ions in studying systems. In the following sections brief overview of theory behind the characterization techniques used in this thesis work is explained.

2.3.1. X-ray diffraction

X-ray diffraction is an important non destructive tool to analyze materials ranging from fluids, powders, polymers and crystals. Identification of polycrystalline phases of various materials and the quantitative phase composition subsequent to the identification as well as elaborated structural elucidation of the material is carriedout by X-ray diffraction technique. Ion exchange property of the synthesized crystalline material depends on the arrangement of polyhedra of the framework [69]. Inter planar distance of the crystalline material is in the order of 100 pm or 1 Å. Wavelength of X-rays is of same order of spacing of atoms thus X-ray diffraction pattern arise from the material gives information about atomic arrangement. When the X-rays are incident on the material, they are either coherently or in-coherently scattered or absorbed. The coherent scattering of X-rays can interfere with each other giving bright constructive interference and dark destructive interference fringes. However, the scattered rays will become constructive only at a particular angle when the path differences between the two rays differ by an integral multiple of incident wavelength. This phenomenon is broadly termed as X-ray Diffraction. The classical Bragg's law of diffraction that relates the possibility of constructive interference to the inter-planar separations is given by the following equation.

$$n\lambda = 2d\ sin\theta \qquad (2.2)$$

Where $'\lambda'$ is the wavelength of X-rays, $'\theta'$ is the glancing angle called as Bragg's angle, d is inter-planar separations and n is the order of diffraction. Each plane is characterized by miller indices given by (h,k,l). A schematic representation of the X-ray Diffraction is illustrated in Fig.2.1.

X-rays are produced when high-energy electrons are bombarded at a metal target which is usually made of copper in a sealed X-ray tube. It should be mentioned here that only a very small fraction of electron energy is used for the X-rays production and the rest is lost in heating the target element. During this process, the target element gets heated and hence it requires a continuous cooling through external water circulation. Since X-rays are emitted in all the directions, slightly divergent X-ray beams are allowed to emit in a particular direction usually through a beryllium window which allows the X-ray beam to pass out with minimum absorption. X-ray beam is allowed to pass through β filters, usually a thin plate of element with atomic number one to two units below the target element to minimize the background and β-radiation. The beam of X-rays is allowed to pass through the soller and divergence slits and then fall on the powder sample. The fine grains of sample are generally spread uniformly over a rectangular area of a glass slide. The sample is adhered to the glass slide by using a binder either collodion or grease or wax. The diffracted X-ray beams from the sample passed through several slits, like soller and receiving slits and then fall on a monochromator before detection. The monochromator separates out the fluorescent radiation as well as stray radiation scattered by the sample and gas molecules in the sample chamber [70]. The details of the typical X-ray spectra and the X-ray production and are explained in several monographs.

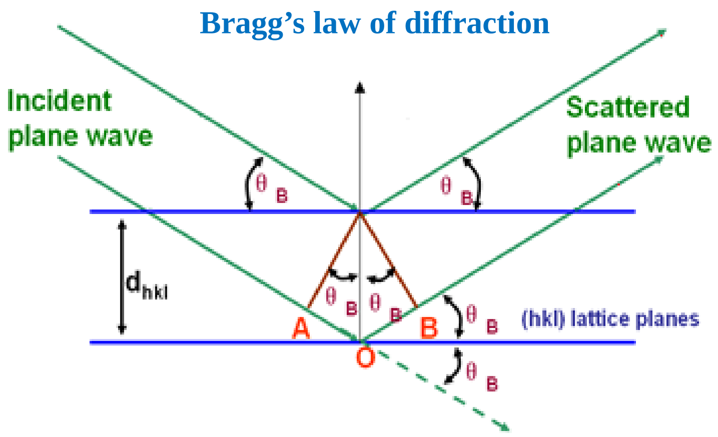

Fig.2.1: Schematic diagram of X-ray diffraction

A powder X-ray diffractometer is generally based on the reflection geometry, in which the divergent and diffracted beams are focused at a fixed radius to the sample position and is commonly referred to as Bragg-Brentano geometry. Powder X-ray diffraction of the synthesized samples was mainly carried out by lab source PANalytical Xpert-PRO and Rigaku instrument based on the Bragg-Brentano reflection geometry diffractometer. The CuK_α from sealed tube was used as the incident beam. A Ni foil was used as a filter and the diffracted beam was monochromatised with a curved graphite crystal. The diffractometer has a proportional counter (Argon filled, commercial name P-10) or NaI (Tl) scintillation counter for the detection of X-rays. The X-ray tube rating was maintained at 40 kV and 30 mA. The goniometer was calibrated for correct zero position using external silicon standard.

2.3.1.1. Data collection and analysis

X-ray diffraction pattern obtained is a plot of diffracted X-rays (counts) versus deviation from incident X-ray direction angle 2θ. The angle where the incident beam meets the Bragg's angle θ for a particular plane, constructive interference among the diffracted X-rays from that plane occurs, giving a sharp intensity peak. The scan time can be optimized for getting good intense peaks. The powder XRD data of the samples ware also recorded by using synchrotron radiation on the ADXRD beamline (on bending magnet port no BL-12) of the Indus-2 (2.5 GeV, 100 mA) Synchrotron Radiation (SR) source at Raja Ramanna Centre for Advanced Technology (RRCAT), Indore, India. Synchrotron radiation is a type of electromagnetic radiations which are produced by synchrotron source where charged particles like electrons or positrons are accelerated (acceleration normal to velocity) almost to the speed of light. Ultra-relativistic charged particles when deflected by applied magnetic field create an extremely bright light. With lab sources the intensity is much lower so the collection times are long. Synchrotron X-ray source has very high intensity, yields diffraction patterns with high signal-to-noise ratio on short time-scales and the beam can be easily monochromatized. Two dimensional detectors based on image plate are generally used for the diffracted X-ray data collection. The properties of image plate are different form conventional X-ray detectors used for lab source like scintillation detectors and ionization chambers.

An image plate (mar 345) was used for recording the scattered X-ray beam and the diffraction image was integrated by using FIT2D program. The obtained 2D XRD patterns were compared with JCPDS (Joint Committee on Powder Diffraction Standards, 1974) files available for reported crystalline samples. Unit cell parameters were obtained by refining the obtained diffraction pattern using Fullprof-2K and *ab initio* structure solutions by simulated annealing methods.

2.3.1.2. Rietveld refinement

Most of the materials of technical interest cannot be grown large crystals hence powder diffraction using small crystallites plays major role in drawing the structure information. Although obtaining structure solution from the powder diffraction pattern is usually tedious, the structure can be optimized for unknown compound if any iso-structural compound is available. Development of Rietveld method made the structure refinement from powder diffraction data possible. In the Rietveld method all reflections for each phase are included in the fit, then minimizing the problem of overlapped peaks. However, in the Rietveld method the texture effects can be considered in the fitting process, leading to a more accurate estimation of relative phase proportions; in addition, the amount of information required for quantitative analysis in the Rietveld method is small and is related to the crystal structure of the phases, precluding the need for a standard. The basic principle of Rietveld refinement is based on the calculation of intensity of an unknown compound assuming a model by doing simulations to all the structure and profile parameters. The structure model assumes the space group; position coordinates of all the atoms and the fairly close unit cell parameters. The profile is defined with specific function namely Gaussian, Lorentzian or their combination as, pseudo Voigt function. A smooth varying function is used for background. Calculated intensity using a model structure as follows

$$Y_{Ci} = Y_{bi} + s\Sigma L \times P \times n \times |F_{hkl}|^2 \Phi(2\theta_i - 2\theta_{hkl}) \times P_{hkl} \times A \qquad (2.3)$$

Where, Y_{ci} = Calculated intensity at the i*th* step

Y_{bi} = Background intensity at i*th* step

L = Lorentz factor

P = Polarization factor

$|F_{hkl}|^2 =$ Structure factor for hkl reflections

$\Phi(2\theta_i - 2\theta_{hkl}) =$ Profile function

P_{hkl} = Preferred orientation function

A = Absorption correction

S = Scale factor

Parameters U, V, W are the FWHM parameters which defines the shape of the peak profile are in turn depend on the angle diffraction as follows.

$$H_{hkl}^2 = U tan^2\theta + V tan\theta + W \qquad (2.4)$$

There are several profile functions defined for fitting the Bragg peaks. It is well known that the X-ray profile shape can be Lorenzian or mixed Gaussian and Lorenzian types. The mixing can be optimized in the course of refinements. The residual function is given as

$$D = \sum_{i=1}^{n} W_i (y_{io} - y_{ic})^2 \qquad (2.5)$$

Where $W_i =$ weighting factor and usually $1/y_{io}$

The quantity D (residual) is minimized in the least square refinements [71]. Optimization of the function to minimize the weighted sum of squared differences between the observed and computed intensity values is carriedout by Rietveld refinement. The weighted profile R-factor 'R_{wp}', follows directly from the square root of the quantity minimized, scaled by the weighted intensities. Statistical concept "chi squared" (χ^2) defined as

$$\chi 2 = \frac{(y_{io} - y_{ic})^2}{\sigma^2 [y_{io}]} \qquad (2.6)$$

$\chi 2$ close to one is considered as model assumed is ideal and the structure parameters drawn are correct. It can also be defined as square of ratio of R_{exp} and R_{wp} describing the goodness of fit. There are several software packages like DBWS, Fullprof, GSAS, Rietan etc. are available for Rietveld refinement. Powder X-ray diffraction refinements reported in this thesis are carried out using Fullprof-2K software.

2.3.2. X-ray fluorescence (XRF)

X-ray fluorescence is an analytical technique used extensively to find the chemical composition of various states of materials like solid, liquid and gaseous samples. The method is fast, accurate, non-destructive and usually requires a minimum of the sample preparation. Both qualitative and quantitative elemental analysis of the sample could be provided by an emission technique such as XRF. In this technique sample is treated with high energy X-rays, which result the ejection of electrons in inner shell generally K or L shell. Inner shell vacancies generated render the atom to be unstable electrons from higher energy levels fill the generated electron vaccencies. The excess energy released from this transition is in the form of photons, characteristic of the element present. Energy of the photon depends on the difference between energy levels, as depicted in Fig.2.2. The fluorescent radiation can be sorted based on energies called as energy dispersive analysis (EDXRF) or wavelengths of the radiation called as wavelength dispersive analysis (WDXRF). EDXRF can be used to analyze Na to U where as WDXRF has even wider range Be to U. Elements with high atomic numbers are having high detection limits compared to low atomic number elements [72].

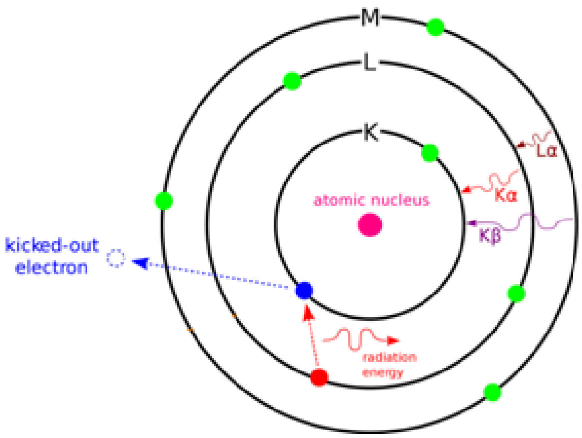

Fig.2.2: Schematic diagram of X-ray fluorescence process

Single channel wavelength dispersive spectrometers are commonly employed for typical lab scale characterization. X-ray source is required in order to excite fluorescent radiation from the material. All conventional X-ray fluorescence spectrometers comprise three basic parts as the primary source unit, spectrometer itself and measuring electronics. The primary source consists of X-ray source in a sealed X-ray tube, has an anode of Cr, Rh, W, Ag, Au or Mo which impinges continuous high intense X-ray beam on analyzing sample. The fluorescent radiation from the sample is many times weaker than primary source beam and the fluorescence from lighter elements is of very low energy to measure and attenuate highly when the beam passes through air for even short distance. High vacuum is maintained from the X-ray tube to sample and to detector path for high-performance analysis. Unwanted signals such as any from the sample holder are cut out by allowing the fluorescent radiation to passe through a mask. The resolution of the spectra is further improved by employing a collimator. Gas filled proportional counters and scintillation counters are the commonly used detectors to measure the fluorescence [73]. XRF studies were carried out to differentiate the chemical composition of virgin and ion exchanged samples. The XRF spectra presented in this thesis were recorded on a XRF spectrometer (EX-3600 M, Jordan Valley, Israel) in wavelength dispersive mode. RhKα was used as excitation source in XRF studies. Analysis of XRF results of various samples are given in further sections.

2.3.3. X-ray photoelectron spectroscopy (XPS)

X-ray photoelectron spectroscopy is a form of electron spectroscopy and commonly used analytical technique for the analysis of surface composition semi quantitatively. In this technique, sample is irradiated with a beam of monochromatic X-rays and the energies of the resulting photoelectron generated from the sample are measured. The basic components of XPS are X-Ray source, sample stage and electron analyzer combined with detection system as shown in the Fig.2.3.

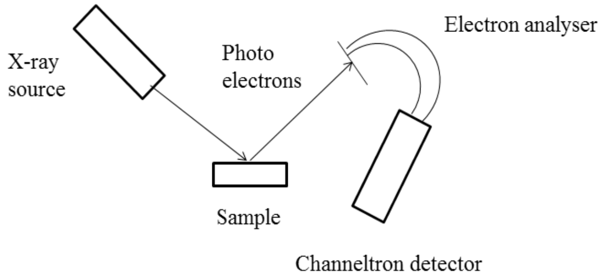

Fig.2.3: Schematic diagram of XPS unit

Experiments using XPS require that the analyzing sample to be under vacuum, where it is bombarded with X-ray photons (200-2000eV) and relies on the photoelectric effect described by Einstein in 1905 where electrons are ejected from a sample after interacting with these high energy photons. Every element has a characteristic binding energy associated with each atomic orbital, in photoemission process, atom absorbs the photon of energy hυ and results the ejection of the core level electron of near surface atom. Binding energy of the electron is the characteristic parameter. The relation between the energy parameters is given by Eq.2.7

$$E_B = h\nu - E_K - W \qquad (2.7)$$

Where, E_B and E_K are the binding and the kinetic energy of the emitted photoelectron respectively, W is the spectrometer work function and hν is the incident photon energy. The photoelectrons emitted contain information regarding electronic structure, oxidation state and local atomic composition. Thus the XPS technique can provide information on the shell structure. Since electrons emitted from atoms lying in layers, deeper within the material have lower chance for reaching the surface and being detected. Hence, this technique provides information about the atoms present within few uppermost atomic layers [74].

X-ray photoelectron spectrum (XPS) of the synthesized sample was recorded in order to confirm the oxidation state of the metal atom present in the specimen. XPS pattern presented in this thesis was recorded on an ESCA analytical instrument M/s Specs Surface Nano Analysis, GmBH, Germany, by using a cold pressed pellet adhered to a carbon tape and Al K_α (1486.6 eV) x-ray as excitation source. The observed C 1s photoelectron peak was used as calibrant for correcting the binding energies.

2.3.4. X-ray absorption near edge structure (XANES)

X-ray absorption spectroscopy has gained much of its reputation of being a powerful analytical and research tool mostly due to the use of synchrotron radiation sources. In this kind of spectrometry, interactions of photons with matter are studied by measuring the photon absorption cross-section. Exciting an atom using an X-ray source, the electron configuration of the atom is changed. The X-ray absorption process is the result of an excitation of an inner level electron to a higher energy level by an incident photon. When the photon energy is large enough, the photo effect in one of the core shells can occur and the step like shape of the absorption results in the spectrum. The increased photo absorption cross-section due to the knocking-out of an electron is called absorption edge representing different core–electron binding energy. Each core shell has a distinct binding energy and thus plot of X-ray absorption as a function of energy the spectrum for different atoms is not similar. Typical schematic of XANES spectrum is shown in Fig.2.4.

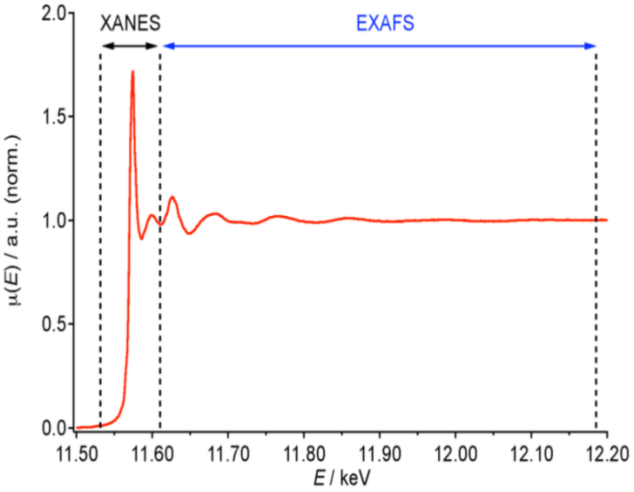

Fig.2.4: Schematic diagram of XANES spectrum

There are several weak transitions possible below absorption edge and some XANES spectra show intense narrow transitions on the rising edge. Above the edge, there are a variety of structures that show generally oscillatory behavior ultimately becoming the EXAFS oscillations [75]. In the near edge region, the photoelectron has low kinetic energy, thus giving it a long mean-free path in addition; damping factor is negligible in XANES region. The absorption edge is not simply a discontinuous increase in absorption, but in fact shows significant structure both in the immediate vicinity of the edge jump and well above the edge. These effects together make the XANES region sensitive to longer distance absorber scatterer interactions which are typically occurred by EXAFS. This generally complicates the simulation of XANES structure since many interactions and a large number of multiple scattering pathways need to be included. There are three main ways in which XANES spectra are used: to determine oxidation state, to deduce three-dimensional structure, and as a probe of electronic structure. XANES spectra presented in this thesis were recorded in fluorescence mode at the same ADXRD beamline (BL-12) of Indus-2 synchrotron source, RRCAT, Indore, India. Powdered sample was placed between two kapton films. The thickness of the sample was about 0.2 mm. The incident photon flux was measured by an ionization chamber while the fluorescent photon flux was measured by using a Peltier cooled energy dispersive detector. Typical energy resolution ($E/\Delta E$) of the beamline is 8000.

2.3.5. Fourier transform infrared spectroscopy (FTIR)

Fourier transform infrared spectroscopy (FT-IR) is one of the techniques used for measuring the intensity of infrared radiation as a function of frequency or wavelength. Infrared radiation is invisible electromagnetic radiation just below the visible electromagnetic spectrum, with wavelength range from 700 nm to 1 mm. Vibrations of bonds and groups which involve a change in the dipole moment resulted due to absorption of infrared radiation forms the basis of IR spectroscopy. Vibrational spectroscopy is the most widely used technique for characterization of functional group present in the sample and in particular the local structure around an atom in a material. For the analysis of solids that are crystalline, microcrystalline, amorphous, or films, this technique is relatively rapid and inexpensive method. Resonance condition describes the absorption of radiation by the molecule in the case of vibrational transitions. The specific oscillating frequency of the absorbed radiation matches the natural frequency of a particular normal mode of the molecular vibration.

Modern IR instruments are based on Fourier transformation method, where the signal to noise ratio is improved considerably. In the FTIR instrument, all the frequencies are used simultaneously to excite all the vibrational modes of different types of bonds present in the sample. The essential piece of hardware in a FT-IR spectrometer is a modified Michelson interferometer which is shown in Fig.2.5.

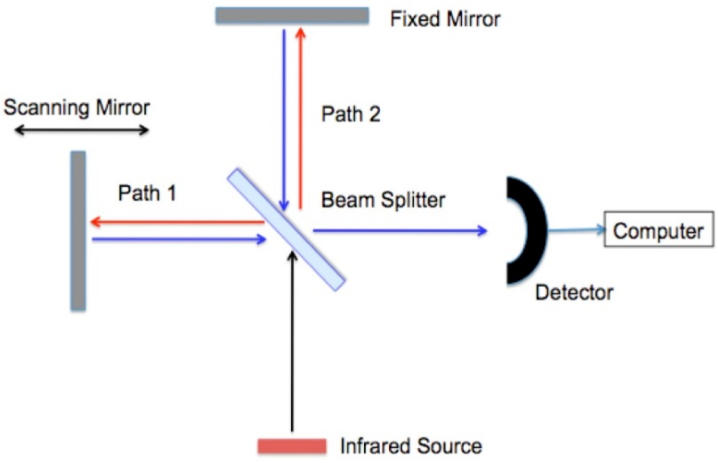

Fig.2.5: Schematic diagram of Michelson interferometer

Michelson interferometer comprises two perpendicular plane mirrors which can adjust mutually along the axis. In the middle between the fixed and the movable mirrors there is a beam splitter. Beam splitter allows 50% of light to pass through the movable mirror while reflecting the other 50% to the fixed mirror. The beam that travels to the fixed mirror is reflected there and returns to the beam splitter again, after a total optical path length of 2L. Same happens in the direction of the movable mirror, the beam that is transmitted by the beam splitter. The result from the interference of the partial waves depends on their optical path difference. After the recombination, the whole beam is then again partially transmitted and partially reflected by the beam splitter. The reflected beam is then passed through a sample compartment and focused on the detector. The detector measures intensity of the transmitted infrared radiation over all wavelengths as a function of the optical path difference between the partial beams. The X-axis of FT-IR spectrum is typically displayed in "wavenumbers in cm^{-1}". This unit is a product of the Fourier transform algorithm operating on the interferogram and is the reciprocal of the actual wavelength of radiation measured in centimeters at a point in the infrared spectrum [76]. FTIR absorption spectrum reported for the synthesized samples were recorded from 400 to 4000 cm^{-1} on a JASCO Corp, in transmission mode. Thin transparent pellets of mixture of sample and KBr were used for FTIR studies.

2.3.6. Raman spectroscopy

When electromagnetic radiation is scattered from a molecule or crystal, most of the photons are elastically scattered thus energy of the scattered photons is same as that of the incident radiation. However, frequencies different from incidnet radiation are observed for a small fraction of scattered light (approximately 1 in 10^7 photons) and usually lower than the frequency of the incident photons. Raman Effect is termed as the process leading to inelastic scattering of the incident radiation. Change in vibrational, rotational or electronic energy levels of a molecule can cause Raman scattering. The scattering is called Rayleigh scattering if the process is elastic and the process is called Raman scattering if it is inelastic. For quick identification of molecules and in studying molecular structure, Raman spectroscopy is a very important practical tool also has important scientific applications. When a photon is incident on a molecule and interacts with the electric dipole of the molecule, Raman Effect arises. Excitation of photons to a virtual state lower in energy than a real electronic transition with nearly coincident de-excitation and a change in vibrational energy is described as the scattering in quantum mechanics. The scattering event occurs in femtoseconds or less. The virtual state description of the scattering is shown in Fig.2.6. The thermal population of vibrational excited states is low, although not zero at room temperature. Therefore, the initial state is called as the ground state and the scattered photon will have lower energy or longer wavelength than the exciting photon. This Stokes shifted scatter is usually observed in Raman spectroscopy compared to Anti-stokes shifted scatter [77].

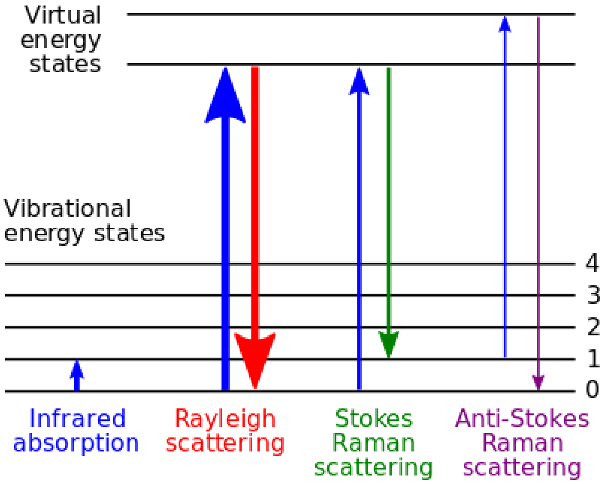

Fig.2.6: Schematic presentation of Raman scattering

A small fraction of the molecules are in vibrational excited states at room temperature. Raman scattering from vibrationally excited molecules leaves the molecule in the ground state. The scattered photon appears at higher energy, called as anti-Stokes-shifted Raman spectrum. At room temperature, Anti-Stokes-shifted Raman spectrum is strong enough to be useful for vibrational frequencies less than about 1500 cm^{-1} though Anti-Stokes-shifted Raman spectrum is always weaker than the Stokes-shifted spectrum. Same frequency information can be obtained form the Stokes and anti-Stokes spectra. Because of poor detector response at lower frequencies the anti-Stokes spectrum can be used when the Stokes spectrum is not directly observable. Raman scattering occurs when a molecular vibration can lead to change in the polarizability of the molecule. The change is described by the polarizability (α) derivative dα/dQ, where Q is the normal coordinate of the vibration. The selection rule for a Raman-active vibration, that there must be a change in polarizability of a molecule during the vibration, i.e

$$\frac{d_{\alpha}}{d_{Q}} \neq 0$$

The selection rule for a molecule to be Raman active is analogous to the more familiar selection rule for an infrared-active vibration, which states that there must be a net change in permanent dipole moment during the molecular vibration. According to group theory if a molecule has a center of symmetry, vibrations that are Raman active will be absent in the infrared and vice versa. Raman scattering intensity is proportional to the square of the induced dipole moment i.e., to the square of the polarizability derivative [78].

The energy of a Raman mode depends on the crystallographic location of atoms in the crystal and their local coordination, cell parameters, bond angle and type of coordination polyhedra and hence explicitly explains the structure of synthesized material. Raman scattering studies of the synthesized materials presented in this thesis was carried out by smearing fine powder of sample to uniform thick layer on a glass slide. Raman measurements were performed in backscattering geometry with a Horiba JobinYvon LabRAM HR UV microspectrometer equipped with an edge filter and thermoelectric-cooled multichannel CCD detector. The 632.8 nm line of the HeNe laser with a power of 10mW was used as excitation source for Raman scattering measurements.

2.3.7. Thermogravimetric analysis

Materials sometimes lose their performance due to thermal, chemical, or mechanical degradation. It has become necessary to understand the temperature impact on stability and also its effect on material properties. Important information about the temperature dependent properties of materials and information about thermally induced processes like phase transition, decomposition, etc. can be obtained using thermal analysis. Thermal Analysis comprises a group of techniques in which the property of a sample is monitored using a thermo balance of high sensitivity, against time or temperature. Moreover the heat treatment of the sample in a specified atmosphere is programmed. In differential thermal analysis (DTA), difference in the temperatures between the sample under study and an inert reference material is recorded as a function of temperature, as both are simultaneously heated or cooled at a predetermined rate. If there is no heat change associated with the sample during the temperature range of interest, the DTA scan will show a steady base line. On the other hand, if there is any physical or chemical change (any heat change) taking place in the sample, the temperature of the sample will either lag behind or increase with respect to that of the reference and the difference in the temperature is recorded as a peak. The area under the peak represents the total heat change. Differential Scanning Calorimetry, (DSC) is a thermal analysis technique that looks at how a material's heat capacity (Cp) and enthalpy is changed by temperature. A sample of known mass is heated or cooled along with a reference material and the changes in its heat capacity are tracked as changes in the heat flow. Nearly same temperature should be maintained throughout the experiment for both the sample and reference. The temperature program for most of the DSC analysis is designed in such a way that the sample holder temperature increases linearly as a function of time. The ease and speed with which the transition in materials detected is the biggest advantage of DSC. Only a few milligrams of material are required to run the analysis, mostly used for quantitative analysis [79]. There are two types of DSC commercially available: Heat Flux (HF) Type and Power Compensation (PC) Type. Fig.2.7 shows the schematic of heat flux and power compensation type DSC [80].

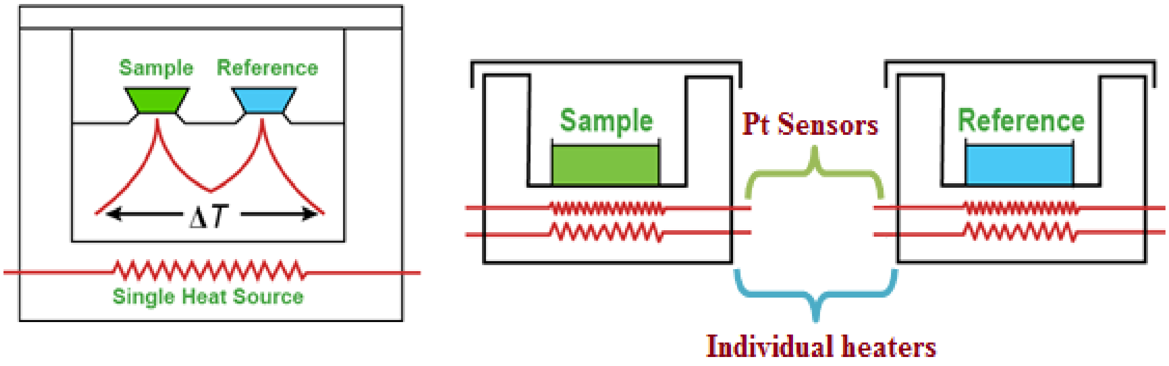

Fig.2.7. Schematic layout of HF type (left) and PC type (right) DSC

TGA experiments present in this thesis were performed, using a SETARAM simultaneous TG/DTA instrument, Model 92-16.18, on the part of the dried gel precursors in the flowing air atmosphere with the heating rate of 10°C/min. Precursor (sample) and reference material (alumina) were placed in two identical platinum crucibles. The weight loss of the sample as a function of temperature was monitored with the help of a thermo-balance whereas difference in temperatures between sample and reference material, as well as sample temperature was monitored simultaneously using two thermocouples.

2.3.8. Scanning electron microscopy (SEM)

Electron Microscopy can be defined as a specialized field of science that employs the electron microscope as a tool and uses a beam of electrons to form an image of the specimen. In contrast to light microscopy, which uses visible light as a source of illumination and optical (glass) lenses to magnify specimens in the range between approximately 10 to 1,000 times their original size, electron microscope is operated in the vacuum and focuses the electron beam also magnifies the images with the help of electromagnetic lenses. Electron microscopy has become an important tool for all types of materials as it can be used to get the substantial information about the structure-property correlation including morphology, crystallographic defects, composition of phases and estimation of the crystallite size etc. Electron microscope takes an advantage of the much shorter wavelength of the electron (λ = 0.005nm at an accelerating voltage of 50kV) when compared to the wavelength of visible light (λ = 400nm to 700nm). Scanning electron microscope is used to confirm the porous morphology of the synthesized ion exchangeable samples. Scanning electron microscopy (SEM) is a powerful method for the investigation of surface structures of the molecules. Large depth of field which means the area of the sample that can be viewed in focus is provided by this technique. The SEM scans a focused beam of electrons across the specimen and measures any of several signals resulting from the electron beam interaction with the specimen. As a result of an inelastic collision of a primary electron beam with an electron of an atom within the specimen, the most commonly used imaging modes are secondary electron (SEM), backscattered electron (BS) and X ray (EPMA). Secondary electrons (SE) are the low-energy electrons produced. Detailed images of surface topography can be obtained by electrons only those produced near surface and escape from the sample, other electrons with low energy are readily absorbed with in the sample. The apparent shadowing in the image is a result of the absorption of the secondary electrons by intermediate parts of the specimen. Backscattered electrons (BE) are high-energy electrons (typically greater than 50eV) that have undergone multiple elastic scattering events within the specimen.

Larger interaction volume and lower spatial resolution compared to the secondary electron image results with the greater energy. Amount of back scattered electrons are more with increase in atomic number of the specimen and thus back scattered electron image reveals the composition variations of the sample. Types of electrons released due to different possible interactions of incident electron beam with specimen are shown in Fig.2.8.

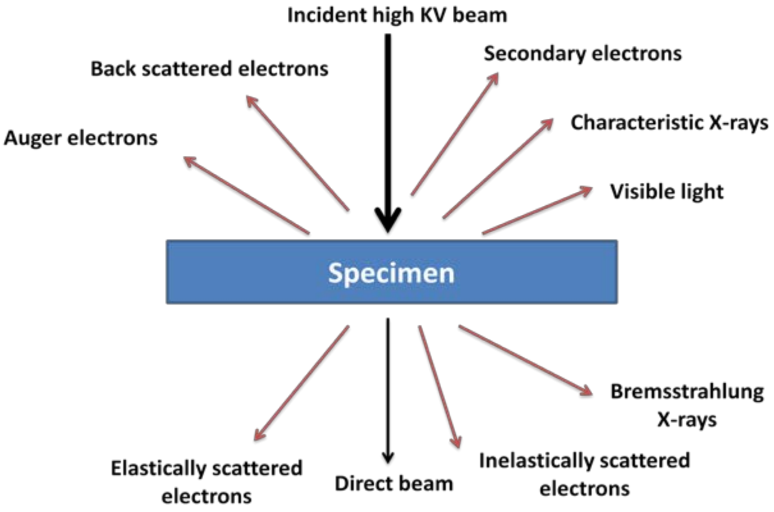

Fig.2.8: Depiction of different phenomena occurring on interaction of electron beam with material

The electron source in an SEM is typically a tungsten filament, acts as an electron source by thermionic emission, although field emission guns (FEGs) are increasingly being used for higher resolution. The electrons are accelerated to energy which is usually between 20-30 KeV. Condenser lenses then demagnify the electron beam until it hits the specimen and it may have a diameter of only 2-10nm. The objective lens is a part of the condenser system and a separate objective lens is located just below the scan coils, which are themselves split into two parts. The secondary electrons ejected from the specimen are detected by a scintillator coated on the tip of the detector and a high voltage of 10KV is applied to it. The secondary electrons from the specimen are attracted to this high negative bias voltage and then generate light when they hit the scintillator. An electric signal is obtained by allowing the light to travel through photo multiplier tube and amplified. Back scattered electrons travelling in the appropriate direction are also detected by the detector and thus always a secondary electron signal is comprised of back scattered electron signal. When the scintillator is given small voltage, secondary electron signal is excluded and only back scattered electron signal is obtained. However electrons travelling along the direct line of sight towards the detector will only be collected [81]. Polycrystalline samples of exchanged and synthesized samples were coated with a thin layer of gold for SEM studies. The SEM images were recorded using FE-SEM (Zeiss, Model: Auriga, Japan). The EDS spectra were recorded using HPGe detector oxford technology mounted on the SEM.

2.3.9. Transmission electron microscopy (TEM)

Transmission electron microscopy (TEM) is a microscopic technique where by a beam of electrons is transmitted through an ultra thin specimen and interacts with it as it passes through. Transmission electron microscope can be used to obtain quantitative measurements of the structural, electronic and chemical properties of the material on length scales down to the sub-Å level. Specimen thickness for high-resolution imaging is below 10nm, the typical specimen is most commonly a 3mm disk that is prepared to be extremely thin at its centre. The specimen holder allows movement of the sample in three spatial directions and tilting about two axes. Short focal length of 1-2mm having objective lens is located directly below the specimen. Design and the stability of the power supply are crucial for the optical performance of the microscope. Magnification of the image is carriedout by the intermediate and projector lenses in the lower part of the column and has a relatively small influence on image quality. After passing the projector lens, the electrons can be observed on a fluorescent screen or recorded on a charge coupled device camera. Selected area electron diffraction patterns from the sample are obtained when TEM operates in the diffraction mode. Using an aperture in the image plane, diffraction region from the specimen is selected. Selected area electron diffraction (SAED) pattern are a projection of the reciprocal lattice with sharp diffraction spots and they are used to identify inter layer spacings and then crystal structures [81b, 82].

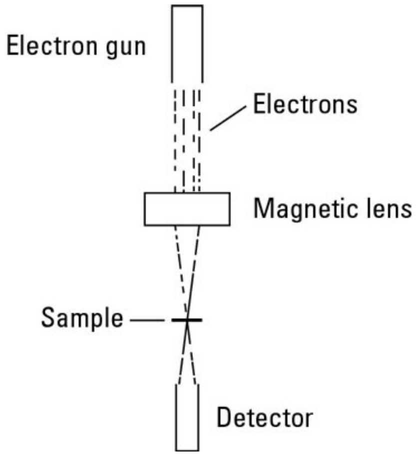

Fig.2.9: Schematic diagram of a TEM instrument

Morphological characterization of the synthesized and ion exchanged samples were carried out by using transmission electron microscopy (TEM). The TEM and high resolution transmission electron microscopic (HRTEM) images were recorded using a Libra 200FE instrument. The samples for TEM investigations were prepared by dispersing the samples in water and then depositing a drop of the colloidal solution on a thin carbon-coated copper grid. The grids loaded with samples were dried under an infrared lamp to get rid of water. Schematic of TEM instrument is shown in Fig.2.9.

2.3.10. Magnetic measurements

The magnetization behavior of the ion exchange samples in between 2-300 K was studied using a 9T PPMS based Vibrating Sample Magnetometer (VSM) (Quantum Design) in zero field cooled (ZFC) and field cooled (FC) conditions with an applied magnetic field of 100 Oe. The hysteresis loops (M vs H curves) were measured up to a maximum field of 90 KOe at several temperatures in between the temperature range 300 and 3K.

The principle of vibrating sample magnetometer is the measurement of electromotive force induced by magnetic sample when it is vibrating at a constant frequency, in the presence of a static and uniform magnetic field. The field dependent magnetic measurements (M vs. H) were carried out on powder samples mounted tightly in the sample holder by varying the magnetic field. The magnetization vs. temperature (M *vs*.T) was measured by vibrating sample magnetometer under a constant applied magnetic field to obtain the Curie or Neel temperature of the sample. The temperature dependent magnetization in zero-field cooled (ZFC) and field-cooled (FC) conditions in a constant applied field were measured by PPMS. In the ZFC measurements, the samples were cooled from 300 to 3K without applying an external field [83]. After reaching 3K, a field was applied and the magnetic moment was recorded as the temperature increased. For the FC measurements, the samples were cooled from 300K to 3K under an applied field and then the magnetic moments were recorded as the temperature increased.

2.3.11. Flame photometry

Table 2.1: Flame color of studied metals

Element	Wavelength (nm)	Flame color
Sodium	589	Yellow
Potassium	766	Violet
Strontium	670	Red

In order to characterize the alkaline and alkaline earth metals, flame photometry is the well known, versatile and simple technique. Flame photometry relies upon the fact that the compounds of the alkali and alkaline earth metals can be thermally dissociated in a flame and that some of the atoms produced will be further excited to a higher energy level. When these atoms return to the ground state they emit radiation which lies mainly in the visible region of the spectrum. Each element will emit radiation at a wavelength specific for that element. The Table 2.1 gives details of the measurable atomic flame emissions of the alkali and alkaline earth metals in terms of the emission wavelength and the color produced.

Light emitted by the element at the characteristic wavelength is isolated by an optical filter and the intensity of that light is measured by a photo-detector, an electrical signal can be obtained proportional to concentration of the element present. A flame photo meter consists of burner, Nebulizer and mixing chamber, color filters and photo detector [84]. The analysis of Na, K, Li, Sr, Ba and Ca are typically determined at low temperatures, i.e. 1500-2000°C, therefore suitable fuel mixtures are propane/air, butane/air and natural gas/air.

2.4. Sorption studies

The ion exchange properties of synthesized materials were studied radiometrically using ^{85}Sr tracer solutions. ^{85}Sr tracer ($t_{1/2}$ = 64.8 d, specific activity = 2.4×10^4 Ci/g) supplied by Board of Radiation and Isotope Technology (BRIT), Mumbai, India, was diluted to get different concentrations of ^{85}Sr solutions. Initial trial ion exchange batch experiments were carried out by shaking 0.05g of sample with 5mL of ^{85}Sr tracer solution for 3h. Equilibration time of 3h was found to be sufficient enough to attain equilibrium between solution and solid sample. Kinetics of ion exchange processes were studied by varying the equilibration time from 30m to 6h. In order to understand the effect of solution medium on ion-exchange behaviors, experiments were carried out by changing pH in the range between 2 and 14. Concentrated HNO_3 or NaOH solutions were used to adjust the pH of ^{85}Sr containing solutions. After equilibration, the solution was centrifuged for 3h and then the clear supernatant liquid was collected in aliquot. The distribution constant (K_d) was calculated from the difference between counts in solution before and after equilibration by using relation: $K_d\,(mL/g) = [(A_i - A_f) / A_f\,] \times V/M$, where A_i = counts before equilibration, A_f = counts after equilibration, V= volume of solution in mL, M = mass of the sorbent in gram.

2.4.1. Sorption kinetics

Sorption kinetics for selective separation of radionuclides is important as it describes the valuable insights about the reaction pathways and into the mechanism of sorption reactions. Details of ion exchange kinetics describe the uptake process with time- evolution until the equilibrium is reached. Such studies yield information about the different transition states involved on the way to formation of final equilibrium product. Kinetic studies of ion exchange help to develop appropriate mathematical models to explain the interactions between adsorbate and adsorbent. Among many kinetic models, pseudo-first order, pseudo-second order models are widely utilized models to explain the ion exchange kinetics and sorption mechanism of several materials.

2.4.1.1. Pseudo-first order model

Lagergren suggested a rate equation for the sorption of solutes from a liquid solution to solid ion exchanger called as pseudo first order rate equation. Lagergren equation is the earliest known one, describing the rate of sorption in the liquid-phase systems. The pseudo first-order equation or the Lagergren rate equation and can be written as

$$\log(q_e - q_t) = \log(q_e) - \frac{k_1}{2.303}t \qquad (2.8)$$

Where q_e and q_t are sorption capacities in mg/g at equilibrium and at time t, respectively, k_1 is the pseudo first order rate constant. A plot between t and $\log(q_e - q_t)$ yields a straight line if the sorption follows pseudo first order kinetics. The values of k_1 and q_e can be determined from the slope and intercept of the straight line respectively. Determining ion exchange capacity exactly using pseudo first order model is tedious because in many sorbate-sorbent interactions, the chemisorption becomes very slow. After the initial fast uptake of sorbate by the sorbent, it is difficult to ascertain whether equilibrium is reached or not. Therefore, it has been reported that, many sorption processes follow Lagergren pseudo first-order model only for the initial 20 to 30 min of contact time [85]. The pseudo first order rate constant k_1 is the measure of the fastness of the sorption process i.e. how fast the equilibrium is achieved. Since pseudo first order model does not describe the interactions between the sorbate and sorbent for entire range of contact time in many cases, higher order kinetic models are employed to analyze the experimental results. External mass transfer and intra particle diffusion will represent the experimental results better where the processes of pore diffusion and film diffusion are negligible.

2.4.1.2. Pseudo-second order model

Pseudo second order reactions are those for which combination of two species is taking place to form the final product in presence of medium, where the role of medium is not considered due to large excess concentration compared to the reacting species. Pseudo second order kinetics is widely applied to many heavy ion pollutant removal systems where chemical reaction is responsible for the sorption and controls the overall sorption kinetics. The pseudo second order kinetic model can be described as

$$\frac{t}{q_t} = \frac{1}{k_2 q_e^2} + \frac{t}{q_e} \tag{2.9}$$

Where k_2 is the pseudo second order rate constant. Plot of ‘t’ versus t/q_t results a straight line with slope equal to $1/q_e$. Pseudo second order rate constant can be obtained from the intercept of the straight line [86].

2.4.1.3. Intra particle diffusion model

Transport of adsorbate ions to the ion exchange sites of material is a gradual process and the mechanism of transport can be explained as follows [87];

1. Migration of metal ions from bulk to the surface of ion exchangeable material (bulk diffusion).

2. Diffusion of metal ions through boundary layer towards the ion exchanger surface (film diffusion).

3. Transport of metal ions from surface to the interior pores of the ion exchanger (intra particle diffusion.

4. Chemical reaction via ion exchange or sorption at active site.

The overall sorption rate may mainly be governed by any one of these steps, or a combination of two or more steps. Usually, the sorbate-sorbent system is under rapid mechanical mixing and hence, the effect of the ion transport in the solution is eliminated therefore, the involvement of bulk transport step on the overall sorption rate can be neglected. Thus, the sorption rate is governed by external diffusion or internal diffusion. Internal diffusion step involves intra particle diffusion or the sorption of solute on the active sites. It is generally known that ion exchange process involves diffusion as prominent mechanism. In order to know the probability of intra particle diffusion; experimental kinetic data was modeled by intra particle diffusion model. The amount of Sr^{2+} taken up by the material is related with intra particle diffusion constant as follows.

$$q_t = K_{id}\sqrt{t} + C \qquad (2.10)$$

Where k_{id} is the intra particle diffusion constant and C (mol gm^{-1}) is a constant that gives an idea about the thickness of the boundary layer around ion exchanging material. The plot of q_t vs $\sqrt{t}$ results in a straight line with slope equal to the intra particle diffusion constant (k_{id}) and this model is called as Webber-Morris model.

2.4.2. Sorption isotherms

The mode and mechanism of interactions between adsorbate and adsorbent can be obtained by fitting the experimental sorption data with various adsorption isotherm models. Most commonly, Langmuir and Freundlich isotherm models are used to study the mechanism of the separation process, due to their simpler and more universal applications.

2.4.2.1. Langmuir adsorption isotherm model

Langmuir isotherm (*eqn-2.11*) is the simplest isotherm model for sorption of a solute from a liquid solution. Langmuir isotherm assumes a monolayer adsorption on the surface of solid where all the active sites have same energy and affinity for the adsorbent. Moreover, according to this model, adsorption active site can accept maximum one ion. However, the adsorption energy, role of adsorbed ions over incoming ions and competition between different ions towards adsorption capacity are not considered [88]. The mathematical expression of Langmuir isotherm is given by equation

$$\frac{1}{q_e} = \frac{1}{q_m} + \frac{1}{K_L q_m C_e} \qquad (2.11)$$

Where q_e is the ion exchange capacity of the material in (mol.g^{-1}), q_m is the maximum capacity at complete monolayer coverage of the material (in mol.g^{-1}) and K_L is the sorption coefficient. Variations of $1/q_e$ with $1/C_e$ show a linear relation, maximum ion exchange capacity q_m can be measured from the slope of the straight line and sorption coefficient can be determined from the intercept of the straight line. The favorability for ion exchange between sorbate ions and sorbent ions can also be expressed in terms of an expression less constant(R_L) called separation factor, using the essential features of Langmuir isotherm can be described as follows;

$$R_L = \frac{1}{1 + K_L C_0} \qquad (2.12)$$

The value of parameter R_L indicates the nature of the isotherm as given below

$R_L > 1$ unfavourable sorption

$0 < R_L < 1$ favourable sorption

$R_L = 0$ irreversible sorption

$R_L = 1$ linear sorption

2.4.2.2. Freundlich adsorption isotherm model

Since the Langmuir adsorption isotherm assumes a reversible process and same probability of adsorption at each site, this model cannot represent a true chemically active system. However, Freundlich isotherm assumes that the ratio of the concentration of solute adsorbed on solid that in solution is dependent on solution concentration and time. Hence the sorption capacity decreases as the concentration of ion in solution decreases and with progress of time. This model also consider heterogeneous surface and preferential adsorption sites, i.e. stronger binding sites are occupied first and the binding strength decreases with increasing concentration of adsorbed ions on them. Thus it represents the realistic situation of any ion exchanging process [88b, 89]. The mathematical expression of Freundlich isotherm is given by equation

$$\mathrm{Log}(q_e) = \mathrm{Log}(K_F) + \frac{1}{n}\mathrm{Log}(C_e) \qquad (2.13)$$

Where K_F is the Freundlich constant, an indicative for ion exchange capacity and n is the Freundlich parameter, an indicative of heterogeneity of the ion exchange material.

2.4.2.3. Hill adsorption isotherm model

Hill isotherm model is a three parameter adsorption isotherm model derived by assuming an ideal gas like behavior of adsorbate and negligible interaction between sorbate and solvent. Also it considers a possibility of multiple adsorbate ions on one receptor site and competition of multiple ions for a receptor site [90]. Sellaoui *et al.* have explained the Hill model by a relation derived by considering the partition function for receptor site as

$$Q = \frac{nN_m}{1 + (\frac{C_{1/2}}{C})^n} \qquad (2.14)$$

Where Q is adsorption capacity, n is number of ions adsorbed per receptor site, N_m is number of receptor sites available for adsorption, C is the equilibrium concentration of adsorbate, $C_{1/2}$ is concentration of adsorbate ions at half saturation.

$$Z_{gc} = 1 + e^{\beta(\epsilon+\mu)} \qquad (2.15)$$

Here, Z is the partition function of a receptor site, β is Boltzmann factor, ϵ is adsorption energy and μ is chemical potential of adsorbed ion. Experimentally obtained Q, C values were fitted using *eqn-2.14* and the obtained values of available receptor sites (N_m), adsorbate ions per receptor site (n) for the ion exchange material gives the insights about feasibility of ion exchange and ion exchange capacity of material.

Chapter 3

$K_2M(PO_4)_2$; M=Ce, Zr inorganic ion exchangers

3.1. Introduction

Owing to high radiation, thermal and mechanical stability of rare earth phosphates, two framework connected phosphates of Ce and Zr with composition $K_2M(PO_4)_2$ (M=Ce, Zr) were synthesized and investigated for their ion exchange properties. Potassium ions present in $K_2M(PO_4)_2$ (M=Ce, Zr) are labile and exchangeable with ions of similar size and charge. ^{90}Sr having high specific activity is produced in large quantity during nuclear reactor operations, has several technological as well as medicinal applications like heat source for thermoelectric generators, generator for carrier free ^{90}Y for cancer therapy and as bone seeker. However, selective separation of ^{90}Sr from spent nuclear fuel remained as a challenge due to high activity, extremely low pH and interference from large number of other ions in HLW. In order to separate ^{90}Sr from nuclear waste, desired materials with high radiation and chemical stabilities are being explored in both organic resins as well as various framework type inorganic materials, like phosphates, titanates, molybdates, tungstates, silicates etc. The flexibility and tenability of the crystal structure and selectivity due to size, charge and concentration gradient, make the inorganic ion exchangers promising for separation of desired cations. Framework connected inorganic materials are more selective for separation of radionuclides and reduces the secondary nuclear waste volume. In addition, these materials can be directly used as an immobilization matrix. Thus development of suitable materials for separation of radioactive ions and subsequently transforming them into immobilization matrix is an important research aspect in nuclear energy sector [60, 91].

Among the framework inorganic ceramics, phosphates with appropriate exchangeable ions are considered as promising materials for separation of ions from high level nuclear waste due to higher separation efficiency and stability in wider range of pH. Several reports on the ion exchange or sorption behaviors of phosphates of Zr^{4+}, Ti^{4+}, Sn^{4+} and Ln^{3+} (rare-earth ions), as well as their complexes with alkali or alkaline-earth metal ions are available in literature [92]. However, most of the studies were carried out with the textured nano or amorphous phosphates. Studies on ion exchange properties of crystalline hydrated phosphates indicate that the structures of exchangers have guiding role for their suitability and selectivity. In order to study the efficacy of the crystalline phosphates and to correlate the structure with ion exchange properties, two complex phosphates $K_2Ce(PO_4)_2$ (KCP) and $K_2Zr(PO_4)_2$ (KZP) are prepared and evaluated their ion exchange properties for ^{90}Sr separation. Structural characterization of both materials shows both have exchangeable K^+ ions and they are located either in the tunnels or in between layers formed by anionic clusters of $[MP_2O_8]^{2-}$, M = Ce^{4+} or Zr^{4+}. Ion exchange mechanisms and kinetics of ion exchange for both KCP and KZP were investigated by modeling the experimentally obtained results with different kinetic models, like pseudo first order, pseudo second order and Weber-Morris models. The mode and mechanism of interactions between adsorbate and adsorbent were obtained by fitting the experimental data with various adsorption isotherm models like Langmuir, Freundlich and Hill models [90a, 93]. Details of models and the results obtained from analysis of kinetic and isotherms are explained in the proceeding sections. The stabilities of the ion exchangers were studied by post characterization of the exchanged products. Subsequently, the temperature effects and stabilities of the exchanged materials for possible immobilization have also been proposed. The results of these studies suggested that these phosphates are promising materials for separation and immobilization of radioactive Sr^{2+} after separation from nuclear waste.

3.2. Experimental method

Both the $K_2Ce(PO_4)_2$ (KCP) and $K_2Zr(PO_4)_2$ (KZP) were prepared by high temperature solid state reaction methods using CeO_2 or ZrO_2, KH_2PO_4 or KPO_3. KPO_3 was obtained by heating KH_2PO_4 at 350°C on a hot plate prior to use. Crystalline sample of KCP was prepared from KH_2PO_4 and CeO_2 by a similar multistep controlled heating procedure as reported earlier [94]. For the preparation of KZP, appropriate amounts of ZrO_2 and KPO_3 were thoroughly homogenized and then pressed into cylindrical pellets. The obtained pre-reacted samples were again homogenized and pelletized and then heated again at 750°C for 24h.

$$2KH_2PO_4 + CeO_2 \longrightarrow K_2Ce(PO_4)_2 + 2H_2O$$

$$2KH_2PO_4 + ZrO_2 \longrightarrow K_2Zr(PO_4)_2 + 2H_2O$$

The obtained final crystalline products for both samples were characterized by X-ray diffraction (XRD) for their phase purity and crystal structures. The synthesized samples were characterized by powder X-ray diffraction, X-ray fluorescence, FT-IR, Raman spectroscopy and morphology of the material was obtained by scanning electron microscopy. Ion exchange characteristics of the materials were obtained radiometrically using ^{85}Sr tracer solutions.

3.3. Results and discussion

3.3.1. Structural characterization of KCP and KZP

Phase formation and structure of KCP sample were ascertained by Rietveld refinement of the XRD data using the earlier reported structural parameters. Presence of trace amounts of $CePO_4$ is detected in the XRD pattern of KCP. The refined unit cell parameters of KCP are: $a = 9.0790(1)$ Å, $b = 10.7859(1)$ Å, $c = 7.6039(1)$ Å and $\beta = 111.143\ (1)$ °; $V = 694.49(2)$ Å^3 (monoclinic, Space Group: $P2_1/n$) and they are in agreement with the earlier reported values. Typical Rietveld refinement plot of the XRD data of KCP is shown in Fig.3.1a.

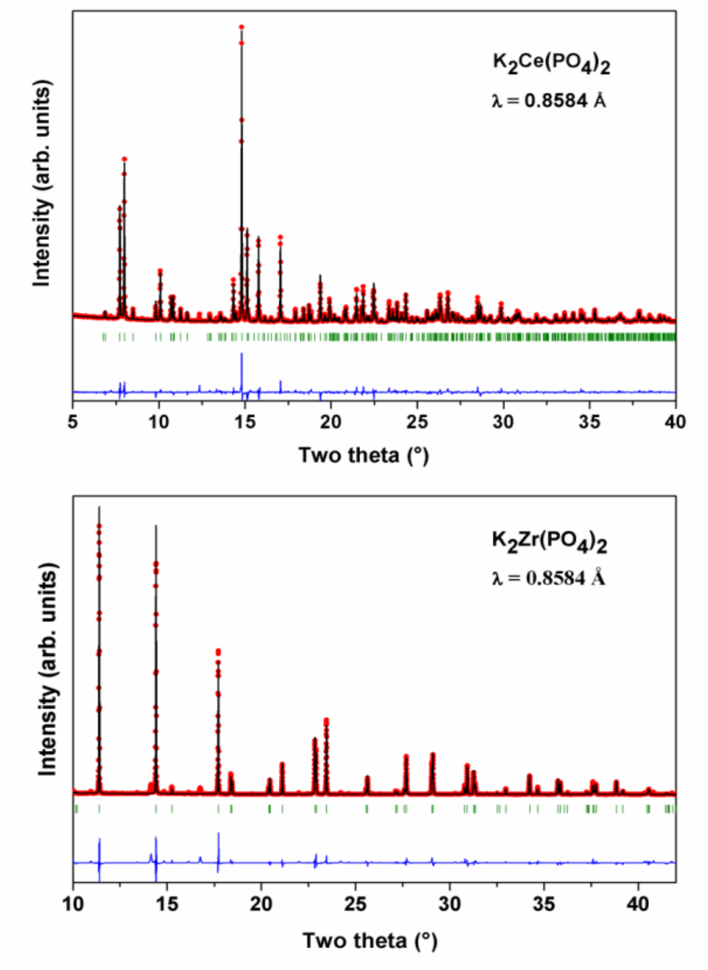

Fig.3.1: Rietveld refinement plots for the XRD data of $K_2Ce(PO_4)_2$ (upper panel) and $K_2Zr(PO_4)_2$ (lower panel)

In a similar manner, the phase purity and crystal structure of KZP sample was studied by Rietveld refinement of its powder XRD data. The reported structural parameters for rhombohedral (Space Group: P-3) $K_2Zr(PO_4)_2$ [95] was used as the initial structural model for Rietveld refinements. It can be mentioned here that Doerffel and Liebertz have used an orientationally disordered PO_4 group for the structure of $K_2Zr(PO_4)_2$ [95]. However, in the present case no disordered PO_4 groups are considered in the model structure and that could satisfactorily explain both the positions and intensity of the complete XRD pattern. Few weak reflections observed in its XRD pattern could not be identified. As their contribution in the XRD pattern is insignificant they were not considered in the refinements. The refined unit cell parameters of KZP are: a = 5.1965(1) Å, c = 9.0422(1) Å, V = 211.456(1) $Å^3$. Typical Rietveld refinement plot for the XRD data of KZP is shown in Fig.3.1b. Refined structural parameters of both KCP and KZP are given in Table 3.1 and Table 3.2 respectively.

Table 3.1: Refined structural parameters of powder X-ray diffraction data of $K_2Ce(PO_4)_2$

Atoms	***wyc.***	**x**	**y**	**z**	**B $(Å)^2$**
CE1	*4e*	0.2777(2)	0.1397(2)	0.0229(3)	0.091(0)
K1	*4e*	0.4538(7)	0.1262(8)	0.6030(9)	0.4(2))
K2	*4e*	0.0420(7)	0.1158(7)	0.3772(9)	1.1(2)
P1	*4e*	0.8644(10)	0.1369(12)	0.7980(13)	0.9(2)
O11	*4e*	0.7541(18)	0.2469(22)	0.7853(25)	2.1(2)
O12	*4e*	1.0349(18)	0.1351(18)	0.9464(23)	2.1(2))
O13	*4e*	0.7591(20)	0.0262(21)	0.7874(28)	2.1(2)
O14	*4e*	0.8725(17)	0.1496(19)	0.6007(22)	2.1(2)
P2	*4e*	0.3679(10)	0.8682(11)	0.8288(13)	0.3(2)
O21	*4e*	0.4921(16)	0.8546(18)	1.0178(21)	0.8(2)
O22	*4e*	0.2739(16)	0.7441(20)	0.7584(22)	0.8(2)
O23	*4e*	0.2414(18)	0.9746(18)	0.8045(26)	0.8(2)
O24	*4e*	0.4860(16)	0.8903(16)	0.7388(22)	0.8(2)

Table 3.2: Refined structural parameters of powder neutron diffraction data of $K_2Zr(PO_4)_2$

Atoms	*wyc.*	X	y	z	B (Å$^{2)}$
Zr1	*1a*	0	0	0	0.13(5)
P1	*2d*	0.3333	0.6667	0.1942(7)	1.5(1)
K1	*2d*	0.3333	0.6667	0.6487(6)	1.7(1)
O1	*2d*	0.3333	0.6667	0.3554(12)	0.3(3)
O3	*6g*	0.6479(13)	0.9126(14)	0.1329(7)	1.7(2)

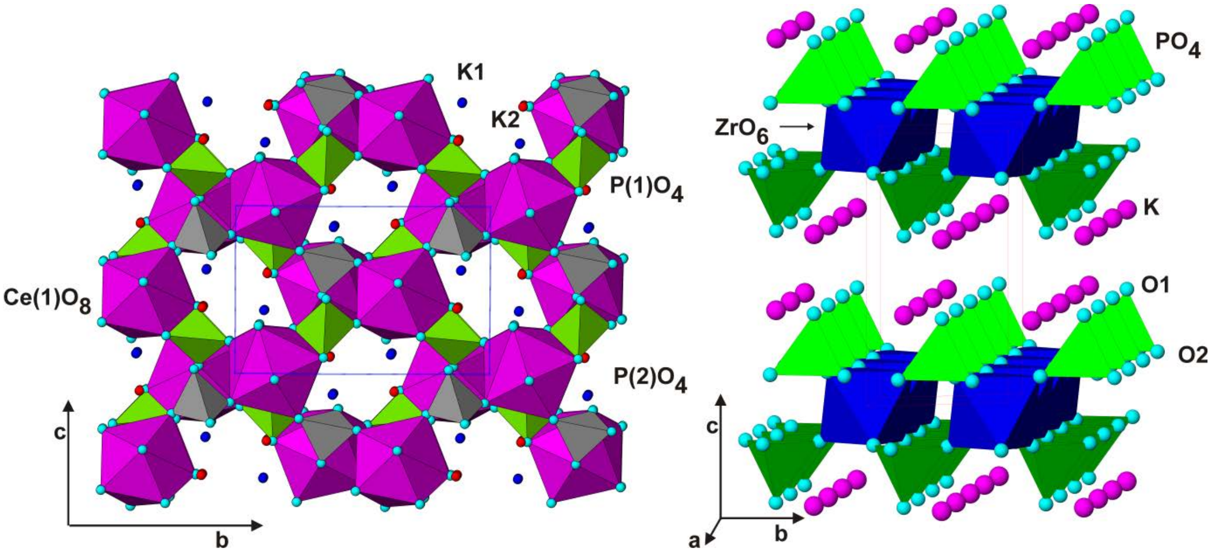

Fig.3.2: Crystal structure of $K_2Ce(PO_4)_2$ (a. left) and $K_2Zr(PO_4)_2$ (b. right)

The analysis of crystal structure of KCP indicates that the unit cell has one type of Ce and two types of P atoms. The Ce atoms are coordinated to eight oxygen atoms forming distorted cubical CeO_8 polyhedra and each of the P atoms are coordinated to four oxygen atoms forming nearly regular PO_4 tetrahedra. The CeO_8 polyhedra are linked to two PO_4 groups by sharing two edges while four other PO_4 groups by sharing corners. Such arrangements of the CeO_8 and PO_4 units lead to a complex 3-dimensional anionic frame with composition $[Ce(PO_4)_2]^{2-}$ and tunnel like 1-dimensional empty spaces. These empty spaces are occupied by two types of crystallographically distinct K^+ ions and maintain charge neutrality in the structure. The K^+ ions are surrounded by eight (for K1) and ten (for K2) oxygen atoms. Typical three dimensional structure of KCP depicting the K^+ ions in the anionic frame of $[Ce(PO_4)_2]^{2-}$ is shown in Fig.3.2a. Similar analysis of the crystal structure of KZP indicates that the unit cell has crystallographically distinct one K, one Zr, one P and two oxygen atoms. The Zr atoms are octahedrally coordinated with oxygen atoms while the P atoms have tetrahedral coordination. The ZrO_6 octahedra share the corner atoms with six different PO_4 tetrahedra forming two-dimensional sheets with compositions $[Zr(PO_4)_2]^{2-}$. These sheets of $Zr(PO_4)_2$ are stacked along the *c*-direction and they are held together by the potassium ions present in between them. Typical crystal structure of $K_2Zr(PO_4)_2$ is shown in Fig.3.2b.

The structural differences between KCP and KZP can be attributed to the differences in ionic radii of tetravalent cations. The larger ionic radius of Ce^{4+} favors for the eight coordinated CeO_8 polyhedra while due to smaller ionic radius of Zr^{4+}, it preferentially form the octahedral ZrO_6. Further due to the formation of larger coordinated polyhedra in the structure of KCP, the CeO_8 and PO_4 polyhedra are connected by sharing both corners as well as edges while in the structure of KZP, the ZrO_6 share only corner oxygen atoms with PO_4 group. It may be noted here that the K^+ ions are ionically bound in the frame of anionic sub-lattice of both structures and thus they are likely to be more labile as well as amenable for exchanging with other cations. According to ionic radii considerations, the exchange of K^+ ions with Sr^{2+} can be easily expected which are confirmed in the present study.

3.3.2. Ion exchange characteristics

3.3.2.1. Batch experiments with $^{85}Sr^{2+}$ solutions

Initial batch experiments were carried out to observe the stability and solubility of both KCP and KZP in various media from acidic to basic. For this, weighed quantities of the solid were treated with various solutions of different pH from 2 to 14. Both KCP and KZP were found to be stable in the complete range of investigated pH. Subsequent experiments were carried out by equilibrating 0.5 g of sample with $^{85}Sr^{2+}$ spiked solutions. The decrease in activity of the solution after separation of solid phase was used for calculating the distribution constant (K_d) (*eqn-1.2*). The concentrations of Sr^{2+} in the solutions after ion-exchange are normalized with respect to the γ activities of $^{85}Sr^{2+}$ ions in the initial solutions. The variation of K_d with pH for both KCP and KZP are shown in Fig.3.3.

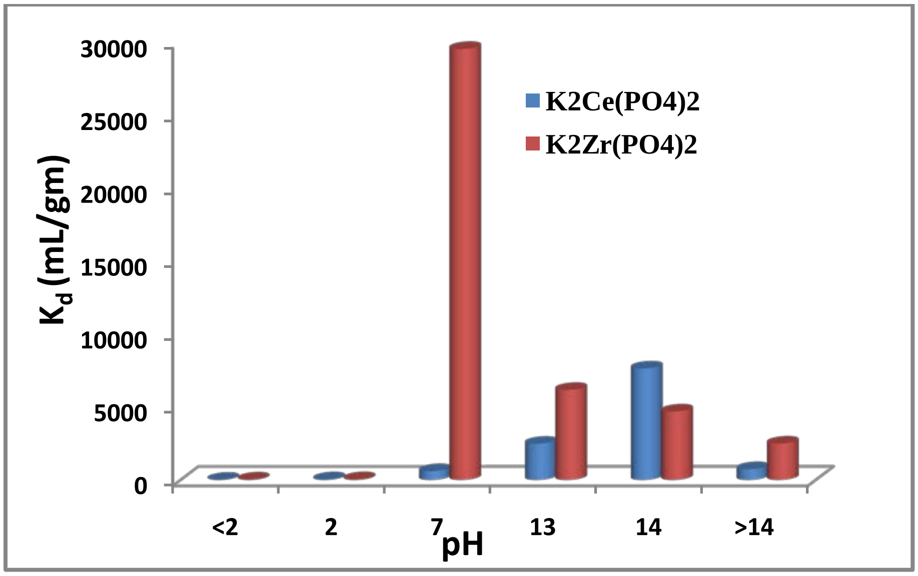

Fig.3.3: Variation of K_d for uptake of Sr^{2+} ions of $K_2Ce(PO_4)_2$ and $K_2Zr(PO_4)_2$ with pH of the medium

It can be seen from figure that the distribution constants of KCP and KZP have distinct pH dependencies. Distribution constant of KCP show increasing trend with increasing pH and show maximum value (~ 8000) at pH 14. However, KZP shows maximum K_d (~ 30,000) in neutral medium and decreases on both increasing as well as decreasing the pH. The larger K_d in KZP compared to KCP suggests that K^+ ions are relatively more labile in former, which can be attributed to its layered structure. In general the pH dependency for anion or cation exchange strongly depends on the variation of surface properties like charge and surface area. Usually at lower pH, the surface of adsorbent becomes positively charged and hence they act as ion exchangers for anions while at higher pH the surface becomes negatively charged and thus preferentially become cation exchanger due to electrostatic attraction between surface of adsorbent and cation of solutions. In addition, the proton exchange due to presence or in situ formation of HPO_4 groups in acidic conditions as in the case of $Zr(HPO_4)_2.H_2O$ governs their pH dependencies [92c]. The HPO_4 groups facilitate cation exchange at higher pH due to release of H^+ and exchange with cations present in the solution [28b, 96]. Since the HPO_4 groups are absent in these compounds, the proton mediated ion exchanges are ruled out. Also surface contributions for separation are expected to be small as the samples are crystalline and have larger crystallite sizes. Thus the smaller values of K_d at lower pH for both samples can be attributed to the involvement of H^+ ions in the exchange process.

It can be mentioned here that the separation of Sr^{2+} is often observed in moderate acidic to highly basic solutions [93d]. In the present study, the maximum K_d for KCP is observed in highly basic solution while that for KZP is observed near neutral solution. The speciation studies of Sr^{2+} in different pH suggest for appreciable concentration of $Sr(OH)^+$

compared to Sr^{2+} at higher pH and absence of precipitated neutral $Sr(OH)_2$ species even at pH 14 [97]. A comparative studies of Cheong *et al.* show minimum separation factor with NaOH solutions even up to pH >12. Thanh and Liu [98] suggested that the presence of free fluorides, carbonates, phosphates, arsenates etc. in the medium facilitate the precipitation of Sr^{2+} as insoluble solid and no precipitation occur in low concentration of Sr^{2+}even at pH ~ 11. In the present case, even though the precipitation cannot be ruled out, the lower separation factors for KCP at still higher pH (> 14) and similar observations in the experiments with KZP suggest that the pH dependency of the exchange behavior of KCP is intrinsic and is related to the concentration and mobilities of K^+ and Sr^{2+} ions as well as presence of excess Na^+ or H^+ ions. As the concentration of K^+ and Sr^{2+} are constant for an experiment, the contribution of Na^+ used for adjustment of pH, is a controlling factor for their uptake behaviors. Thus the interferences of H^+ or Na^+ ions are the main controlling factors for the pH dependencies of K_d in KCP and KZP.

In order to optimize the minimum weight of sample desired for maximum K_d, different amounts of powder samples of KCP and KZP were equilibrated with solution containing Sr^{2+} ions at their respective optimized pH. The plots for variations of K_d and % removal of Sr^{2+} ions (defined as $(c_i\text{-}c_f /c_i) \times 100$) with the weight of the exchangers are shown in Fig.3.4. In both cases, percentage of separation increases to the maximum value with increasing weight of the sample and then remains almost constant. Thus it is concluded that the maximum separation is attained with about 0.05g of solid sample. The lower values of K_d with sample weight lower than 0.05g can be due to insufficient amounts of exchangeable K^+ ions compared to the available Sr^{2+} ions in solution while the lower values of K_d at higher mass can be attributed to the excess mass than desired. Such decrease in K_d

with weight of sorbent higher than the optimum weight is due to inverse relationship between K_d and weight of the material [99].

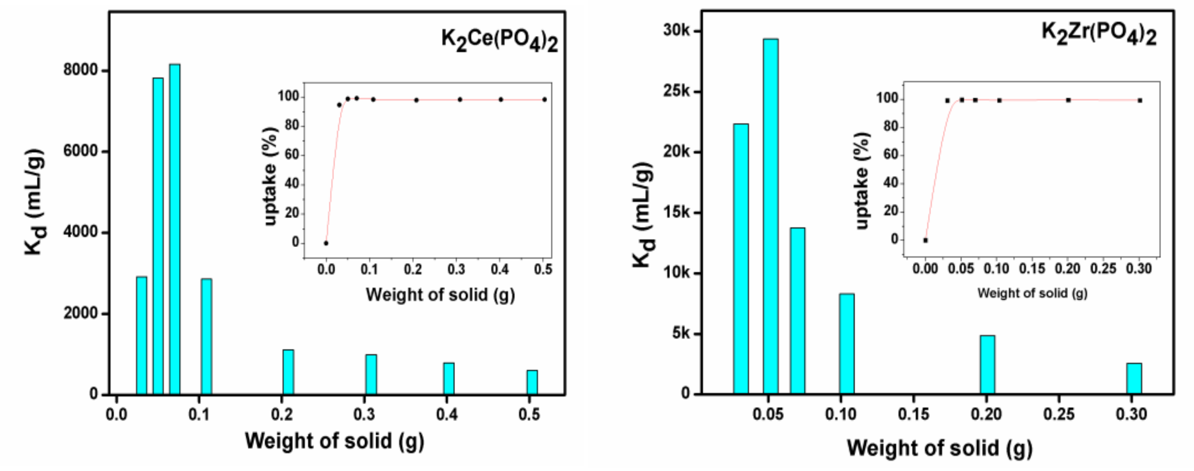

Fig.3.4: Variation of K_d and % uptake for Sr^{2+} ions with weight of sorbents

Usually the separation of ions by the solid ion exchangers occur via dual mechanisms, like exchange of ions from the bulk lattice as well as by sorption of Sr^{2+} ions on the surface of the samples and then diffusion of ions into the bulk. Thus the studies on kinetics and isotherms of exchange process provide information on such mechanisms. In order to understand the mechanistic aspects of separation process, the kinetics and isotherms of exchange for both materials have been investigated by using the optimized sample weight and pH [100].

3.3.2.1.1 Kinetics studies

In general the sorption capacity (q_t ($\mu mol/g$), defined as $[C_i - C_t] \times V/M$, (where C_i and C_t are concentration ($\mu mol/mL$) of Sr^{2+} in solution at time $t = 0$ and t, respectively; V = volume of solution in mL and m = mass of sorbent in g) depends on several factors, viz. concentration and nature of sorbent like surface area, structure and morphology as well as temperature of equilibrium, pH of the medium etc. The surface contribution for separation of Sr^{2+} is likely to be minimum due to larger crystallite sizes and highly crystalline nature of the samples. Sorption kinetics for both KCP and KZP were studied by equilibrating optimized weight of sorbent (0.05g) and pH (pH = 14 for KCP and 7 for KZP) with $^{85}Sr^{2+}$ spiked solution for different equilibration times. The variation of K_d with time for both the materials are shown in Fig.3.5.

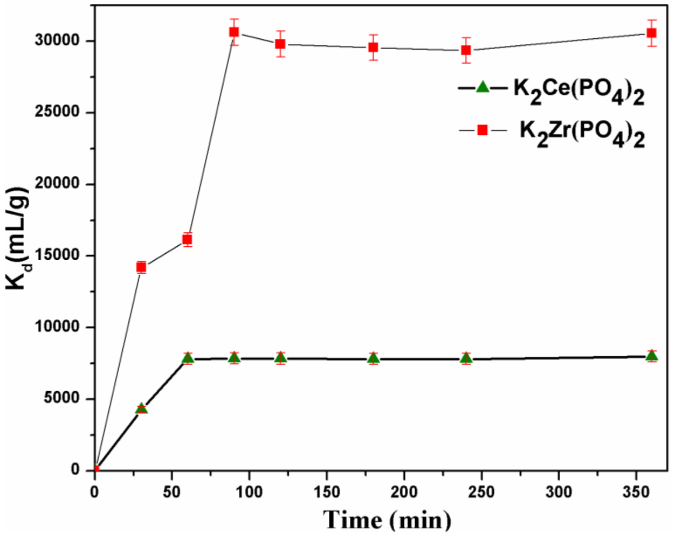

Fig.3.5: Variation of distribution constant (K_d) of $K_2Ce(PO_4)_2$ and $K_2Zr(PO_4)_2$ with contact time

The maximum uptake of Sr^{2+} ions by KCP is observed within 1h and then it remains almost constant. Similarly, maximum uptake in KZP is attained in about 90 min. High affinity of both materials for Sr^{2+} ions can be a reason for faster kinetics. In the initial stage, both the materials show fast uptake of Sr^{2+} ions and this behavior can be attributed to more availability of exchangeable sites on solid as well as high concentration of Sr^{2+} ions in the solution. As the equilibration time increases, both absorption and desorption phenomena as well as diffusion of ions from the surface to bulk and *vice versa*, govern the equilibrium. As a consequence, the values of K_d remain almost constant with time and hence the rate of separation becomes slower. In general, the rate determining factors for exchange are the consequence of physisorption or chemisorption processes and diffusion of ions through the medium, surface films and pores in bulk solid, are formulated as different kinetic models [93b, 101]. The kinetic data were fitted with various models like pseudo first order, pseudo second order and Weber-Morris diffusion models to obtain information about the ion transport mechanism.

The k_1 (min^{-1}) and k_2 (g μmol^{-1} min^{-1}) are pseudo first order and pseudo second order rate constants, respectively. The k_{id} in the Weber-Morris model is the intra particle diffusion constant and C (μmol gm^{-1}) is a constant that gives information about the thickness of boundary layer around ion exchanging material. The q_e and q_t are calculated from the concentration of Sr^{2+} ions in solution, volume of solution and mass of sorbent. The typical plots for pseudo first order and pseudo second order models for KCP and KZP are shown in Fig.3.6. The parameters like rate constants, equilibrium sorption capacity and the typical residual (R^2) as obtained from different kinetic models are given in Table 3.3.

From Fig.3.6, as well as from Table 3.3, it is evident that the pseudo second order kinetic model fits the experimental data with correlation factor ≥ 0.99 than other models. The values of k_2 and q_e for KCP are 0.12 g μmol^{-1} min^{-1} and 98.8μmol/g, respectively and those for KZP are 0.0034g μmol^{-1} min^{-1} and 98.52 μmol/g respectively. It can be mentioned here that the pseudo second order kinetic model assumes that the rate determining step is due to chemisorption which may be by either electrostatic forces or sharing/exchange of electrons between ion-exchanger and sorbate ions i.e. Sr^{2+} ions. Thus the initial concentration of Sr^{2+} ions and amount of Sr^{2+} taken up by the sorbent will have a dominating role on pseudo second order rate constant. Since the pseudo first order kinetic model is based on assumption of reversible adsorption and desorption process, the amount sorbed (i.e. q_e-q_t) should linearly vary with time. Linear relation between amount sorbed and time is not observed for both KCP and KZP. This suggests for a predominant contribution of chemisorption process and hence follow pseudo-second order kinetic model. Thus it can be inferred that the separation of Sr^{2+} is a favorable chemisorptions process and follow pseudo-second order kinetics.

The mechanism of ion transport can be explained by individual or cumulative of several phenomena like (a) migration of metal ions from bulk to the surface of ion exchangeable material (bulk diffusion), (b) diffusion of metal ions through boundary layer towards the ion exchanger surface (film diffusion), (c) transportation of metal ions from surface to the interior pores of the ion exchangers (intra particle diffusion) and (d) chemical reaction via ion exchange or sorption at active sites. Since the pseudo-second order rate relation does not provide much information on the diffusion process, experimental kinetic data were modeled by Webber-Morris intra particle diffusion model. The variation of q_t with $\sqrt{t}$ for KCP and KZP are shown in Fig.3.6 respectively.

For both KCP and KZP, two distinct behaviors are observed in the studied time range. The steep rise of q_t in the initial stage (within 1h), can be attributed to faster accumulation of Sr^{2+} ions on the surface of the solid exchanger and diffusion of ions through the film formed by them on their surfaces. The slow variation of q_t at higher time can be attributed to the diffusion of the accumulated Sr^{2+} ions from the surface to the bulk of the ion exchangers, which essentially is the rate controlling step of these ion exchangers. It can be suggested here that the Sr^{2+} ions diffuse faster through the surface film while slowly in to the bulk of materials. The intra particle diffusion constants (K_{id}) were obtained from the slope of straight lines. Typical values of the K_{id} (µmol/g/$\sqrt{min}$) for KCP and KZP are: -0.0028 and -0.00154, respectively. The thickness of boundary films on KCP and KZP are obtained from the values of C and they are 98.86 µmol/g and 98.78 µmol/g, respectively.

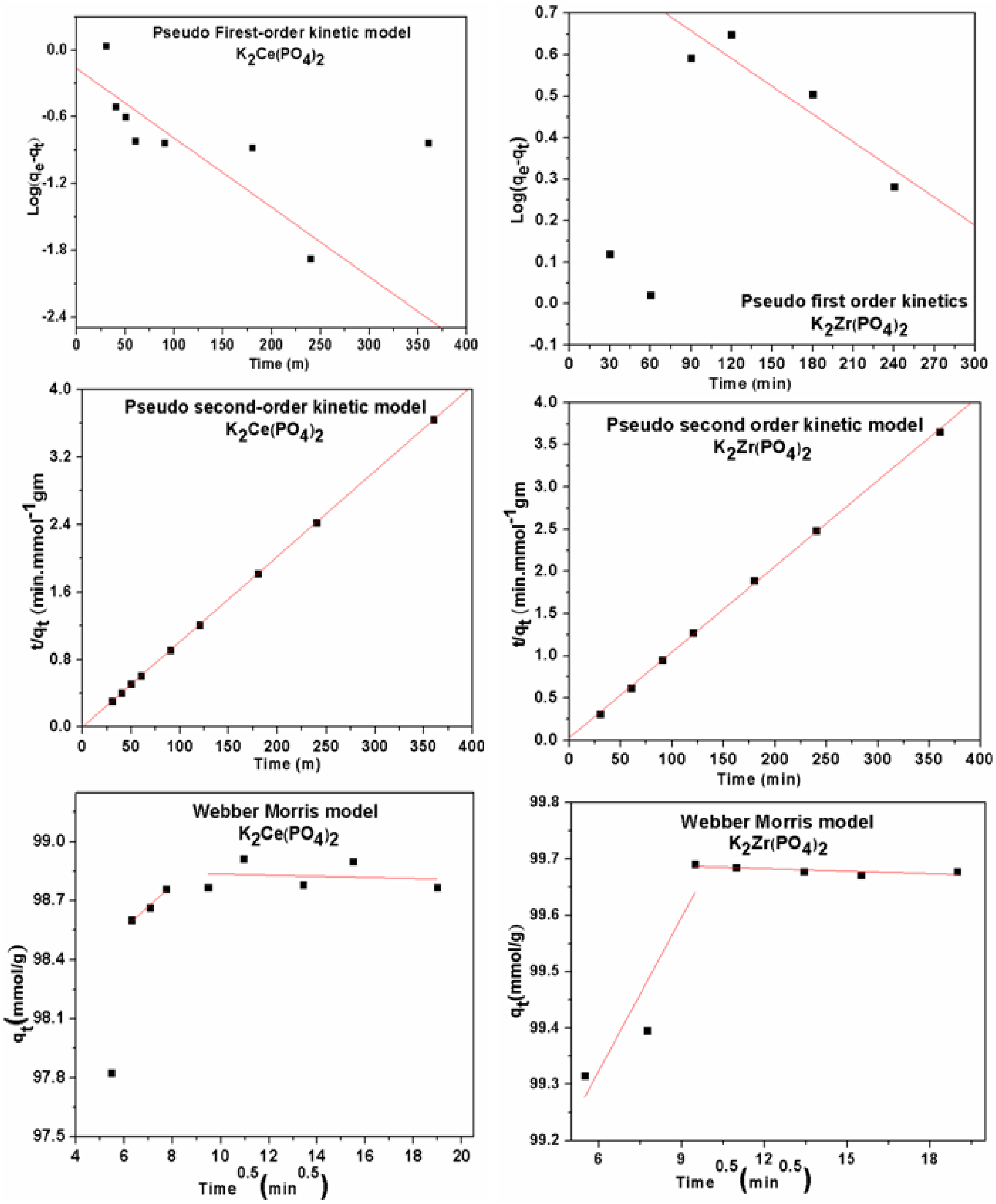

Fig.3.6: Sorption kinetics of $K_2Ce(PO_4)_2$ and $K_2Zr(PO_4)_2$ fitted with different kinetic models

Table 3.3: Summary of results obtained from different kinetic models for Sr^{2+} ion exchange with $K_2Ce(PO_4)_2$ and $K_2Zr(PO_4)_2$

Kinetic model	**$K_2Ce(PO_4)_2$**			**$K_2Zr(PO_4)_2$**		
Pseudo first order	R^2=0.71074	q_e=0.68µmol/g	K=0.014min^{-1}	R^2=0.77597	q_e=7.23µmol/g	K=5.136 min^{-1}
Pseudo second order	R^2=1	q_e=98.8µmol/g	K_2=0.12g µmol^{-1} min^{-1}	R^2=0.99938	q_e=98.52µmol/g	K_2=0.0034 g µmol^{-1} min^{-1}
Weber Morris	R^2=0.94708	I=98.86 µmol/g	K_{id}=-0.0028 µmol/g.min$^{-0.5}$	R^2=0.4226	I=98.78 µmol/g	K_{id}=-0.00154 µmol/g.min$^{-0.5}$

3.3.2.1.2. Ion exchange isotherms

Most commonly, Langmuir and Freundlich isotherm models are used to study the mechanism of the separation process, due to their simpler and more universal applications [99]. Freundlich isotherm model assumes a preferential adsorption of sites and consider stronger binding sites to occupy first. Often such assumptions hold well for chemisorption processes. Langmuir isotherm model assumes a monolayer reversible physisorption process where each site accepts a maximum of one molecule or ion of adsorbate. Additionally, the energetics of adsorption process and preferences of adsorbate for a specific site are explained by later developed model like Hill model [90]. Adsorption capacities, amounts adsorbed at equilibrium and equilibrium constants were estimated using these models.

The ion exchange capacities (q_e) of both KCP and KZP were measured as a function of initial concentrations of Sr^{2+} ions (from 1mmol/L to 100mmol/L). All these experiments were carried out at constant temperature (300K) and for constant equilibration time (3h). Ion exchange capacities (q_e) for both materials are found to increase with increasing the concentration Sr^{2+} ions in the solution. In case of higher initial concentration of Sr^{2+}, the mass transfer is enhanced in the beginning and then slowed down due to minimum availability of exchangeable sites [99].

Typical values of q_e are 52µmol/g and 60µmol/g and for KCP and KZP, respectively. Uptake of Sr^{2+} by KCP and KZP materials fitted by Langmuir, Freundlich and Hill isotherms and they are shown in Fig.3.7. The typical fitting parameters for different isotherms are summarized in Table 3.4. Brief details of each model and results obtained from them are explained in this section.

3.3.2.1.2.1. Langmuir isotherm

Variations of $1/q_e$ with $1/C_e$ show significant deviation from the linear relation which is also reflected from the correlation coefficient of the fitting (R^2) and hence the inadequacy of Langmuir isotherm model can be concluded. The q_m and K_L are obtained from the slope and intercept of the linear fits which are given in Table 3.4. For the KCP sample, the Langmuir sorption coefficient K_L, which is related to the apparent energy of ion exchange between K^+ and Sr^{2+}, is 1.44 L.mmol^{-1} and the maximum uptake of Sr^{2+} is found to be 0.29 mmol/g. The values of K_L and q_m for the KZP sample are 1.28 L.mmol^{-1} and 0.22 mmol/g, respectively. The higher values of q_m suggest for an ease of exchange of K^+ ions and Sr^{2+} ions. The favorability for ion exchange between K^+ and Sr^{2+} can be expressed in terms of a dimension less constant (R_L) called as separation factor.

The calculated value of R_L is less than one which indicates favorable Sr^{2+} exchange process for both KCP and KZP. Also, the positive value of K_L for both KCP and KZP suggests for an irreversible sorption process [88b] and the irreversibility is expected to be more with KCP compared to KZP.

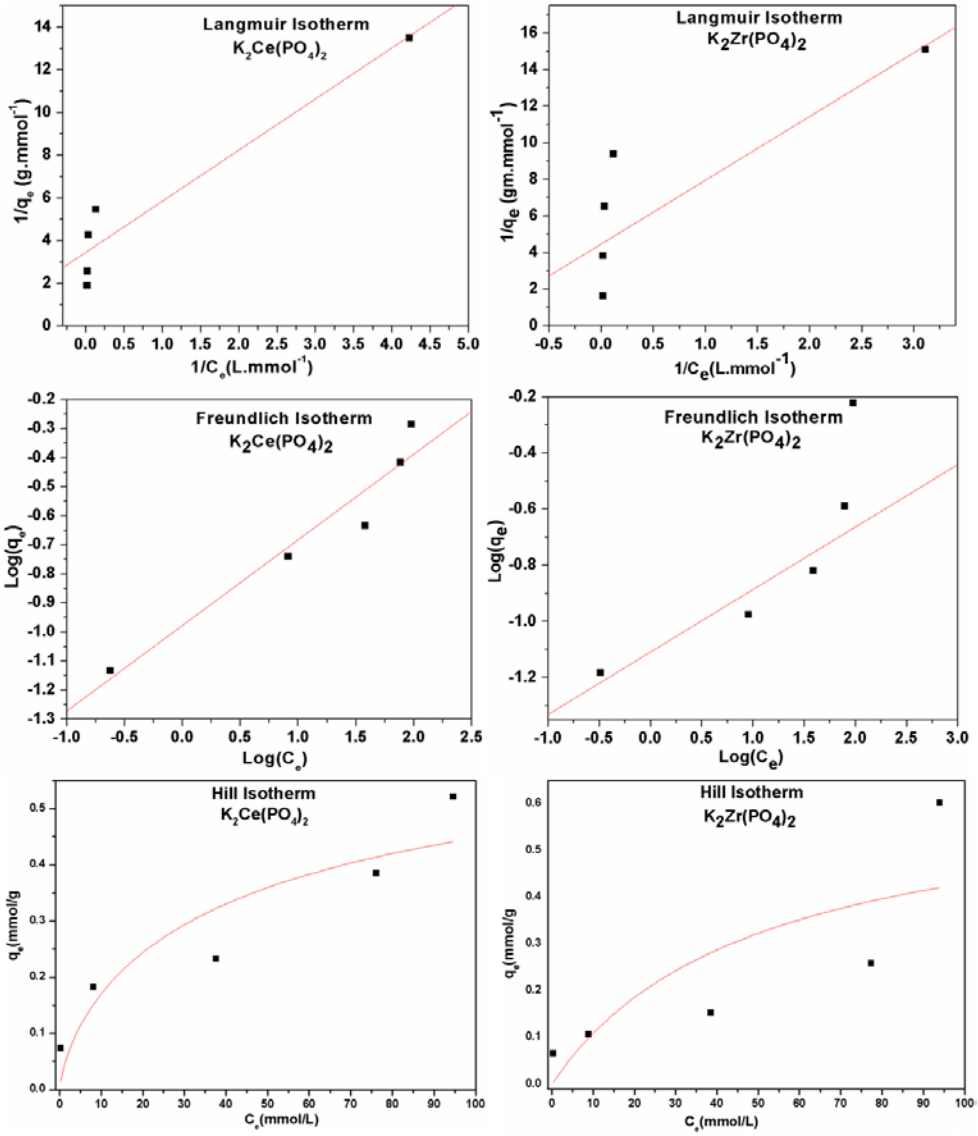

Fig.3.7: Sorption isotherms of $K_2Ce(PO_4)_2$ and $K_2Zr(PO_4)_2$ fitted with Langmuir, Freundlich and Hill isotherm models

3.3.2.1.2.2. Freundlich isotherm

The observed uptake data of both KCP and KZP were analyzed using the linear form of Freundlich isotherm and they are shown in Fig.3.7. Better values of correlation coefficients (R^2) compared to those observed for Langmuir isotherm suggest the validity of Freundlich isotherm for the experimental observations. Further the value of Freundlich parameter (n) indicates a favorable exchange process in KCP (n = 3.4) and KZP (n = 2.89) (for $n < 10$, ion exchange is favorable [89]. The values for Freundlich constants (K_F) for KCP and KZP are 0.11 and 0.078 mmol/g, respectively. Lower exchange capacity of KZP compared to KCP might be due to possible reversibility of exchanged Sr^{2+} ions due to easier migrations in its layered structure.

Table 3.4: Summary of results obtained from different isotherm models for Sr^{2+} ion exchange with $K_2Ce(PO_4)_2$ and $K_2Zr(PO_4)_2$

Isotherm	**$K_2Ce(PO_4)_2$ Q_{theo}=2.45 mmol/g**			**$K_2Zr(PO_4)_2$ Q_{theo}=2.78 mmol/g**		
Langmuir	R^2=0.89517	q_m=0.29 mmol/g	K_L=1.44 $L.mmol^{-1}$	R^2=0.62157	q_m=0.22 mmol/g	K_L=1.28 $L.mmol^{-1}$
Freundlich	R^2=0.91043	K_F=0.11	n=3.4	R^2=0.83012	K_F=0.078	n=2.89
Hill	R^2=0.7871	n=0.7260	N_m=0.9903	R^2=0.6203	n=0.9925	N_m=0.6506

3.3.2.1.2.3. Hill isotherm model

Experimentally obtained Q, C values were fitted using (*eqn-2.16)* and the obtained values of available receptor sites (N_m), adsorbate ions per receptor site (n) for KCP are 0.99 and 0.73 respectively, and those for KZP are: 0.65 and 0.99, respectively. Typical fitting of the experimental results with Hill model is shown in Fig.3.7. Concentration of adsorbate ions at half saturation ($C_{1/2}$) for both the systems is considered as 50 mmol/L. Number of adsorbate ions per receptor site is greater for KZP compared to KCP which is in agreement with the higher distribution coefficient (K_d) of KZP compared to KCP.

The results obtained from all the three isotherms (summarized in Table.3.4) suggest that KCP has better separation capacity than KZP, even though the latter show higher K_d. This can be due to competing reversible desorption probability of the latter. Since KZP has a layered structure, the ion migrations are relatively easier and hence sorption and desorption may occur depending on concentration. From the correlation coefficients (R^2) Langmuir and Freundlich isotherms fits well with experimental data. In both cases the separation of Sr^{2+} ions occurs by chemisorption process. The fittings with Hill model provided additional parameters on exchange site, maximum exchange sites and their energetics of exchange. The Hill isotherm model further indicate that KCP has more accessible receptor sites compared to KZP while less number of adsorbate ions per available receptor site. Also the Hill model indicated that the number of adsorbate ions per site (n) is close to 1.

3.3.2.1.3. Interferences studies

In order to study the interference of other additional ions in the medium to the separation of Sr^{2+}, studies were also carried out by adding various inferring ions (all as their nitrates), viz. Ca^{2+} and Na^+ ions in case of KCP, Al^{3+} and Na^+ ions in case of KZP. As mentioned earlier, both materials show interferences with Na^+ and H^+ ions significantly, but differently and hence show high distribution constant only in particular range of pH. The variation of K_d with different concentration of interfering ions are shown in Fig.3.8.

The distribution constant (K_d) for Sr^{2+} uptake by KCP decreases with increase in concentration of Al^{3+} or Na^+ ions. Effect of interfering ions is significant in case of KZP.

This can be expected from the structural differences of KCP and KZP. As the structure of KZP has a layered structure, the selectivity is expected to be lower due to lesser preferences of ionic size or charge. Any available counter ions can balance the net charge of the negative frame of the structure and thus appreciable interference from Ca^{2+}, Na^+ and H^+ ions are observed in KZP. In the structure of KCP, only specific ions with suitable charge and ionic radii are expected to occupy the tunnels and thus likely to be governing factor for Sr^{2+} uptake due to similar ionic radius with K^+ ions.

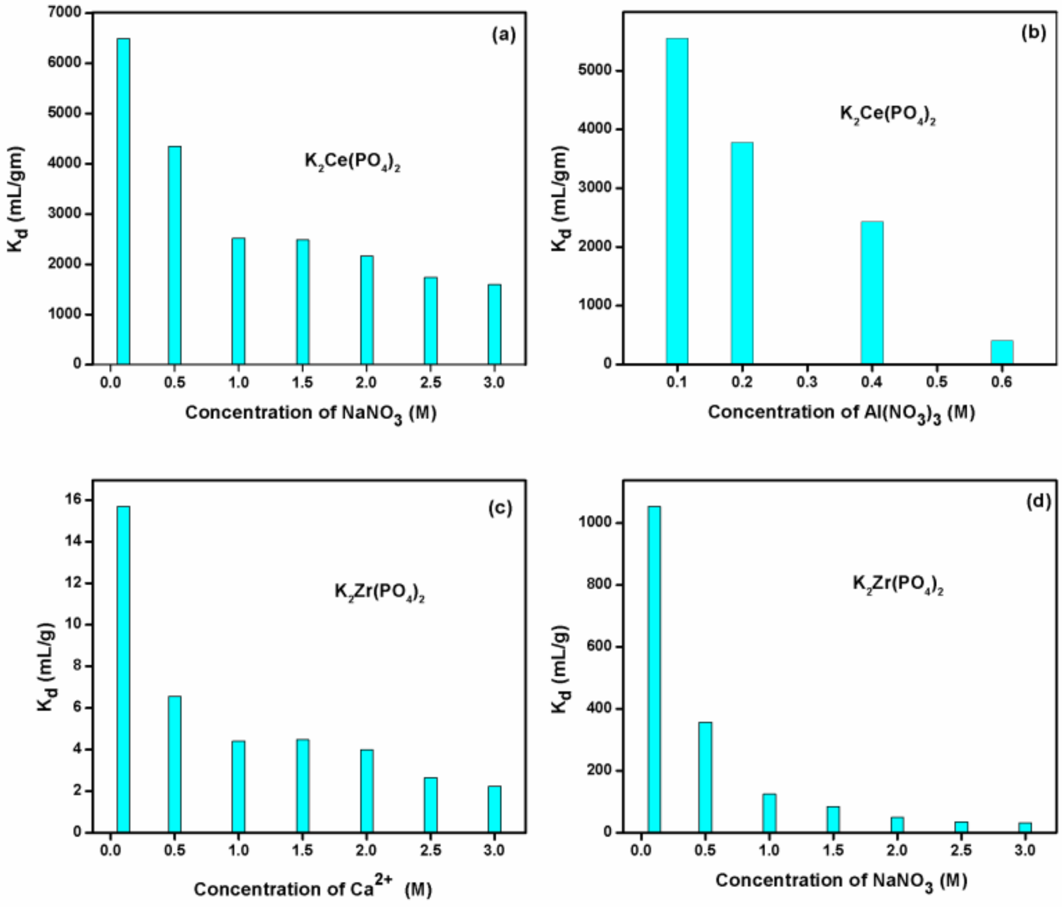

Fig.3.8: Interference of other ions on Sr^{2+} uptake behavior of $K_2Ce(PO_4)_2$ and $K_2Zr(PO_4)_2$

3.3.2.1.4. Exchanged products transformation to stable phases

Additionally, to transform ^{90}Sr loaded matrix directly to possible waste form for immobilization, solid state reactions with different amounts of $SrCl_2$ and temperatures were carried out. The evolutions of XRD patterns under different experimental conditions with stoichiometry as well as with temperature are shown in Fig.3.9.

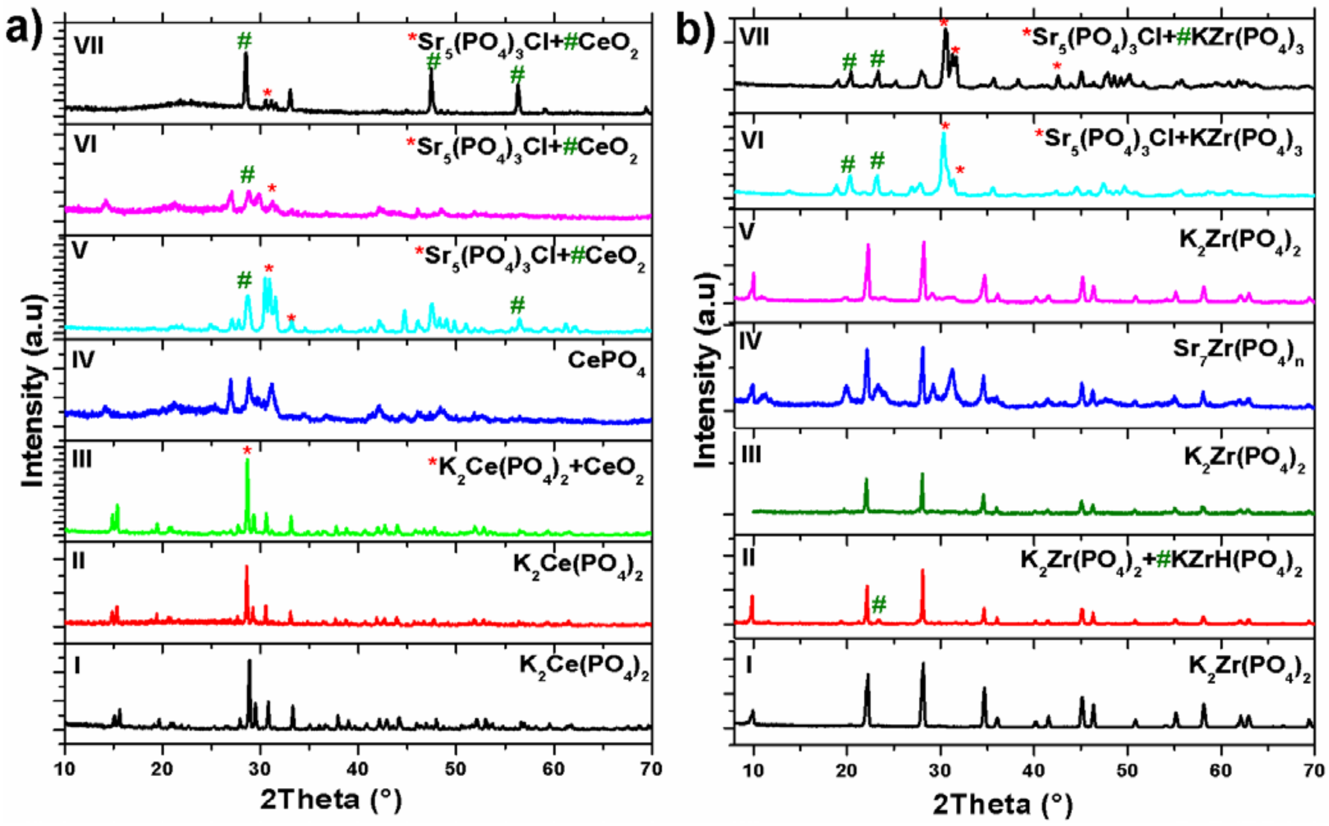

Fig.3.9: XRD patterns of the interaction products of (a) $K_2Ce(PO_4)_2$ and (b) $K_2Zr(PO_4)_2$ with Sr^{2+} salts

It has been explained earlier no significant change in structure or morphology of both KCP and KZP occurs by exchanging the Sr^{2+} ion from dilute solution. However, the reactions carried out at higher temperature revealed change in structure in both the samples. The analysis of phases formed in different conditions is given in Table 3.5.

Table 3.5: Phases formed by the interaction of $K_2Ce(PO_4)_2$ and $K_2Zr(PO_4)_2$ with Sr^{2+} salts in different conditions

Expt. No.	Reactions	Identified Phases		
I	Untreated sample	**$K_2Zr(PO_4)_2$**		
II	KZP+ 10 mol $SrCl_2$ solution, equilibrated for 1h and then washed	$K_2Zr(PO_4)_2$	$KZrH(PO_4)_2$	
III	KZP + $SrCl_2$ heated at 300°C and then washed	$K_2Z_r(PO_4)_2$		
IV	KZP + $SrCl_2$ (1:1) heated at 500°C and then washed			$Sr_7Zr(PO_4)_n$
V	KZP + $SrCl_2$ (1:10) heated at 500°C and washed	$K_2Zr(PO_4)_2$		
VI	KZP + $SrCl_2$ (1:1) heated at 700°C and washed	$Sr_5(PO_4)_3Cl$	$KZr(PO_4)_3$	
VII	KZP + $SrCl_2$ (1:10) heated at 700°C and washed	$Sr_5(PO_4)_3Cl$	$KZr(PO_4)_3$	
I	Untreated sample	**$K_2Ce(PO_4)_2$**		
II	KCP+ 10 mol $SrCl_2$ solution, equilibrated for 1h and then washed	$K_2Ce(PO_4)_2$		
III	KCP + $SrCl_2$ (1:1) solution dried and heated at 300°C and then washed	$K_2Ce(PO_4)_2$	CeO_2	
IV	KCP + $SrCl_2$ (1:1) heated at 500°C and then washed	$CePO_4$		
V	KCP + $SrCl_2$ (1:1) heated at 700°C and washed		$Sr_5(PO_4)_3Cl$	CeO_2
VI	KCP + $SrCl_2$ (1:10) heated at 500°C and then washed	$CePO_4$	$Sr_5(PO_4)_3Cl$	CeO_2
VII	KCP + $SrCl_2$ (1:10) heated at 700°C and then washed		$Sr_5(PO_4)_3Cl$	CeO_2

It is observed that at higher temperature both the compounds transform to apatite type phases. Besides, KZP transforms to NZP type phase. The peaks due to $CePO_4$ could be observed with KCP due to transformation of $Ce^{4+}$to Ce^{3+} at higher temperature. This suggests that the Sr^{2+}adsorbed ion exchangers can be transformed to stable immobilization matrices like apatite, monazite or NZP type materials with the adsorbent. These results are comparable to those reported with other phosphates where the direct transformation of exchangers to apatite or NZP type lattices is demonstrated [102].

3.4. Batch experiments with stable Sr^{2+}solutions

Weighed quantities (0.1 g) of KCP and KZP were equilibrated with a solutions of $Sr(NO_3)_2$ (1 molar) for a period of 24h. The solid mass was separated by filtration and thoroughly washed with nano pure water to remove any loosely attached Sr^{2+} ion on them. The filtrate was studied by atomic adsorption spectroscopy and confirmed for the presence of K^+ ions. The solid masses were dried in air and then investigated by XRD, IR, XRF and electron microscopy.

3.4.1. X-ray diffraction studies

It can be seen that the powder XRD patterns remains almost unchanged except a small variation in intensity distribution. The observed unit cell parameters of the exchanged and virgin samples are closely similar but slightly higher unit cell volume is observed in exchanged samples compared to the virgin samples. Rietveld refinement plots of the KCP and KZP materials after ion exchange are shown in Fig.3.10. The observed unit cell parameters are obtained by fitting the profile of diffraction patterns and they are as: KCP: a = 9.1024(3) Å, b = 10.8131(4) Å, c = 7.6241(3) Å, β = 111.151(3)°, V = 699.84(4) $Å^3$; KCP-

Sr: a = 9.1070(4) Å, b = 10.8197(4) Å, c = 7.6291(3) Å, β = 111.169(3) °, V = 701.00(5) Å^3; KZP: a = 5.1770(1) Å, c = 9.0080(3) Å, V = 209.08(1) Å^3; KZP-Sr: a = 5.1809(2) Å, c = 9.0043(5) Å, V = 209.31(2) Å^3. The variation of unit cell parameters is only marginal and hence any drastic change of strain in the structure cannot be concluded. The differences in intensity variation are related to the preferred orientation of grains in the samples. Thus it can be suggested that both KCP and KZP retain their original structure and crystallinity by exchange of Sr^{2+}ions.

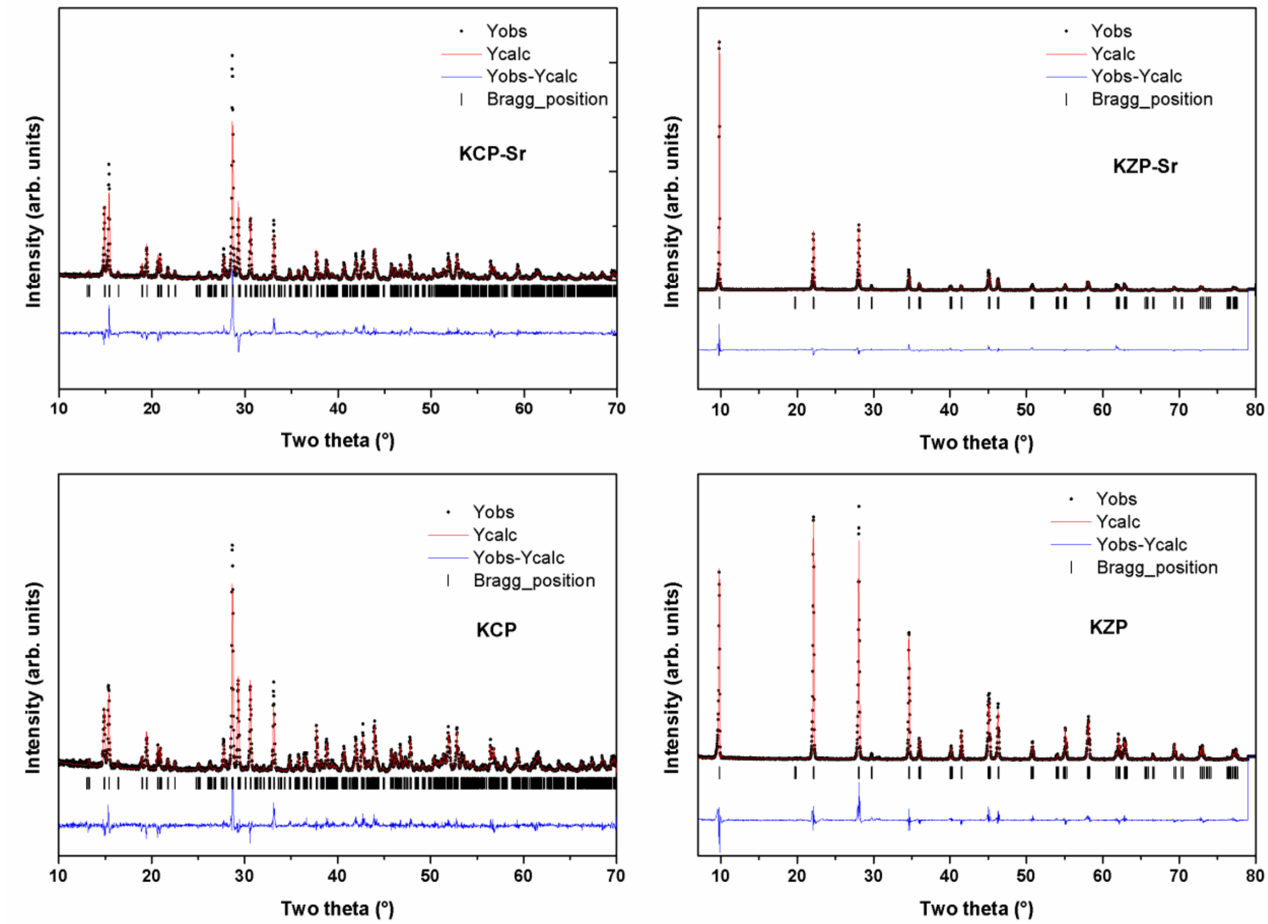

Fig.3.10: Rietveld refinement plots for powder XRD patterns of K$_2$Ce(PO$_4$)$_2$ (KCP) and K$_2$Zr(PO$_4$)$_2$ (KZP) Sr ion exchanged Sr-KCP, Sr-KZP samples (CuKα X-ray)

3.4.2. Infrared spectroscopy studies

Comparisons of IR Spectra of the KCP and KZP sample before and after ion exchange (Fig.3.11) suggest that no appreciable change occur in the structure. No absorptions near 1600 and 3600 cm^{-1} in the FTIR spectra of both KCP and KZP confirm the absence of any OH$^-$ and H_2O in the samples [94, 102-103].

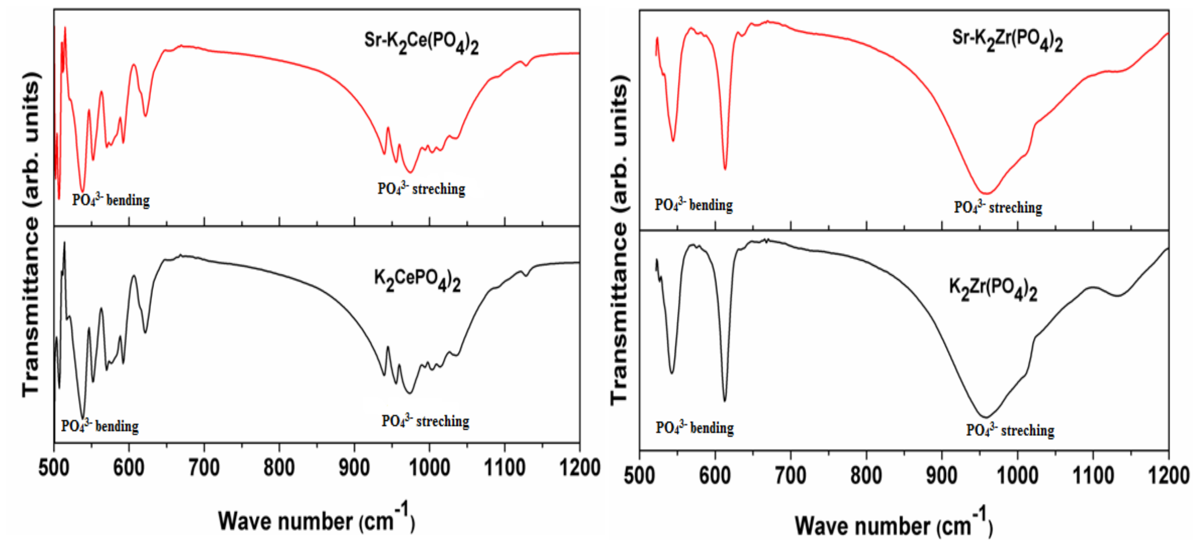

Fig.3.11: FTIR spectra of $K_2Ce(PO_4)_2$ and $K_2Zr(PO_4)_2$ samples before ($K_2Ce(PO_4)_2$ and $K_2Zr(PO_4)_2$) and after exchanging Sr^{2+} ions

Thus the equilibration process does not introduce any water of hydration in the ion exchanged samples as well as confirms any hydroxides precipitation. Similarly, the absence of band around 1250 cm^{-1} in the IR spectra confirms the absence of HPO_4^{2-} groups in them [94, 103]. The stretching modes associated with PO_4^{3-} observed as band in between 1000 and 1100 cm^{-1} remains almost unchanged and hence it can be concluded that the PO_4^{3-} groups do not have any influence on ion exchange process. The asymmetric bending modes observed at around 548 and 615 cm^{-1} in both KCP and KZP are also similar in their respective exchanged samples. Vibrations from the bending motion of PO_4^{3-} in KZP are also unaffected by the exchange process. The low frequency lattice modes of both KCP and Sr^{2+} exchanged KCP are also closely similar [94, 103].

3.4.3. X-ray fluorescence studies

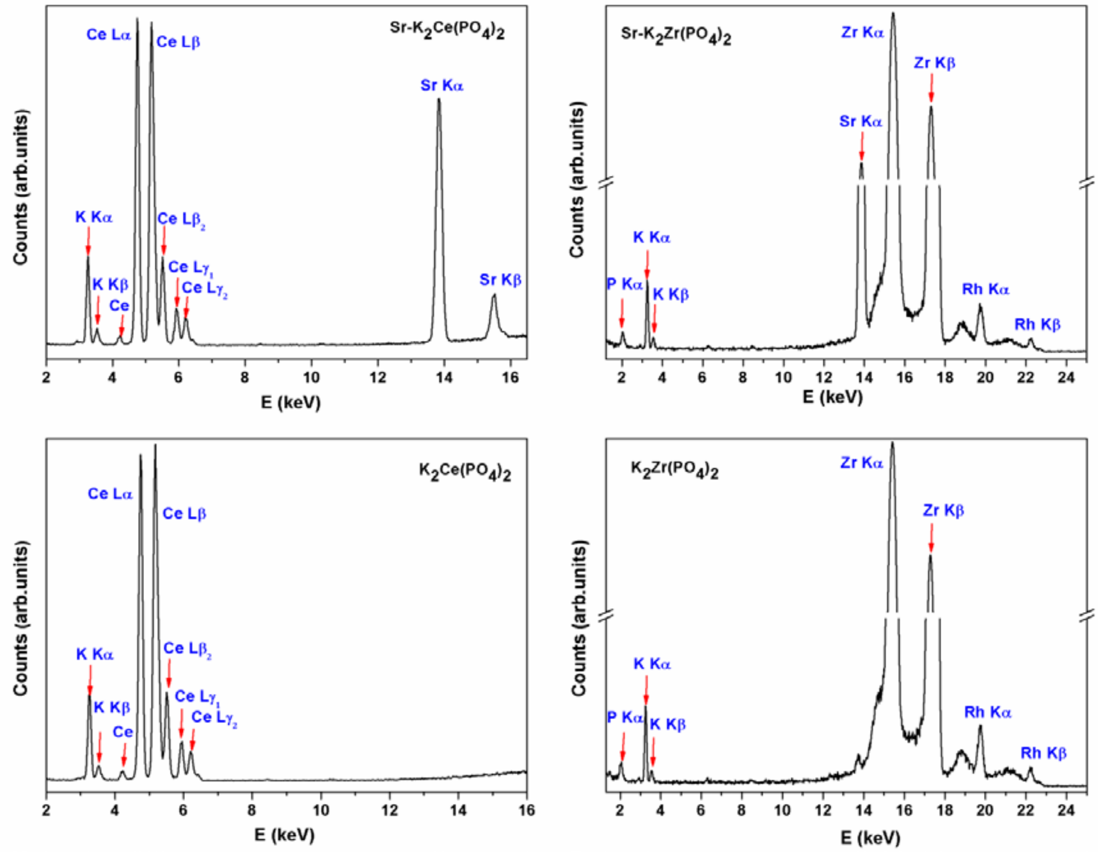

Fig.3.12: XRF spectra of $K_2Ce(PO_4)_2$ and $K_2Zr(PO_4)_2$ and after (Sr-$K_2Ce(PO_4)_2$ and Sr-$K_2Zr(PO_4)_2$) exchanging Sr^{2+} ions

In order to further support the Sr^{2+} incorporation in the KCP and KZP samples, the exchanged samples were investigated by X-ray florescence spectroscopy. The XRF spectra of Sr^{2+} exchanged KCP, KZP and their corresponding virgin samples are shown in Fig.3.12. Significant amounts of Sr^{2+} presence was confirmed from the Sr Kα (13.8 keV) X-ray from the exchanged sample which is otherwise absent in the parent samples. Additionally, the

XRF spectra also confirm the absence of any elements other than those expected in the corresponding composition.

3.4.4. Scanning electron microscope studies

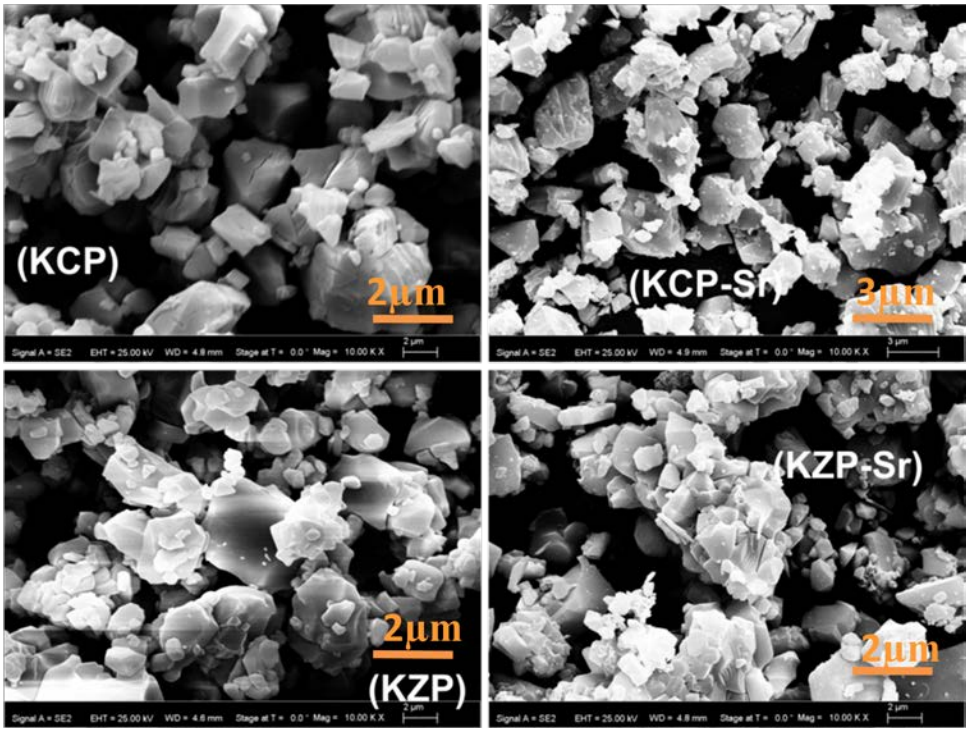

Fig.3.13: SEM images of $K_2Ce(PO_4)_2$ and $K_2Zr(PO_4)_2$ before (KCP and KZP) and after (KCP-Sr and KZP-Sr) exchanging Sr^{2+} ions

The variation of morphology and distribution of Sr^{2+} in the samples were investigated by SEM and mapping of the X-ray by EDS. The SEM images of the samples before and after exchange are compared in Fig.3.13. The SEM images show crystalline and well developed grains for both KCP and KZP samples. The larger grain sizes observed in the samples are due to the adopted high temperature processing procedures. The crystallinity and morphology of both samples remains almost similar after exchange (Fig.3.13). The elemental distributions in samples were studied in area scan mode and the distributions of X-rays are shown in Fig.3.14.

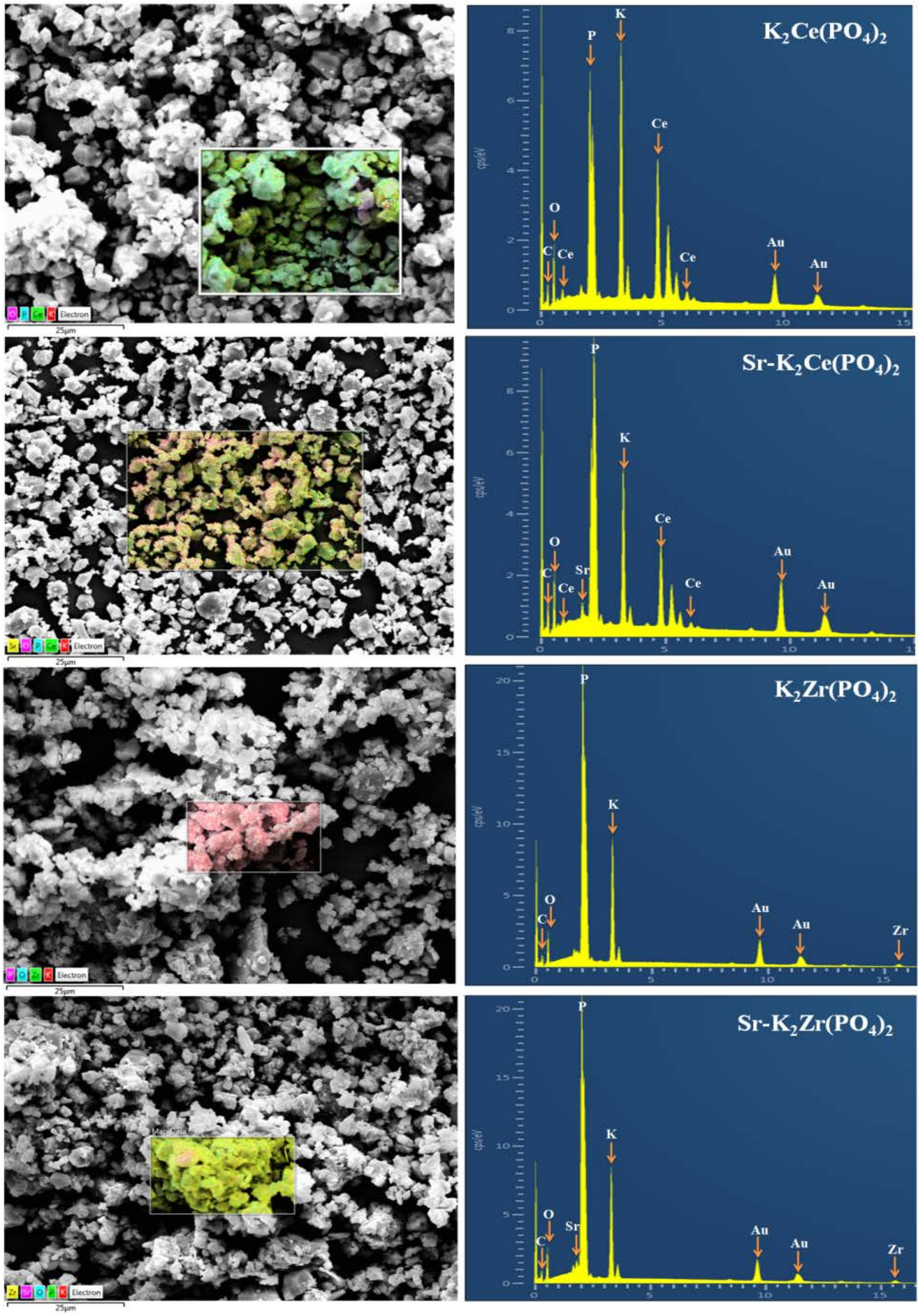

Fig.3.14: EDS spectra of $K_2Ce(PO_4)_2$ and $K_2Zr(PO_4)_2$ before (KCP and KZP) and after (KCP-Sr and KZP-Sr) exchanging Sr^{2+} ions

Uniform distribution of Sr^{2+} over all the grains of the samples indicates all the grains have participated in the ion exchange process. From the characterization of batch experiment samples, it can be concluded that both KCP and KZP can efficiently separate Sr^{2+} ions from solution. Also no structural and morphological changes occur in the exchange process and exchange occurs uniformly over all the grains of the samples. These results are closely similar to crystalline inorganic ion exchangers, like phosphates, silicotitanites and titanites etc. [97a, 99, 104] However, the change in crystal structure at higher temperature or at higher concentration of Sr^{2+} cannot be ruled out. In this study we have indicated that at higher temperature these phases transform to more stable phases containing Sr^{2+} ions.

3.5. Conclusions

In summary, this study revealed ion exchange properties of two complex phosphates for Sr^{2+} ions and in particular a novel complex phosphate of Ce^{4+} ion. Quantitative uptake of Sr^{2+} by KCP and KZP from solution indicated their potential for the separation of Sr^{2+} ions from nuclear waste. It is also inferred that the structure of the phosphate lattice plays an important role in the separation efficiency and selectivity. The study also revealed that KZP is an efficient lattice for separation of Sr^{2+} but has low selectivity due to its layered structure, while the KCP is more selective due to its tunnel like structure. Both lattices show low exchange in acidic and highly alkaline conditions due to strong inference of H^+ and Na^+ ions, respectively. The studies on kinetics and exchange isotherm revealed that they follow pseudo-second order rate law and exchange is mainly by favorable chemisorption process. It is proposed that these lattices can also be directly converted to stable apatite or NZP type host matrices with the separated Sr^{2+} ions.

Chapter 4

High temperature studies on $K_2Ce(PO_4)_2$

4.1. Introduction

$K_2Ce(PO_4)_2$ has been further characterized to investigate the high temperature stability of the material owing to its immobilization capabilities with left over ^{90}Sr in the lattice after elution of radionuclides. Crystalline inorganic phosphates have been considered as an important class of materials due to their diversified crystal chemistry depending on composition, preparation condition as well as external parameters like temperature and pressure. In addition they possess interesting physical properties amenable for varieties of technological applications [53, 105]. Several of such materials like apatite, zircon, monazite, cheralite etc. as well as nasicon type and zirconium phosphate have been considered as potential host matrices for immobilization of radioactive elements. Radionuclides separated from the high level nuclear waste (HLW) can be directly immobilized using such lattices due to their rock analogous properties viz. high thermal and chemical stability, high radiation resistance and insignificant leachability by water. Rich crystal chemistry of phosphates with the variation of nature and ionic radius of cations has been explored in several reports [102b, 106]. In particular, such phosphates with tetravalent ions form densely packed structure and which make them amenable for immobilization of various actinides like uranium, neptunium and plutonium. Besides the complex phosphates with layer and tunnel structures having appropriate exchangeable ions have been considered as promising materials for selective separation of ions from high level nuclear waste or heavy metal ion pollutants from environment [60, 107]. A large numbers of studies have demonstrated efficient exchange or sorption properties for separation of various ions from aqueous solution in a wider range of pH [106]. In particular, orthophosphates of Zr^{4+}, Ti^{4+}, Sn^{4+} and rare-earth ions along with alkali or alkaline-earth metal ions are being considered for such applications due to their ion-exchangeability with various radioactive elements [108]. Also, studies on such complex phosphates with suitable luminescent ions bear significant interest in the fundamental understanding of optical properties as well as technological relevant optical materials [109]. Among the complex phosphates of tetravalent cations, studies with Ce^{4+} are limited due to its structural complexity as well as instability of the tetravalent Ce^{4+} ions in phosphate matrix. Though the structural chemistry of Ce^{4+} has been extensively studied in oxide matrix, the studies are limited with acidic groups like phosphates, vanadates etc. as cerium ion easily transform from Ce^{4+} to Ce^{3+} state [110]. However, analogous phosphates with U^{4+}, Th^{4+}, Pu^{4+} are widely observed in phosphate matrix, which can be attributed to their higher stability in wider chemical environment. Existence of Ce^{4+} in CeP_2O_7 lattice is known and has been explored for negative thermal expansion, mixed ionic and electronic conduction as well as catalytic properties. For the latter two applications, the presence of mixed oxidation states and easier variation of oxidation states are the key features possessed by them. However at higher temperature, the Ce^{4+} reduces to Ce^{3+} and thus the structure of CeP_2O_7 collapses due to formation of Ce^{3+} [111].

Xu *et al*. have reported a complex hydrated phosphate as $(NH_4)_2Ce(PO_4)_2.H_2O$ with Ce(IV) by hydrothermal reaction of CeO_2-NH_3-P_2O_5-H_2O system [112]. Later Xu *et al.* have also reported a similar hydrated phosphate $K_2Ce(PO_4)_2.H_2O$, by hydrothermal reactions and assigned an orthorhombic lattice from powder X-rays diffraction (XRD) studies [113]. Salvado *et al.* [110a]. have reported a series of such hydrated phosphates with K^+, Rb^+, Cs^+ and NH_4^+ ions and investigated detailed crystal structure from powder XRD studies [114]. Crystal structures of these hydrated phosphates have been explained by either an orthorhombic (*Imma*) or tetragonal ($I4_1/amd$) lattices where the distorted cubic CeO_8 and tetrahedral PO_4

units form the building blocks, H_2O and M^+ ions are occupied in the tunnels formed by these units [111d, 114]. Differential thermal analysis studies of Xu *et al.* [113] on hydrothermally prepared $K_2Ce(PO_4)_2.H_2O$ indicated a dehydrated phase at higher temperature (HT) which undergoes a phase transition before its decomposition. However, no details on structure of hydrated, dehydrated or transformed phases have been reported by them. Ogorodnyk *et al* [115]. have prepared a complex phosphate with mixed tetravalent cations having composition $K_4CeZr(PO_4)_4$, by high temperature molten flux method. $K_4CeZr(PO_4)_4$ crystallizes in a tetragonal ($I4_1/amd$) structure with orientationally disordered PO_4^{3-} ions and random distribution of Ce^{4+} and Zr^{4+} ions. The orientation disorder of the PO_4^{3-} ions in this structure has been attributed to the local variation of coordination number around the tetravalent ions i.e. due to a random distribution of ZrO_6 and CeO_8 polyhedra. Popa *et al.* [111c, d] studied a number of complex phosphates of tetravalent cations and concluded that such complexes with Ce^{4+} are non-existent due to transformation of Ce^{4+} to Ce^{3+} during preparation procedure**.** The anhydrous phase of $K_2Ce(PO_4)_2$ was prepared and characterized**,** tetravalent Ce^{4+} is confirmed from both X-ray photoelectron and X-ray absorption spectroscopic studies and a monoclinic ($P2_1/n$) structure with distorted cubic CeO_8 and tetrahedral PO_4 units as structural building units is revealed. Differential scanning calorimetry (DSC) and preliminary HTXRD studies on this anhydrous phase indicated a phase transition at temperature similar to that reported by Xu *et al.* [113] while the details of the high temperature phase still remained unsolved due to limitation of high temperature XRD data as well as decomposition of the sample at higher temperature [94].

Complex phosphates of tetravalent cerium are ideal to simulate the thermophysical properties of tetravalent Pu and other minor actinides as well as for materials with mixed ionic and electronic conduction and redox catalyst. Due to the easy fluctuation of oxidation state of cerium, their structural and high temperature properties bear significant importance. In order to understand the temperature dependent structural properties as well as stability of $K_2Ce(PO_4)_2$, detailed structure of high temperature phase from *in situ* HTXRD data using synchrotron radiation was investigated and established that the ambient monoclinic phase reversibly transforms to a tetragonal phase. Also this study revealed a significant disorder in the K^+ ions located along the tunnels compared to the PO_4^{3-} ions. The HT phase shows appreciably lower expansion compared to the ambient temperature phase. The structure of HT phase and phase transition are also supported by *ab initio* density functional theoretical calculations and *in situ* temperature dependent Raman spectroscopic studies. Also electronic properties of the phases from both experimental studies as well as electronic structure calculations were elaborated in the preceding sections [116].

4.2. Experimental methods

The ambient temperature monoclinic phase of $K_2Ce(PO_4)_2$ was prepared by synthesis method as mentioned in the earlier chapter using KH_2PO_4 and CeO_2 as precursors [94]. The yellow product was characterized by powder XRD, Raman, combined thermogravimetric and differential thermal analysis (TG-DTA) prior to further temperature dependent structural studies. The powder XRD data of the sample were recorded by using synchrotron radiation. XRD patterns at low temperature (up to 60 K) were recorded in transmission mode by using image plate (mar 345) while the data above ambient temperature were recorded in reflection mode using scintillation counter or a Mythen strip detector. For low temperature studies, well ground sample was placed in between two Kapton films and placed in between two copper blocks connected to a liquid helium cryostat. The sample was cooled to 60 K and allowed to equilibrate for about 1h. The XRD pattern at several temperatures in between 60 and 300 K were recorded by heating sample to the desired temperature. For high temperature XRD studies, a small amount of sample was spread over a thin quartz plate placed on a custom made resistive heater and data were recorded while heating the sample from ambient temperature to a specified temperature. Data were also recorded while cooling the sample from high temperature. The temperature of heater was controlled by Eurotherm temperature controller and a stability of ± 1K is ensured prior to the measurement of diffraction data. The diffraction data collected on image plate were integrated by using FIT2D software to obtain 1D diffraction patterns [117]**.**

4.2.1. Theoretical calculations

The calculations were performed using *ab initio* density functional theory (DFT) [118] method implemented in Vienna *ab initio* simulation package (VASP) [119,120]. All the possible structures inferred from the XRD studies and reported structures for similar compositions were relaxed using conjugate gradient algorithm. The band structure and electronic density of states were calculated using very fine mesh. The zone centre phonon frequencies were calculated using density functional perturbation method [121, 122].

4.3. Results and discussion

4.3.1. X-ray diffraction studies

In order to further characterize the synthesized phase, two more compositions with different K:P ratio were prepared under similar conditions. In both of these additional compositions, Ce^{4+} of CeO_2 transformed to Ce^{3+} and thus they crystallize in structures analogous to the trivalent rare-earth ions. Further, the powder XRD data reported for the

$K_2Ce(PO_4)_2.H_2O$ [113] and $K_4Ce_2P_4O_{15}$ [123] were also compared. The phase purity and structure of prepared $K_2Ce(PO_4)_2$ sample were confirmed by Rietveld refinement of the XRD data recorded at 300 K. The ambient temperature XRD patterns recorded on heating stage as well as on cooling assembly were used for the correction of the instrumental parameters of the respective experimental run. Earlier mentioned structural details for $K_2Ce(PO_4)_2$ [94] were used as initial parameters for model structure. The background of the diffraction patterns recorded on image plate (low *T*) was refined by linear interpolation of selected points to create a smoothly varying background profile. Data collected by scintillation counter or strip detector (high *T*) was modeled by using 5th order polynomial functions. The Bragg peaks of the XRD patterns were modeled by a split-Pearson profile or pseudo-Voigt profile function with an angle dependent mixing parameters (η) defined as: $\eta = \eta_0 + X \times 2\theta$, where η_0 and X are refinable parameters. Further, the scale, unit cell parameters and position coordinates followed by isotropic thermal parameters were refined. Some of the weak peaks attributable to monazite type $CePO_4$ were observed in some XRD patterns. The complete diffraction pattern recorded at 300 K could be explained by this considered model and the refined structural parameters are in agreement with those reported earlier by us [94].

The refined unit cell parameters and residuals of refinement of the ambient temperature phase are given in Table 4.1. The final Rietveld refinement plot for the XRD data of $K_2Ce(PO_4)_2$ at 300 K is shown in Fig.4.1. In an analogous manner, the XRD pattern recorded at 60 K could be satisfactorily refined by using the observed structural parameters at 300 K. It is observed that the unit cell parameters decrease only marginally with decreasing temperature up to 60 K, the lowest temperature of the present XRD studies. Typical Rietveld refinement plot for the XRD data recorded at 60 K is included in Fig.4.1. No significant changes or splitting of any peaks are observed in the low temperature data which suggests for absence of any structural change at lower temperature. Low temperature neutron diffraction studies up to 6 K were also carried out using CCR based cryostat on 5-Linear PSD based powder neutron diffractometer at Dhruva nuclear reactor, BARC, Mumbai. The analysis of powder neutron diffraction data also suggest for the absence of structural change up to 6 K.

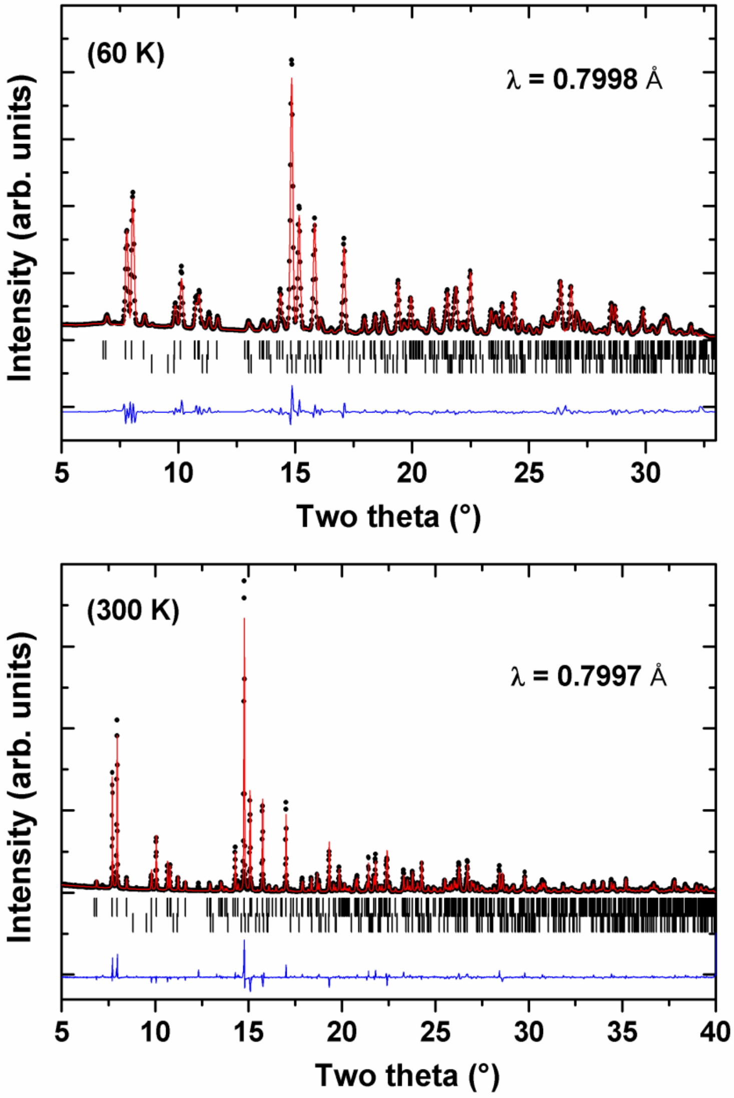

Fig.4.1: Rietveld refinement plots of $K_2Ce(PO_4)_2$ recorded at 300 K and 60K

Table 4.1: Experimental and theoretical unit cell parameters of different structural models of $K_2Ce(PO_4)_2$. DFT calculated unit cell parameters are at 0 K

	Str-I: Monoclinic **$P2_1/n$ (No. 14)**				**Str-III: Tetragonal** **$I4_1/amd$ (No. 141)**		**Str-II: Orthorhombic** **Imma (No. 74)**	
	DFT	**Expt.**			**DFT**	**Expt.**	**DFT**	**Expt.**
Temp	0 K	60 K	300 K	885 K	0 K	885 K	0 K	885 K
a (Å)	9.2889	9.0755(1)	9.1020(1)	9.1761(2)	6.9184	6.83658(3)	6.9181	6.8363(3)
b (Å)	11.0347	10.7823(2)	10.8132(1)	10.8571(2)	6.9184	6.83658(3)	6.9187	6.8369(3)
c (Å)	7.7894	7.5994(1)	7.6231(1)	7.7096(2)	17.9441	17.5091(1)	17.9440	17.5090(1)
β (°)	110.767	111.142(1)	111.14(1)	111.289(2)	90	90	90	90
Z	4	4	4	4	4	4	4	4
V $(Å)^3$	746.549	693.58(2)	699.78(2)	715.66(3)	858.882	818.35(1)	858.881	818.35(5)
Rp, Rwp (%)		5.08, 6.88	9.87, 12.7	9.20, 11.8		9.20, 11.8		9.33, 12.0
$\chi 2$		2.81	5.34	6.22		6.22		6.41
R_B, R_F		3.91, 3.25	8.58, 4.50	11.7, 8.68		7.42, 4.77		7.79, 4.26
E (ev/F.U.)	-92.30				-92.31		-92.31	

The details of structural arrangement in monoclinic $K_2Ce(PO_4)_2$ have been explained in Chapter 3 and various reports.[94] For the convenient and completeness of this section, it is mentioned here that the structure of monoclinic phase has distorted eight coordinated CeO_8 polyhedra and nearly regular PO_4 tetrahedra as structure building units. The CeO_8 units are connected to two PO_4 units by sharing its two nearby edges while to four other PO_4 units by sharing other corner oxygen atoms. The anionic clusters formed by such arrangement are linked together forming a three dimensional structure containing tunnel like open space. The K^+ ions are occupied in these open tunnels of the structure. It can be mentioned here that the structure of analogous complex phosphates of thorium, like $Na_2Th(XO_4)_2$ (X = P and As) have been reported with closely similar monoclinic lattices but with different unit cell parameters [124, 125]. The lowering of symmetry and doubling of unit cell in the latter structures are not only due to the splitting of the sites of tetravalent ions but also due to the differences in the linkages of the ThO_8 and PO_4 units. In the present case, none of the XRD patterns recorded at lower temperature down to 60K or powder neutron diffraction data at 6K, indicate any feature attributable to lowering of symmetry. Thus it can be concluded that the ambient temperature monoclinic phase remains unchanged at lower temperature [126].

4.3.2. Structural description

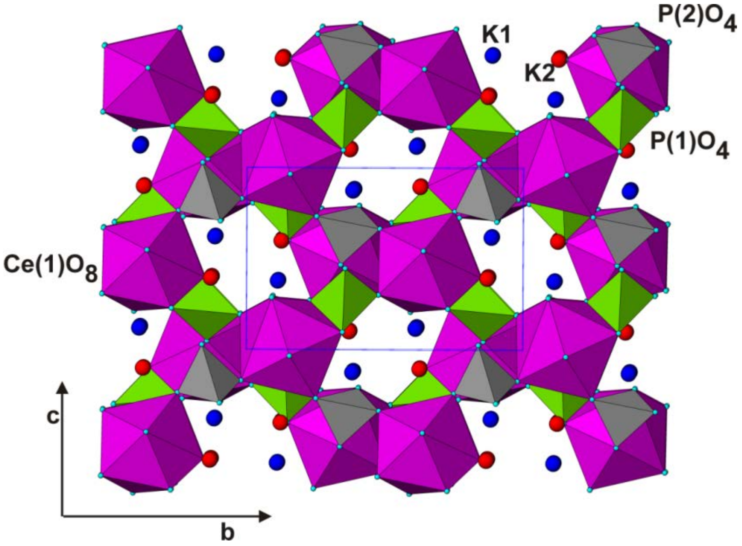

Fig.4.2: Crystal structure of $K_2Ce(PO_4)_2$ in <100> projection

Analysis of the refined structural parameters of $K_2Ce(PO_4)_2$ indicates two distinct and nearly regular tetrahedral phosphate groups ($P(1)O_4$ and $P(2)O_4$) and one Ce in eight coordinated polyhedra with oxygen atoms. The typical P-O bond lengths in both PO_4 tetrahedra are in range of 1.55 to 1.56 Å as observed in regular orthophosphate groups. The typical Ce-O bond lengths are in the range of 2.20- to 2.54 Å. The bond valence sum calculations for CeO_8 polyhedra indicates the total valence of Ce is 4.17 (R_o = 2.096, B = 0.37) [110d] which is in agreement for the Ce^{4+} ion in the structure. This is further confirmed by the XPS results explained subsequently. The $P(1)O_4$ and $P(2)O_4$ tetrahedra share one edge and two corners oxygen atoms with CeO_8 polyhedra and form a three dimensional lattice with tunnel like empty space along the <100> direction. The empty channels are occupied by two K^+ ions which balance the net charge in the structure. The observed K-O bond lengths are in the range of 2.52 to 3.05 Å and the separation between two K^+ ions is 3.35 to 3.44 Å (viz. K1-K1 = 3.436, K2-K2 = 3.353 and K1-K2 = 3.421 Å) which is similar to that reported by Ogorodnyk *et al*. for $K_4CeZr(PO_4)_2$ [115]. Within the bond distance limit of 3.1 Å, both K(1) and K(2) can be considered as distorted and asymmetric eight coordinated polyhedra. The typical three dimensional structure of the $K_2Ce(PO_4)_2$ is shown in Fig.4.2. Typical local surrounding around the CeO_8 showing PO_4 tetrahedra is shown in Fig.4.4.

Studies on $Na_2Th(PO_4)_2$ by Galesic *et al.* [124] indicated two closely related lattices with symmetry $C2/c$ and $P2_1/n$ for its structure. In both the polymorphs of $Na_2Th(PO_4)_2$, Th^{4+} ions form eight coordinated polyhedra within the Th-O bond length limit of 2.7 Å and P^{5+} ions from nearly regular tetrahedra. The reported unit cell parameters of both the phases of $Na_2Th(PO_4)_2$ are closely similar. The unit cell parameters of the presently studied $K_2Ce(PO_4)_2$ can be related to those reported for $Na_2Th(PO_4)_2$ by unit cell relations as: $a' = a$, *b' = 2b, c' = c*, where the prime indicates the parameters of Galesic *et al.* [124]. The preliminary inspection of the powder XRD pattern calculated from a model generated from $Na_2Th(PO_4)_2$ with the corresponding unit cell parameters for $K_2CeP_2O_8$ shows significant differences in the intensity distribution. Further refinements of the powder XRD pattern with this model lead to no success. Thus it can be concluded that the observed phase of $K_2Ce(PO_4)_2$ has distinct structural features compared to earlier reported $Na_2Th(PO_4)_2$ [111b] or $K_2CeZr(PO_4)_2$ [115]. Further comparison of these three structure types indicates distinct structural arrangements of MO_8 (M = Th, Ce or Ce/Zr) and PO_4 polyhedra.

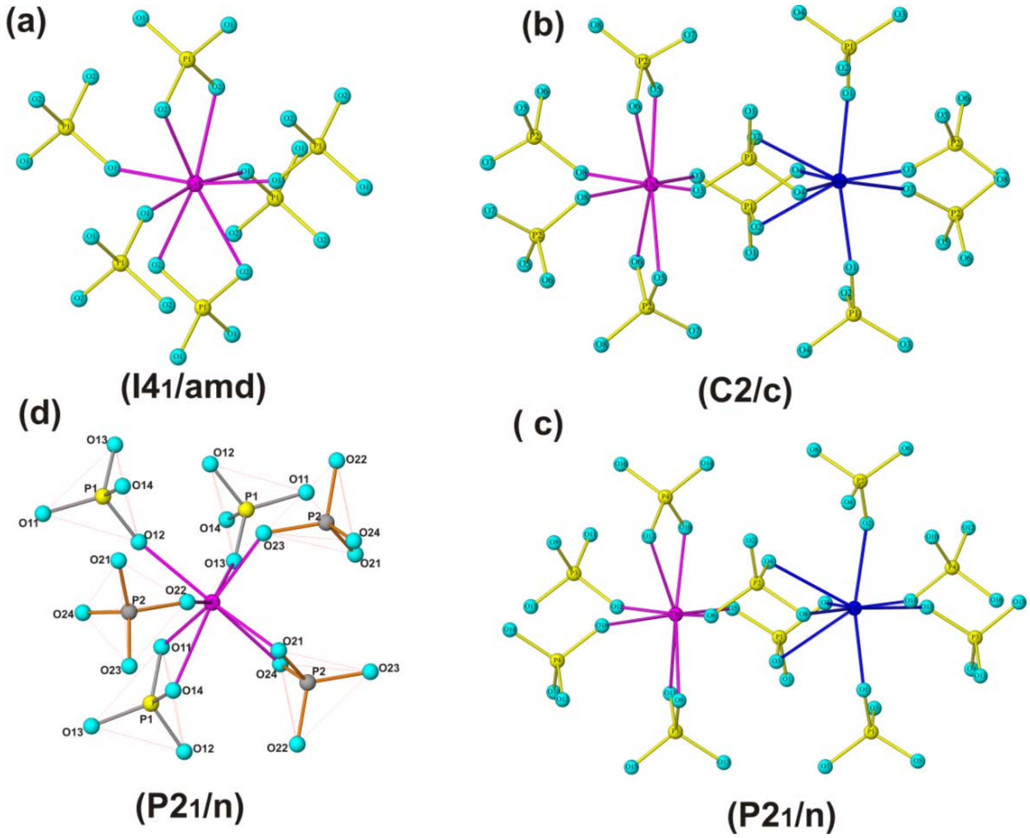

Fig.4.3: Typical connections of distorted cubic AO_8 polyhedra and tetrahedral PO_4 in different $A_2B(PO_4)_2$ structures. (a.) $(NH_4)_2Ce(PO_4)_2H_2O$ [112]), (b) and (c) for $Na_2Th(PO_4)_2$ [111a], (d) $K_2Ce(PO_4)_2$ of present study

In the reported structures of $K_2CeZr(PO_4)_2$ or $(NH_4)_2Ce(PO_4)_2$, the PO_4 tetrahedra are connected to MO_8 distorted bisdisphenoid by sharing two *trans* edges of latter while in the present structure of $K_2Ce(PO_4)_2$, the PO_4 tetrahedra share two *cis* edges of CeO_8 polyhedra. This arrangement is similar to that observed for $A_2Th(AsO_4)_2$, where A = K^+ and Rb^+ [125]. Interestingly the structure reported for $Na_2Th(PO_4)_2$ shows both kinds of connections with two crystallographically distinct Th^{4+} ions [115]. Typical structures depicting the differences in the polyhedral arrangements in these three compounds are shown in Fig.4.3.

It can be mentioned here that the PO_4 groups in $K_2CeZr(PO_4)_2$ has orientational disorder due to the differences in the size of Ce^{4+} and Zr^{4+}, while no such disorder is observed in $Na_2Th(PO_4)_2$. However, two different symmetries are formed in $Na_2Th(PO_4)_2$ compounds due to ordering and disordering of Th^{4+} sites. Similar comparison with the reported structures for $Na_2Zr(PO_4)_2$ or $K_2Zr(PO_4)_2$ indicates a clear differences in them. In these Zr^{4+} analogous compositions, the Zr forms octahedral units and they are connected to PO_4 by sharing its corner oxygen atoms only. Thus it is reasonable to say that the inter-cation (M^{4+} and P^{5+}) repulsion favor for such corner connected polyhedral structure with such smaller tetravalent cations. It can be expected that the structural differences between $K_2Ce(PO_4)_2$ and $Na_2Th(PO_4)_2$ may arise from the difference in the ionic radii of Ce^{4+} (0.97 Å in coordination number 8) and Th^{4+} (1.05 Å, in coordination number 8). However, smaller size of CeO_8 compared to ThO_8 should destabilize the *cis* connected MO_8 and PO_4 structure of the $K_2Ce(PO_4)_2$. The preliminary analysis of the structure of $K_2Ce(PO_4)_2$ at high temperature indicates a trans connected MO_8 and PO_4 structure and has a significantly larger volume compared to the structure of ambient temperature phase. In addition, the observation of a similar structure in $K_2Th(AsO_4)_2$ as in the ambient temperature structure of $K_2Ce(PO_4)_2$, suggests nature of charge balancing counter cations like Na^+ (radius 1.02 Å) or K^+ (ionic radius 1.38 Å) as well as preparation conditions might be the structure directing factors in the crystal chemistry of the phosphates of tetravalent ions. Thus the formation of structure $A_2M^{4+}(PO_4)_2$ is not only sensitive to the nature of tetravalent (M^{4+}) cation but also to the ionic radii of A^+ ions. Also, it appears that the structure of such mixed phosphates of alkali and tetravalent cations are mainly controlled by the ionic radii and local structure around the tetravalent cation.

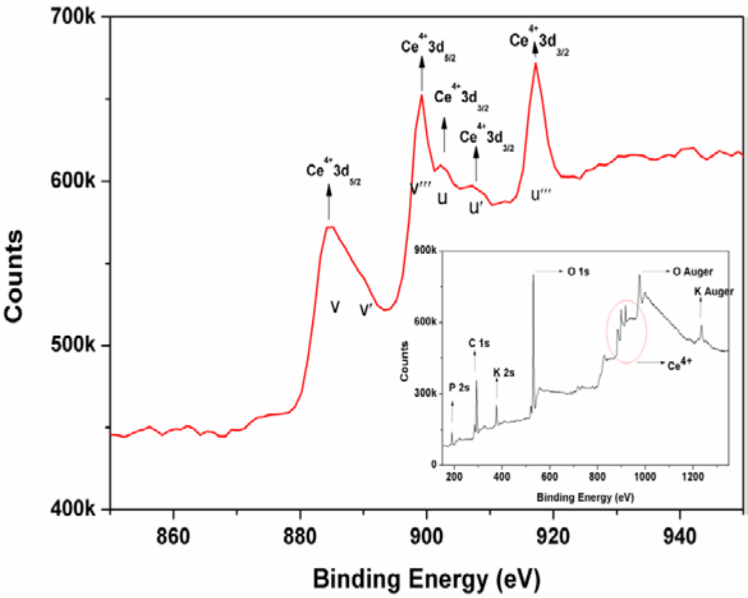

Fig.4.4: XPS spectra of $K_2Ce(PO_4)_2$

The presence of Ce^{4+} as concluded from the valence calculations is further confirmed from the XPS spectrum of the sample. The observed XPS spectrum of the sample is shown in Fig.4.4. The characteristic 3d photoelectron spectra of the sample are closely similar to that reported for Ce^{4+} in CeO_2. The presence of $3d_{5/2}$ satellite peak (u‴) around 917 eV clearly indicates the +IV oxidation state of cerium in the sample. It needs to mention here that the composition $K_4Ce_2P_4O_{15}$ studied by Szczygiel *et al.* [123] does have the characteristic u‴ suggesting that composition with major Ce^{3+}. Popa *et al.* [111d] have compared the 3d photoelectron spectra of Ce^{3+} and Ce^{4+} and suggested a significant difference in line shapes of the peaks and noticeable differences in the intensity of the u ($3d_{3/2}$) and v‴ ($3d_{5/2}$) peaks. The present observed line shape and intensities of u and v‴ peaks of $K_2Ce(PO_4)_2$ further support the presence of Ce^{4+}.

Further support for the oxidation state of cerium was obtained by comparing the L-II adsorption edge of $K_2Ce(PO_4)_2$ and CeO_2. The normalized absorption for both XANES spectra for $K_2Ce(PO_4)_2$ and CeO_2 were shown in Fig.4.5. The L-II edge of CeO_2 is in agreement with that reported earlier in literature [125]. The characteristic absorption at L-II edge of Ce are closely similar in both the studied materials and thus supports for Ce^{4+} in $K_2Ce(PO_4)_2$. Hence it could be unequivocally concluded that the present studied composition is formed with Ce^{4+}.

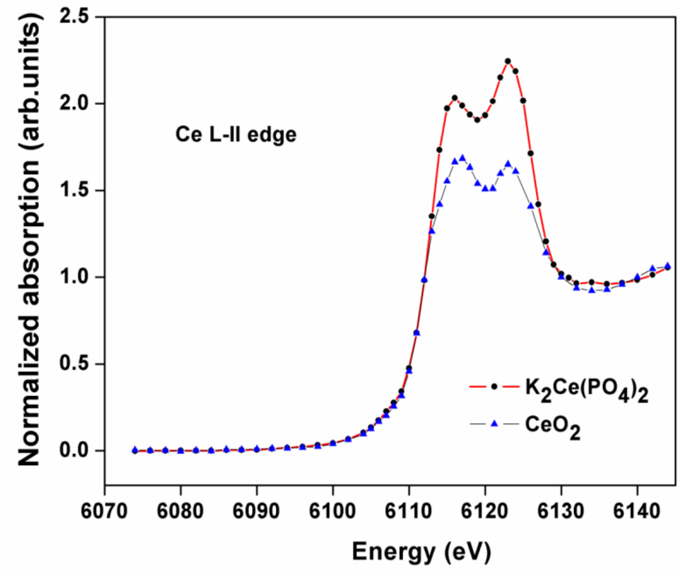

Fig.4.5: XANES spectra of $K_2Ce(PO_4)_2$ and CeO_2 at the L-II edge

4.3.3. Thermal studies

Thermogravimetric plots of the prepared composition are recorded while heating from ambient to 900°C and shown in Fig.4.6a. It can be seen that weight loss in sample occurs in two steps. The first step of weight loss is sharp, with an onset temperature of about 850°C. However, the second weight loss step overlaps with the first one at around 880°C. The initial weight loss amounting to 1.8 % can be accounted to a loss of one oxygen atom and subsequent loss can be accounted to the loss of P_2O_5 molecules.

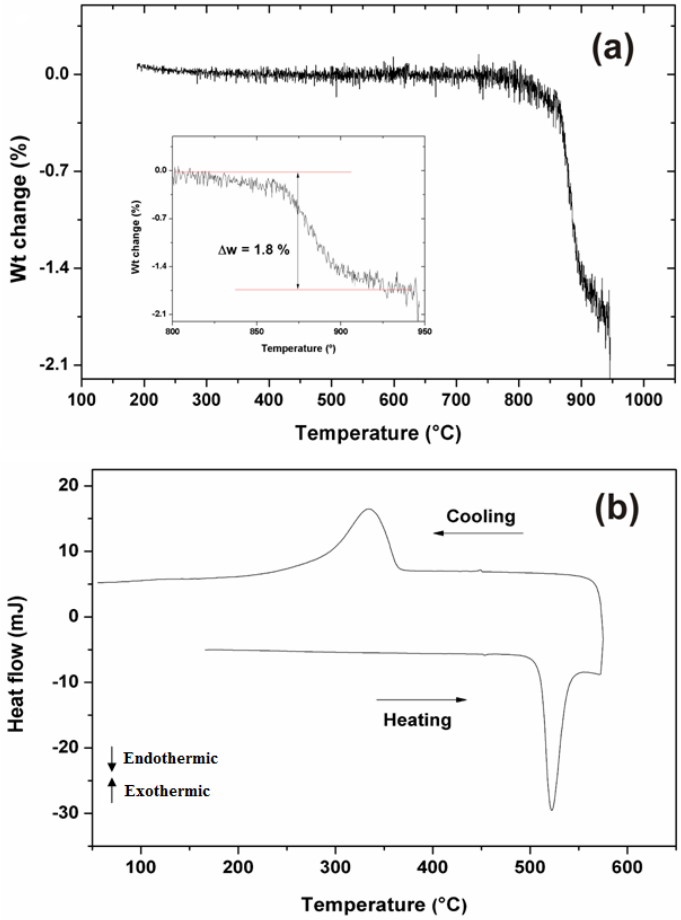

Fig.4.6: Typical thermogravimetric curves of $K_2Ce(PO_4)_2$ in heating cycle (a) and the DSC plots indicating the phase transition are shown in (b)

Szczygiel *et al.* [123] have reported a similar two step weight loss for the $K_4Ce_2P_4O_{15}$ sample, but attributed for the loss of P_2O_5. The analysis of initial weight loss suggests the composition as $K_4Ce_2P_4O_{16}$ with all cerium in 4+ oxidation state. Around 880°C, the composition decomposes peritectically to $CePO_4$, $K_3Ce(PO_4)_2$ and P_2O_5. Xu *et al.* [113] have reported the decomposition behavior of $K_2Ce(PO_4)_2.H_2O$ and suggested three weight losses, namely loss of water molecules to an anhydrous phase around 175°C, decomposition accompanied by reduction of Ce^{4+} to Ce^{3+} around 850°C and subsequently a peritectic decomposition to $K_3Ce(PO_4)_2$, $CePO_4$ and P_2O_5 around 880°C. The DSC traces of the sample shown in Fig.4.6 show an endothermic peak around 525°C attributable to a structural transition.

A similar endothermic peak has been reported by Szcygiel *et al.* for $K_4Ce_2P_4O_{15}$ sample [123]. Xu *et al.* [113] have also reported a structural transition at around 500°C for the anhydrous product obtained from $K_2Ce(PO_4)_2.H_2O$. Comparing results of Xu *et al.* [113]. with the present observation, it can be concluded that the dehydration $K_2Ce(PO_4)_2.H_2O$ leads to an anhydrous phases which is similar to that observed in present study as well as that of Szcygiel *et al.* [123]. However, in both the earlier studies, structure of hydrated or anhydrous products was not investigated to confirm the composition. It can also be seen from the DSC trace that the endothermic peak observed in heating cycle reverts back while cooling but with a large hysteresis in temperature. Thus the phase transition might be a reconstructive type with significant change in structure. The enthalpy of phase transition as obtained from the area of the DSC peak in heating cycle is 69.5 J/g. The observed enthalpy change is also close to that reported by Szcygiel *et al.* [123]. Thus it is convincing that the composition studied by Szcygiel *et al.* is $K_4Ce_2P_4O_{16}$ and similar to the presently studied phase as well as the anhydrous phase of Xu *et al.* [113]. Since the composition undergoes irreversible decomposition at higher temperature no single crystal could be obtained for further study. Hence the structural studies from powder diffraction were carried out [127].

In order to understand the temperature induced structural changes, the XRD patterns recorded at different temperatures were analyzed. The unit cell parameters and structure of monoclinic phase could be successfully accounted in all the high temperature XRD patterns. The complete structural analysis of high temperature phase was carried out from the XRD data recorded at 885 K in the heating cycle due to its higher resolution and they were used as initial structural parameters for refinement of all other temperatures. Excluding the peaks attributable to monoclinic phase, all other peaks observed in the XRD pattern recorded at 885 K are attributed to the high temperature phase and can be accounted by a tetragonal as well as a feebly distorted pseudo-orthorhombic lattice. The observed unit cell parameters are close to the reported tetragonal lattices for $(NH_4)_2Ce(PO_4)_2.H_2O$ [112], $K_4CeZr(PO_4)_4$ [115] and orthorhombic lattice for $(NH_4)_2Ce(PO_4)_2.H_2O$ [112]. The reported structural details of these materials were used as initial models for refinement of the XRD data.

Rietveld refinements with model structures based on tetragonal [114] and orthorhombic [110a] of $(NH_4)_2Ce(PO_4)_2H_2O$ can successfully explain the reflections as well as peak intensities of the high temperature phase of $K_2Ce(PO_4)_2$. It is also revealed that about 33 wt % of monoclinic phase coexist at this temperature. In the tetragonal model structure, one cerium (Ce1), one K (K1), and one P (P1) are respectively occupied in *4a*, *8d* and *8e* sites of the space group $I4_1/amd$, while two oxygen atoms (O1 and O2) are occupied in *16h* sites. Similarly, in the orthorhombic (space group: *Imma*) model, one Ce at *4c*, two K (K1 and K2 at *4a* and *4d*, respectively), two P (P1 and P2 at *4e* and *4e*, respectively) and four oxygen

(O1, O1a, O2, O2a at *8h*, *8i*, *8h*, *8i*, respectively) are considered. The refined unit cell parameters and residuals of refinement of these two models are: (tetragonal, $I4_1/amd$), $a = b = 6.83658(3)$ Å, $c = 17.5091(1)$ Å, $V = 818.35(1)$ Å^3, $R_p = 9.20$ %, $R_{wp} = 11.8$ %, $\chi^2 = 6.22$, $R_B = 7.42$, $R_F = 4.77$ %; (orthorhombic, *Imma*), $a = 6.8363(3)$ Å, $b = 6.8369(3)$ Å, $c = 17.5090(1)$ Å, $V = 818.35(5)$ Å^3, $R_p = 9.33$ %, $R_{wp} = 12.0$ %, $\chi^2 = 6.41$, $R_B = 7.79$ %, $R_F = 4.26$ %.

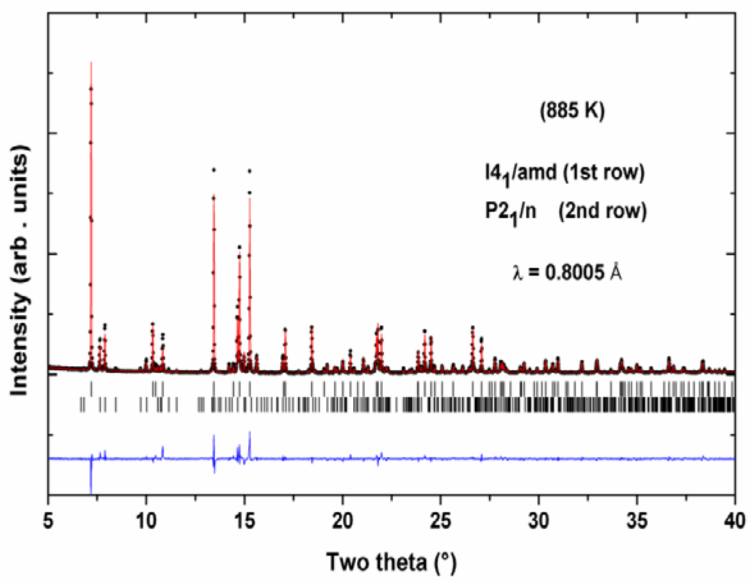

Fig.4.7: Rietveld refinement plot of the XRD pattern $K_2Ce(PO_4)_2$ refined with tetragonal ($I4_1/amd$) symmetry

The typical observed orthorhombicity ($|b - a|/|b + a|$) is estimated as 4.3×10^{-5}, which is almost zero and thus the lattice can be treated as a tetragonal lattice. In addition, the residuals obtained for tetragonal lattice are relatively lower as compared to those observed for orthorhombic lattice. From the point of view of higher symmetric lattice and relatively better residuals, it is logical to accept the tetragonal structure as the structure of high temperature phase. Typical Rietveld refinement plot of the XRD pattern of $K_2Ce(PO_4)_2$ refined with tetragonal symmetry is shown in Fig.4.7.

It can be mentioned here that the tetragonal (*I4₁/amd*) and orthorhombic (*Imma*) lattices are related by group-subgroup transformation where the K1, P1, O1, and O2 sites split into two distinguishable sets. Further it is noticed that the shifting of the potassium (K1) atoms from the special positions *8c* to *16h* in $I4_1/amd$ structure reduces the amplitudes of thermal parameters of K atoms significantly, which indicate the K^+ ions are disordered in the lattice and have ½ occupancy in *16h* site. This also suggests the K^+ ions are of dynamic nature, and in particular at higher temperature. Typical crystal structure of orthorhombic $K_2Ce(PO_4)_2$ is shown in Fig.4.8, crystal structure of tetragonal $K_2Ce(PO_4)_2$ is shown in Fig.4.9.

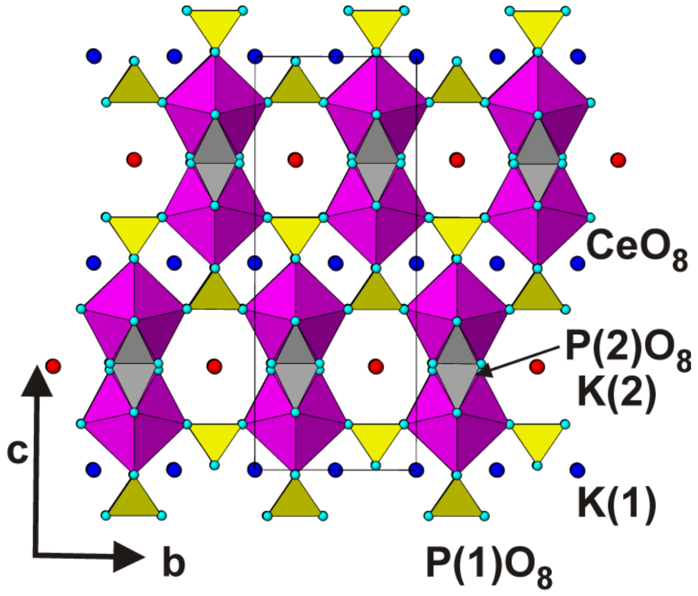

Fig.4.8: Crystal structure of $K_2Ce(PO_4)_2$ in orthorhombic structure

Similar structural analysis for a possible disorder of tetrahedral PO_4 group in the structure were also carried out using the model structure based on parameters reported by Ogorodnyk *et al.* [115]. It has been mentioned earlier that the tetragonal structure reported by Ogorodnyk *et al.* for $K_4CeZr(PO_4)_4$ differed from the tetragonal structure reported by Salvado *et al.* for $(NH_4)_2Ce(PO_4)_2.H_2O$ [110a]. The present tetragonal structure is different from these reported structures in the linkages of PO_4 units with the polyhedra around tetravalent cation. In case of tetragonal structure of $(NH_4)_2Ce(PO_4)_2H_2O$, the Ce^{4+} ions have distorted eight coordinated CeO_8 polyhedra; while in $K_4CeZr(PO_4)_4$, due to the larger difference in ionic radii of Ce^{4+} and Zr^{4+} ions they form CeO_8 and ZrO_6 polyhedra respectively. The statistical distribution of these CeO_8 and ZrO_6 polyhedra resulted in an orientationally disordered PO_4 sub-lattice. Although such scenario is not expected in the present case due to the presence of only one type tetravalent ion, attempts were made to refine the XRD pattern expecting orientational disorder due to temperature effect. In this model, Ce and K are occupied in *4b* and *8c* sites of space group $I4_1/amd$, while P atoms are occupied statistically in 8*e* and *16h* sites in the ratio of 1:1. The oxygen atoms are distributed over four different sites namely *16h*, *16h*, *8e*, and *16h* with occupancies 1, 0.5, 0.5, and 0.25, respectively. A good match between the experimental and calculated diffraction data is observed in this case also. However, despite having larger number of free parameters, the residuals are not better than those obtained for the ordered tetragonal structure. Thus the structure of present high temperature phase does not have disorder in PO_4 group rather it has disorder in K^+ sites.

The analysis of the structural parameters of $K_2Ce(PO_4)_2$ in the tetragonal structure indicate that the phosphorous atoms have a tetrahedral PO_4 configuration with two O1 and two O2, while Ce atoms have eight coordinated distorted cubic CeO_8 configuration with four

O1 and four O2. The CeO_8 units are linked to two PO_4 units by sharing the edges along the *c*-axis while to four other PO_4 units by sharing corners along the *ab* plane forming a cluster with composition $[Ce(PO_4)_2]^{2-}$. The structural arrangement of CeO_8 and PO_4 units forms tunnel like empty space along the <100> direction which are occupied by the K^+ ions and they balance the net negative charge of $[Ce(PO_4)_2]^{2-}$ in the lattice. The typical crystal structure of monoclinic and HT tetragonal $K_2Ce(PO_4)_2$ showing linkages of CeO_8 and PO_4 units of $[Ce(PO_4)_2]^{2-}$ are depicted in Fig.4.9.

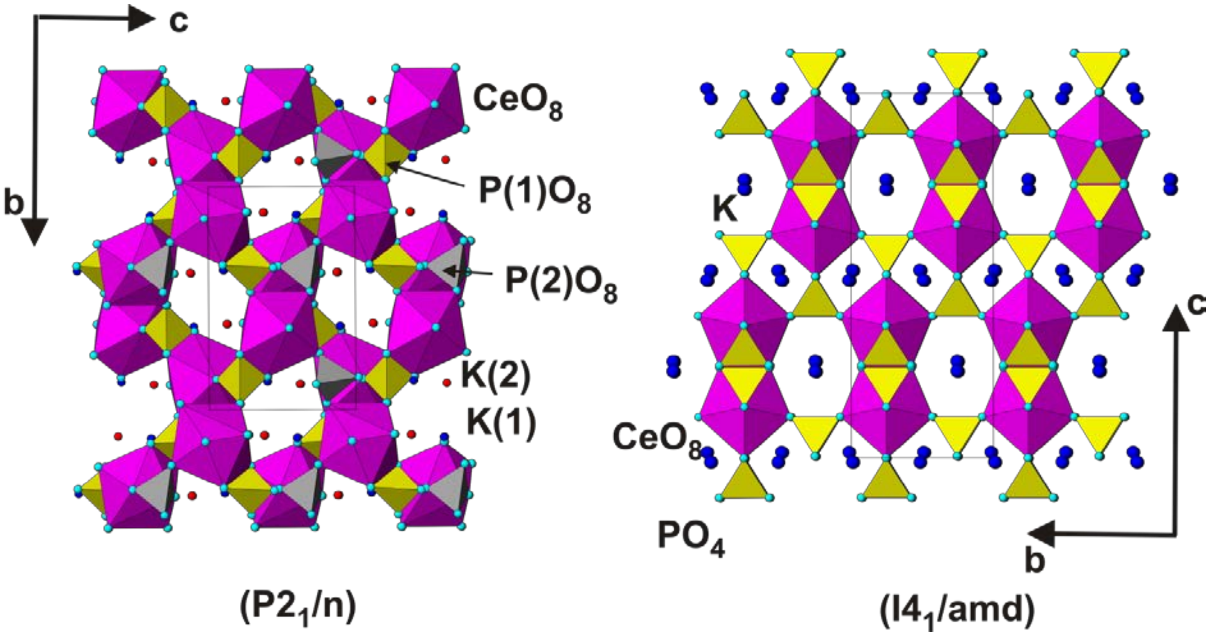

Fig.4.9: Crystal structure of $K_2Ce(PO_4)_2$ in monoclinic and tetragonal structure

Similar structural analysis on orthorhombic studies indicated that the K and P atomic sites are split into two sets of different sites and the oxygen atoms are occupied in four different sites, whereas the Ce and P atoms have similar CeO_8 and PO_4 polyhedra and their connections are also closely similar to that observed in the tetragonal structure. As mentioned earlier, the tetragonal (*$I4_1/amd$*) and orthorhombic (*Imma*) structures are related and they differ only in ordering of K^+, anions and hence one can expect that the dynamic disorder of K^+ ions of the former structure may segregate or relax to ordered equilibrium sites either by long annealing or by cooling under certain procedure. However, this could not be concluded in this study as the XRD patterns recorded while heating or cooling do not show any significant differences. Also it can be mentioned here that the local surrounding of the CeO_8 as well as PO_4 units are more distorted in orthorhombic structure compared to that in tetragonal structure. However, in both the cases the distortions are found to be lower than the ambient monoclinic structure.

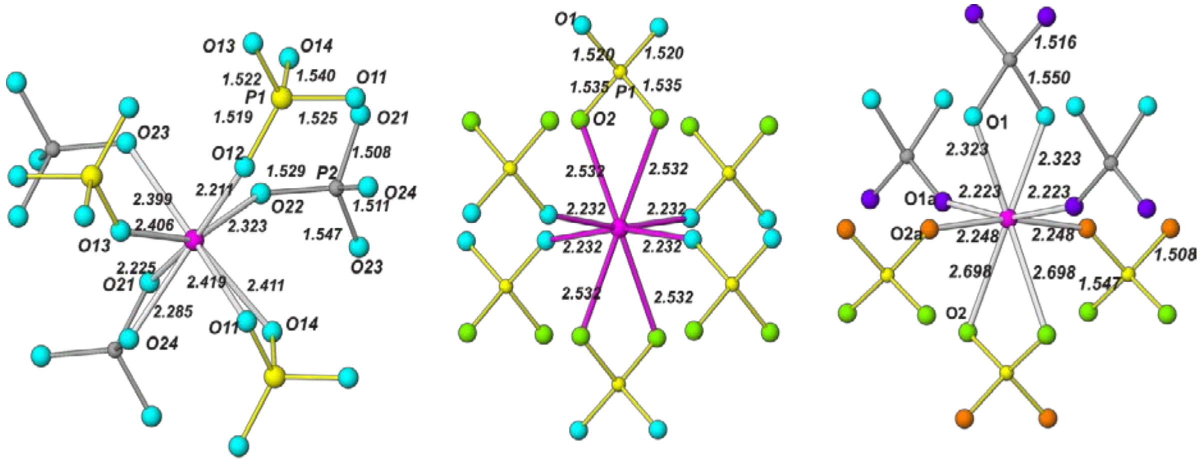

($P2_1/n$) ($I4_1/amd$) (Imma)

Fig.4.10: Polyhedral connections of $K_2Ce(PO_4)_2$ in monoclinic (*$P2_1/n$*), tetragonal (*$I4_1/amd$*) and orthorhombic (*Imma*) structures. (Digits are typical bond lengths)

4.3.4. Theoretical calculations

Further to understand the crystal structure and phase transition in $K_2Ce(PO_4)_2$, *ab initio* density functional theory (DFT) calculations were performed. The equilibrium structure of $K_2Ce(PO_4)_2$ for different structural models, namely monoclinic (*P*2_1*/n*, *P*2_1*/c* and *C2/c*), orthorhombic (*Imma*) and tetragonal (*I*4_1*/amd*) structures were calculated. The calculated unit cell parameters and the energy per formula units are given in Table 4.1. As explained earlier, the structural parameters calculated on symmetry *P*2_1*/c* and *C2/c* equivalent to $Na_2Th(PO_4)_2$ structures cannot explain the experimentally observed data either at lower or higher temperature and thus are excluded from further considerations. As expected the equilibrium volume of monoclinic (*P*2_1*/n*) lattice for ambient temperature phase is overestimated by about 7.6 % due to the underestimation of the cohesion energy in GGA formalism**.** The calculated position coordinates for the ambient temperature monoclinic phase are in close agreement with the experimental results. A comparison of equilibrium lattice energy for different structures suggests that the monoclinic (*P*2_1*/n*) lattice is the stable lattice for $K_2Ce(PO_4)_2$ compared to all other considered lattices. From the pressure dependent equilibrium volume of the equilibrium monoclinic (*P*2_1*/n*), tetragonal and orthorhombic structures, the bulk modulus were obtained by using the 3rd order Birch Murnaghan (BM-III) equation of state. The calculated bulk moduli for the *P*2_1*/n*, *I*4_1*/amd* and *Imma* structures are 45.18, 64.98 and 64.98 GPa, respectively. The pressure derivatives (K′) Band reference volumes (V_0) of the phases are: 5.10, 747.04 Å^3 (for *P*2_1*/n*), 5.04, 847.32 Å^3 (for *I*4_1*/amd*) and 5.62, 856.36 Å^3 (for *Imma*). The calculated bulk moduli are closely similar to those experimentally observed bulk modulus of complex phosphates containing alkali metal ions [128]**.** In addition they are appreciably lower compared to the zircon or monazite type phosphates [129]**.** Despite lower packing of the high temperature structures, they show relatively higher bulk modulus compared to the ambient temperature phases. This can be attributed to the zircon type connections of polyhedra in the latter structures compared to that in monoclinic *$P2_1/n$* structure. However, the calculations indicated that the orthorhombic and tetragonal structures have almost similar energy and both are relatively more stable compared to $Na_2Th(PO_4)_2$ type monoclinic lattices [125]. It can be mentioned here that in the present material, the $Na_2Th(PO_4)_2$ type monoclinic *$P2_1/c$* structure is expected only at larger volume, and hence that may crystallize with larger tetravalent cations. However, the transition may not occur due to the intervening stable orthorhombic or tetragonal structures as well as instability of the structure due to reduction of Ce^{4+} ions at higher temperature as concluded earlier**.**

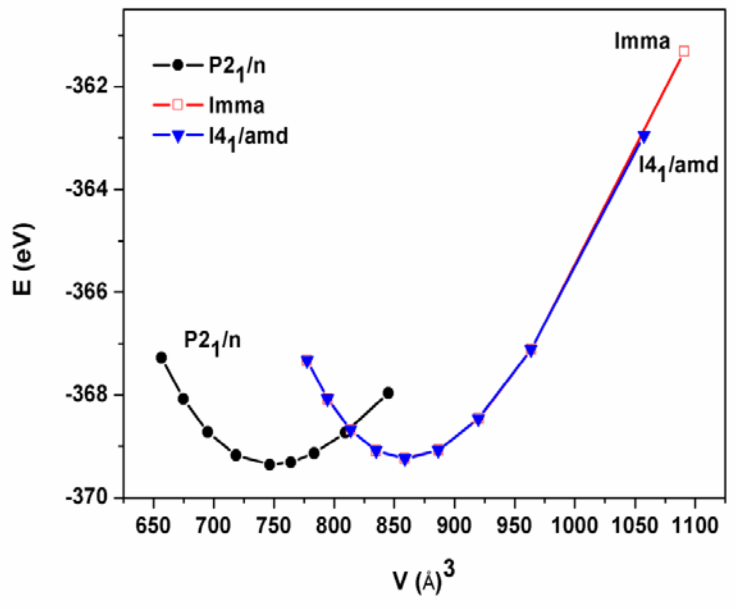

Fig.4.11: The variation of lattice energy with unit cell volume of $K_2Ce(PO_4)_2$ for monoclinic (*$P2_1/n$*) phase and tetragonal (*$I4_1/amd$*) and orthorhombic (*Imma*) structures

The formation of $Na_2Th(PO_4)_2$ can thus be related to the larger ionic radii of Th^{4+} ions compared to Ce^{4+}. Though the equilibrium molar volume of monoclinic *C2/c* structure is comparable to that in monoclinic *$P2_1/n$* structure, the structure is not experimentally observed in $K_2Ce(PO_4)_2$ down to 60 K by XRD and down to 6 K by PND. Essentially the $Na_2Th(PO_4)_2$ type structures have two different types of $[Th(PO_4)_2]^{2-}$ clusters, one equivalent to that in monoclinic phase while the other equivalent to that in high temperature tetragonal or orthorhombic phases. Thus these $Na_2Th(PO_4)_2$ type monoclinic structures can be considered as intermediate structures in between the high temperature and ambient temperature structures of $K_2Ce(PO_4)_2$. The variations of lattice energy with molar volume for different structures are shown in Fig.4.11. From this figure, it can be seen that the expansion of molar volume of monoclinic ($P2_1/n$) phase of $K_2Ce(PO_4)_2$ by about 8% will destabilize the lattice and will transform to orthorhombic or tetragonal structure. From the calculations, it can be suggested that the tetragonal structure has marginally higher stability compared to orthorhombic structure. Thus it can be inferred that the temperature has an important role for stabilization of these structures. No significant improvement in residuals in Rietveld refinements and no additional reflections due to lowering of symmetry in the present experimental studies are in favor of tetragonal structure. The orthorhombic structure, if at all exists, will transform to tetragonal structure at higher temperature.

Further comparison of the ambient monoclinic ($P2_1/n$) phase and high temperature tetragonal ($I4_1/amd$) phase (Fig.4.9) indicates that even though both have CeO_8 and PO_4 polyhedra they have different topology in their linkages. It can be mentioned here that in the monoclinic phase, two of the PO_4 tetrahedra are connected to CeO_8 by sharing two nearby edges and thus lead to a distorted and compact lattice, while in the latter case they are connected by sharing two opposite edges of CeO_8. The arrangement of CeO_8 and PO_4 polyhedra in tetragonal phase is similar to that in zircon type structures. In zircon type structures, the infinite chains of edge shared MO_8 and PO_4 units propagate along the *c*-

direction which is equivalent to the *c*-axis of the present tetragonal phase. However, the unit cell is doubled in the *c*-axis of tetragonal $K_2Ce(PO_4)_2$ structure due to the variation of periodicity arising from the disruption of chains at every clustered unit of two tetrahedra and one CeO_8 bisdisphenoid, i.e. every alternate CeO_8 unit. Moreover this structural transformation does not change the net tunnel type structure of ambient monoclinic phase. In both the cases the empty tunnels are occupied by K^+ ions, which are along the <100> and <101> in the monoclinic phase while along the <100> and <010> direction in the tetragonal phase. The restructuring of the local arrangement around the CeO_8 cannot be explained by a simple rotation of polyhedra while they are restructured by reconstruction of the PO_4 and CeO_8 polyhedra. The expansion of the CeO_8 polyhedra thus relaxes the structure to a higher symmetric structure, while at temperature above 1123 K the sample is found to decompose due to unstable nature of Ce^{4+} in phosphate matrix**.**

In order to compare the expansion behaviors of $K_2Ce(PO_4)_2$, the unit cell parameters of monoclinic and tetragonal phase at different temperature are obtained and they are shown in Fig.4.12. It can be seen from this figure that, the unit cell parameters of monoclinic phase smoothly increases from lowest temperature and can be explained by second order polynomial relations. However, the temperature dependent unit cell parameters of tetragonal phase show anomalous behavior, viz. expansion along *a*- and *b*-axes while a contraction along the *c*-axis. The coefficients of average thermal expansion of monoclinic phases in the temperature range 60 to 885 K are: $\alpha_a = 13.71 \times 10^{-6}$ K^{-1}, $\alpha_b = 8.46 \times 10^{-6}$ K^{-1}, $\alpha_c = 19.28 \times 10^{-6}$ K^{-1}, $\alpha_\beta = 2.04 \times 10^{-6}$ K^{-1}, and $\alpha_V = 41.30 \times 10^{-6}$ K^{-1}, while those of tetragonal phase in between 400 to 900 K are: $\alpha_a = 9.61 \times 10^{-6}$ K^{-1}, $\alpha_c = -15.3 \times 10^{-6}$ K^{-1} and $\alpha_V = 3.83 \times 10^{-6} K^{-1}$.

The large negative thermal expansion along the *c*-axis resulted in significantly lower volume thermal expansion in the tetragonal structure.

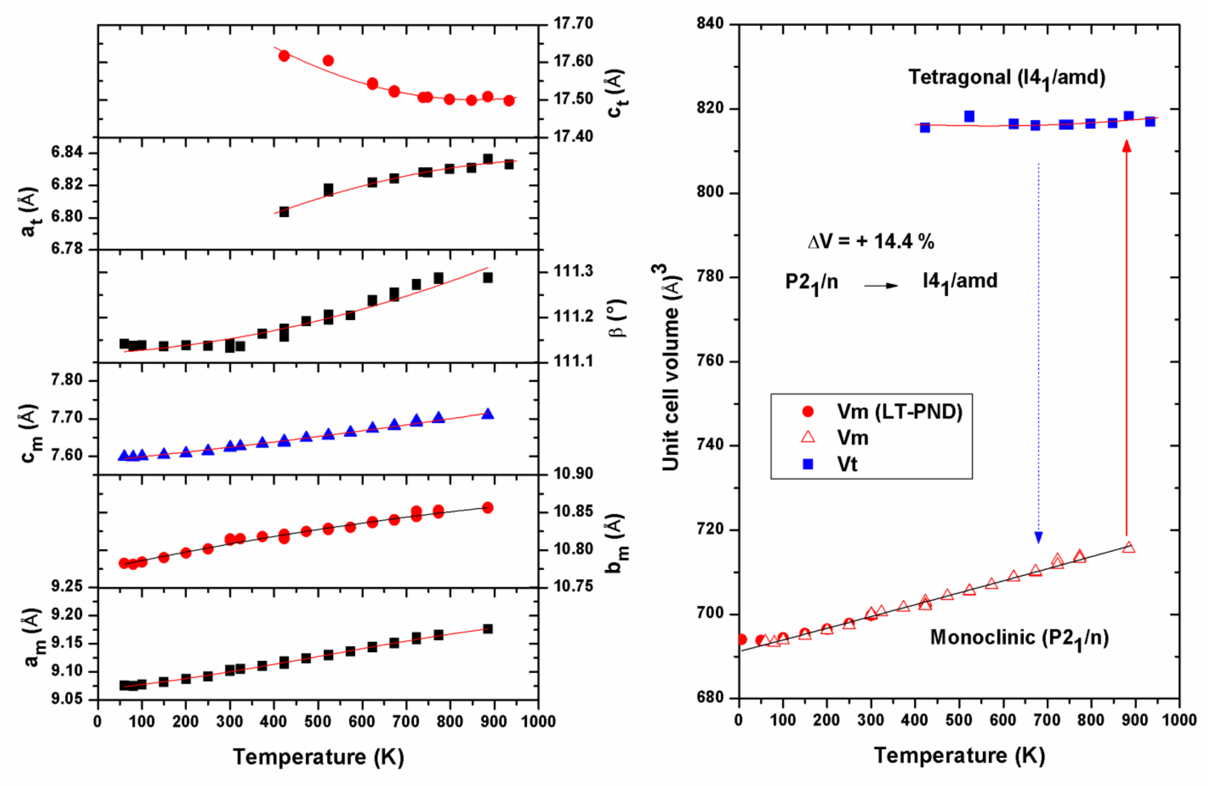

Fig.4.12: Variation of unit cell parameters of monoclinic (*$P2_1/n$*) and tetragonal (*$I4_1/amd$*) phases of $K_2Ce(PO_4)_2$ with temperature

As seen from the variation of unit cell volume with temperature (Fig.4.12), the transition from monoclinic *$P2_1/n$* to tetragonal *$I4_1/amd$* structure is accompanied by about 14.4 % rise in volume, which is also in accordance with the volume difference calculated by DFT. The resulted open structure of high temperature phase is more prone to exhibit either lower or negative thermal expansion. Phase transitions accompanied by such larger volume discontinuity exhibiting lower or negative thermal expansion have been reported earlier on several systems [130]. However, as mentioned earlier the bulk modulus of tetragonal phase is relatively higher compared to the monoclinic phase of $K_2Ce(PO_4)_2$. This can be due to the zircon type arrangements where the CeO_8 polyhedra share two opposite edges by incompressible and rotationally hindered PO_4 tetrahedra.

4.3.5. Raman studies

Further accounts on structural changes are obtained from the *in situ* variable temperature Raman spectroscopic studies. Since, the phosphates of tetravalent Ce^{4+} are relatively unknown and metastable, the spectroscopic details and in particular; their vibrational properties are mostly obscure in literature. In order to study the temperature induced change in local structures and phase transition, Raman spectroscopic investigations are carried out as they are often reflected in their phonon behaviors**.** Raman spectroscopy is often used as a complementary technique to XRD for studying the thermodynamic and structural properties as it probes in the microscopic length scale compared to macroscopic probing of the XRD. The phase transition or structural distortions occur due to change in symmetry or movement of ions at microscopic length scale can thus be obtained from the Raman spectroscopic studies more accurately. In order to complement the observed spectroscopic finding, the Raman and IR modes for all the considered structures such as monoclinic ($P2_1/n$), tetragonal ($I4_1/amd$) and orthorhombic (*Imma*) phases were calculated using computation [131].

As mentioned earlier, the structure of ambient temperature monoclinic $K_2Ce(PO_4)_2$ (Space group $P2_1$/n) has four formula units per primitive unit cell (Z = 4). Therefore, one can expect a total of 156 vibrational degrees of freedoms which are distributed as optical and acoustic phonon modes at Brillouin zone centre (q = 0). From factor group analysis, the total irreducible representation can be obtained as $\Gamma = 39A_g + 39A_u + 39B_g + 39B_u$. Out of which the total irreducible representation for optical phonon is $\Gamma_{optic} = 39A_g + 38A_u + 39B_g + 37B_u$ and that for acoustic is $\Gamma_{acoustic} = A_u + 2B_u$. Therefore, 78 Raman active modes ($39A_g + 39B_g$) and 75 infrared active modes ($38A_u + 37B_u$) are expected. Fig.4.13 shows a Raman spectrum recorded at ambient temperature (300 K).

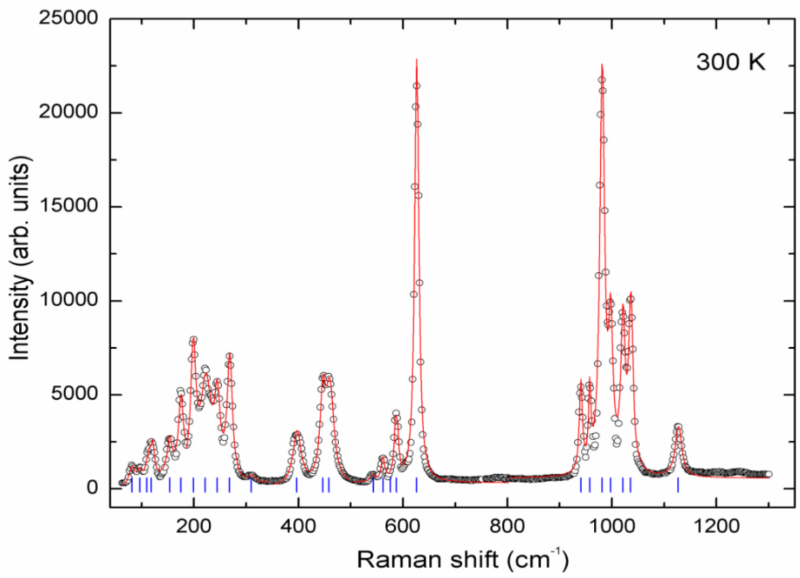

Fig.4.13: Raman spectra of $K_2Ce(PO_4)_2$ at ambient temperatures. Solid curves are the Lorentzian least-square fits to the data including a suitable background

At ambient temperature, the major Raman bands are located at 199, 269, 397, 624, 982, 1127 cm^{-1}. A total of 26 peaks are precisely obtained using peak fitting. The total simulated pattern along with the experimental data and the individual Raman band positions are shown in Fig.4.13. These mode frequencies are close to our earlier reported frequencies [132]. Due to an increase in phonon life-time at lower temperature, the Raman modes generally become narrow and hence the overlapping modes are often resolved at lower temperature. Thus the initial analysis of Raman modes were carried out from the spectrum recorded at

83K. The deconvolution of peaks of this spectrum using multi-Lorentzian profile shape yields 35 modes. These mode frequencies and the location of mode position are marked in Fig.4.14. There are no modes observed in the spectral range 660-920 cm^{-1} in the Raman spectra. The less number of observed modes than that expected from group theoretical analysis may be either due to weak intensity arising from the small polarizability of several modes or accidental degeneracy related overlapping [133]. Assignments of the observed modes are carried out by using the computed *eigen* vectors obtained from our DFT calculations. The observed band frequencies close to those obtained from calculation for zone centre phonons are assigned to the corresponding *eigen* vector symmetry. The observed and calculated mode frequencies along with their assignment are presented in Table.4.2. Most of the observed and calculated Raman frequencies show good matching with each other within a maximum of ~4 % mismatch, which can be due to the difference between the experimental and the relaxed unit cell volume obtained from first-principle calculations.

Since the PO_4 units are tightly bound, they can be treated as rigid units and hence one can expect internal modes resulting from the vibration of oxygen ion against the central phosphate ion in the oxygen cage. On the other hand, the comparatively loosely bound CeO_8 polyhedra contributes only lattice modes associated with the Ce^{4+} ion translational vibration in the potential well formed by the surrounding oxygen cage. Similarly, the K^+ ions can contribute only lattice translation modes. Therefore, in the present Raman spectra of $K_2Ce(PO_4)_2$, the lattice modes involving Ce^{4+} and K^+ ions can be seen in the low frequency region whereas the vibration involving PO_4 units are expected in the high frequency region. Using the assignments reported earlier for $K_2Ce(PO_4)_2$, the observed modes are assigned in Table 4.2. The internal modes are assigned in the range 390-1130 cm^{-1}. Raman modes observed in high frequency range 940-1130 cm^{-1} are attributed to the stretching mode of the PO_4 units, while the bending modes are in the frequency range 390-627 cm^{-1}. Lattice translational mode related to K^+ and Ce^{4+} ions and librational modes involving PO_4 rigid units are observed in the low frequency range 80-313 cm^{-1}. In order to examine the changes in phonon behaviors at elevated temperature, *in situ* Raman spectra of $K_2Ce(PO_4)_2$ was measured using a Linkam stage up to 853 K. Fig.4.15 shows representative Raman spectra between 83 and 853 K. Upon increasing temperature, most of the Raman bands soften continuously and their intensities decrease. A few Raman bands located at 81, 396 and 446 cm^{-1} show abnormal hardening.

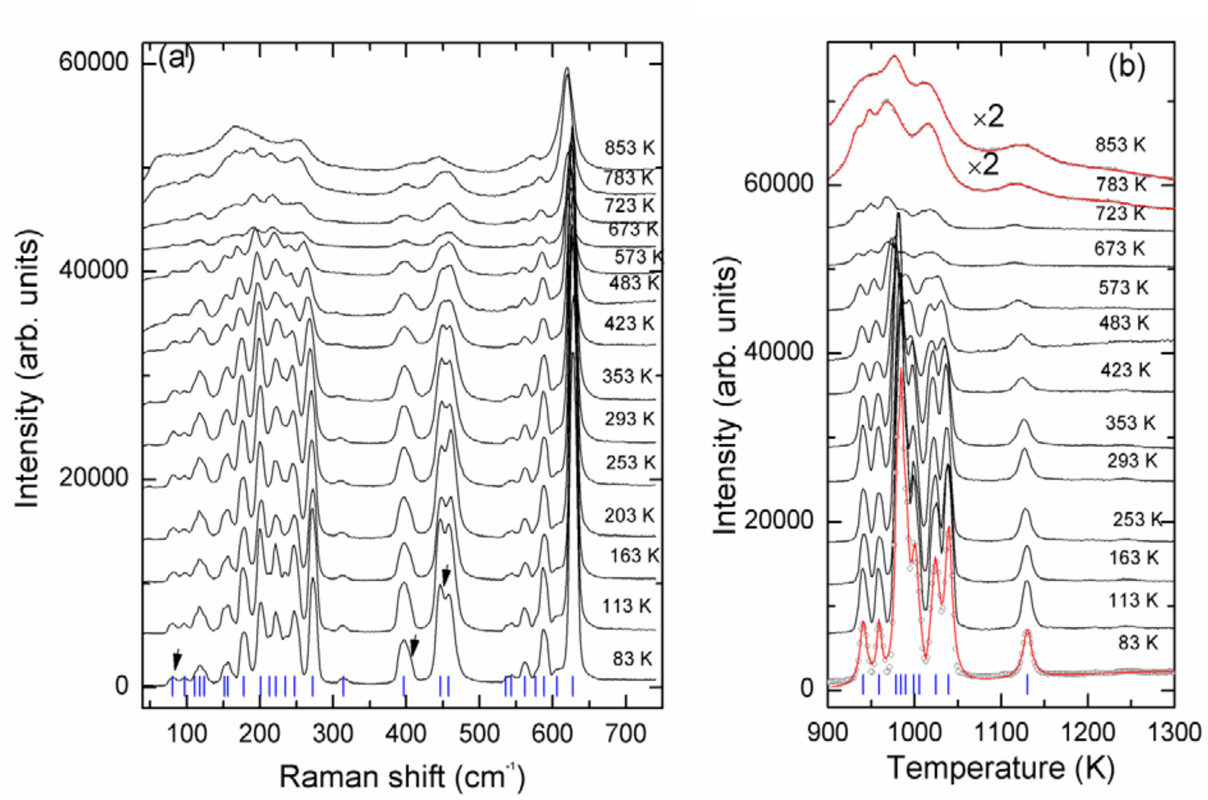

Fig.4.14: Raman spectra of $K_2Ce(PO_4)_2$ at different temperatures (a) low frequency region (b) high frequency region showing the stretching modes of PO_4 ion. Blue tick marks indicate the Raman bands at 83 K

Table 4.2: Observed Raman mode frequencies in monoclinic $K_2Ce(PO_4)_2$ at 83 K

mode	ω_{cal} (cm^{-1})	ω_{obs} (cm^{-1}) (80 K)	$d\omega/dT$ (cm^{-1}/K)	$1/\omega_0(d\omega/dT) \times 10^5$ (K^{-1})	γ_T	
Ag	44.02					
Ag	71.04					
Bg	72.52					
Ag	82.57	80.8	0.00709(4)	8.77	2.12464	
Bg	84.28					
Ag	89.00					
Bg	92.20					
Bg	98.805	97	0.0001(4)	0.010	0.02496	
Ag	101.10					
Ag	109.98	110.7	-0.00464(5)	-4.19	-1.01489	
Bg	111.72					
Ag	114.90					
Bg	117.46	118.2	0.0004(4)	0.34	0.08194	
Bg	125.21	123.9	0.0003(8)	0.24	0.05863	Lattice and External modes
Ag	126.21					
Bg	135.11					
Ag	135.75					
Bg	137.85					
Ag	140.79					
Bg	141.68					
Ag	147.25					
Bg	147.75	151.8	-0.01927(6)	-12.69	-3.07369	
Ag	156.37	156.5	-0.00513(9)	-3.28	-0.79369	
Ag	166.47					
Bg	167.48					
Bg	172.76					
Ag	176.90	178.1	-0.01527(4)	-8.57	-2.07599	
Bg	180.52					
Ag	184.38					
Bg	186.69					
Bg	191.06					
Ag	195.12	201.2	-0.01251(9)	-6.22	-1.50549	
Ag	198.52					
Bg	199.51					
Ag	209.78					
Bg	210.04	213	-0.03570(5)	-16.76	-4.05825	
Ag	218.85					
Ag	220.57					

Under the influence of temperature, mode frequencies are normally expected to decrease due to expansion of bonds. Sometimes a few bands may show opposite behavior which can be attributed to the stiffening of bonds resulting from steepening of potential well associated with their atomic vibration. The hardening behaviors of vibrational modes have been reported in several systems. With increasing temperature, the line-width of several Raman bands of $K_2Ce(PO_4)_2$ are broadened which is normally due to enhanced phonon scattering processes. Fig.4.14 shows the significant broadening of internal modes at 853 K, which appears like only 4 Raman bands. The modes at 446 and 457cm^{-1}, 1024 and 1039 cm^{-1} were merged at 783 K and they appeared as broad bands centered at 453 and 1138cm^{-1}, respectively. These new bands continue to appear above this temperature. Raman bands centered at 81, 110, 562 and 999 cm^{-1} have disappeared at 783 K. Some of the bands are disappeared even below 783 K. At the highest temperature, 853 K, only 11 bands were observed. The merging of modes and disappearance of several modes at ~ 783 K suggest the transition is accompanied by increase in symmetry. As the ambient monoclinic phase transforms to the HT phase, the temperature dependency of internal modes of PO_4 units show change in slope, which is clearly observed at around 783 K Fig.4.14. In addition, between 783 and 853 K, phonon modes of both the monoclinic and high symmetric phase are observed in the spectra, suggesting a coexistence of the phases in this temperature range, which is consistent with the findings, from the present *T*-dependent XRD studies.

Group theoretical analysis for the structure of high temperature tetragonal ($I4_1/amd$; $Z = 4$) predict 78 vibrational degrees of freedom. Excluding the acoustic phonons, factor group analysis of tetragonal structure (without considerations of disorder in K^+ atoms) indicates the total irreducible representations of optical phonons are: $\Gamma_{optics} = 5A_{1g} + 3A_{1u} + 2A_{2g} + 7A_{2u} +$

$6B_{1g} + 3B_{1u} + 2B_{2g} + 7B_{2u} + 11E_u$ (doubly degenerate) + $9E_g$ (doubly degenerate). Thus there are distinct 18 IR modes with irreducible representation $\Gamma_{\text{optic (IR)}} = 7A_u + 11E_u$ and 22 distinct Raman modes with irreducible representation $\Gamma_{\text{optic (R)}} = 5A_{1g} + 6B_g + 2B_{2g} + 9E_g$ are expected. Similar analysis for the structure of orthorhombic (*Imma*; Z = 4) phases indicates total 75 optical phonons with representations: $\Gamma_{\text{optic}} = 11A_g + 6A_u + 4B_{1g} + 14B_{1u} + 9B_{2g} + 11B_{2u} + 9B_{3g} + 11B_{3u}$. Out of these representations, there are 36 modes IR active ($\Gamma_{\text{optic (IR)}} = 14B_{1u} + 11B_{2u} + 11B_{3u}$) and 33 modes Raman active ($\Gamma_{\text{optic (R)}} = 11A_g + 4B_{1g} + 9B_{2g} + 9B_{3g}$). The calculated Raman modes for both tetragonal and orthorhombic structures are listed in Table 4.2. The less number of observed modes at higher temperature is an indication of higher symmetry of the high temperature phase and most favourably a tetragonal structure. Fig.4.15 shows the temperature dependences of band frequencies. Several bands of the monoclinic phase have disappeared and a few merged together because of the transformation to tetragonal phase. It can be seen that several of the IR mode frequencies of the considered high temperature phases of $K_2Ce(PO_4)_2$ have negative frequencies (B_{3u}, -42.87 cm^{-1} in orthorhombic (*Imma)* and E_u, -42.87 cm^{-1} in tetragonal ($I4_1/amd$)), which suggest all these structures are dynamically unstable with respect to the ambient temperature monoclinic ($P2_1/n$) structure. These modes are essentially the rotational motion of PO_4 tetrahedra and largely by translational motion of the K^+ ions. This is in accordance with the unstable nature of all these phases at lower temperature and hence they revert back to ambient phase on cooling. The temperature coefficient (χ) of Raman bands in the monoclinic phase are obtained by fitting the ω *vs.* T plot (Fig.4.15) using linear equation $\omega(T) = \omega_0 + \chi T$, where ω_0 mode frequencies at absolute zero temperature. To avoid contribution from higher order temperature coefficients, the data was fitted in the low temperature range (83-500 K).

Similarly, the reduced slopes of the identified modes of transformed high temperature phases are obtained by linear fitting and they are included in Table 4.2.

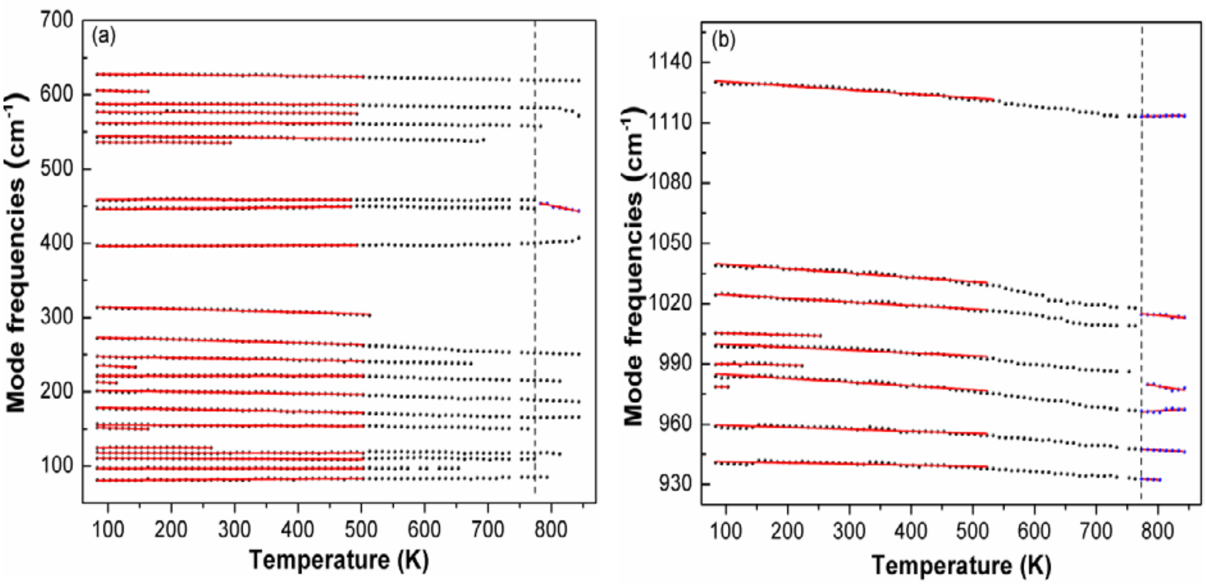

Fig.4.15: Raman mode frequencies of $K_2Ce(PO_4)_2$ as a function of temperature

Reduced slope essentially represents the total anharmonicity of phonon modes and are contributed by two effects [131], viz. (a) pure temperature effect related to phonon-phonon interaction (explicit contribution) and (b) due to change in volume of lattice (implicit contribution). Furthermore, a comparison of magnitude of total anharmonicity of phonon modes indicates the low frequency lattice and external modes such as 81, 152, 178, 213, 234, 272 and 313 cm^{-1} indeed have large anharmonicities. These large values indicate large contribution to thermal expansion and indicating that these modes are flexible and sensitive to temperature. On the other hand, the high frequency internal modes of phosphate ions are not strongly anharmonic. These results indicate that the internal modes involving PO_4 unit are less sensitive to temperature suggesting the strong bonding in PO_4 tetrahedral unit, as observed in our XRD analysis and thus implying its covalent bonding character. It is observed that the low frequency modes are mainly contributing to the thermal expansion and differences in the magnitude of thermal expansion of both ambient and high temperature phases.

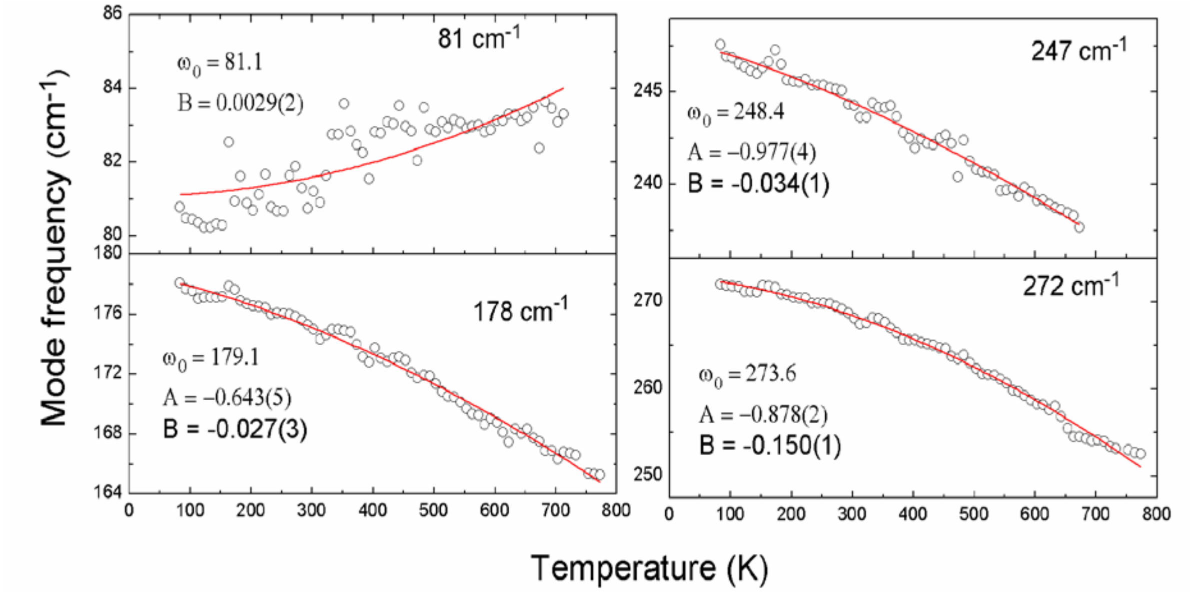

Fig.4.16: Variation of mode frequencies (ω) of some modes (below 400 cm^{-1}) with temperature. Continuous curves are fitted lines

As mentioned earlier, the change in mode frequencies with temperature is a consequence of anharmonicity. In fact, the cubic, quartic and even higher order term present in the expansion of interatomic interaction potential that arise from atomic displacement from their mean equilibrium position contribute to the shift in mode frequencies [134]. Due to the cubic and quartic anharmonicity, a phonon of frequency ω_0 decays into two phonons of frequency $\omega_0/2$, or three phonons of frequency $\omega_0/3$, respectively. Therefore, the resulting contribution to the shift in mode frequencies can be analyzed by using cubic and quartic anharmonicity formalism: using relation:

$$\omega = \omega_0 + A\left[1+\frac{2}{\exp(x)-1}\right] + B\left[1+\frac{3}{\exp(y)-1}+\frac{3}{(\exp(y)-1)^2}\right] \qquad (4.1)$$

Where ω_0 is the frequency at absolute zero temperature; $x = \hbar\omega_0/k_B T$ and A is the coefficient of cubic anahramonicity; $y = \hbar\omega_0/3k_B T$ and B is the coefficient of quartic anharmonicity.

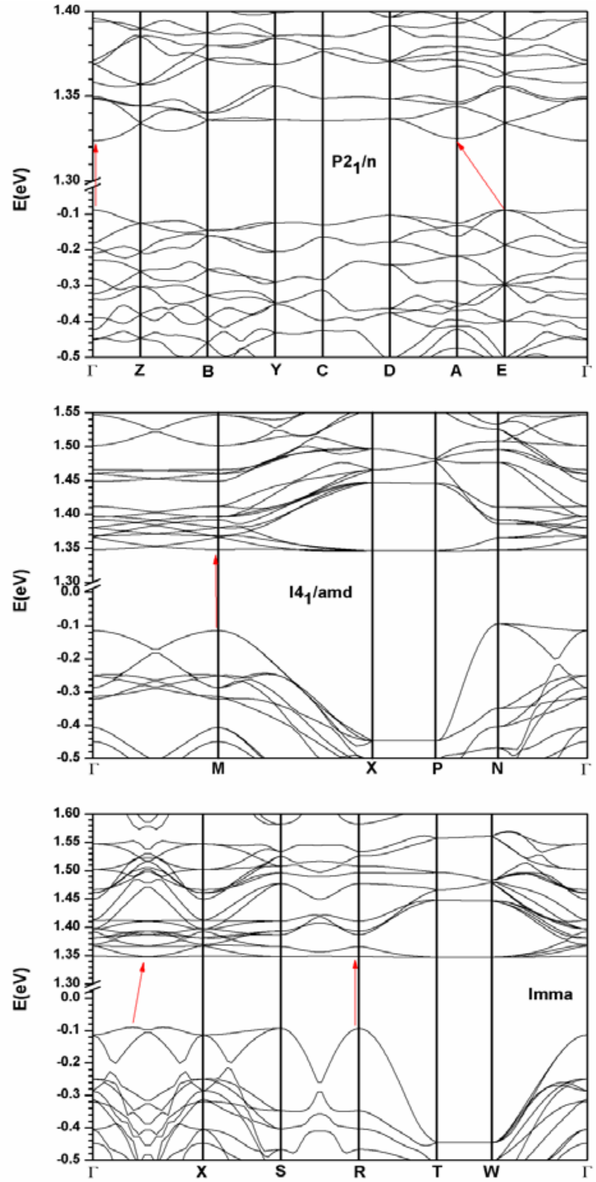

Fig.4.17: Electronic band structures of $K_2Ce(PO_4)_2$ in equilibrium *P2$_1$/n*, *I4$_1$/amd* and *Imma* structures

Some of the observed mode frequencies (lattice and external modes) obtained in this analysis, which are highly anharmonic are fitted using the above expression. The fitted parameters, ω_0, A and B are given in Fig.4.16.

4.4. Conclusions

The *in-situ* variable temperature XRD studies on $K_2Ce(PO_4)_2$ in a wider range of temperature revealed that the ambient temperature monoclinic phase remains unchanged at lower temperature while it transforms to a tetragonal structure with large (~ 14.4 %) expansion of unit cell volume at higher temperature. The high temperature phase reverts back to ambient phase with a larger hysteresis in temperature and also coexists with monoclinic phase in a wider range of temperature. The detailed structural analysis of the ambient and high temperature phases suggests a reconstructive 1st order type phase transition. Highly open and loosely packed structure of HT tetragonal phase shows anisotropic thermal expansion with larger negative thermal expansion along *c*-axis (-15.3×10^{-6} K^{-1}) and that in turn resulted in an appreciable low volume thermal expansion (3.83×10^{-6} K^{-1}) as compared to that observed in ambient temperature monoclinic phase (41.30×10^{-6} K^{-1}). Temperature dependent Raman spectroscopic studies indicate the on-set of structural transition from monoclinic to a high symmetry tetragonal phase at 783 K. The phonon frequencies in the monoclinic phase which are highly anharmonic are identified. Several mode frequencies in this compound are dominated by three-phonon contributions. Abnormal hardening of 81 cm^{-1} lattice mode arises from quartic anharmonicity. In addition to lattice modes at 81 cm^{-1}, several other librational modes of PO_4 tetrahedral units are observed to be strongly anharmonic. The optical absorption studies on monoclinic phase of $K_2Ce(PO_4)_2$ indicates a direct band-to-band transition with band gap of 2.46 eV.

Chapter 5

Synthetic Na and K-birnessites as inorganic ion exchangers

Chapter 5

5.1. Introduction

Layered manganese oxides are well studied porous materials and behave as ion sieves due to their compositionally flexible and layered crystal structure. Owing to various medicinal as well as technological importances of ^{90}Sr, separation of this radionuclide attracts huge research interest. In view of this, inorganic framework materials like phosphates, molybdates, titanates, silicates have been extensively explored for ^{90}Sr separation from nuclear waste. [56b, 60, 135] Inorganic ion exchangers like aluminosilicates have shown high distribution coefficients for ^{90}Sr separation but aluminum leaches out of the lattice in acidic pH conditions and also lacks in selectivity because of large pore sizes [49, 136]. Though layered materials like titanates, silicotitanates possess stability in nuclear waste conditions, effective use of these materials are limited for ^{90}Sr separation in acidic pH because of proton inhibition [137]. In order to develop an efficient ion exchange material for ^{90}Sr separation, Ryu *et al.* [138] have studied sodium titanate nanotubes and explained the ion exchange behaviour of Na^+ in fiber like titanate nanotubes with $^{90}Sr^{2+}$ ions from sea water. These studies have revealed that, though the material is stable in wide pH range, Sr^{2+} uptake was hindered significantly in presence of Ca^{2+} ions.

Zhang *et al.*[135] have reported series of antimonites like antimony silicate, tin antimonite and manganese antimonite for Sr^{2+} uptake from acidic waste waters and which have shown stability and tenability of antimony lattices for ^{90}Sr uptake. Doping of tetravalent Mn^{4+}, Sn^{4+}, Si^{4+} ions into the stable pyrochlore structured Sb_2O_5 lattice results different structures with respect to extent of doping. Pyrochlore structured $SnSbO_5$ is selective for separation of ^{90}Sr, whereas higher concentration of Sn results in the formation of rutile phase and selective for separation of ^{60}Co. Practical usage of antimonates is limited due to the release of toxic $SbCl_5$ vapours during their synthesis and also leaching of antimony into the drain solutions [138-139].

Considerable research efforts have been invested in exploring various hydrous metal oxides for separation of heavy metal pollutants and radioactive cations from aqueous media selectively because they are cost effective and able to form stable inner sphere complexes with foreign ions and thus ion selective [140]. Uptake of transition metal ions such as Co^{2+}, Ni^{2+}, Cu^{2+}, Zn^{2+} by amorphous δ-Manganese dioxide phase was reported by Bhusan *et al.* [141] It is mentioned that electrostatic interactions between adsorbate and adsorbent are responsible for sorption. Comparison of sorption behaviors of amorphous manganese metal oxides with birnessite reveals that birnessite has shown faster sorption kinetics, higher adsorption capacities and high stability in aqueous medium for transition metal ions compared to the amorphous manganese oxide. Crystalline birnessite is stable in wide pH range and sorption capacity is not altered much with pH variations, where as amorphous phase is sensitive with changes in pH, which may be due to specific surface being not available for adsorbate in amorphous phase compared to birnessite [90a, 93b, c, 142].

In view of this, synthetic crystalline birnessite mineral with Na^+ and K^+ ions as exchangeable ions have been studied for ^{90}Sr separation from simulated nuclear waste conditions. The separation efficacy and immobilization compatibility have also been explored with these low cost materials. Birnessite belongs to phyllomanganate family and exists naturally along with different transition, alkaline and alkaline earth metals intercalated in between the layers. Na-birnessite (NMO), K-birnessite (KMO) were synthesized by vigorous oxidation of $Mn(OH)_2$ and layers of MnO_6 octahedra in these are connected to each other in lamellar fashion. Large inter layer distance renders the exchange of monovalent ions with other ions of similar size and charge. Ion exchangeability of these materials with Sr^{2+} ions was studied radiometrically using ^{85}Sr tracer solutions ($t_{1/2}$=64d, γ-emitter, 512KeV). Both NMO, KMO have shown high affinity for ^{90}Sr separation with distribution coefficient (K_d) ~ 28000 mL/g for NMO and K_d ~ 26000 mL/g for KMO. Characterization of samples before and after ion exchange confirmed the ion exchange mechanism and flexibility of the structure to incorporate Sr^{2+} ions. Details of the ion exchange process are discussed in further sections [135a].

5.2. Experimental methods

Birnessite can be synthesized either by oxidation of Mn^{2+} containing solutions in high basic medium or by reduction of MnO_4^- ions in acidic solutions and also redox reactions between Mn^{2+} and MnO_4^- results birnessite formation. Reduction of permanganates and redox reaction methods requires more time for synthesis and aging process. Oxidation of Mn^{2+} salts can be achieved by using various oxidizing agents such as $S_2O_8^-$, H_2O_2 or by O_2 flow [143]. Desired samples were synthesized by oxidation of $Mn(OH)_2$ in presence of excess NaOH for NMO and KOH for KMO. Oxygen flow at a rate 24L/m was purged for 6h in order to oxidize $Mn(OH)_2$ to form MnO_2 layers. Clear solution of $MnCl_2$ was made by dissolving 11.25 g of $MnCl_2$ in 75 mL of water, NaOH/KOH solution was prepared by dissolving 30 g of NaOH/KOH in 125 mL of water. To the saturated solution of $MnCl_2$, NaOH/KOH solution was added drop wise in presence of oxygen flow. Addition of NaOH/KOH results in the formation of black color precipitate and the reaction mixture was stirred for 6h at high oxygen flow rate which results in the formation of desired birnessite phase. Reaction time of 6h is required to avoid presence of unnecessary phase like β-MnOOH as reported by Cai *et al.* [143] The obtained final crystalline products of both samples were characterized by X-ray diffraction (XRD), X-ray fluorescence and TG-DTA for their phase purity and crystal structures. Ion exchange characteristics of these materials were carried out by equilibrating the weighed amount of sample with tracer solutions of ^{85}Sr ($t_{1/2}$ = 64.8 d, specific activity = 2.4×10^4 Ci/g). Morphology of the materials before and after ion exchange was investigated using transmission electron microscopy.

5.3. Results and discussion

5.3.1. Structural characterization of NMO and KMO

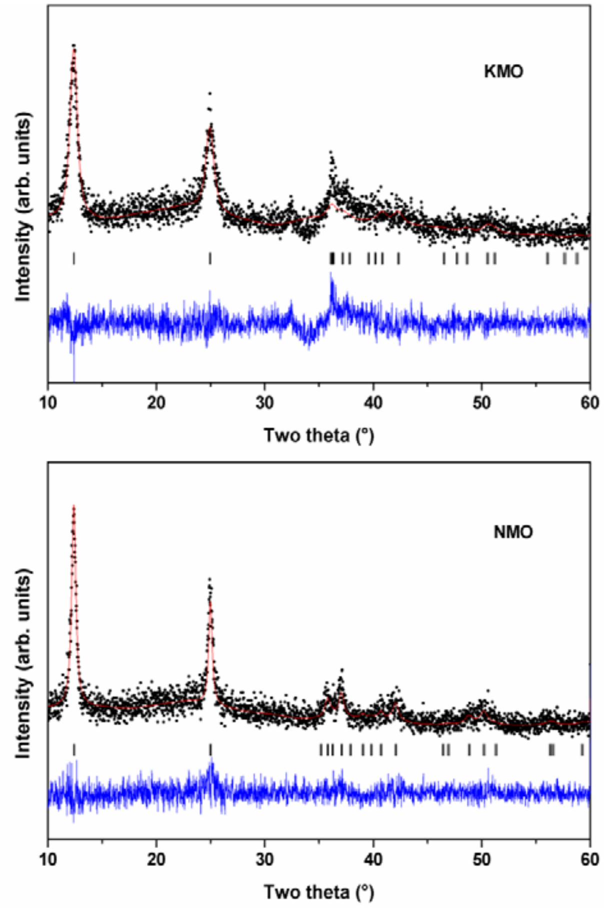

Fig.5.1: Rietveld refinement plot of Na-birnessite and K-birnessite

The powder XRD pattern of the NMO sample is closely similar to that reported earlier for the hydrated Na-birnessite ($Na_{0.55}Mn_2O_4.1.5H_2O$) reported by Cai *et al.* [143] The KMO sample also show similar XRD pattern as that of NMO but the peaks are broader and less intense compared to NMO. However, all the peaks of NMO and KMO could be assigned to monoclinic (C2/m) lattices. The XRD patterns were fitted with structural details of Na-birnessite reported by Cai *et al.* to obtain unit cell parameters. The refined unit cell parameters of NMO and KMO samples are: a = 5.147(7) Å, b = 2.851(4) Å, c = 7.309(6) Å, β = 102.9(2)°, V = 104.6(2) $Å^3$ (for NMO); a = 5.045(9), b = 2.883(6), c = 7.268(5), β = 100.7(2), V = 103.9(3) (for KMO). The typical Rietveld refinement plots of powder XRD data of NMO and KMO are shown in Fig.5.1. It can be seen from the powder XRD data that both the materials show intense reflection attributable to (001) reflection of layered birnessite structure, which corresponds to the spacing between MnO_6 octahedral layers of birnessite. Typical crystal structure of Na/K birnessite showing the octahedral layer and interlayer species, Na^+/K^+ and H_2O are shown in Fig.5.2.

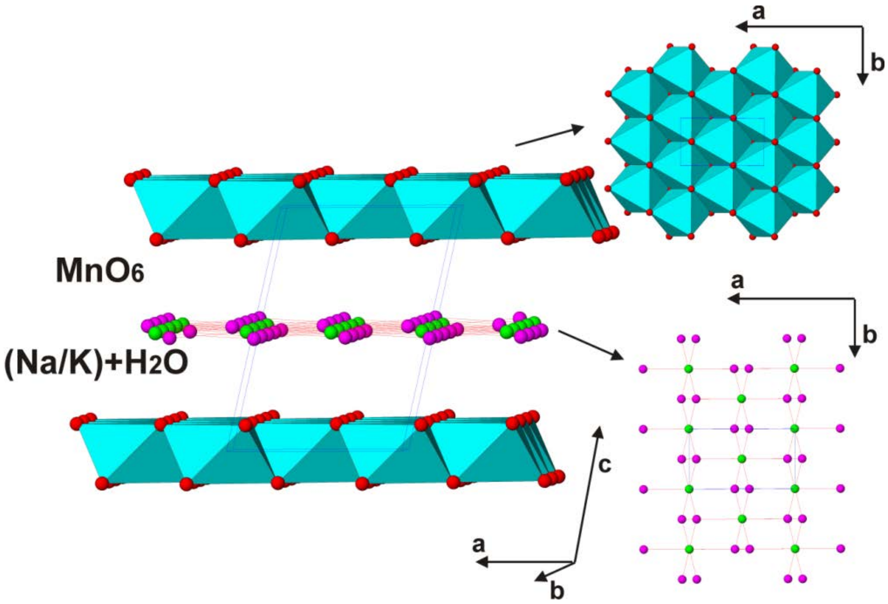

Fig.5.2: Layered arrangement of Na/K-birnessite

The net negative charge in the octahedral MnO_6 layer is governed by the amount of Mn^{3+} and Mn^{4+} in it and they are balanced by the interlayer Na^+ and K^+ ions. From the adopted preparation procedure, only a partial filling of Na^+ or K^+ is observed. The net water content in the interlayer spacing was determined from thermogravimetric analysis, which is explained in subsequent sections. Considering the water contents as observed in TG, the composition of synthesized Na/K-birnessite was obtained. Composition of Na^+ and K^+ ions in the interlayer were obtained from the present XRD and from literatures of similar preparation conditions [143]. Considering the thermogravimetric and XRD results, the tentative composition of the prepared birnessite samples are assigned as: $Na_{0.5}Mn_2O_4.0.96H_2O$ and $K_{0.5}Mn_2O_4.0.57H_2O$. The presence of water molecules in both lattices are evidenced from the broad absorption at 3500 cm^{-1} in the FTIR spectra of the samples. The details of thermogravimetry and IR spectra are explained in subsequent sections explaining characterization of ion exchanged samples of the batch experiment studies. It also can be mentioned here that, the ordering of Na^+/K^+ and water molecules are usually not observed and also cannot be easily deciphered from XRD studies [144]. Thus in the structural model, both the water and Na^+/K^+ ions are distributed over same crystallographic sites. It can be mentioned here that the Na^+ or K^+ ions should be separated by water molecules due to electrostatic reasons. Thus the Na^+/K^+ and water molecules form a hexagonal net with each Na^+/K^+ ions surrounded by water molecules.

It can be mentioned here that birnessite type phylomangantes can crystallize in a variety of unit cell symmetry like triclinic, orthorhombic and hexagonal etc. while retaining the similar stacking of MnO_6 octahedra layers. The variation of such phyllomangates structure arise from the disorder in the stacking sequence which are generally due to the water contents and nature of cations in the interlayer spacing as well as preparation conditions. Florence *et al.* [145] have reported that the natural birnessite sample exists in triclinic lattice while the synthetic birnessite crystallizes in hexagonal or monoclinic lattices. Also the authors have mentioned that the triclinic phase transforms to the hexagonal form on protonation [146]. Most commonly encountered polytypes of birnessite are monoclinic, triclinic and hexagonal types. The triclinic and monoclinic polytypes are closely related with almost similar XRD pattern, while the hexagonal polytype is differentiated from the relative intensity of (110) reflections. In the present studies, the relative intensity of (110) reflection of KMO is suggestive from the coexistence of hexagonal polytype along with monoclinic birnessite (Fig.5.1). Thus the coexistence of hexagonal phase cannot be completely ruled out for KMO sample. Since all the polytypes are closely related and the present interest of ion exchange are not expected to be significantly affected.

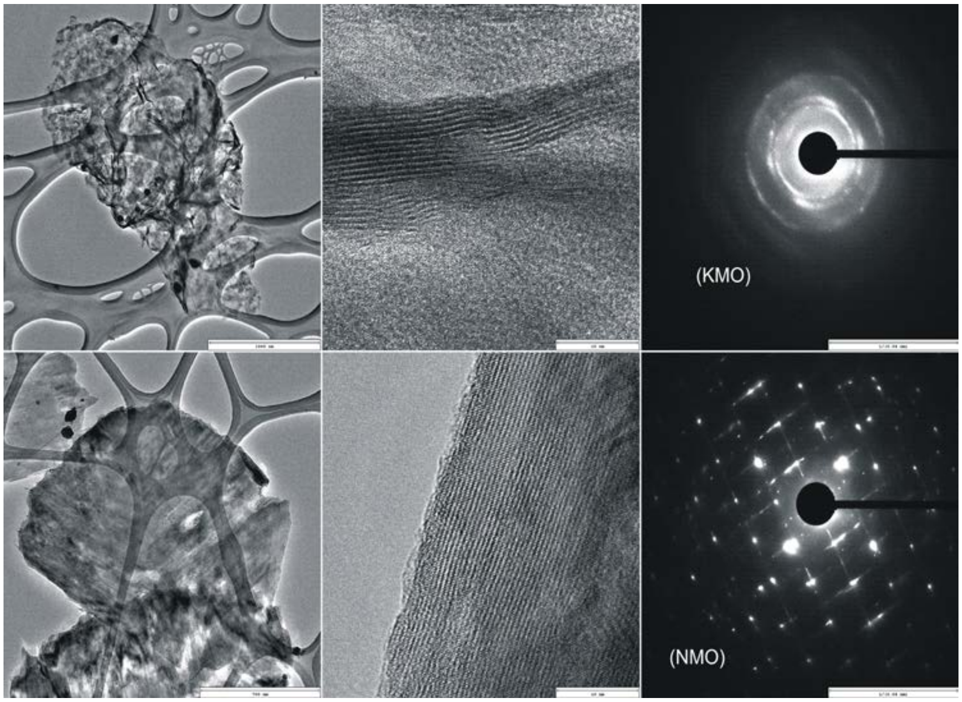

Fig.5.3: TEM and HRTEM images and SAED patterns of birnessite samples

Further characterization of structure and morphology of birnessite samples were carried out by TEM studies. The high resolution TEM images recorded on both NMO and KMO samples indicate their sheet type morphologies. The crystalline natures of the samples are also reflected in their clear fringes in HRTEM images and distinct spots in the SAED patterns of both samples. Typical TEM images and SAED patterns of both NMO and KMO are shown in Fig.5.3. A comparison of HRTEM images and SAED patterns of NMO and KMO samples shows that the fringes are well defined in case of NMO compared to the KMO. This is also confirmed in well defined peaks of XRD peaks in NMO compared to KMO. Also the presence of disorder as suggested from the XRD can be reason for the observed broad spots in SAED patterns of KMO sample. Also it can be mentioned here that the prepared KMO samples have smaller crystallites compared to NMO as evident from broader XRD peaks of latter. The dynamic light scattering studies on both NMO and KMO confirmed smaller size of KMO sample (average particle size ~ 500nm) compared to NMO (average particle size ~ 1μm).

5.3.2. Ion exchange characteristics

5.3.2.1. Batch experiments with $^{85}Sr^{2+}$solutions

The material to be used as ion exchanger for nuclear waste treatment needs to be chemically and mechanically stable in harsh chemical conditions, like very low pH and ionic strength as well as in high radiation field. Thus the initial experiments for understanding the ion exchange characteristics of NMO and KMO were carried out in various pH media using radioactive Sr^{2+} ions. Chemical and mechanical stabilities of NMO and KMO were investigated by equilibrating them in different pH media starting from 2 to 14. Both the materials did not show any dissolution in the studied pH range. Further experiments were carried out to measure distribution constant (K_d) (*eqn-1.2*) for Sr^{2+} uptake in different pH. In order to observe the pH dependency of K_d, about 0.05g of KMO and NMO samples were equilibrated with 5mL of ^{85}Sr tracer containing solution maintained at different pH. Variation of K_d for uptake of Sr^{2+} ions by NMO and KMO at different pH are shown in Fig.5.4.

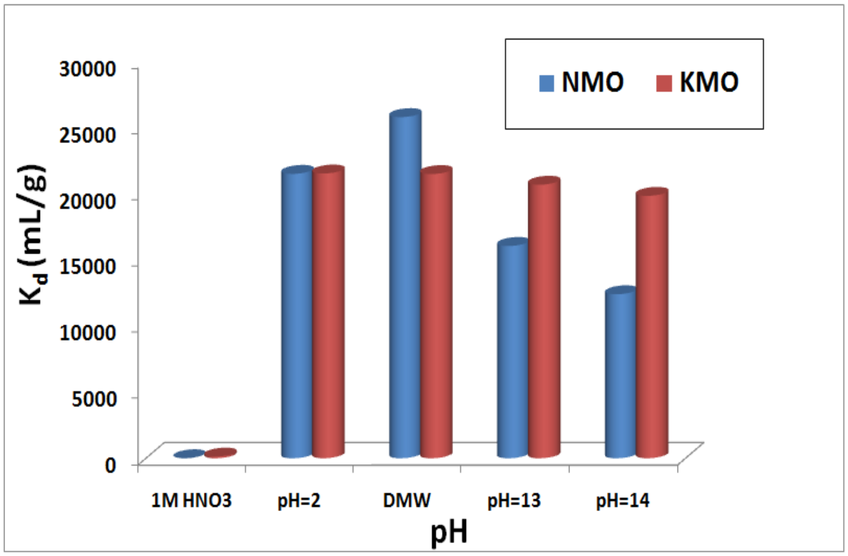

Fig.5.4: Distribution constant (K_d) variation with pH of medium

Effect of contact time on amount of ^{85}Sr uptake by title materials was studied by equilibrating 0.05g of material in 5mL of ^{85}Sr tracer solution at pH = 2 from a time range 30 min to 4 h. Maximum time required to achieve highest distribution constant for both the materials is ~ 120 min, which indicates the tendency of material for uptake of Sr^{2+}, flexibility of the materials and availability of the Na^+, K^+ ions located in between the ions for ion exchange with Sr^{2+} ions. Variation of ion exchange capacity with contact time for both NMO and KMO is shown in Fig.5.5. It can be seen from this figure that, the distribution constants of NMO is higher (K_d ~ 27000mL/g) in neutral medium while it decreases on both increasing and decreasing pH. However, the K_d did not show appreciable variation in between pH 2 to 14. The maximum K_d by KMO (K_d ~ 26000 mL/g) was observed at pH = 2. The small difference in K_d can be related to the difference in the particle size and crystallinity of NMO and KMO samples. The uptake becomes almost negligible at pH < 2 for both materials, which was due to the dissolution of the lattice at this pH. The dissolution of the lattices in highly acidic solutions like concentrated acid region (pH<2) resulted in a brown solution [135a].

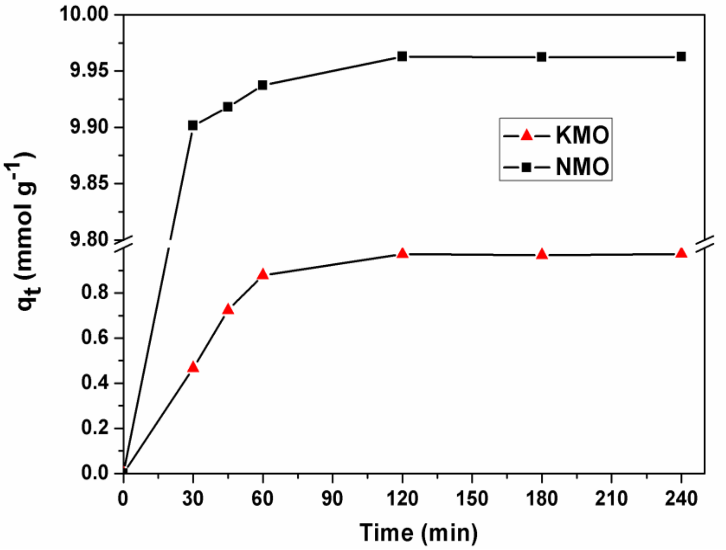

Fig.5.5: Variation of ion exchange capacity with time

It can be mentioned here that the pH dependency of K_d of a sorbent is related to the surface character as well as the nature of exchangeable ions. Since the surface charge of the sorbent depends strongly on the pH, the nature of the ion exchanger changes with varying pH. Wide range of materials behaves as sorbent for cations at higher pH because of large accumulation of OH^- ions and hence the surface becomes negatively charged. Similarly, at lower pH they become sorbent for anions due to formation of positively charged surface because of accumulation of H^+ ions on the surface. Also the presence of large excess of H^+ or Na^+ ions in the solution alter the ion exchange characteristics and K_d due to the competitions of these ions with the ions of interest. Such strong pH dependency has been reported earlier in the several complex phosphates, silicates, as well as various nanocrystalline and amorphous materials [147]. In the present studied materials, only NMO shows noticeable pH dependency compared to KMO in the range of pH between 2 and 14. The decrease of K_d at higher pH in NMO indicates appreciable interference of Na^+ ions with the uptake of Sr^{2+} ions. Almost similar K_d with KMO in this pH range suggested no appreciable interference of H^+ or Na^+ ions for exchange of Sr^{2+} ions. However, it is required to mention here that the Na^+ or K^+ ions can be exchanged well with the H^+ ions, which will be further explained in subsequent sections dealing with interference and batch experiments on NMO and KMO samples. Earlier studies of Ghaly *et al.* on cobalt and strontium uptake by crystalline hexagonal K-birnessite indicated chemical stability at $pH \geq 5$, while the dissolution of lattice below $pH = 5$ and above $pH = 14$ [148]. About 100 % of Co and Sr separation as $CoCl^+$ and Sr^{2+} is reported under acidic ($pH = 5$) and separation efficiency decreases on both increasing and decreasing pH. The authors have also indicated the separation of $CoCl^+$ and Sr^{2+} occurs via single or two step chemical reactions. Puppa *et al.* [149] have compared the sorption behaviour of K-birnessite and amorphous hydrous MnO_2 for various metal ions like Cu^+, Cd^{2+}, Zn^{2+}, Pb^{2+} and indicated almost similar separation efficiency for both while pH sensitivity is more for the latter than the former [57].

5.3.2.2. Batch experiments with stable Sr^{2+} solutions

In order to study the mechanism and structural variation in ion exchange process, studies were also carried out with inactive Sr^{2+} ions. 0.1g of title materials were equilibrated with 10mL of 1M $Sr(NO_3)_2$ solution for 24 h. Similarly 0.1 g of sample was equilibrated with 10mL of 1M HNO_3 solution for 24 h to prepare protonated birnessites (H-NMO and H-

KMO). The Sr^{2+} loaded and the protonated samples were filtered out and washed several times with nano pure water and then dried at room temperature. For Sr loaded samples, filtrate was analyzed by flame photometry for the presence of exchanged Na^+ and K^+ ions. The yellow and violet color flames confirmed the presence of exchanged Na^+ and K^+ ions in the filtrate respectively with amounts proportional to the amount of the Sr^{2+} ions loaded in the lattice of birnessite. Thus the exchange of Na^+ and K^+ with Sr^{2+} in the lattice is confirmed. The incorporation of Sr^{2+} in the NMO and KMO sample in ion exchange are confirmed by X-ray florescence (XRF) spectroscopic studies on the exchanged samples.

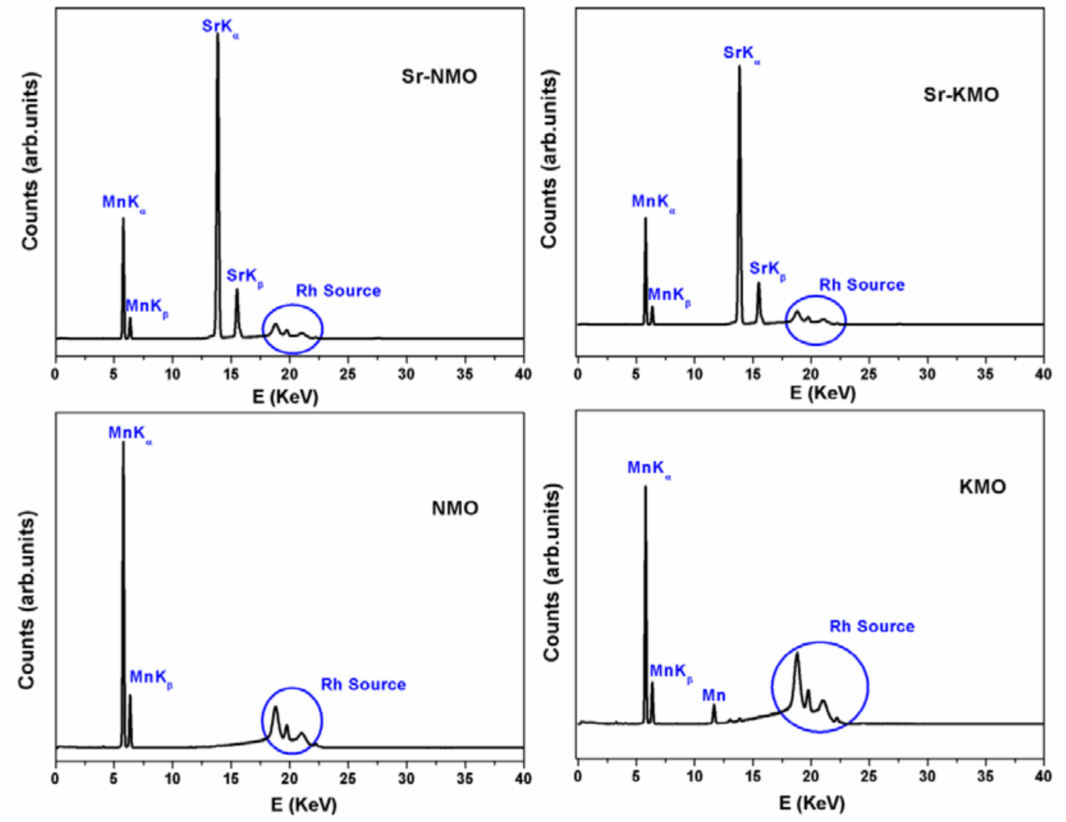

Fig.5.6: X-ray fluorescence spectra of birnessite samples before and after ion exchange

The X-ray fluorescence spectra of the Sr-NMO and Sr-KMO samples are shown in Fig.5.6 and compared with their corresponding virgin samples, which are also included in the figure. Sr Kα (13.8 keV) X-ray from the exchanged sample confirms the presence of Sr^{2+} in the exchanged samples. Structural changes of the Sr loaded (Sr-NMO and Sr-KMO) and protonated (H-NMO and H-KMO) samples were investigated using XRD, FTIR, TG and electron microscopy. A comparison of the XRD patterns of Sr^{2+} loaded and protonated NMO and KMO with their corresponding virgin samples are shown in Fig.5.7.

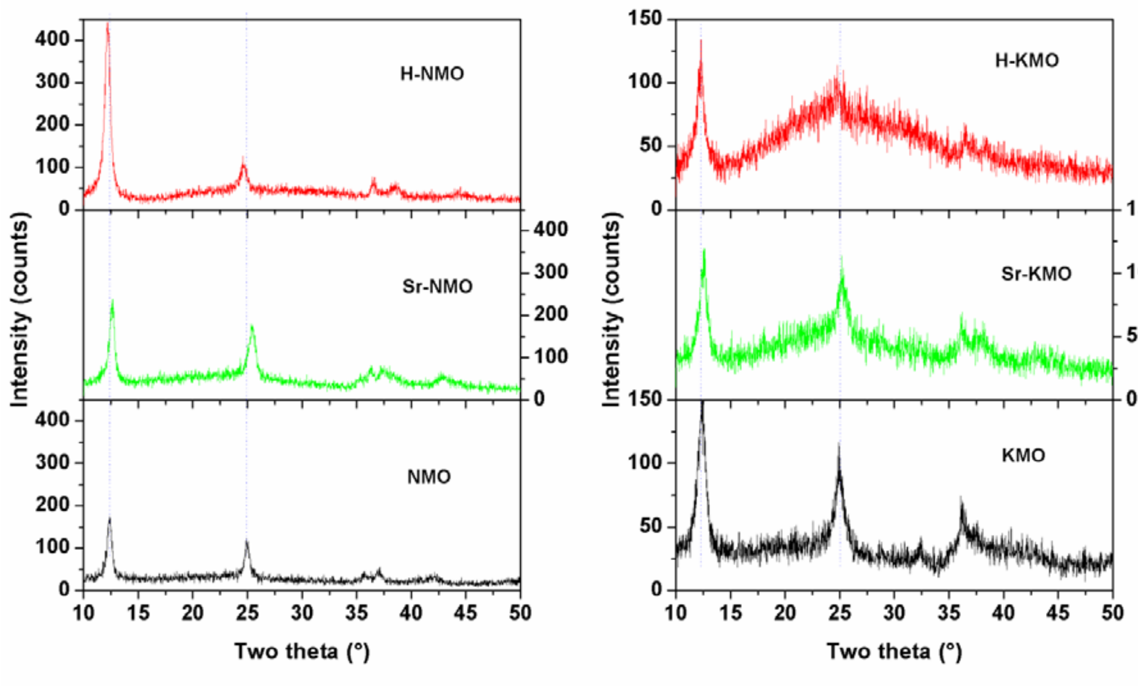

Fig.5.7: X-ray diffraction plot of birnessite samples before and after ion exchange

The presence or absence of any new peaks in the XRD patterns of Sr^{2+} loaded and protonated samples compared with the original sample indicate the retention of structure in the exchanged process. However, the peaks corresponding to (001) and (002) planes show noticeable shifts in the exchanged samples. Interlayer spacing of the Sr-NMO and Sr-KMO samples are reduced compared to the parent samples while protonated birnessite samples H-NMO and H-KMO interlayer spacings are enlarged with respect to the parent samples. The variations of interlayer distances can be attributed to the ionic radii of the exchanged ions as well as water content in the exchanged sample. Earlier Manos *et al*. have reported an increase in the interlayer distances of $K_{2x}Mn_xSn_{3-x}S_6$ (KMS) lattice on exchange of K^+ ions by Sr^{2+} ions [91]. Also the authors have indicated the Sr^{2+} ion exchanged KMS formed as hydrated products, due to larger hydration tendency of the Sr^{2+} ions. It can be mentioned here that ion exchange of the two K^+ ions are required for one Sr^{2+} ions to neutralize the lattice charge. Thus the variation of the ionic radii of the interlayer cation solely cannot govern the interlayer spacing; rather the water of hydrations plays a key role for this. This is also supported from the larger value of unit cell volume and c-axis of NMO compared to KMO ($d_{(001)NMO}$ = 7.128 Å $d_{(001)KMO}$ = 7.118 Å). In the present cases, the interlayer distances ($d_{(001)}$) of Sr-NMO and Sr-KMO are 6.996 Å and 7.035 Å, respectively. However, in the case of protonated (H-NMO and H-KMO) samples, the (001) peaks shifts to lower angle indicating expansion in the interlayer spacing (($d_{(001)H\text{-}NMO}$ = 7.228 Å $d_{(001)H\text{-}KMO}$ = 7.177 Å). The H^+ ion in the aqueous medium enters the lattice as H_3O^+ ions, incorporation of water molecules results in the larger interlayer spacing. Also it is interesting to note here that the (002) peak in the XRD patterns of Sr^{2+} or H^+ exchanged samples show distinct feature. The (002) peak is smeared in the H^+ and Sr^{2+} exchanged KMO samples. This might be due to disordering of the cations and water molecule in the interlayer spacing. Due to larger X-ray scattering contrast of O^{2-} and K^+, compared to O^{2-} and Na^+ they are seen clearly in the KMO samples. Incorporation of H^+ ions in between the layers also effects in a similar manner. The net water molecules in the Sr^{2+} and H^+ exchanged samples were obtained from the thermogravimetric studies.

Thermogravimetric and differential thermal analysis (TG-DTA) traces of NMO and KMO and their corresponding Sr^{2+} exchanged samples are shown in Fig.5.8. It can be seen from the TG curves that all the samples have two distinct steps for weight loss. The weight loss at lower temperature (below 300°C) are due to the adsorbed water molecules in inter layer spacing, while the weight loss occur at higher temperature is related to loss from the plane of MnO_6 octahedra due to the conversion of Mn^{4+} to Mn^{3+} and Mn^{2+}[150]. From the TG traces, losses due to water molecules from NMO and KMO are 8.5% and 5.0% respectively. These are in accordance with the stoichiometry $Na_{0.5}Mn_2O_4.0.96H_2O$ and $K_{0.5}Mn_2O_4.0.6H_2O$ for NMO and KMO, respectively.

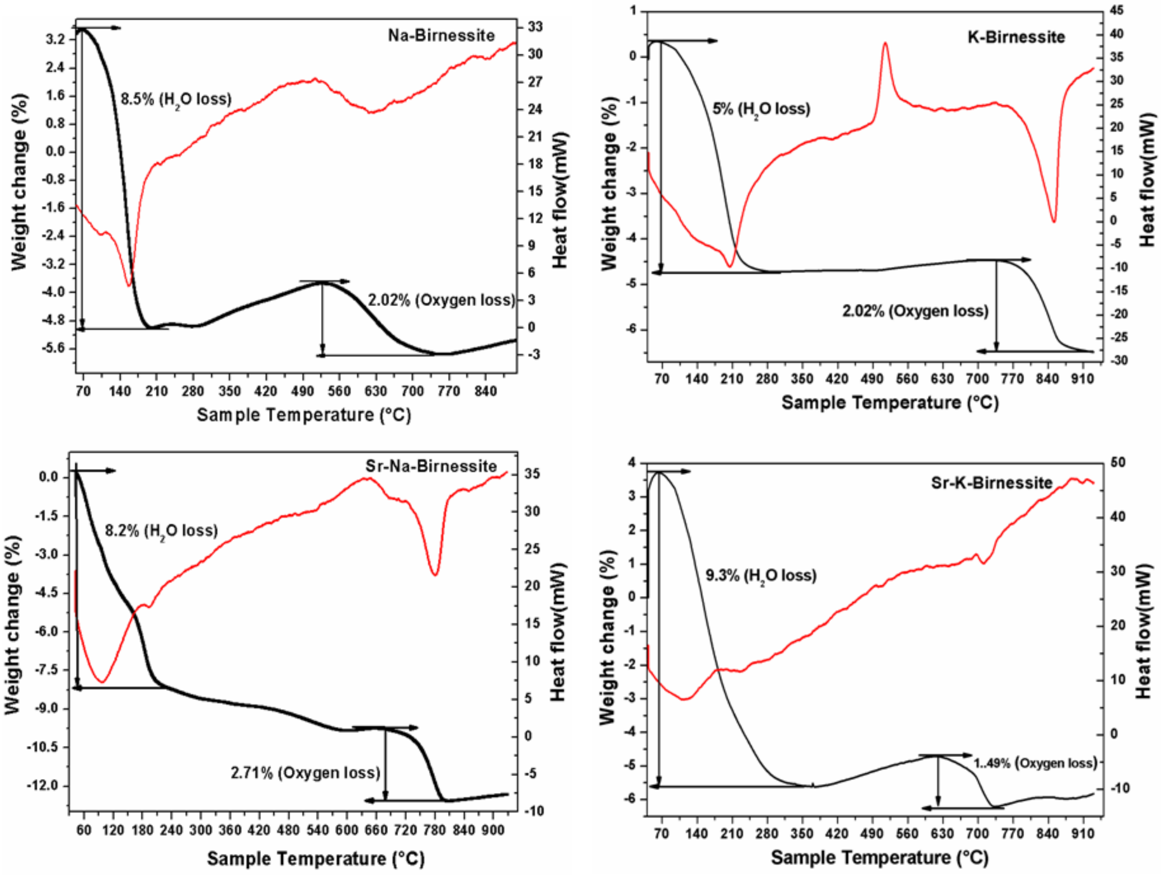

Fig.5.8: TG analysis of birnessite samples before and after ion exchange

In case of Sr-NMO, a sharp loss in weight (8.2 %) occurs within 200°C and then a gradual loss (~ 1.7 %) occurs over a wide range of temperature (200-550°C). In the corresponding temperature range, NMO shows a gradual gain in weight. This behaviour can be due to the oxidation or reduction of Mn^{3+} and Mn^{4+} of MnO$_6$ octahedral layers. In case of Sr-KMO, the net water content is significantly higher (9.3 %) than the pristine KMO (5.0 %). This indicates that the Sr^{2+} ions in the KMO lattice is more hydrated than the NMO. The two counter effects like decreasing contribution from the average ionic radii of interlayer cations by the replacement of two K^{+} ions by one Sr^{2+} ion and increasing contribution from interlayer water are reflected only a smaller variation in the interlayer spacing compared to NMO. At higher temperature (> 550°C) all the materials show another sharp weight loss where the Mn^{4+} are reduced to Mn^{3+} by loss of oxygen atoms. TG curves of the protonated samples (H-NMO and K-MNO) are also closely similar to the other samples. TG-DTA plot for protonated birnessite samples were shown in Fig.5.9.

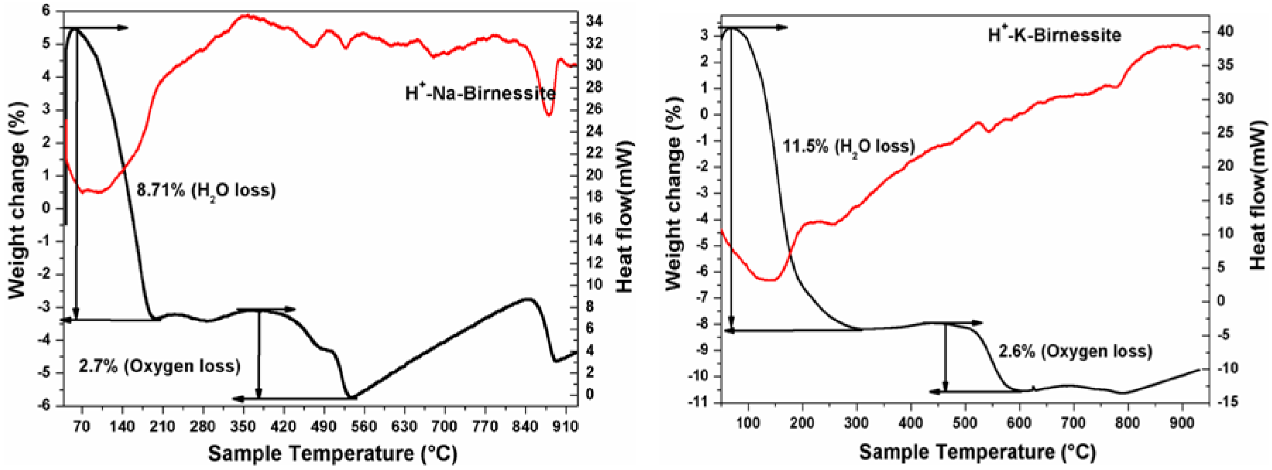

Fig.5.9: Thermogravimetric analysis of H^{+}-birnessite samples

In case of protonated samples, the net water contents in the lattice are larger (8.71% in H-NMO and 11.5%. in H-KMO) than the pristine and Sr^{2+} loaded samples. From the XRD and TG studies, it can be concluded that the H^{+} exchanged KMO and NMO are formed with larger water of hydration and swelling of interlayer spacing. While hydration behaviour of

Sr^{2+} exchanged KMO and NMO samples are different, but both resulted in contraction in the interlayer spacing. Thus the larger interlayer distance in the birnessite samples can easily accommodate various ions without significant alteration of the basic structural arrangements. Additional analysis of TG residue of exchanged samples indicates formation of Mn_3O_4 (in case of H^+-exchanged samples) and Mn_3O_4, $SrMnO_2$ and $SrMn_3O_6$ like phases in Sr-exchanged samples. The formation of such products indicates H^+ and Sr^{2+} are incorporated in the lattices of NMO and KMO and also suggests that materials can be transformed to solid immobilization matrix with the separated Sr^{2+} ions [142a].

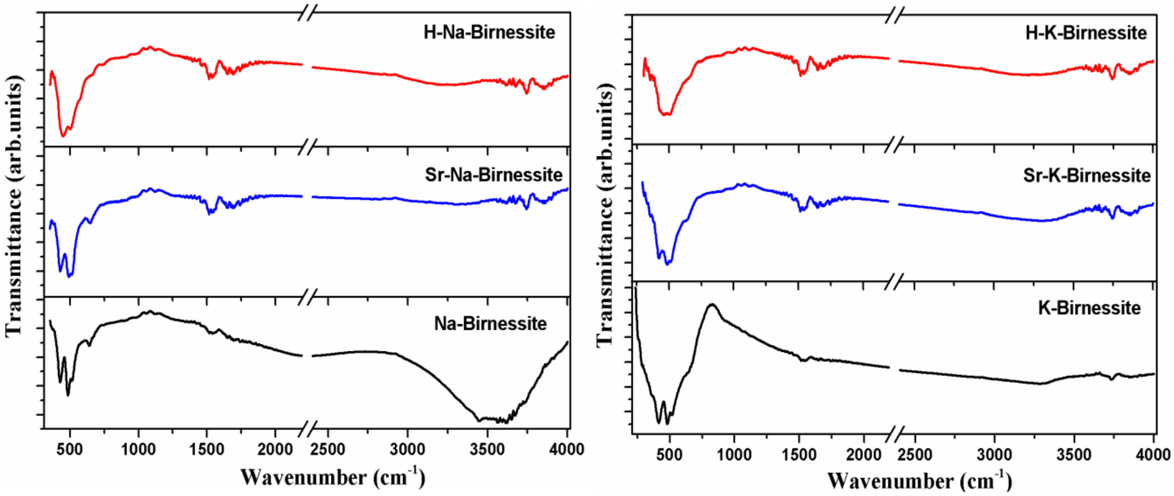

Fig.5.10: FTIR spectra of birnessite samples before and after ion exchange

The pristine as well as the Sr^{2+} and H^+ exchanged NMO and KMO samples were also characterized by FTIR spectroscopy. The FTIR spectra of these samples are shown in Fig.5.10. All the exchanged samples are closely similar to their corresponding virgin samples. NMO and its exchanged derivatives show clear broad absorption bands at 3500, 1530 cm^{-1} due to stretching of O-H bond and bending vibration of H-O-H respectively. This is in consistent with the presence of water molecules. However, these modes in the KMO and its derivative samples are not clearly observed. This might be due to the greater broadening of these modes. The bands observed at around 416, 480 and 512 cm^{-1} in NMO are the characteristic modes due to Mn-O stretching vibrations resulted in MnO_6 octahedra. In KMO sample, the characteristic Mn-O stretching modes are observed at around 408, 480, 517 cm^{-1}, while the stretching vibrations of O-H bond and bending mode of H-O-H bonds are observed at 3290 cm^{-1} and 1530 cm^{-1} respectively [151]. Thus the vibration frequencies of both NMO and KMO are almost similar which are due to identical structural features. The differences in FTIR spectrum are expected only at Na-O and K-O vibration modes, which could not be accessed in the present experimental facility. Similarly all the modes due to MnO_6 and H_2O are almost similar in Sr^{2+} or H^+ exchanged samples. The small differences and excessively broadened modes could not be used to extract information on minor variations in hydrogen boding. Absorption mode at 2300 cm^{-1} correspond to stretching vibration of CO_2 is observed in all samples which can be attributed to atmospheric CO_2 in sample chamber.

The morphology and structural variation of NMO and KMO as well as their Sr^{2+} exchanged derivatives were investigated by transmission electron microscopy and typical TEM images are shown in Fig.5.11. The low resolution TEM images of NMO and KMO (Fig.5.3) indicated their thin platelet type morphology and clear platy habits are retained in the exchanged samples. The high resolution transmission electron microscopy (HRTEM) images and SAED pattern of NMO shown in Fig.5.11 suggested their crystalline nature and clear lattice fringes. However, the clarity of the lattice fringes are deteriorated in KMO samples suggesting a possible disorder or deformed structure. This is in accordance with the conclusions inferred from XRD and DLS studies. The FFT transformation of the HRTEM images was used to find the spacing between the fringes and they are around 3.59 Å for both

NMO and KMO. The distances and periodicity of fringes of NMO and KMO also support for the better structural periodicity of NMO compared to KMO. Also it can be seen that the lattice fringes and SAED patterns of exchanged samples becomes deformed and extended indicating disorder and distortion in the lattice. Inter planar distances measured from the lattice fringes indicate a small but noticeable decrease which supports the conclusions obtained from XRD studies.

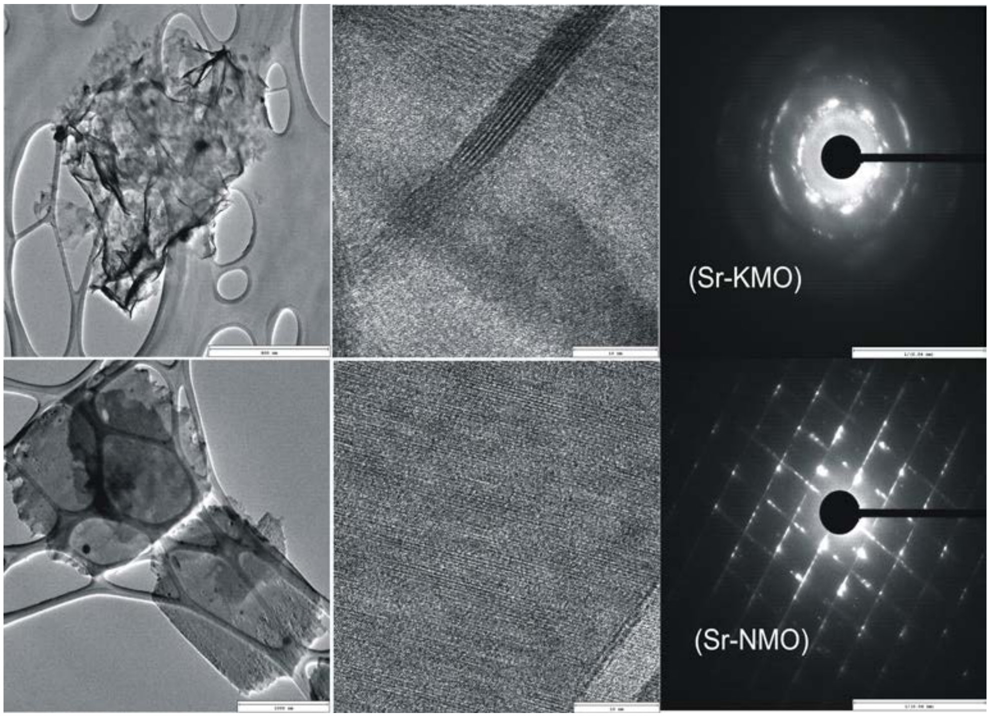

Fig.5.11: TEM and HRTEM images and SAED patterns of Sr-birnessite samples

5.3.2.3. Kinetics studies

In order to gain the insights of ion exchange mechanism, nature of the sorption process, ion exchange capacity (q_t) (defined as $[C_i - C_t] \times V/M$, (where C_i and C_t are concentration (*mmol/L*) of Sr^{2+} in solution at time $t = 0$ and t, respectively; V = volume of solution in mL and m = mass of sorbent in g) of the materials for the uptake of $^{85}Sr^{2+}$ was measured with time. All the measurements were carried out at pH = 2 and in between the time scale of 30 min to 4 h. The variation of ion exchange capacities of NMO and KMO with contact time are shown in Fig.5.5. From this figure, it can be seen that the ion exchange capacity of both NMO and KMO increases sharply and reaches to saturation level within 2h. The fast uptake in the initial one 1 h suggest the high affinity of the materials for Sr^{2+} ions as well as large concentration gradient of Sr^{2+} in between the solid and solution. As the concentration of Sr^{2+} ions in solution as well as number of available sites on the solid for uptake decreases, the kinetics of exchange becomes sluggish and finally saturates.

Also it is observed that the ion exchange capacity of NMO (~10mmol/g) is higher than that of KMO (~1mmol/g), while the variation of q_t with time is only marginal in case of NMO compared to KMO. The higher values of ion exchange capacity of NMO can be due to crystalline nature of NMO and larger interlayer spacing where ease migration of Na^+ ions to exchange with Sr^{2+} is facilitated. The poor crystallinity, lower water of hydration and small particle size induced agglomeration of KMO are also likely to hinder the facile migration of K^+ ions to exchange with Sr^{2+} ions. But quantitatively both NMO and KMO have affinity for the uptake of Sr^{2+} ions. The rate of ion exchange process, mechanism of the Sr^{2+} ions uptake and dynamic ion exchange behaviour of the NMO and KMO were investigated by modeling the experimentally obtained kinetics data with *pseudo* first order model and *pseudo* second order model. The q_e and q_t are calculated from the concentration of Sr^{2+} ions in solution, volume of solution and mass of sorbent. The typical plots for pseudo first order and pseudo second order models for NMO and KMO are shown in Fig.5.12.

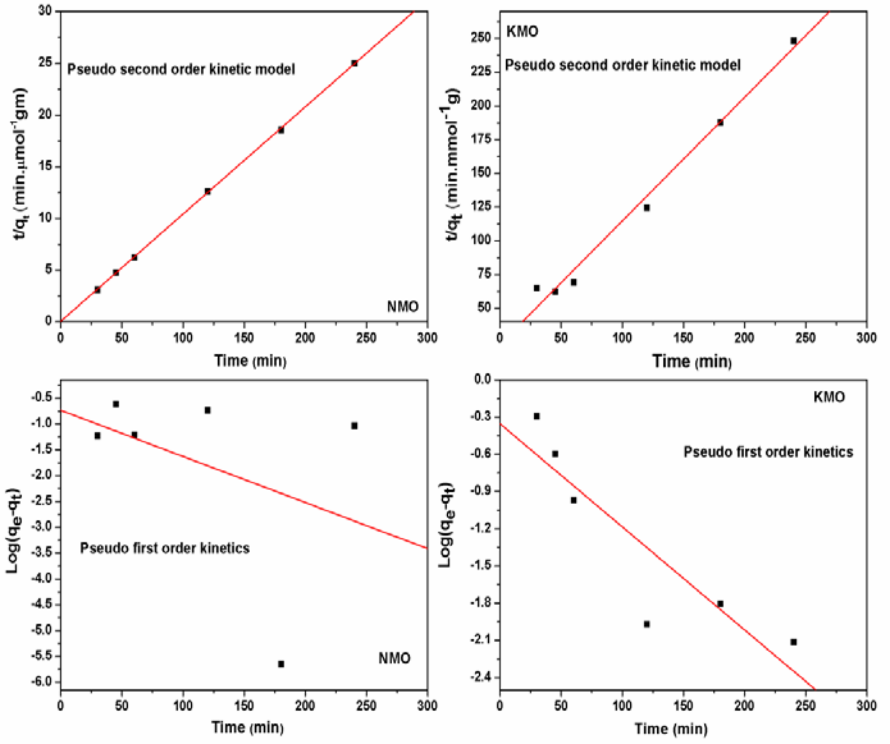

Fig.5.12: Kinetic fittings of ion exchange results

The parameters like rate constants, equilibrium sorption capacity and the typical residual (R^2) as obtained from different kinetic models are given in Table 5.1. From the Fig.5.12 it is clear that for both NMO and KMO, the plot between log(q_e-q_t) and time shows large deviation at high contact times. Also the obtained rate constant, ion exchange capacities are not in agreement with the experimental results. The larger deviation from experimental observations, poor correlation factors suggests that the ion exchange process of NMO and KMO is not physisoprtion type pseudo first order process [93a, 152]. Experimentally obtained kinetic results are fitted by using *pseudo* second order kinetic model by plotting q/t with time. By this kinetic model, the experimental data could be fitted well and the calculated ion exchange capacities of both NMO and KMO are comparable with experimental values. The correlation factors (goodness of the fit, R^2) for pseudo second order model fits are 0.999 and

0.984 for NMO and KMO, respectively. This suggests that the Na^+/K^+ and Sr^{2+} exchange kinetics in NMO and KMO follow *pseudo* second order rate process. According to *pseudo* second order model, the ion exchange process is a chemisorption process and the accumulation of Sr^{2+} ions over the adsorbate surface is the rate determining step [86]. The calculated *pseudo* second order rate constants (K_2) for NMO and KMO are 0.25g $mmol^{-1}$ min^{-1} and 0.036 g $mmol^{-1}$ min^{-1}, respectively. Also, the maximum ion exchange capacity (q_e) for NMO and KMO are 9.64 mmol/g and 1.09 mmol/g, respectively. The higher value of rate constant (K_2) and higher ion exchange capacity (q_e) of NMO compared to KMO suggests that NMO is more efficient for Sr^{2+} removal. This can be attributed to the poor crystallinity and more disorder in KMO which hinder the facile migration of K^+ ions in the bulk [135a].

Table 5.1: Summary of results obtained from different kinetic models for Sr^{2+} ions exchange with NMO and KMO

	NaMnO			KMnO		
Pseudo First order	R^2=-0.063	q_e=0.18 mmol/g	K=0.02 min^{-1}	R^2=0.76267	q_e=0.44 mmol/g	K=0.019 min^{-1}
Pseudo second order	R^2=0.99984	q_e=9.64 mmol/g	K_2=0.25 g $mmol^{-1}$ min^{-1}	R^2=0.9836	q_e=1.09 mmol/g	K_2=0.036 g $mmol^{-1}$ min^{-1}

5.3.2.4. Ion exchange isotherms

In order to further investigate the mechanism of ion exchange and nature of interactions between adsorbate and adsorbent, the ion exchange capacity of the NMO and KMO were measured at different initial concentrations of ^{85}Sr spiked $Sr(NO_3)_2$ solutions. Weighed quantities of exchangers are equilibrated for 3 h with solutions containing different concentration of Sr^{2+} ions (1 mmol/L to 100 mmol/L). The ion exchange capacities (q_e) of both samples observed with different initial concentration of Sr^{2+} ions are shown in Fig.5.13.

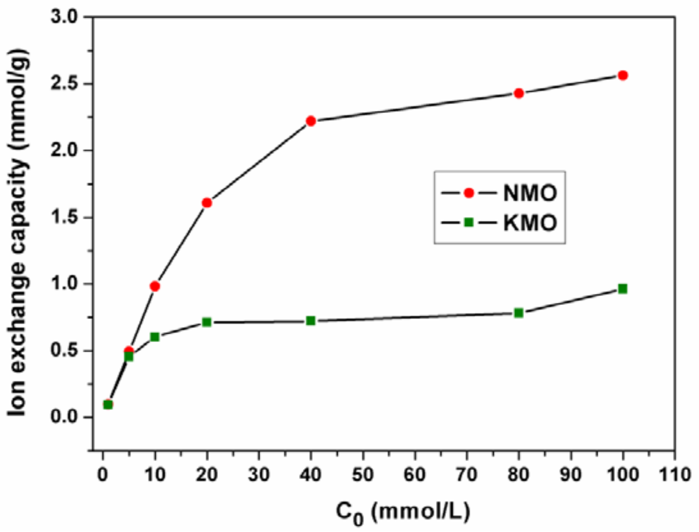

Fig.5.13: Variation of ion exchange capacity with initial concentration of Sr^{2+}

Initially, the ion exchange capacity of both samples show rapid increasing trend with increasing the concentration of Sr^{2+} ions and then becomes almost invariant. The large variation of q_e at lower initial concentration of Sr^{2+} ions can be attributed to greater availability of exchangeable sites and higher available concentrations of Sr^{2+} ions. As the concentration of Sr^{2+} ions in the solution increases, hindrance caused by already occupied Sr^{2+} ions in the available exchangeable sites dominates for further uptake [88b]. For both the samples, the maximum ion exchange capacity was observed at concentration of Sr^{2+} ions 100 mmol/L and the maximum ion exchange capacities of NMO and KMO are ~ 2.7mmol/g, and ~1 mmol/g respectively. Experimentally obtained adsorption isotherm results were simulated with most widely used Langmuir, Freundlich and Hill isotherm models because of their simplicity in application, explanation of the theoretical results obtained. Typical fittings of the experimental data with Langmuir, Freundlich and Hill adsorption models are shown in Fig.5.14. The details of analysis of different isotherm models are explained below. As shown in Fig.5.14, experimentally obtained isotherm results are fitted well with Hill adsorption isotherm model compared to Langmuir and Freundlich isotherm models. The explanation of the isotherm modeling results are as follows:

5.3.2.4.1. Langmuir adsorption isotherm

Langmuir adsorption isotherm model is the universal model, applicable to large varieties of adsorption systems, originally designed to explain gas adsorption on activated charcoal [101b]. Typical fitting parameters for both the materials are given in Table.5.2. In case of KMO, q_m=0.78 mmol/g, K_L=3.32 L/mmol. Moreover the dimensionless quantity (R_L) called as separation constant for NMO is 0.18 and for KMO R_L is 0.23. Adsorption is favorable if $0<R_L<1$. Typical Langmuir fittings for NMO and KMO are shown in Fig.5.14, obtained q_m and K_L values from Langmuir fit for NMO are 2.26 mmol/g and 4.69 L/mmol, respectively.

5.3.2.4.2. Freundlich adsorption isotherm

Obtained K_F values for NMO and KMO are 0.93mmol/g and 0.42mmol/g respectively; whereas calculated Freundlich parameter 'n' for NMO is 34.81 and for KMO (n) is 5.36. From the isotherm fitting figure it is clear that goodness of fit is better in case of Langmuir isotherm model compared to Freundlich isotherm model and Langmuir model explains the results better compared to Freundlich model. Typical Fraundlich fitted plot of both NMO, KMO materials is shown in Fig.5.14, fitting parameters are given in Table 5.2.

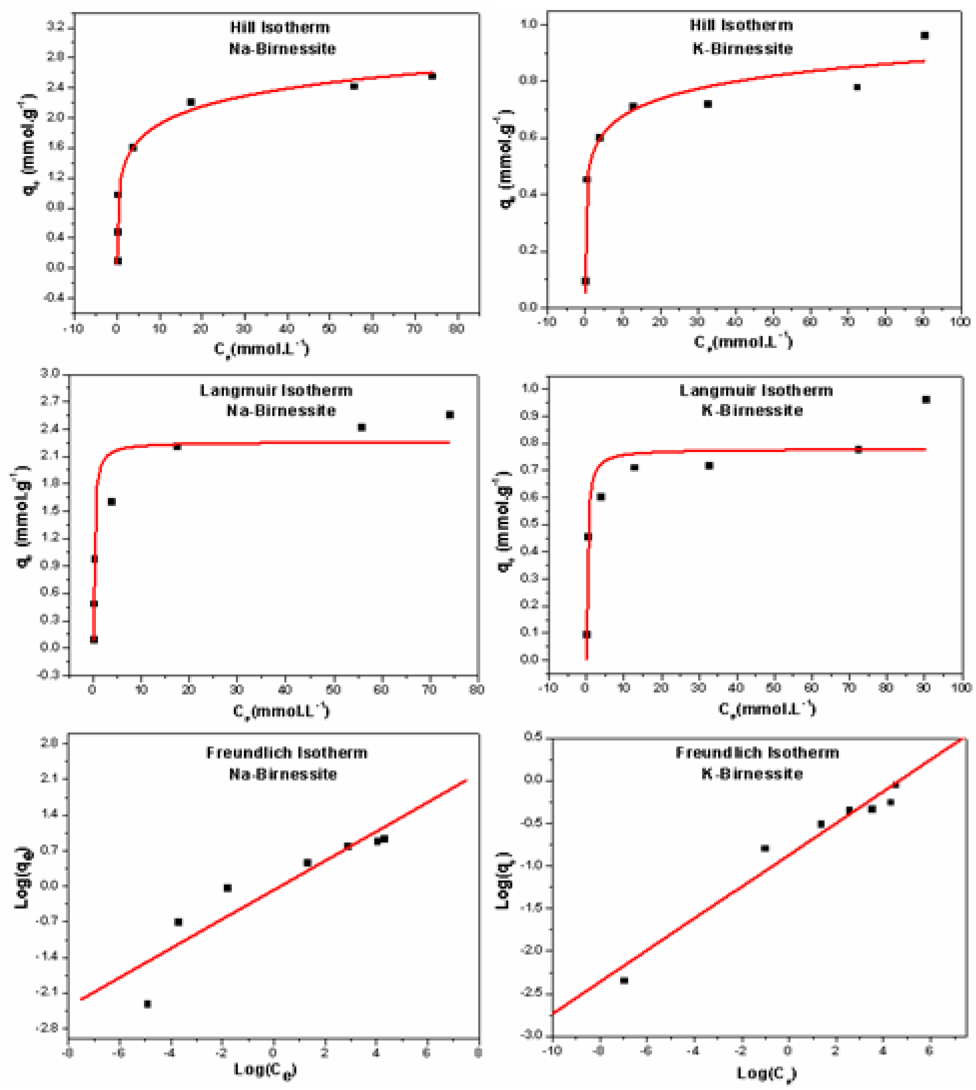

Fig.5.14: Sorption isotherms of Na-birnessite and K-birnessite fitted with Langmuir, Freundlich and Hill isotherm models

5.3.2.4.3. Hill adsorption isotherm

Hill adsorption isotherm model is a three parameter model developed in order to investigate the actual interactions between the adsorbate and the adsorbent. Adsorption fitting parameters are better with Hill adsorption isotherm model compared to Langmuir and Freundlich isotherm models, typical isotherm fittings for both NMO and KMO, fitting parameters are shown in Fig.5.14 and Table 5.2, respectively. Obtained n, N_m values for NMO are 0.28, 17.42 respectively and for KMO, n=0.22, N_m=7.5. It is clearly indicating that number of available adsorptions sites and number of ions anchored per site are more in case of NMO compared to KMO thus behaving as a better sorbent material compared to KMO.

Table 5.2: Fit parameters of isotherm models for Sr^{2+} ion exchange with NMO and KMO

	NaMnO			KMnO		
		Q_{theo}=1.28 mmol/g			**Q_{theo}=1.24 mmol/g**	
Langmuir	R^2=0.90047	q_m=2.26 mmol/g	b=4.69 $L.mmol^{-1}$	R^2=0.83547	q_m=0.78 mmol/g	b=3.32 $L.mmol^{-1}$
Freundlich	R^2=0.81059	K_F=0.93	n=34.81	R^2=0.94604	K_F=0.42	n=5.36
Hill model	R^2=0.97386	n=0.28	N=17.42	R^2=0.94684	n=0.21801	N=7.51487

5.3.3. Interference studies

Reprocessing of nuclear waste is a tedious task due to presence of high concentrations of sodium, calcium, aluminum in their nitrate forms along with minor concentrations of rare earth elements. Hence role of interfering ions over Sr^{2+} ions uptake by the title materials has been investigated by measuring their Sr^{2+} ion exchange capacities in presence of high concentrations of Na^+, Ca^{2+} and Al^{3+}. To the mixture of $Sr(NO_3)_2$, solution of interfering ions in their nitrate form with concentration ranging from 1 mM/L to 100 M/L ^{85}Sr solution has been spiked, distribution coefficients were measured at different concentration of interfering ion solutions for both KMO and NMO.

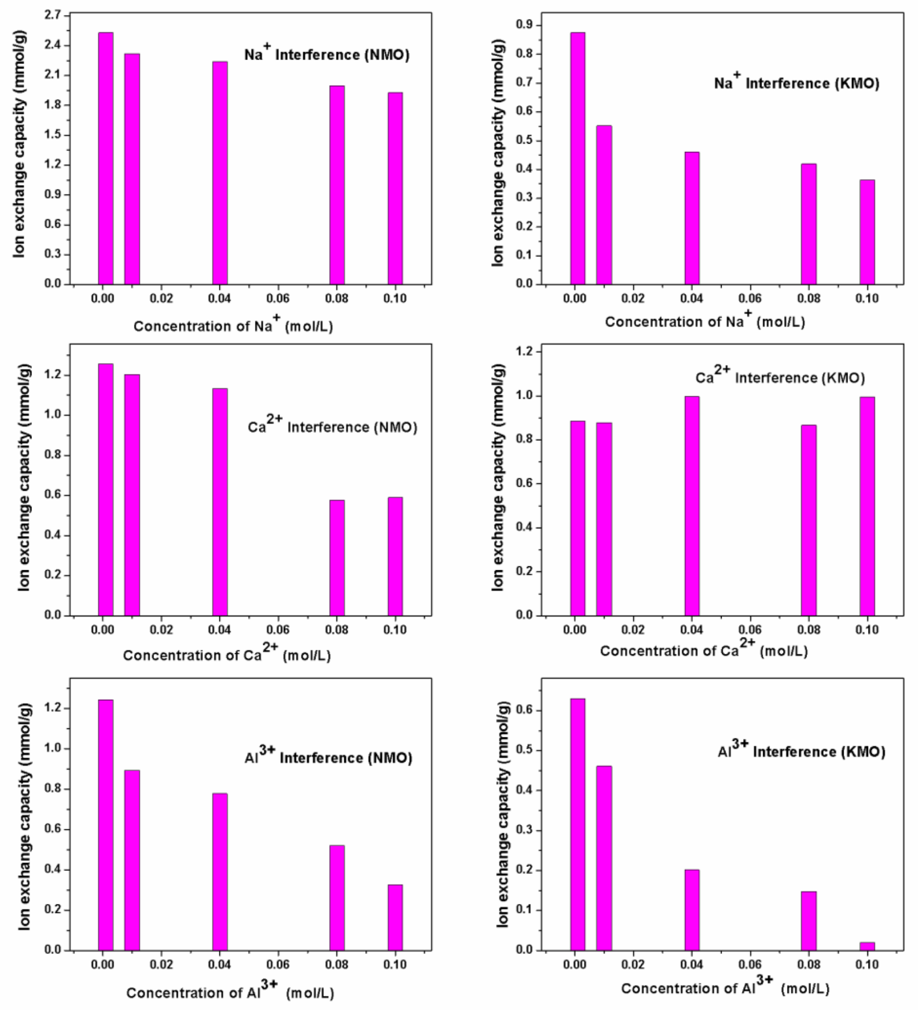

Fig.5.15: Interference of different ions on Sr^{2+} uptake behaviour of NMO and KMO

Interfering ions presence has affected the uptake of Sr^{2+}, ion exchange capacity is found to be decreased with increase in concentration of interfering ions. Distribution constants for Sr^{2+} ions uptake by both the materials was most affected in presence of Al^{3+} compared to $Ca^{2+}$and Na^{+} ions. Effect of interfering ions for NMO is $Al^{3+}>Ca^{2+}>Na^{+}$ whereas for KMO effect of interfering ions followed the trend $Al^{3+}>Na^{+}>Ca^{2+}$. Typical figure showing the effect of interfering ions over ion exchange capacity of title materials is shown in Fig.5.15. Role of Na^{+} ions upon the uptake of Sr^{2+} ions is very important because of high concentrations of Na^+ in the nuclear waste. From the Fig.5.15 it is clear that though the presence of Na^+ ions reduced the ion exchange capacity of both NMO and KMO, distribution constant value is reasonably high even in the presence of large concentrations of interfering ions which indicates that selectivity of the studied materials towards the uptake of Sr^{2+} ions.

5.4. Conclusions

In summary, this study revealed ion exchange properties of two manganese oxides namely Na-birnessite and K-birnessite for Sr^{2+} ions separation from nuclear waste. Quantitative uptake of Sr^{2+} by NMO and KMO from solution indicated their potential for the separation of Sr^{2+} ions from nuclear waste. It is also inferred that the structure of the materials plays an important role in the separation efficiency and selectivity. The study also revealed that NMO is an efficient lattice for separation compared to KMO due to favorable exchange conditions. Both the lattices show low exchange in strong acidic medium and highly alkaline conditions due to instability of the manganates at low pH and strong inference of Na^+ ions at alkaline pH. The studies on kinetics and exchange isotherm revealed that they follow pseudo-second order rate law and exchange is mainly by favorable chemisorption process. It is proposed that these lattices can be directly used for separation of ^{90}Sr from nuclear waste solutions and also compatible for immobilization.

Chapter 6

Temperature dependent structure properties of $K_3Gd_5(PO_4)_6$

6.1. Introduction

Complex inorganic phosphates attract huge research interest due to their composition and preparation condition dependent physical properties as well as their diversified crystal chemistry as a function of temperature and pressure. They also exhibit interesting physical properties amenable for varieties of technological applications. In particular, the complex phosphates of rare earth ions along with mono and divalent cations are well utilized as ionic conductors [153], photocatalysts [154] and host lattices for luminescent ions for optical applications [109]. Such complex phosphates containing mono or divalent cations are also considered as promising materials for selective separation of ions from high level nuclear waste and heavy metal ion pollutants from environment. Efficient exchange or adsorption possibilities for separation of various ions from aqueous solution in a wide range of pH by phosphates of Zr^{4+}, Ti^{4+} and Sn^{4+} as well as rare-earth ions or alkali and alkaline-earth metals have been reported in literature [105, 153, 155]. Apatite, zircon, monazite, cheralite and nasicon type phosphates are also being considered as potential host matrices for immobilization of radioactive elements separated from the high level nuclear waste (HLW) due to their rock analogous properties viz. high thermal and chemical stability, high radiation resistance and insignificant leachability by water. It may be mentioned here that the phosphates of lighter trivalent lanthanide ions crystallize primarily in monazite type structures. Monazite-type lattices can accommodate a wider variety of actinides or radioactive lanthanides and hence are considered to be promising host matrices for immobilization of minor actinides. Higher waste loading capacity in particular for lower rare earths and actinides as well as higher stability of monazite type phosphates are the favorable features making them promising matrices for immobilization of actinides. Rich crystal chemistry of mixed phosphates with monovalent alkali (M^+) and rare-earth (Ln^{3+}) ions is a consequence of difference in the ionic radii of M^+ and Ln^{3+} ions and their stoichiometry. Often such phosphates crystallize in layer or tunnel type structures, where the basic structural frame is built by PO_4^{3-} and Ln^{3+} ions, while the M^+ ions are accommodated inside the tunnels or layers for maintaining the charge neutrality. Thus the M^+ ions are in general exchangeable with other ions and hence they are considered as promising materials for selective separation of ions from high level nuclear waste or heavy metal ion pollutants from environment [156].

Among the mixed cation double phosphates in M^+-Ln^{3+}-P-O system, the commonly encountered phases are $MLn(PO_3)_4$ and $M_3Ln(PO_4)_2$, which have distinct crystal structures namely infinite chains of tetrahedral PO_4 units in the former while isolated tetrahedral PO_4 units in the latter structures [157]. In the $MLn(PO_3)_4$ type structures, the rare-earth ions have eight coordinated polyhedra which are connected by chains of PO_4 units while in the $M_3Ln(PO_4)_2$ types, the rare-earth ions have eight or six coordinated polyhedra depending on the radius of Ln^{3+} ions and preparation temperature, which are connected to isolated PO_4 tetrahedra. In addition to these two compositions, another compound with composition $K_3Gd_5(PO_4)_6$ has been reported by Zhu *et al.* [158] which has a distinct structure type with chains of condensed $[Gd_5(PO)_6]^{3-}$ units made from GdO_n (n = 8 and 9) polyhedra and PO_4 tetrahedra. Detailed structural analysis of this compound at ambient temperature indicated that the GdO_8 and GdO_9 polyhedra are connected in three dimensions forming tunnel like empty spaces along *c*-direction and these tunnels are occupied by K^+ ions. The phosphate groups are connected to the GdO_n polyhedra by sharing edge or corners. Optical absorption studies on this compound suggested absorption is mainly due to Gd^{3+} ions and the corresponding emission in the UV region [158]. Besides these studies, not many reports on thermophysical or structural properties are available for this material or analogous of such complex phosphates. The second isostructural material $K_3Bi_5(PO_4)_6$ in K-Bi-P-O system has been isolated by Terebilenko *et al.* [159] and Hizhnyi *et al.* [160] from the K_2O-Bi_2O_3-MoO_3/WO_3 molten flux. The structural analysis of $K_3Bi_5(PO_4)_6$ revealed almost similar coordination polyhedra around Bi^{3+} despite having lone pair electrons in it. Subsequently, rare-earth ion doped $K_3Gd_5(PO_4)_6$ has been investigated by Meng *et al.* [161], where the authors have revealed only a partial substitution of Gd^{3+} by Ce^{3+} whereas an appreciable substitution by Eu^{3+}. The authors have also mentioned about the existence of an isostructural Eu^{3+} analogous $K_3Eu(PO_4)_6$ materials. Existence of the $K_3Eu_5(PO_4)_6$ is confirmed in this study and its properties are explained in other chapters. Since such complex phosphates are of significant interest in the aspect of optical properties such as X-rays scintillation, luminescent materials for plasma display panel as well as for lighting and stimulated emission applications, these materials need more detailed investigations with respect to their structural behaviour and vibrational properties with temperature [94, 162].

To investigate the influence of temperature on its structural and vibrational properties, the stoichiometric compound $K_3Gd_5(PO_4)_6$ was prepared and investigated its crystal structure in a wide range of temperature from 20 to 1073 K by variable temperature XRD using a lab source and synchrotron X- rays as well as Raman spectroscopy in the temperature range of 77 to 873 K. The structure is found to be stable in the entire range of temperature and shows anisotropic thermal expansion with minimum expansion along the *b*-axis as compared to the other two axes. In addition the magnetic and ion exchange properties of $K_3Gd_5(PO_4)_6$ were also studied.

6.2. Experimental details

The title sample was prepared by solid state reactions of KH_2PO_4, $NH_4H_2PO_4$ and Gd_2O_3. Stoichiometric amounts of reactants were ground thoroughly and melted in a platinum crucible at 573 K for 4 h. Solidified molten mass was rehomogenized and pressed into a pellet. The pellet was heated at 773 K for 24 h and then rehomogenized and repelletized. The pellet was finally heated at 1123 K for 24 h. The powder XRD pattern of the final product was recorded on a rotating anode based powder X-ray diffractometer using Cu Kα radiation. The observed XRD pattern agrees well with that reported by Zhu *et al.* [158]. Absence of any additional unaccounted reflections confirms the phase purity of the sample. For detailed temperature dependent structural study above ambient temperature, high temperature X-ray diffraction of the synthesized sample was carried out. The XRD patterns were recorded in the two theta range of 10-90° in steps of 0.02° with step time 1.5s. The sample was heated to a desired temperature and then held for about 10 min to obtain temperature equilibrium prior to collection of diffraction data. The XRD data below ambient temperature were recorded by using synchrotron radiation (wavelength: 0.6621 Å). The low temperature X-ray diffraction studies were carried out by placing sample in between two kapton films and placed in between two copper blocks with a small opening for the X-ray beam which are connected to a liquid helium cryostat. The sample was cooled to 20 K and allowed to equilibrate for about 1 h and then diffraction data were collected. The sample was then heated to a desired temperature and again held for about 10 min before collection of XRD data. The diffracted radiations were recorded on an image plate (mar 345). Typical time for recording the each diffraction pattern was 6 min. The recorded images were integrated by using FIT2D software. The recorded XRD patterns in both low and high temperature regions were analyzed by Rietveld method by using Fullprof-2K [96]. Raman spectra were recorded in the back scattering geometry which cover the wave number range 30-1250 cm^{-1}. Thermal stability of the sample was studied by simultaneous thermogravimetric (TG) and differential thermal analysis (DTA) technique. The magnetization behavior of the sample in between 2-300 K was studied using a 9T PPMS based Vibrating Sample Magnetometer. The ion exchange property of the sample was studied by equilibrating a weighed quantity of solid material with an aqueous solution of radioactive Sr^{2+} (as $^{85}Sr(NO_3)_2$).

6.3. Results and discussion

6.3.1. XRD studies

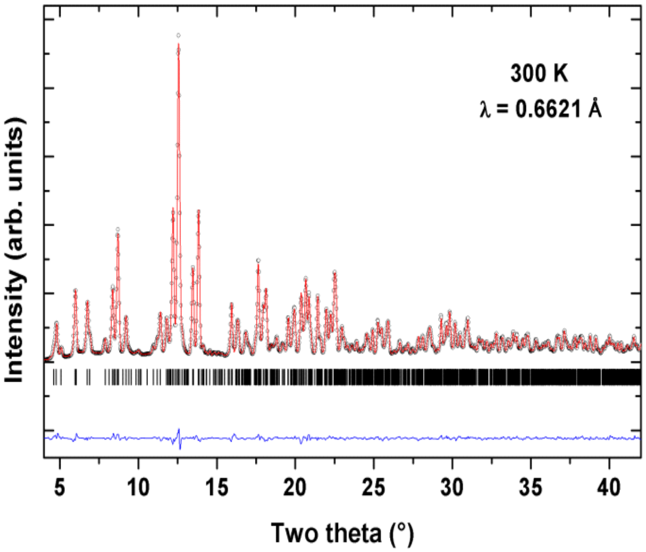

Fig.6.1: Rietveld refinement plot of the powder XRD pattern of $K_3Gd_5(PO_4)_6$

Formation of the desired $K_3Gd_5(PO_4)_6$ phase from the components was monitored by recording the powder XRD pattern after each stage of high temperature reaction. The XRD pattern of the product obtained after heating at 773 K showed the formation of $GdPO_4$ which further reacted at higher temperature to the desired product. The reaction is found to proceed sluggishly and predominantly through monazite type $GdPO_4$ formed as an initial reaction product. After heating this preheated sample at 1023 K for 24 h, monophasic $K_3Gd_5(PO_4)_6$ could be obtained. Detailed characterization of the phase was carried out by Rietveld refinement of the powder XRD pattern recorded at ambient temperature (300 K) by using synchrotron radiation source.

The reported position coordinates of $K_3Gd_5(PO_4)_6$ by Zhu *et al*. were used as the initial structural model for refinement. Only one thermal parameters (B_{ov}) is considered for initial analysis of the data. The background of the diffraction pattern was simulated by linear interpolation of selected points for a smoothly varying background profile. The Bragg peaks of the XRD pattern were fitted to a pseudo-Voigt profile function with an angle dependent mixing parameters (η) defined as: $\eta = \eta_0 + X \times 2\theta$, where η_0 and X are refineable parameters. The scale and unit cell parameters were initially refined for appropriate matching of the peak positions and intensity. All the observed peaks could be accounted by the assumed model which further confirms the absence of any other secondary phase in the sample. Micro absorption corrections were applied for all the powder XRD data recorded in synchrotron source. Subsequently, the position coordinates of all the atoms along with B_{ov} parameter were refined in the later cycles of refinement. Finally the B_{ov} was assigned to individual atoms and refined along with all other parameters. The refinements of thermal parameters of the individual atoms were carried out by constraining them as per their mass. Appreciably good refinement was concluded from the difference plots between the observed and calculated diffraction pattern as well as from the residual of the refinement. The residuals factors of refinement of the ambient temperature XRD data are: R_p: 3.25, R_{wp}: 4.50, $\chi2$: 3.50, R_B: 2.57 and R_F = 1.90. The refined unit cell parameters of $K_3Gd_5(PO_4)_6$ at 300 K are: a = 17.4717(4) Å, b = 6.9345(2) Å, c = 18.1088(4) Å and β = 114.409(2)°, V = 1997.92(8) $Å^3$.

These observed unit cell parameters as well as position coordinates are in close agreement with those reported earlier by Zhu *et al.* [158]. The final Rietveld refinement plot for the XRD data of $K_3Gd_5(PO_4)_6$ at 300 K is shown in Fig.6.1. The position coordinates of $K_3Gd_5(PO_4)_6$ at 300K are given in Table 6.1.

Table 6.1: Refined position coordinates of $K_3Gd_5(PO_4)_6$ at 300 K

Atom	***Wyc.***	**x**	**y**	**z**	**U(eq) (Å)^2**
Gd1	*4e*	0	0.3660(5)	1/4	0.0042(2)
Gd2	*8f*	0.14295(14)	-0.4145(2)	0.48045(14)	0.0042(2)
Gd3	*8f*	0.21939(13)	0.1249(3)	0.29181(12)	0.0042(2)
K1	*8f*	0.0759(2)	0.9029(5)	0.0756(2)	0.014(2)
K2	*4e*	0	0.8236(7)	1/4	0.014(2)
P1	*8f*	0.1382(2)	0.0897(6)	0.4133(2)	0.0011(9)
P2	*8f*	0.2098(3)	0.6253(6)	0.3403(2)	0.0011(9)
P3	*8f*	-0.0759(3)	0.4044(6)	0.3788(3)	0.0011(9)
O1	*8f*	0.2022(4)	0.7813(8)	0.2752(4)	0.0234(15)
O2	*8f*	-0.0970(4)	0.2445(8)	0.3115(3)	0.0234(15)
O3	*8f*	0.2348(4)	0.072(2)	0.4250(5)	0.0234(15)
O4	*8f*	0.1238(7)	0.2349(9)	0.4689(6)	0.0234(15)
O5	*8f*	0.2477(4)	0.6719(13)	0.4326(3)	0.0234(15)
O6	*8f*	-0.1468(4)	0.5309(9)	0.3862(4)	0.0234(15)
O7	*8f*	0.0021(3)	0.5201(8)	0.3799(4)	0.0234(15)
O8	*8f*	0.1004(4)	-0.1001(7)	0.4328(4)	0.0234(15)
O9	*8f*	-0.0455(5)	0.3160(10)	0.4658(3)	0.0234(15)
O10	*8f*	0.2725(4)	0.4652(8)	0.3432(4)	0.0234(15)
O11	*8f*	0.1183(3)	0.5463(11)	0.3288(4)	0.0234(15)
O12	*8f*	0.0871(4)	0.1312(10)	0.3226(3)	0.0234(15)

The analysis of structural data (Table.6.1) of $K_3Gd_5(PO_4)_6$ indicate three crystallographically distinct Gd atoms (Gd1, Gd2 and Gd3), two K atoms (K1 and K2), three P atoms (P1, P2 and P3) and twelve O atoms (O1-O12) in the unit cell. All atoms except Gd1 and K2 are occupied in *8f* sites while the Gd1 and K2 are occupied in *4e* sites of space group *C2/c*. The estimated inter-atomic distances indicated that all the P atoms have nearly regular tetrahedral coordination with typical P-O bond lengths in the range between 1.50 Å and 1.62 Å as commonly observed in various orthophosphates [156c]. Similarly the examination of Gd-O bonds in $K_3Gd_5(PO_4)_6$ indicate that the Gd1 and Gd3 have eight coordinated GdO_8 polyhedra while Gd2 has nine coordinated GdO_9 polyhedra.

Typical Gd-O bond lengths in $K_3Gd_5(PO_4)_6$ are in the range of 2.23 to 2.76 Å. Besides, all the GdO_n polyhedra are distorted and the dispersions in bond lengths are appreciably larger in the $Gd1O_8$ and $Gd3O_8$ polyhedra compared to the $Gd2O_9$ polyhedra. The polyhedral distortions were calculated from the dispersion of bond lengths ($Distt. = {}^{1}/_{n} \sum_{i=1}^{n} (|d_i - \bar{d}|/\bar{d})$, where, d_i is the bond length of the ith bond and $\bar{d}$ is the average bond length in the coordination polyhedra).

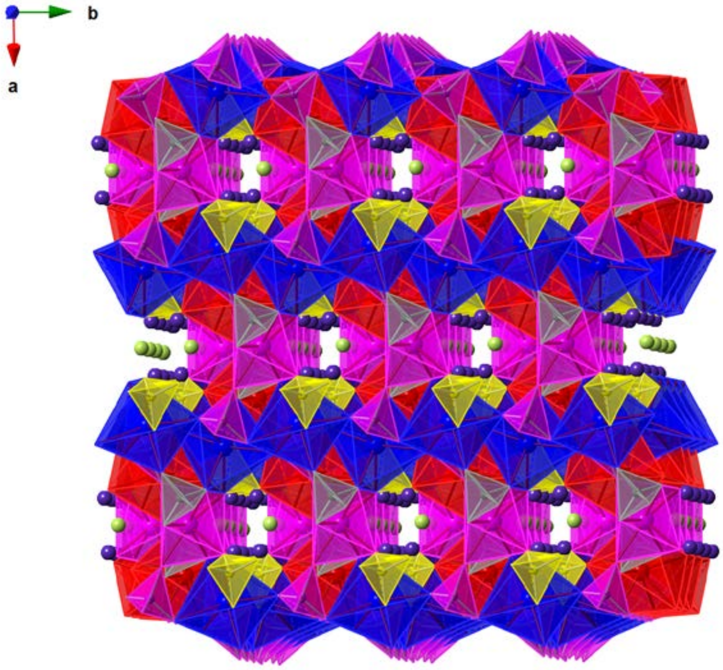

Fig.6.2: Crystal structure of $K_3Gd_5(PO_4)_6$. The $Gd1O_8$ (pink), $Gd2O_9$ (red) and $Gd3O_8$ (blue) polyhedra and PO_4 units are shown. K1 and K2 are shown as spheres

For $Gd1O_8$, $Gd2O_9$ and $Gd3O_8$, the polyhedra distortions are 33.39×10^{-4}, 10.79×10^{-4} and 31.86×10^{-4}, respectively. The PO_4 tetrahedra are connected to the GdO_n polyhedra by sharing corners as well as edges forming a complex $[Gd_5(PO)_6]^{3-}$ ion which are eventually connected periodically forming an open tunnel containing three dimension structure. The tunnels formed in the arrangements of $[Gd_5(PO)_6]^{3-}$ are occupied by K^+ ions (K1 and K2) to maintain the charge neutrality. Typical three dimensional structure indicating the GdO_n and PO_4 polyhedra and K^+ ions is shown in Fig.6.2, further analysis of the linkages of the GdO_n and PO_4 polyhedra in $K_3Gd_5(PO_4)_6$ indicate that the GdO_n polyhedra are linked together by sharing their edges (Fig.6.3).

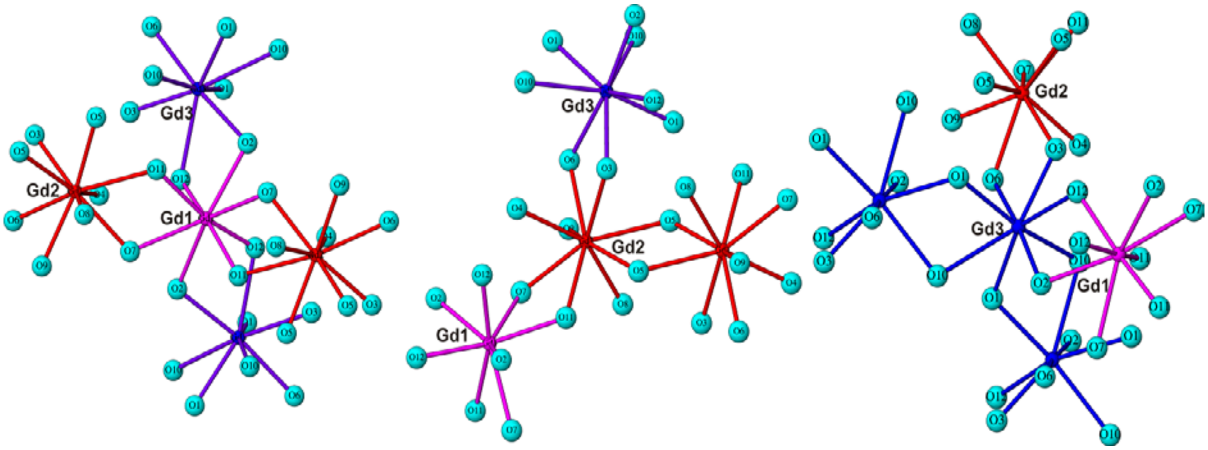

Fig.6.3: Typical connections of GdO_n polyhedra in $K_3Gd_5(PO_4)_6$

The typical connections of these polyhedra are closely similar to those observed in zircon type orthophosphates of rare-earths [162a]. It can be mentioned here that the zircon type orthophosphates are observed with only smaller rare-earth ions i.e. ions smaller than Gd^{3+} ions, while all other ions including Gd^{3+} ions form monazite type phosphates [129]. The coordination number around the rare-earth ions in zircon and monazite type orthophosphates are 8 and 9 respectively. The GdO_n polyhedra observed in the present $K_3Gd_5(PO_4)_6$ structure are similar to these polyhedra. However in zircon type structures, each of the LnO_8 polyhedra are linked to four others symmetrically with $\bar{4}m2$ site symmetry at the Ln^{3+} ions. In the present case the $Gd1O_8$ and $Gd3O_8$ polyhedra are linked to four other GdO_n polyhedra (Fig.6.3) while the $Gd2O_9$ is linked only to three other GdO_n polyhedra.

Similar analysis on the linkages of PO_4 to GdO_n polyhedra in $K_3Gd_5(PO_4)_6$ also indicate a close similarity with zircon type structures where the GdO_n polyhedra are connected to two PO_4 units by sharing edges while four (five in case of Gd2) other PO_4 units by sharing corners. The typical connection of GdO_n polyhedra and PO_4 tetrahedra of the present structure is shown in Fig.6.4. Thus in the present structure, the Gd1 and Gd3 are linked to PO_4 like zircon while Gd2 is connected to five PO_4 units like monazite structure. The formation of nine coordinated polyhedra around the rare-earth ions in monazite type structure is observed due to the shift of the PO_4 ions towards the regular LnO_8 polyhedra [129]. Ideally the local surroundings around the Gd^{3+} ions of the present structure are closer to those of the rare-earth phosphates. Hence it is expected that the response of $K_3Gd_5(PO_4)_6$ to the non-ambient conditions might be controlled by the coordination polyhedra around the Gd^{3+} and K^+ ions as usually observed in ABO_4 type rare-earth orthophosphate [163]. Since the presence of K^+ ions in the structure is just for charge neutrality reasons, the structural parameters as well as elastic properties are expected mainly from the GdO_n arrangements. Later in this chapter it has been explained that the three dimensional frame made from GdO_n polyhedra of the $K_3Gd_5(PO_4)_6$ governs its thermal properties. In order to study the thermo-elastic and thermo-physical properties of $K_3Gd_5(PO_4)_6$, structural analysis below and above ambient conditions were carried out and they are explained below.

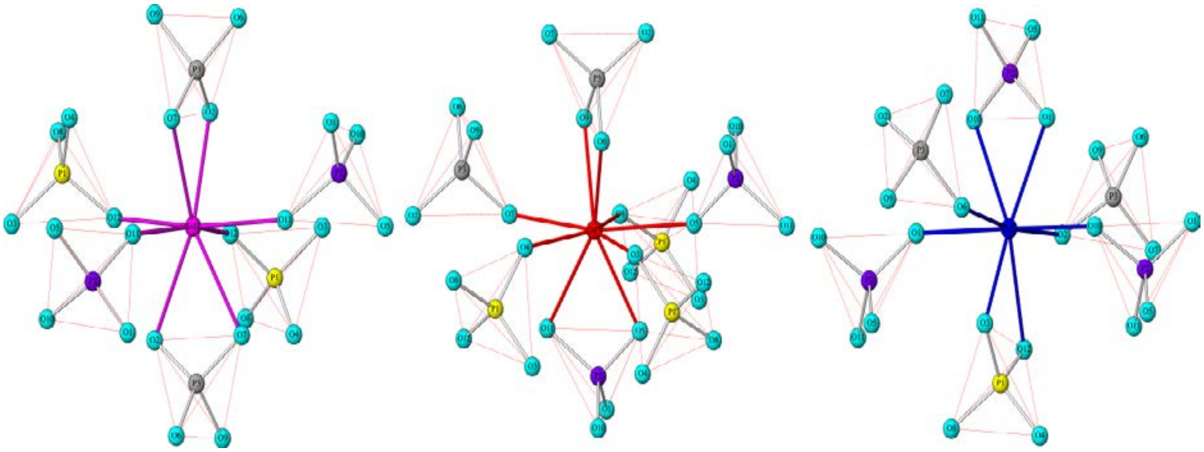

Fig.6.4: Typical connections of GdO_n and PO_4 polyhedra in $K_3Gd_5(PO_4)_6$

6.3.2. Low temperature studies

Table 6.2: Refined positional parameters of $K_3Gd_5(PO_4)_6$ at 20 K

Atom	***Wyc.***	**x**	**y**	**z**	**U(eq) (Å)^2**
Gd1	*4e*	0	0.3656(4)	1/4	0.0028(2)
Gd2	*8f*	0.14206(12)	-0.4151(2)	0.48074(11)	0.0028(2)
Gd3	*8f*	0.21910(11)	0.1247(3)	0.29200(11)	0.0028(2)
K1	*8f*	0.0761(2)	0.9044(5)	0.0763(2)	0.0003
K2	*4e*	0	0.8249(7)	1/4	0.0003
P1	*8f*	0.1354(2)	0.0888(6)	0.4138(2)	0.0007(9)
P2	*8f*	0.2094(2)	0.6252(6)	0.3415(2)	0.0007(9)
P3	*8f*	-0.0726(3)	0.4031(6)	0.3816(2)	0.0007(9)
O1	*8f*	0.2027(4)	0.7801(6)	0.2761(3)	0.0156(15)
O2	*8f*	-0.0962(3)	0.2465(7)	0.3129(3)	0.0156(15)
O3	*8f*	0.2325(3)	0.069(2)	0.4256(4)	0.0156(15)
O4	*8f*	0.1216(7)	0.2361(7)	0.4687(6)	0.0156(15)
O5	*8f*	0.2476(3)	0.6712(11)	0.4339(3)	0.0156(15)
O6	*8f*	-0.1443(3)	0.5312(9)	0.3861(3)	0.0156(15)
O7	*8f*	0.0014(3)	0.5240(8)	0.3794(3)	0.0156(15)
O8	*8f*	0.0991(4)	-0.1020(6)	0.4332(3)	0.0156(15)
O9	*8f*	-0.0421(4)	0.3170(9)	0.4683(3)	0.0156(15)
O10	*8f*	0.2726(3)	0.4664(6)	0.3440(3)	0.0156(15)
O11	*8f*	0.1173(3)	0.5469(10)	0.3286(3)	0.0156(15)
O12	*8f*	0.0862(3)	0.1313(8)	0.3231(3)	0.0156(15)

The powder XRD patterns recorded below the ambient temperature were analyzed by Rietveld refinement using the refined structural parameters of ambient temperature phase as the initial model. As in the case of ambient temperature data, the background and peak profile of the low temperature XRD data were modeled. Initially the unit cell parameters were refined along with scale factors. The complete diffraction pattern could be fitted with the assumed structural model which indicates no structural transition down to 20K. The position coordinates of all the atoms and isotropic thermal parameters were refined in the final cycles and the refined structural parameters at 20 K are given in Table 6.2.

A comparison of the position coordinates of various atoms at 20K with those for the structure at 300K indicated no significant variation, which further support for the absence of any structural transition. The refined unit cell parameters of $K_3Gd_5(PO_4)_6$ at 20 K are: a = 17.4267(4) Å, b = 6.9243(2) Å, c = 18.0410(3) Å, β = 114.388(2)° and V = 1982.70(7) $Å^3$. Final Rietveld refinement plot for the XRD data at 20K is shown in Fig.6.5. Only a subtle decrease in unit cell parameter due to the temperature effect is noticed down to lowest temperature. In a similar manner, all the XRD patterns recorded in between 20 and 300 K were refined. The XRD patterns of $K_3Gd_5(PO_4)_6$ above ambient temperatures were recorded by rotating Cu anode based X-ray diffractometer. The data recorded at 294 K was refined using the refined unit cell parameters and structural parameters obtained from our refinement of synchrotron XRD data recorded at 300 K. The diffractometer zero correction was carried out prior to the refinement of the unit cell parameters. The background profiles of the high temperature XRD data were modeled by using 5th order polynomial function while the profiles of the Bragg peaks were generated by using *pseudo*-Voigt peak shape function.

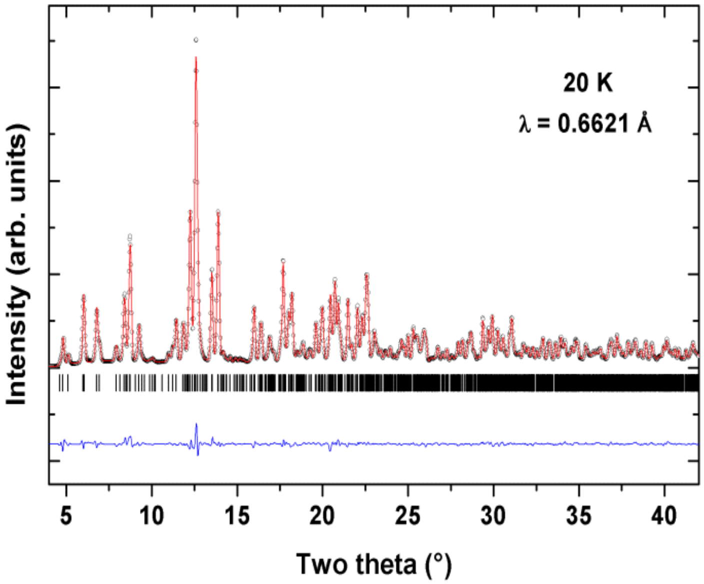

Fig.6.5: Rietveld refinement plot of $K_3Gd_5(PO_4)_6$ at 20K

6.3.3. High temperature studies

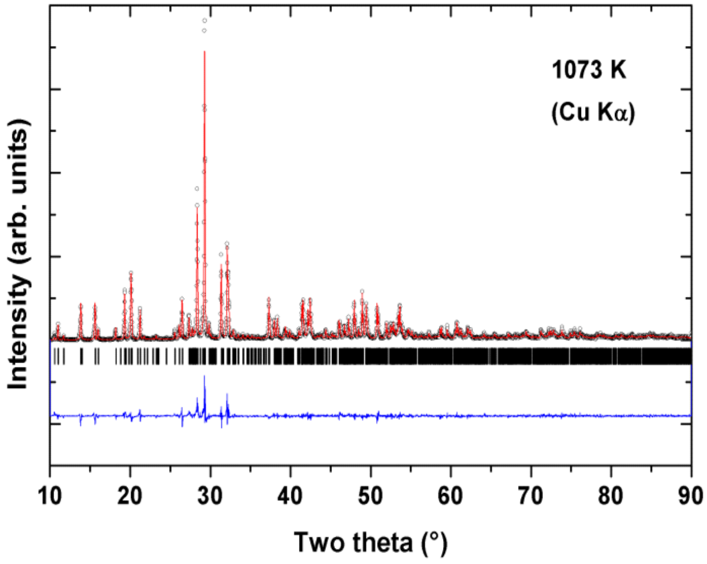

Fig.6.6: Rietveld refinement plot of $K_3Gd_5(PO_4)_6$ at 1073 K

The unit cell parameters and position coordinates of $K_3Gd_5(PO_4)_6$ at successive temperatures were obtained by Rietveld refinement of the XRD data using an initial model based on the refined structural parameters at previous temperature. Similar to the low temperature XRD data, upon increasing temperature up to 1073 K, no drastic change in XRD patterns except a shift in peak positions towards lower angle (2θ) due to thermal expansion is noticed. This suggests no structural transition in $K_3Gd_5(PO_4)_6$ even at higher temperature. Furthermore the structural stability was corroborated by recording simultaneous TG-DTA patterns up to 1273 K. The refined structural parameters at 1073 K are given in Table.6.3 and the final Rietveld refinement plot for the corresponding XRD data is shown in Fig.6.6.

In order to find the effect of temperature on the crystal structure, refined structural parameters at various temperatures are compared. Fig.6.7 shows the temperature variation of the unit cell parameters.

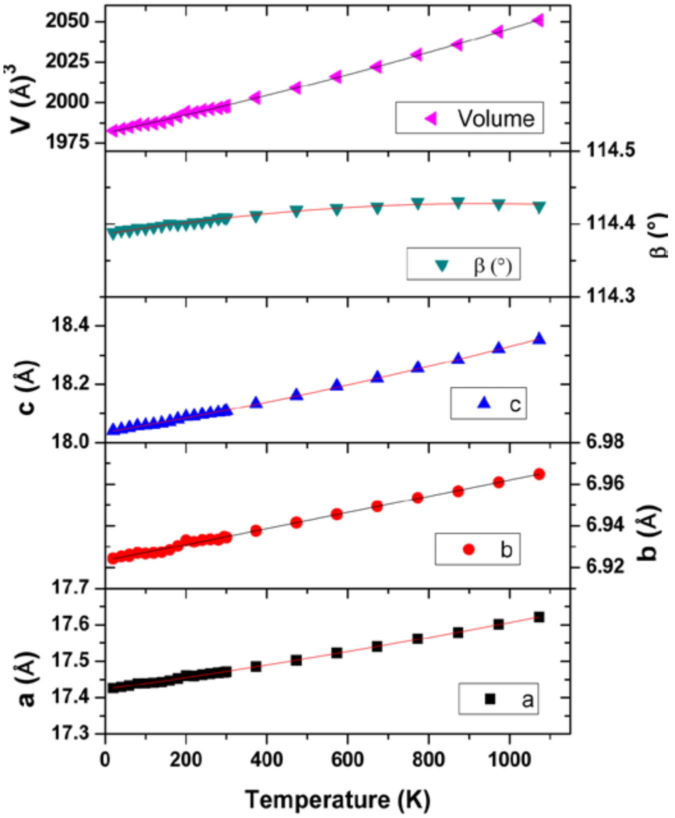

Fig.6.7: Variation of unit cell parameters of $K_3Gd_5(PO_4)_6$ with temperature

It can be seen that the unit cell parameters increase smoothly from 20 to 1073 K. However close to 20 K a deviation from the linearity is noticed but cannot be accounted for any phase transition. Also the monoclinic angle (β) has a tendency to saturate or decreasing trend at higher temperature. Further it is observed that the increases in unit cell parameters are anisotropic with larger expansion along the *a*- and *c*-axes compared to the *b*-axis. The average axial thermal expansion coefficients between 20 and 1073 K are: $\alpha_a = 10.6 \times 10^{-6}$ K^{-1}, $\alpha_b = 5.5 \times 10^{-6}$ K^{-1} and $\alpha_c = 16.4 \times 10^{-6}$ K^{-1}. The temperature dependencies of unit cell parameters were fitted by using 2nd order polynomial functions.

Table 6.3: Refined positional parameters of $K_3Gd_5(PO_4)_6$ at 1073 K

Atom	**Wyc.**	**x**	**y**	**z**	**U(eq) (Å)^2**
Gd1	*4e*	0	0.3669(7)	1/4	0.0268(10)
Gd2	*8f*	0.1446(2)	-0.4132(4)	0.48124(19)	0.0268(10)
Gd3	*8f*	0.2206(2)	0.1245(5)	0.29128(18)	0.0268(10)
K1	*8f*	0.0739(2)	0.9071(5)	0.0748(3)	0.060(5)
K2	*4e*	0	0.8269(8)	1/4	0.060(5)
P1	*8f*	0.1376(3)	0.0897(7)	0.4132(2)	0.022(2)
P2	*8f*	0.2086(3)	0.6238(7)	0.3387(2)	0.022(2)
P3	*8f*	-0.0717(3)	0.3952(6)	0.3808(3)	0.022(2)
O1	*8f*	0.1993(4)	0.7831(8)	0.2739(4)	0.075(4)
O2	*8f*	-0.0957(4)	0.2443(8)	0.3116(3)	0.075(4)
O3	*8f*	0.2307(5)	0.069(3)	0.4223(6)	0.075(4)
O4	*8f*	0.1277(8)	0.2311(10)	0.4723(6)	0.075(4)
O5	*8f*	0.2483(4)	0.6605(14)	0.4307(3)	0.075(4)
O6	*8f*	-0.1385(4)	0.5392(9)	0.3841(4)	0.075(4)
O7	*8f*	-0.0015(4)	0.5242(8)	0.3790(4)	0.075(4)
O8	*8f*	0.0997(4)	-0.0970(7)	0.4325(4)	0.075(4)
O9	*8f*	-0.0444(5)	0.3116(10)	0.4677(3)	0.075(4)
O10	*8f*	0.2722(4)	0.4655(8)	0.3435(5)	0.075(4)
O11	*8f*	0.1187(3)	0.5509(12)	0.3261(4)	0.075(4)
O12	*8f*	0.0893(4)	0.1257(10)	0.3222(3)	0.075(4)

The anisotropy in expansion of $K_3Gd_5(PO_4)_6$ can be related to the polyhedral connections along the <101> which is mainly formed by the edge shared GdO_n (Fig.6.8). It can be recalled that the thermal expansion coefficients of zircon type orthophosphates are also anisotropic where larger expansion along the directions (*a*-axis) of the edge shared LnO_8 polyhedra is observed compared to that along the directions with intervening PO_4 tetrahedra. Due to the rigid nature of the PO_4 polyhedra, the lower thermal expansion along this direction is often observed in zircon type rare-earth phosphates. The average coefficient of volume thermal expansion in the studied temperature range is 32.5×10^{-6} K^{-1}. The temperature dependent unit cell volume could be fitted with Einstein relation $V=V_0+ \varepsilon/(e^{\theta/T}-1)$ where V_0, ε, θ are fitting parameters. The typical fitting parameters are: $V_0 = 1984.0(4)$ Å^3, $\varepsilon = 12.5(1.7)$ and $\theta_E = 187(24)$ K. The observed value of Einstein temperature (θ_E) is comparable for soft ceramic materials [164].

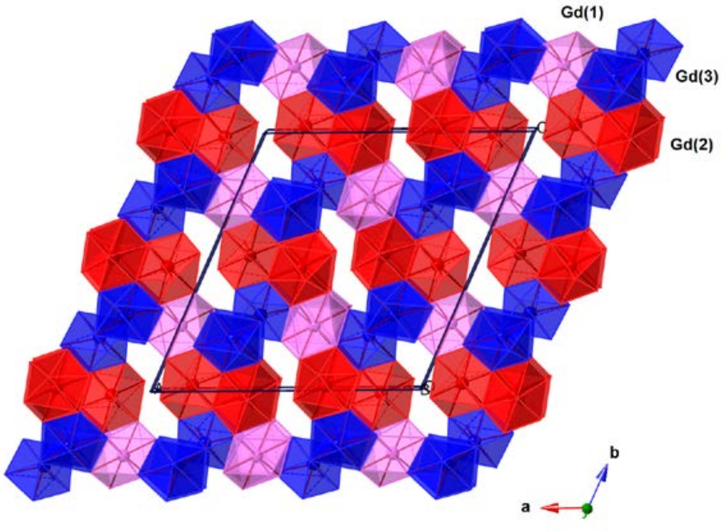

Fig.6.8: Arrangement of GdO_n polyhedra in the structure of $K_3Gd_5(PO_4)_6$. The $Gd1O_8$ (pink), $Gd2O_9$ (red) and $Gd3O_8$ (blue) units are shown

For a better insight into the origin of thermal expansion and the anisotropic expansion behavior, the derived structural parameters are compared. Typical variation of average Gd-O bonds in GdO_n polyhedra and P-O bonds in PO_4 tetrahedra with temperature are shown in Fig.6.9. It can be noticed from the Fig.6.9, that the P-O bonds do not vary appreciably in the studied temperature range as expected from the rigid nature of the PO_4 unit, while the Gd-O bonds, in particular; the Gd1-O and Gd2-O ones expand significantly with temperature. The rigid nature of PO_4 polyhedra unit is further confirmed by Raman results discussed subsequently. This suggests the high temperature structural evolution is mainly controlled by the Gd-O bond length which is due to their soft and ionic natures.

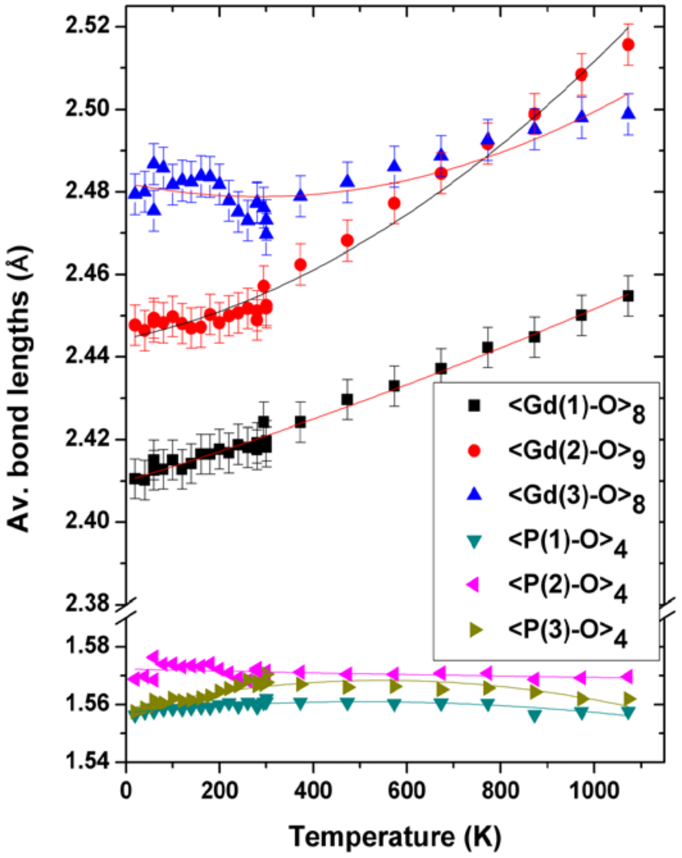

Fig.6.9: Variation of average Gd-O and P-O distances in the structure of $K_3Gd_5(PO_4)_6$ with temperature

The temperature evolutions of polyhedral volumes of PO_4 and GdO_n are shown in Fig.6.10, which also infer similar conclusions on thermal expansions. The temperature evolution of distortion indices of the polyhedra indicates a gradual decreasing trend with increasing temperature, while those of $Gd2O_9$ and $K2O_8$ polyhedra show increasing trend with temperature (Fig.6.11). The increasing distortion in $Gd2O_9$ unit suggests a possible instability in structure at higher temperature. Although, decomposition of this phase at higher temperature can be expected as evidenced in the studies on various reported phases in K-Gd-P-O system [109], TG-DTA studies up to 1273 K and subsequent XRD analysis of the residue indicate no significant change in the phase. Thus it can be concluded that the decomposition temperature may be higher than 1273 K [165].

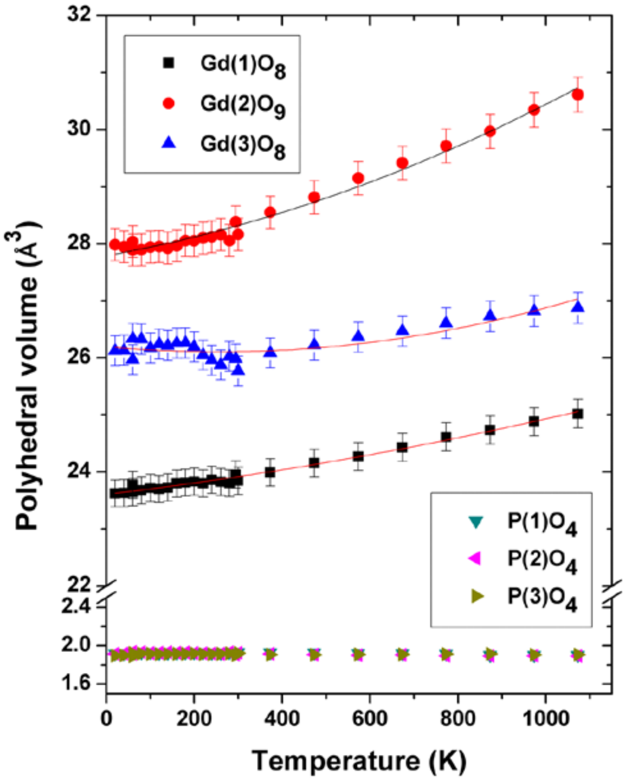

Fig.6.10: Variation of average GdO_n and PO_4 polyhedral volume in the structure of $K_3Gd_5(PO_4)_6$ with temperature

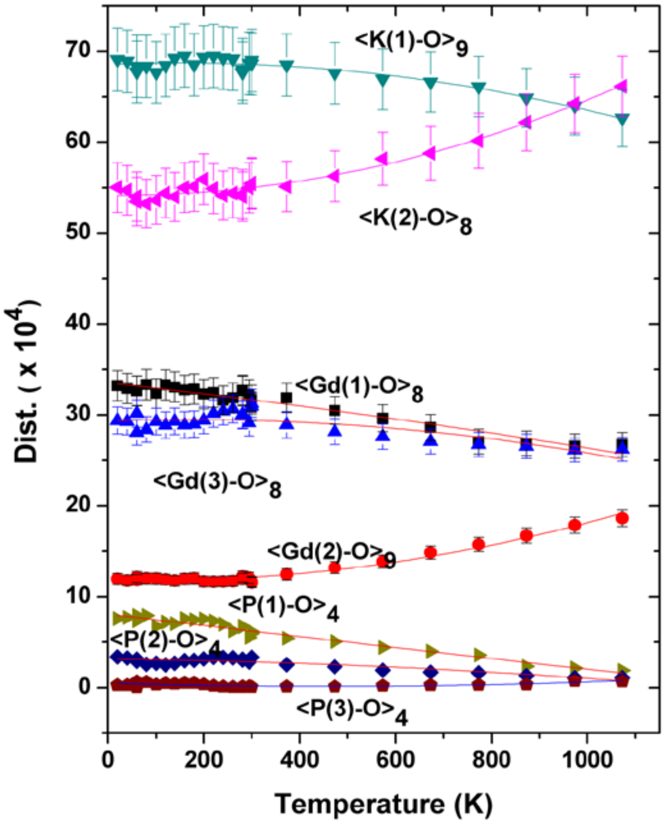

Fig.6.11: Variation of polyhedral distortion in the structure of $K_3Gd_5(PO_4)_6$ with temperature

As mentioned earlier, the K^+ ions are occupied within the tunnels for charge balance reason and thus they are likely to be affected more with temperature. From the structural details, it can be indicated that the K atoms (K1 and K2) are arranged as a wavy chain along the *b*-direction. The analysis of K-O bond lengths indicate that the K1 atoms are coordinated to 9 oxygen atoms while the K2 atoms are coordinated to 8 oxygen atoms within the bond length limit of 2.47 to 3.24 Å. A larger bond dispersion but smaller average bond length is observed around the K1 atoms than K2 atoms. Effectively with increasing temperature, the average K-O bond lengths increase systematically, while only the distortion around the K1 atoms decreases. Similarly, the analysis of bond lengths and distortions around K2 indicate an increasing trend with temperature. However from the variation of bond lengths around K atoms indicates that their coordination polyhedra are relatively stable and maintain the same coordination up to 1000K.

To understand further on the structural variations in $K_3Gd_5(PO_4)_6$ with temperature analogous studies by Raman spectroscopy were carried out. It can be mentioned here that for probing structural change in a materials with respect to any thermodynamic parameters like temperature and pressure, XRD and Raman spectroscopy are often used as complementary techniques [166]. Since Raman spectroscopy is a local probe, it provides information on a microscopic scale and in particular changes in microscopic structures like coordination polyhedral or ionic movement with temperature or pressure.

6.3.4. Raman studies

As mentioned earlier, $K_3Gd_5(PO_4)_6$ crystallizes in a monoclinic structure with space group *C2/c* (C_{2h}^{6}) with two formula units in the primitive unit cell. Therefore, 228 degrees of freedom arise from the 76 atoms in the primitive monoclinic unit cell, out of which 225 are optical degrees of freedom. The Gd1 and K2 occupy the *4e* sites; all other Gd, K, P and O atoms occupy the *8f*-sites. Factor group analysis was carried out using correlation method using their site symmetries [167]. Group theory predicts the total irreducible representation of optical phonon to be $\Gamma_{opt} = 56A_g + 58B_g + 55A_u + 56B_u$ and all 225 modes are non-degenerate. Out of these, 114 Raman active ($56A_g + 58B_g$) and 111 IR-active ($55A_u+56B_u$) modes are expected. As mentioned earlier, the bonds in PO_4 group are strong and the PO_4 group acts as rigid molecular unit. The 180 degrees of freedom corresponding to this rigid molecular unit (PO_4) can be sub-divided into 108 internal ($27A_g+27B_g+27A_u+27B_u$), 36 rigid translations ($9A_g+9B_g+9A_u+9B_u$) and 36 rigid rotational (librational) ($9A_g+9B_g+9A_u+9B_u$) degrees of freedom. Raman spectrum of $K_3Gd_5(PO_4)_6$ at 80 K is shown in Fig.6.12.

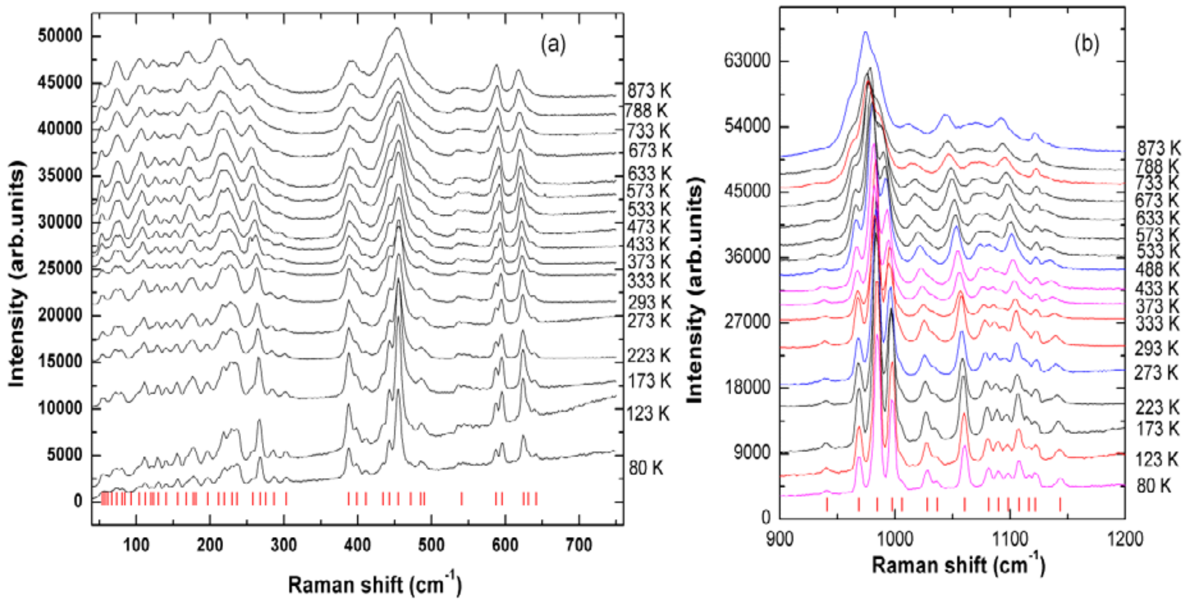

Fig.6.12: Raman spectra of $K_3Gd_5(PO_4)_6$ at different temperatures

A total of 58 distinct Raman modes could be identified in the wavenumber range 50-1200 cm^{-1}. In addition to these modes, a few weak peaks/shoulders can also be seen; however, these weak modes/shoulders do not evolve systematically with temperature. The observation of less number of Raman modes than group theoretical prediction could be due to insufficient intensities resulting from small polarizabilities of several modes [168].The observed mode frequencies of $K_3Gd_5(PO_4)_6$ are assigned by comparison with earlier reported phosphates. The observed spectral features of $K_3Gd_5(PO_4)_6$ are similar to $K_2Ce(PO_4)_2$ [94], $K_4Ce_2P_4O_{15}$ [168] and exhibit no Raman modes between 650-950 cm^{-1}. Unlike $K_2Ce(PO_4)_2$, in the present system the modes at low frequencies are expected below 100 cm^{-1} since Gd is heavier than Ce. As pointed earlier, $K_3Gd_5(PO_4)_6$ consists of an edge/corner-shared network of PO_4 tetrahedra and GdO_n (n = 8, 9) polyhedra, PO_4 tetrahedra are more strongly bound units compared to GdO_n. Therefore, in the Raman spectra of $K_3Gd_5(PO_4)_6$, the internal modes of PO_4 tetrahedral can be identified while those of GdO_n could not be identified. One can expect only the lattice modes associated with Gd translation in the potential well of the surrounding oxygen polyhedra. The internal modes of PO_4 are assigned in the wave number range 380-1200 cm^{-1}. These modes are associated with the vibrations of oxygen ion against the central phosphate ion in the oxygen cage. Several prominent modes observed in the high wavenumber region 940-1150 cm^{-1} are assigned to the stretching mode of PO_4 while the bending modes are observed in 380-640 cm^{-1}. These modes often exhibit merging due to its higher site symmetry and reduction in correlation splitting. Lattice, rigid translation and librational modes of phosphate ion appear in the low wavenumber range 50-380 cm^{-1}.

Raman spectra of $K_3Gd_5(PO_4)_6$ recorded in the complete range of phonon wavenumbers at different temperatures are included in Fig.6.12. On increasing temperature, intensities and wavenumber of most of the Raman modes decreases continuously except the modes at 387, 540 and 1121 cm^{-1} which show abnormal hardening. As expected, several modes show broadening with increasing temperature due to decrease in phonon life time in scattering processes. The nearby modes at 73 and 80 cm^{-1}, 219 and 229 cm^{-1}, 1081 and 1089 cm^{-1} are merge into single broad band around 75, 216 and 1070 cm^{-1}, respectively. Several modes could not survive up to 873 K, which is the highest temperature of the present studies. At 873 K, only 26 Raman modes could be identified. The less number of Raman modes at high temperature is due to insufficient intensity of weak modes. Several modes as mentioned above soften continuously with temperature and no discontinuities in the slope of ω vs T plot are observed Fig.6.13. Furthermore, no signature of appearance of any new Raman mode is noticed in the entire temperature range. It may be mentioned here that any change in crystal symmetry could in principle change the crystal spectral selection rule and they are reflected in spectral features. Such a change in Raman spectral feature is not noticed in this present system. This suggests that the system is stable and does not undergo any structural transition in the studied temperature range as inferred also from the XRD studies. The temperature coefficients $\frac{d\omega}{dT}$ were obtained by linear fits to the ω vs T curve (Fig.6.13).

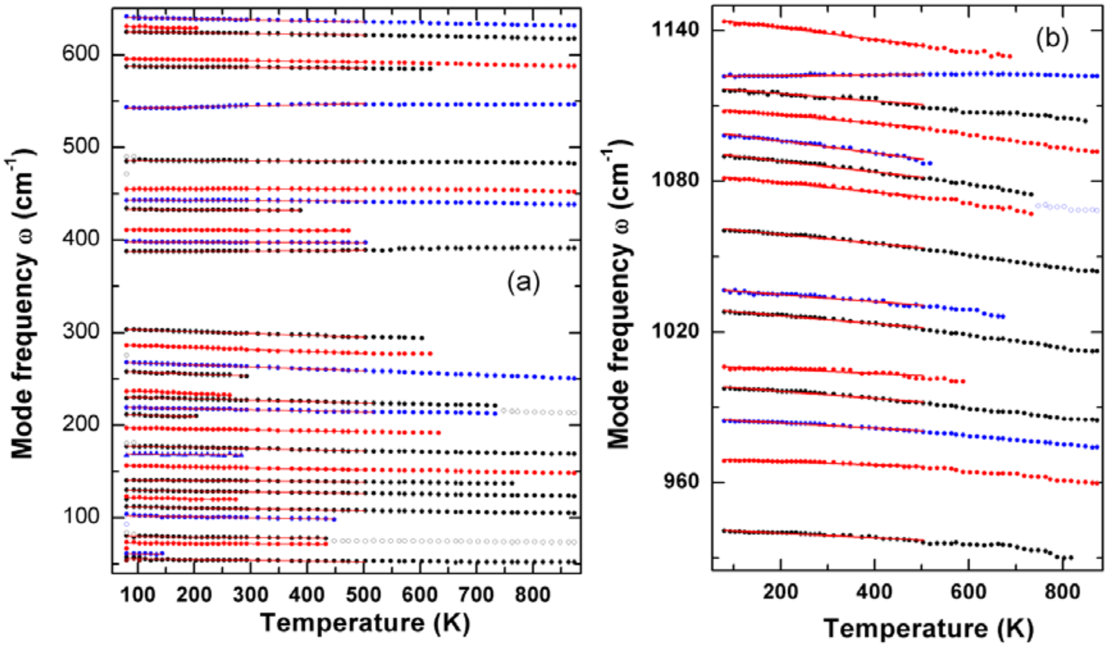

Fig.6.13: Raman mode frequencies of $K_3Gd_5(PO_4)_6$ as a function of temperature

This exercise was performed by using the linear equation $\omega(T) = \omega_0 + \omega' T$, where ω_0 is the mode wavenumber at absolute zero temperature, ω' is the first order temperature coefficient of vibrational mode, to fit the data in lower temperature region (< 500 K). The slope of the fitted curves (ω') represents the temperature coefficients $(\frac{d\omega}{dT})$ of the corresponding mode. The contributions of higher order temperature coefficients are neglected since they are significant only at higher temperatures. The normalized slopes, $\frac{1}{\omega}\frac{d\omega}{dT}$ which essentially represent the total anharmonicity [169] are calculated for all 58 modes observed at 80 K. The variation of Raman mode wavenumber with temperature at constant pressure $\frac{1}{\omega}\frac{d\omega}{dT}$ arises from two effects: one is the contribution from the volume effect or thermal expansion of lattice, (quasi-harmonic) and the other is due to pure temperature effect known as true-anharmonic contribution [170]. Hence, it can be expressed in the form of these two terms: $\frac{1}{\omega_i}\frac{d\omega_i}{dT}\Big|_P = \frac{1}{\omega_i}\frac{d\omega_i}{dT}\Big|_V - \gamma_i\alpha$, where γ_i is the mode Grüneisen parameter and α is the volume thermal expansion coefficient. Here the first term on the right hand side is the true-anharmonic contribution and the second is the pure volume effect. Hence pure temperature effect (true-anharmonicity) on phonon mode can be separated out from the total anharmonicity from the knowledge of γ_i and α. It can be noticed that most of the phonons have negative anharmonicity implying softening of phonons at high temperature. The hardening of those modes at 387, 540 and 1121 cm^{-1} is due to the stiffening of force constant which can occur due to steepening of potential well resulting from their respective ionic vibrations as observed in other systems [171]. It can be noticed that the magnitude of anharmonicity is larger for several low frequency modes (lattice, rigid translation and librational modes), viz., 57, 61, 103, 112, 129, 156, 123, 236, 158, 267, 286 and 303 cm^{-1} in comparison to high frequency internal modes of PO_4 units which suggests they have larger contribution towards thermal expansion. The smaller magnitude of anharmonicity of stretching modes of PO_4 units suggest stronger bonding within the PO_4 tetrahedral units, which are insensitive to temperature compared to flexible low frequency modes. This observation also indicates its covalent nature of bonding and supports the findings of XRD studies.

6.3.5. Magnetic studies

In order to see other physical properties of the materials, the temperature dependent magnetization of $K_3Gd_5(PO_4)_6$ was investigated from ambient to 2 K. Due to clustered arrangements of Gd^{3+} ions, higher and coupled magnetic moment can be expected in this material. However, the typical paramagnetic like magnetization is observed in *M* vs *T* and no hysteresis loop at lowest temperature confirms its paramagnetic nature (Fig.6.14a and b).

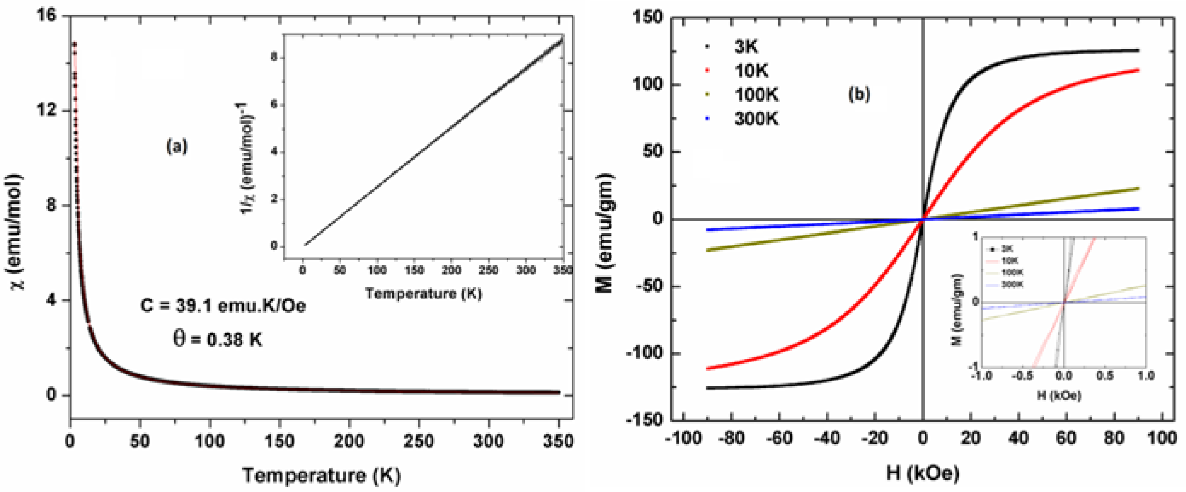

Fig.6.14: (a) Temperature and (b) field dependent magnetization in $K_3Gd_5(PO_4)_6$

The magnetic susceptibility could be fitted well with typical Curie-Weiss relation and the obtained effective magnetic moment per Gd^{3+} ion is 7.91 μ_B and Weiss constant is 0.38 K. The observed effective moment is similar to free ion moment of Gd^{3+} which suggests no magnetic interaction among the Gd^{3+} ions. It may be mentioned here that the monoclinic monazite type $GdPO_4$ has an antiferromagnetic interaction below 0.8 K. From the structural analysis it is observed that the typical shortest inter-atomic distances of Gd^{3+} ions in $K_3Gd_5(PO_4)_6$ are in the range of 3.96 Å (Gd1-Gd3) and 4.19 Å (Gd2-Gd2) while the inter-atomic separation between the Gd^{3+} ions in $GdPO_4$ are about 4.00 Å [172]**.** Thus the inter-atomic separation and the network connection of GdO_n polyhedra in $GdPO_4$ and $K_3Gd_5(PO_4)_6$ suggest a closely similar magnetic properties in both of them. A comparison of typical distances between Gd^{3+} ions of the present studied material and that reported in $GdPO_4$ suggests that such interaction in $K_3Gd_5(PO_4)_6$ may be observed at still lower temperature. However, the observed positive Weiss constant suggests that the interaction is ferromagnetic instead of antiferromagnetic as in $GdPO_4$ [173]. Almost similar magnetic behavior as free ion magnetic moment with positive Weiss constant is reported in GdF_3. From the magnetic hysteresis loops, it can also be noticed that at lower temperature magnetization increases sharply as a case of superparamagnetic materials and tends to saturate at field above 20 kOe. However almost no coercive field and remanent magnetization are observed at any temperature down to 3 K which suggests for a superparamagnetic behavior of $K_3Gd_5(PO_4)_6$. The larger saturation magnetization at relatively lower applied field is in contrast to $GdPO_4$ may be due to clustered units of GdO_n polyhedra. The superparamagnetic like behavior and positive Weiss constant may be attributed to the possible ferromagnetic like ground state of $K_3Gd_5(PO_4)_6$ at lower temperature.

As seen from the structural features and temperature dependent structural evolutions, the K^+ ions provide charge neutrality to the anionic frame of unit cell. Thus it can be expected that the K^+ ions in $K_3Gd_5(PO_4)_6$ can be exchanged by other ions. In order to observe any possible ion exchange properties in this, weighed quantity of the material is equilibrated with aqueous solution of radioactive Sr^{2+} ions (^{85}Sr) and the decrease in activity of filtered solution were analyzed radiometrically. The distribution constant (K_d) estimated from the initial and final activity is significantly low (Kd ~ 5). This suggests that the K^+ ions are not strictly exchangeable with Sr^{2+} ions. An analogous study is carried out by using non-radioactive Sr^{2+} solution. The solid residue isolated from this solution was analyzed by ICP for detection of strontium in it. The presence of Sr^{2+} ion in the solid residue confirms incorporation of only feeble amount of Sr^{2+} ion. Thus it could be concluded that only a small amount of K^+ ions are exchanged by Sr^{2+} ions. This might be due to stronger bonding of the K^+ ions with the anion frame or the wavy arrangement of K^+ ions in the tunnels where the motion of the ions are restricted by the adjacent ions. From the present structural investigation, an increasing trend for amplitudes of vibration parameters of K^+ is observed. Although anisotropic displacement parameters could be of some help to understand the possible motion of K^+ ions, due to the limitation of the powder XRD they could not be obtained. To understand the motion of K^+ ions more detailed study on diffusion aspects is required.

6.4. Conclusions

A complex phosphate, $K_3Gd_5(PO_4)_6$, is prepared by solid state reaction and characterized in detail by X-ray diffraction in a wide temperature range from 20 to 1073K and by Raman spectroscopy in the temperature range of 77 to 873 K. The material is found to be stable in the studied temperature range. The temperature evolution of the unit cell parameters is anisotropic with larger expansion along the *a*- and *c*-axes compared to the *b*-axis. The temperature evolution of distortion indices of the polyhedra except $Gd2O_9$ and $K2O_8$ polyhedra indicates a gradual decreasing trend with increasing temperature suggesting symmetrization in the coordination polyhedra. Both thermal expansion and its anisotropy are largely controlled by the temperature effect on the GdO_n polyhedra and their linkages. The temperature dependent Raman spectroscopic studies also indicated no structural change. The intensities of most of the Raman modes decrease and their line widths increase at elevated temperature due to enhanced phonon scattering. Several mode positions show softening with increasing temperature whereas a few Raman modes at 387, 540 and 1121 cm^{-1} show abnormal hardening with temperature. In addition to the lattice modes, several external modes of PO_4 rigid unit are found to be strongly anharmonic. The temperature and field dependent magnetic measurements indicated no long range ordering down to 2K. The field dependent magnetization and saturation at lower temperature suggests the superparamagnetic nature of the sample. The compound does not show appreciable exchange of K^+ ions with Sr^{2+} indicating the K^+ ions are held tightly in the structure. Thermal stability of the material in a wide range of temperature signifies that $K_3Gd_5(PO_4)_6$ is a promising lattice for immobilization of nuclear waste.

Chapter 7

Pressure and temperature dependent structure properties of $K_2Fe_2Ti_6O_{16}$

7.1. Introduction

Hollandite type materials, in particular manganite or titanates are observed in nature and they possess significant structural stabilities under geological conditions. Silicates with hollandite type structure are also known to occur in lower mantle region of earth or in similar conditions. Weathering of the hollandite type minerals under geological condition often resulted in wide varieties of compositions with diversified monovalent cations like alkali and divalent cations like alkaline earth and Pb^{2+} cations [174]. Thus hollandite ($A_xB_8O_{16}$, where B are cations suitable for octahedral coordination and A are larger cations, like Cs, Ba etc.) type materials are considered as a component phase in the *Synroc* ensemble to immobilize radioactive Cs^+ and Ba^{2+} produced in nuclear reactor. Besides, hollandite type materials show promising interest for various physical and chemical properties. Spin transition and Mott-Peierls transitions have been reported in several transition metal containing hollandites. Hollandite type materials with smaller cations exhibit fast cation conduction due to the free motion of ions in the channels [173, 175].

Ideally the hollandite type structures are formed by rutile like edge and corner sharing of octahedral BO_6 units. The typical connections of BO_6 octahedra lead to 1-D tunnel like empty spaces and the larger A cations are filled in these empty spaces. In Hollandite structure, the walls of the channels are formed by two octahedra (2 × 2) while other closely related structures are formed with higher number of octahedra in the walls [176]. In particular the titanate hollandites are observed with a wider range of compositions $A_x(Ti,B)_8O_{16}$, where A = Na^+, K^+, Rb^+, Cs^+, Sr^{2+}, Ba^{2+} and B =Mg^{2+}, Al^{3+}, Ga^{3+}, etc. and transition metal ions. Thermophysical properties and structural transitions of some of the hollandite and related materials have been reported in literature [177]. It has been observed that the structure of

Hollandite is sensitive to the concentration as well as ionic radii of the A^+ ions as well as oxygen stoichiometry. Most commonly for A = K^+, Rb^+ and Cs^+, tetragonal (I4/m) structure with 2 × 2 channels is observed while for smaller ions like Na^+ and Li^+ other low symmetric structures like tetragonal super structures, orthorhombic, monoclinic etc. are observed [177-178].

As mentioned the ionic radii of the interstitial cations play significant role in governing the structure and smaller the size of cations low symmetric structures are formed. Incorporation of smaller cations in the channel of tetragonal hollandites displace the octahedral units and then transform it to lower symmetric structures by destroying the four fold symmetry of the original lattice. Such structural differences are clearly observed in Na^+ and K^+ containing hollandite type ferrotitanates and aluminotitanate compositions [178b]. Ba^{2+} substituted Cs^+ hollandites also show transition from tetragonal to monoclinic structure beyond certain concentration of Cs^+ ions. $Ba_xTi_8O_{16+x}$ also show structural transition with the variation of Ba^{2+} ion concentrations. The distorted structures formed due to the chemical pressure induced displacement of cations of the octahedral units are relaxed with increasing temperature [177]. Low temperature studies on Fe containing titanates, like $A_2Fe_2Ti_6O_{16}$, A = K^+ show specific heat anomaly at around 50 K, which the authors have attributed to a possible structural transition. However, due to lack of structural information at lower temperature, this transition remains as unexplained. Electronic or magnetic transitions at lower temperature have been reported in transition metal ion containing tetragonal as well as orthorhombic hollandites. However, no low temperature structural transition or specific heat anomaly has been observed in hollandite type $KAlSi_3O_8$ [179]. It can be mentioned here that the external thermodynamic parameters like pressure and temperature plays opposite roles on the structure. Effect of pressure and temperature on such materials is useful to understand their crystal chemistry than the studies by chemical substitutions. It can be expected that pressure can introduce strain and distortion similar to those caused by the chemical substitution. Besides, pressure can lead to structural transition, decomposition or amorphization in materials depending on the crystal structure and composition of the system. Several studies indicating pressure induced structural transition due to the anisotropic elastic properties or collapsing of loosely packed structure to denser or amorphous phases have been reported in literatures [180]. Thus loosely packed and framework type materials are expected to show structural transition or amorphization under compression. As the unit cell of tetragonal hollandite type $K_2Fe_2Ti_6O_{16}$ has large fractions of empty spaces (about 46 %), diversified crystal chemistry can be expected under pressure or temperature.

In order to understand the structural stabilities of $K_2Fe_2Ti_6O_{16}$ with pressure and temperature, *in situ* high pressure XRD studies in DAC and variable temperature X-ray and neutron diffraction studies were carried out. It is observed that at moderate pressure (~ 3 GPa), the tetragonal structure reversibly transforms to a monoclinic structure with large increase in structural distortions. Evolutions of crystal structures and compressibility behaviors have also been investigated. Temperature dependent studies indicated no structural transition in a wider range of temperatures (6 - 1273 K) and nearly isotropic expansion in the tetragonal $K_2Fe_2Ti_6O_{16}$. The evolutions of structure and pressure-volume equation of states are explained in the following sections.

7.2. Experimental methods

Polycrystalline sample of $K_2Fe_2Ti_6O_{16}$ was prepared by solid state reaction of K_2CO_3, Fe_2O_3 and TiO_2. In order to remove any adsorbed moisture or OH groups, Fe_2O_3 and TiO_2

were preheated overnight at around 300°C and 800°C, respectively. K_2CO_3 was heated at around 200°C just before weighing. Weighed quantities of K_2CO_3, Fe_2O_3 and TiO_2 (molar ratio 1.1:1:6) were thoroughly mixed in an acetone medium and then dried in air. The dry mixture of reactants was pelletized and heated at progressively increasing temperature viz. 500°C/12h, 800/12h and 1250°C/12h with intermittent grindings. The products obtained after heating at 1250°C for 12h was characterized by powder XRD and used in this study.

$$K_2CO_3 + Fe_2O_3 + 6TiO_2 \longrightarrow K_2Fe_2Ti_6O_{16} + CO_2$$

Regular and nearly spherical grain of the powder along with few particles of gold (pressure marker) were loaded into a 100 μm hole of a pre-indented tungsten gasket of thickness ~ 40 μm in a modified Mao-Bell kind of diamond anvil cell. The tungsten gasket transmit the scattered X-ray only through the sample hole and hence effectively reduce the background and significantly improve signal to noise ratio. Methanol:ethanol (4:1) mixture was used as pressure transmitting medium (PTM) and the pressure was determined from the equation of state of gold. To ensure that the sample experiences hydrostatic or quasi hydrostatic pressure conditions at higher pressure, very little amount of sample was filled into the gasket hole. These experiments were carried out at the BL11 beamline of the INDUS-2 synchrotron source using the X-rays of wavelength 0.5026 Å up to pressures 31 GPa with increasing and decreasing pressure. The data was collected with the help of a two dimensional imaging plate detector MAR345. CeO_2 was used to determine the sample to detector distance (230 mm) and also to calibrate the imaging plate detector. The two dimensional diffraction images were converted to one dimensional diffraction patterns using the *FIT2D software* [181].

About 4g of powder sample was filled in a thin platinum tube and sealed for high temperature neutron diffraction studies. The neutron diffraction data were collected with a linear 5-PSD based Debye-Scherrer type powder diffractometer (PD-2) at 100 MW Dhruva Research Reactor, BARC, Mumbai using beams of monochromatic (λ = 1.2443 Å) neutrons. The sealed platinum tube was placed inside a vanadium tube under high vacuum. This vanadium container was placed inside ILL type high-temperature furnace with a dynamic vacuum better than 10^{-6} mbar.

Eight cylindrical vanadium foils were used as heating element and heat shield to maintain uniformity of the temperature across the sample. The sample temperature is raised to a desired temperature and equilibrated for 1h and then the diffraction data were collected. The diffraction data at each temperature were accumulated over a period of 8h. The scattered signals were corrected for the contribution of platinum and empty furnace background. About 6 g of finely ground sample of $K_2Fe_2Ti_6O_{16}$ was filled in a vanadium can and capped for low temperature neutron diffraction studies. For low temperature study, the vanadium can filled with sample was placed inside a CCR based cryostat. The sample was cooled to lowest temperature, i.e. 6K and allowed to equilibrate for 6 h before data collection. The sample was heated inside the cryostat to a desired temperature and again equilibrated for 1 h prior to the collection of diffraction data. High temperature XRD data were collected by using CuKα radiation on a rotating anode based X-ray diffractometer (Rigaku, Japan). The structural analysis and refinements of all the temperature and pressure dependent diffraction data were performed by using *Fullprof-2000 package* [96].

7.3. Results and discussion

7.3.1. X-ray diffraction studies

The powder XRD pattern of the dark brown color product shows intense reflections attributable to tetragonal hollandite type $K_2Fe_2Ti_6O_{16}$ reported earlier in literature [178a]. However few weak additional reflections at two-theta around 11.3, 24.0, 29.0, 34.2, 38.9° etc. observed in the XRD pattern could not be accounted by the tetragonal hollandite type phase. The analysis of these peak positions suggest that they belong to a layered lepidocrocite type phase [182]. The formation of such layered phase has been investigated in several studies and they indicate that the composition as well as temperature of reaction have significant role on their formation. The K rich compositions are primarily formed at lower temperature and on decomposition they transforms to piredite or hollandite type $K_x(Fe/Ti)_8O_{16}$ compositions at higher temperature. A slight K-excess lepidocrocite type phase observed as secondary phase in the sample is found to be stable up to 1250°C, the maximum temperature of preparation. The composition of such lepidocrocite (FeOOH type) or α or α′ phases have needle or plate type habits and crystallize in either body centered or C-centred lattices [183]. All the extra reflections could be assigned to the reported C-centered orthorhombic phase of $K_xFe_{2+y}Ti_{6-x}O_{16}$.

The ambient temperature XRD pattern was analyzed by Rietveld refinement using the structural data of tetragonal (I4/m) hollandite type phase and Cmcm (α-phase, $K_xFe_2Ti_6O_{16}$ [183]) phase as model parameters. The complete powder XRD pattern could be successfully refined by considering these two phases and the refined unit cell parameters are: a = 10.1258(1) Å, c = 2.9778(1) Å, V = 305.31(1) Å^3, for tetragonal $K_2Fe_2Ti_6O_{16}$ phase and a =

3.8051(8) Å, b = 15.771(3) Å, c = 2.9688(8) Å, V = 178.16(7) Å^3 for orthorhombic (Cmcm) $K_xFe_2Ti_6O_{16}$ with x ~ 1.2 phase. Typical Rietveld refinement plot for the ambient condition powder XRD data is shown in Fig.7.1.

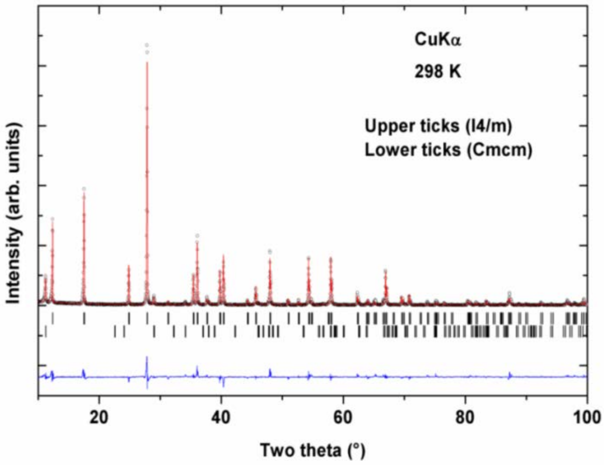

Fig.7.1: Rietveld refinement of XRD data of $K_2Fe_2Ti_6O_{16}$ at 298 K

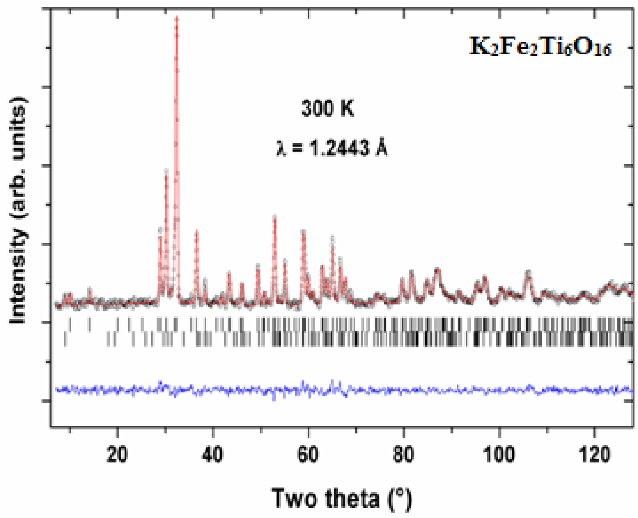

Fig.7.2: Rietveld refinement plot of powder neutron diffraction data of $K_2Fe_2Ti_6O_{16}$

Further characterization of the structure has been carried out from the powder neutron diffraction data recorded at 300 K. The powder neutron diffraction data was refined by considering the identified phase in a similar manner as in the case of XRD data. The refined unit cell parameters of the hollandite type phase are a = 10.1241(5) Å, c = 2.9791(2) Å, V =

305.35(3) Å^3 and they are in good agreement with those observed from XRD studies. The final Rietveld refinement plot of the powder neutron diffraction data recorded at 300 K is shown in Fig.7.2.

7.3.2. Neutron diffraction studies

The refined structural parameters of tetragonal $K_2Fe_2Ti_6O_{16}$ phase as observed from powder neutron diffraction data are given in Table 7.1.

Table 7.1: Refined structural parameters of $K_2Fe_2Ti_6O_{16}$ at 300K

Atom	*wyc*	x	y	z	Occ.
K1	*2a*	0.0000	0.0000	0.0000	1
Ti1:Fe1	*8h*	0.3376(4)	0.1500(3)	0.0000	0.75:25
O1	*8h*	0.0424(2)	0.3371(4)	0.0000	1
O2	*8h*	0.2968(3)	0.3426(3)	0.0000	1

The quantitative estimation of the hollandite type phase as observed from the Rietveld refinement is about 85(1) wt %. Both Ti and Fe are statistically occupied in *8c* sites and the K^+ ions are considered in *2a* sites. The typical inter-atomic distances in the octahedral BO_6 (where B = 0.75Ti+0.25Fe) units are: B-O1 =1.948(5) Å, B-O1 = 1.927(3) Å × 2, B-O2 = 1.993(4) Å, B-O2 = 2.019(3) Å × 2. From the dispersion of bond lengths, the distortion in the octahedral BO_6 unit is found to be 4.090×10^{-4}. This suggests that a nearly regular octahedron is formed around the B^{n+} ions. The temperature and pressure dependent structural studies were carried out by using the refined structural parameters from powder neutron diffraction data as model structure. As mentioned earlier, the habits of the hollandite and α-phase are different, hollandite phase can be discriminated easily under microscope and tiny grains of hollandite phase was separated and used for studying under high pressure while the bulk sample containing both phases were used for temperature dependent studies and they are explained below.

7.3.3. High pressure studies

Typical XRD patterns of the sample recorded in DAC at different pressures in both up and down stroke are shown in Fig.7.3. The data recorded at the lowest pressure in DAC show only reflections due to the tetragonal hollandite type phases. However no reflections due to the layered α-phase indicate that the selected grains belong to tetragonal hollandite type phase. Additional reflections due to ‘Au’ which is used as pressure marker and W, used as gaskets are observed in the diffractions data. The analysis of the XRD data was carried out by considering all these three phases. The Rietveld refinements were carried out by considering the unit cell and structural parameters observed in ambient condition. It may be noted here that only one thermal parameter (overall thermal parameters) was used in the refinement. The background was modeled by linear interpolation of selected points to create a smoothly varying profile for background. The peak profile was generated by *pseudo*-Voigt profile function. The refined unit cell and position coordinates observed at 0.4 GPa are summarized in Table 7.2. The final Rietveld refinement plot for the corresponding XRD data is shown in Fig. 7.4a. A comparison of the XRD patterns recorded at different pressure (Fig. 7.3) shows a distinct difference in the pattern recorded at pressure 3.8 GPa compared to that recorded at 1.6 GPa.

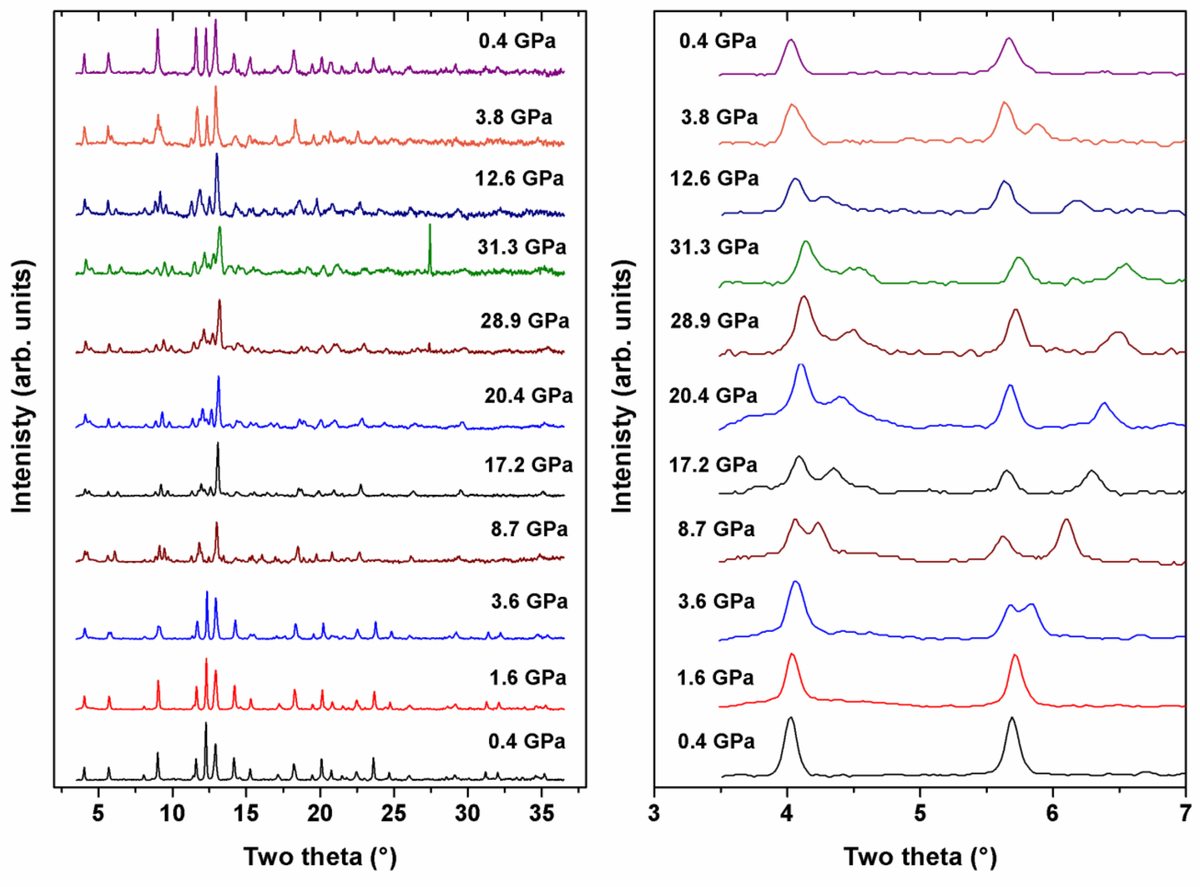

Fig.7.3: Powder XRD pattern of $K_2Fe_2Ti_6O_{16}$ at different pressures, λ is 0.5026 Å

Table 7.2: Structural parameters of tetragonal $K_2Fe_2Ti_6O_{16}$ at 0.4 GPa

Atom	*wyc*	x	y	z	Occ.
K1	*2a*	0.0000	0.0000	0.0000	1
Ti1/Fe1	*8h*	0.341(7)	0.158(7)	0.0000	0.75:0.25
O1	*8h*	0.038(11)	0.343(5)	0.0000	1
O2	*8h*	0.296(9)	0.334(10)	0.0000	1

The typical features like splitting of peaks, broadening of some peaks as well as appearance of new peaks are in accordance with a possible structural transition around this pressure. Further it can be seen that all the intense peaks are observed at almost similar positions as those observed in the ambient pressure tetragonal phase. This indicates that the transition is displacive-type and occurs without much alteration in the original structure. Well defined peaks of the transformed phase could be observed at higher pressure (~ 8.7 GPa). Further comparison of the evolution of the peaks shows the separation of splitting of peaks increases with pressure and positions of some of the peaks shift faster to higher angles compared to others which suggests appreciable anisotropy in the compression behavior and this aspect is further discussed in subsequent sections. In order to deduce the structure of the transformed phases, analysis of the XRD pattern recorded at 8.7 GPa pressure was carried out. A comparison of the splitting and relative intensity of the peaks indicates a monoclinic hollandite type structure for the high pressure phases. Further all the observed peaks of the transformed phase could be indexed on a monoclinic (I2/m) lattice similar to those reported for $Ba_{2-x}Mn_8O_{16}$ type phases [184]. The unit cell parameters of the monoclinic (I2/m) structure are closely related to those of original tetragonal (I4/m) structure and they can be related as $a_m \sim a_t$, $b_m \sim c_t$ and $c_m \sim b_t$ and $\beta \sim 90°$. The refinement of the observed XRD data was carried out in a similar manner as that of the lower pressure. The position coordinates of $Ba_{2-x}Mn_8O_{16}$ were used as initial model parameters.

The position for K atoms in hollandite structure is sensitive to the external thermodynamic conditions, like pressure as well as temperature and is often displaced from the special position. The structural analysis of monoclinic hollandite structure suggests for anisotropic displacement of K atoms and displaces predominantly along the *c*-axis of tetragonal lattice. The complete XRD pattern could be refined considering this monoclinic phase, Au and W. The final Rietveld refinement plot for the XRD data recorded at 8.7 GPa is shown in Fig. 7.4. The refined position coordinates for the high pressure monoclinic structure are given in Table 7.3.

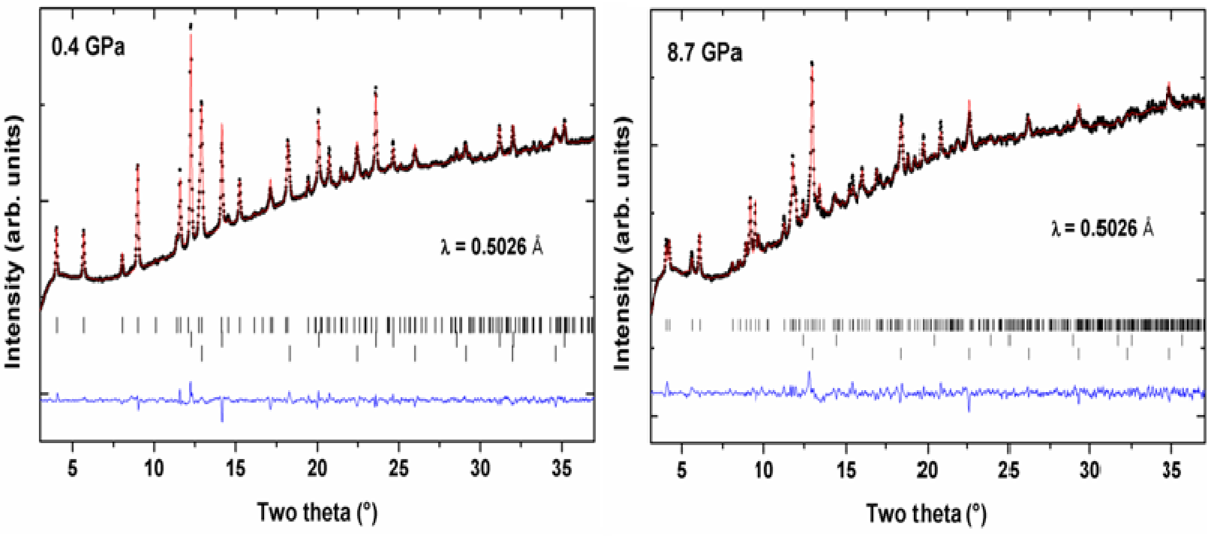

Fig.7.4: Rietveld refinement plots of $K_2Fe_2Ti_6O_{16}$ at 0.4 GPa and 8.7 GPa

Table 7.3: Structure parameters of high pressure monoclinic $K_2Fe_2Ti_6O_{16}$ at 8.7 GPa

Atoms	*Wyc*	**x**	**y**	**z**	**Occ**
K	*4g*	0.00000	0.43(7)	0.0000	0.5
Fe1:Ti1	*4i*	0.161(6)	0.0000	0.341(8)	0.25:0.75
Fe2:Ti2	*4i*	0.357(8)	0.0000	-0.167(6)	0.25:0.75
O1	*4i*	0.214(16)	0.0000	0.142(16)	1
O2	*4i*	0.164(17)	0.0000	-0.203(17)	1
O3	*4i*	0.135(14)	0.0000	0.524(16)	1
O4	*4i*	0.530(14)	0.0000	-0.204(17)	1

The analyses of the structures of ambient and high pressure phases indicate that both structures are closely similar to each other and occur through a feeble distortion in the octahedral walls. The B^{n+} cation sites split into two sets of sites and thus the four fold rotation axis of I4/m structure is transformed to a 2-fold rotation axis with the monoclinic angle (β) ~ 90°. Such structural transition in hollandite type structures is of ferroelastic nature and observed earlier with temperature, pressure as well as compositions [180]. Typical crystal structures showing the octahedral frame of BO_6 in the ambient and high pressure phases are shown in Fig.7.5.

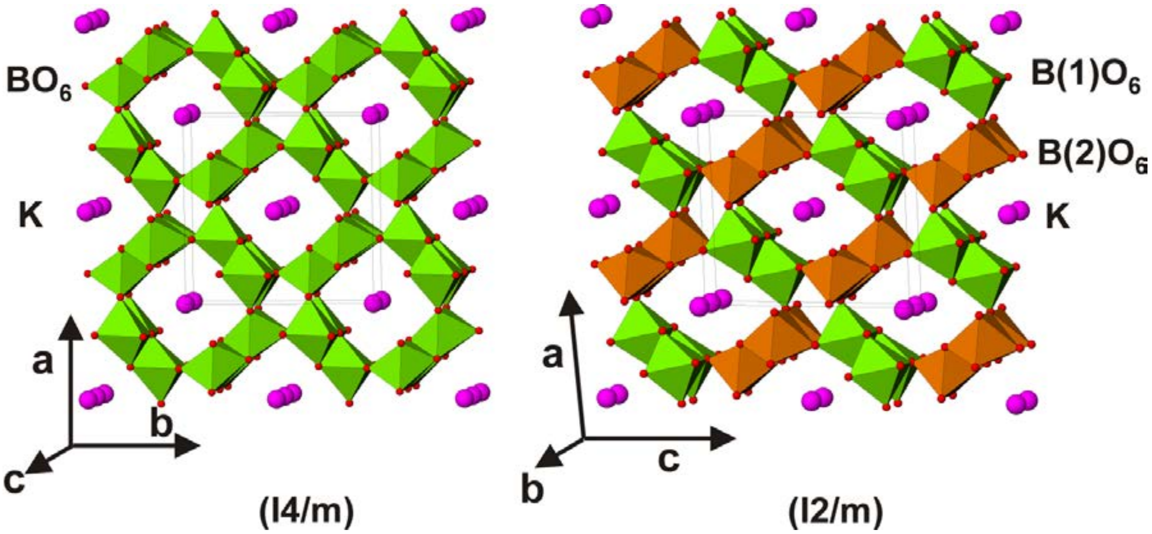

Fig.7.5: Crystal structures of tetragonal and monoclinic $K_2Fe_2Ti_6O_{16}$

The basic arrangements of the octahedral units in 2 × 2 hollandite tunnel as well as 1 × 1 rutile tunnels are also closely similar. The shift in the positions of B^{n+} cations and the distortion in the octahedral units deform the regular tunnels and thus lower the symmetry. In general, the deformation of the hollandite structures can be observed from the diameter of the tunnels, or by comparing the shortest distance of the oxygen atoms in the tunnels. It is observed that the deformation distort the tunnels which can be noticed from the original bond distances of cubical KO_8 (O1-O1 (7.01 Å) and O2-O2 (5.32 Å) of ambient pressure phase and those of high pressure phase (viz. O1-O1 (5.03 Å), O2-O2 (5.21 Å), O3-O3 (7.51 Å) and O4-O4 (5.60 Å)) (Fig.7.6). This dispersion is originated from the rotations and deformations of octahedral BO_6 units. The typical distortion (D) in the octahedral units at 0.4 GPa are 12.53×10^{-4} and average B-O bond lengths are 1.96 Å, while those in the monoclinic phase at 8.7 GPa are <B1-O> 1.95 Å and <B2-O> 1.94 Å and D = 20.28×10^{-4} and 10.29×10^{-4}. The decreases in octahedral bond lengths are only noticeable in both the octahedra. The deformation is also reflected in increasing coordination around the K^+ ions, i.e. the regular cubes (KO_8) of tetragonal phase transform to ten coordinated (bi-capped cube, KO_{10}) polyhedra in monoclinic phase.

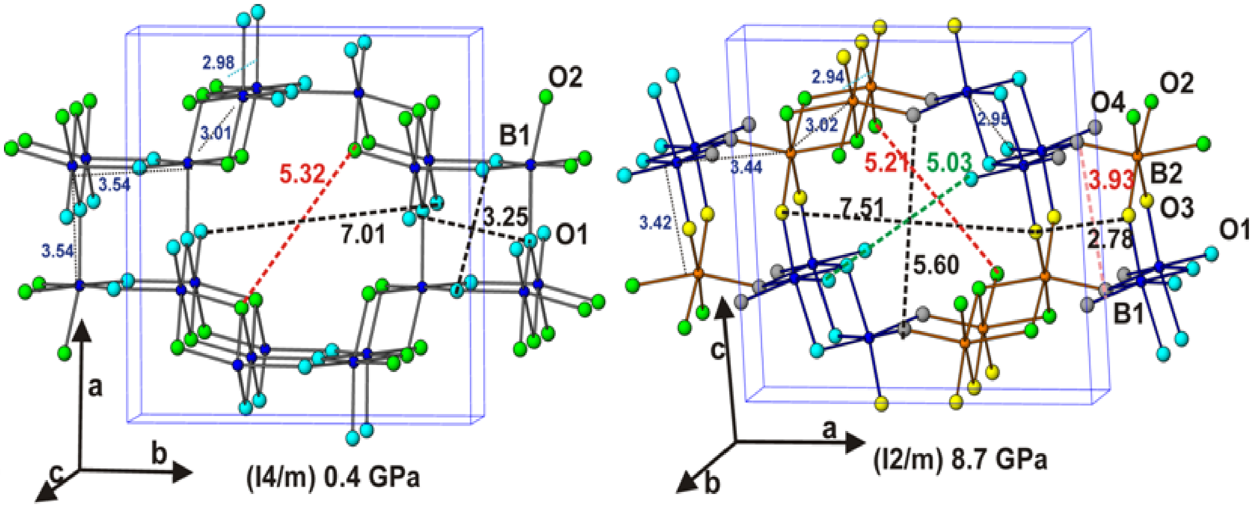

Fig.7.6: Typical 2 × 2 and 1 × 1 tunnel formed by BO_6 octahedra in the tetragonal and monoclinic structures of $K_2Fe_2Ti_6O_{16}$ are shown

In the tetragonal phase, the K atoms are surrounded by O2 atoms of BO_6 octahedra forming a regular cube. The typical K-O2 distances in the KO_8 of tetragonal phase are 3.08(8) Å (at 0.4 GPa). As the structural distortion occurs, the KO_8 becomes distorted and two additional oxygen atoms from the octahedral MO_6 become closer to K and thus form

KO_{10} polyhedra in monoclinic phase. Typical K-O bonds in the monoclinic phase are K-O1 = 2.82(17) Å ×2, K-O1 = 3.02(17) Å ×2, K-O2 = 2.90(18) Å ×2, K-O4 = 2.81(16) Å ×2, K-O4 = 3.10(18) Å ×2, and K-O3 = 3.76(15) Å ×2.

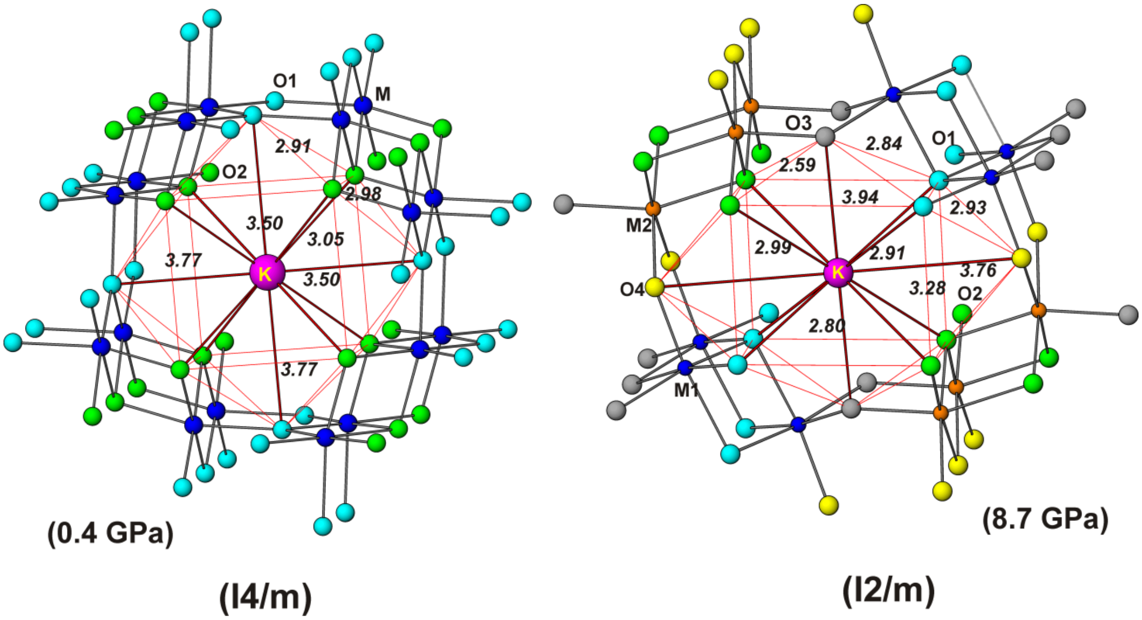

Fig.7.7: Typical surroundings of K^+ ions in tetragonal (at 0.4 GPa) and high pressure monoclinic phase (at 8.7 GPa)

The typical surroundings of K^+ ions in KO_n (n = 8 and 10, within the limit of 3.1 Å) polyhedra in the 2 x 2 tunnel of tetragonal and monoclinic phases are shown in Fig.7.7 and Table 7.4. From the bond length dispersions, the distortions (D) around the K in KO_8 of the tetragonal (0.4 GPa) and monoclinic (8.7 GPa) phases are 0.002×10^{-4} and 8.96×10^{-4}, respectively. The average K-O bond lengths in KO_8 decreases from 3.05 Å to 2.89 Å on increasing pressure from 0.4 to 8.7 GPa. Considering the additional two K-O4 bonds, the distortion in the KO_{10} (average bond length 2.93(5) Å) of the high pressure phase is 15.33×10^{-4}. This suggests that the tunnel formed in the 2 × 2 hollandite distorts appreciably with increasing pressure.

Table 7.4: Typical atomic distances (Å) in tetragonal (at 0.4 GPa) and monoclinic (at 8.7 GPa) of $K_2Fe_2Ti_6O_{16}$

0.4 GPa		**8.7 GPa**	
K1-O2	3.0502(832)	K1-O1	2.8156(1682)
K1-O2	3.0502(832)	K1-O1	3.0221(1736)
K1-O2	3.0502(850)	K1-O1	2.8156(1682)
K1-O2	3.0502(850)	K1-O1	3.0221(1736)
K1-O2	3.0502(832)	K1-O2	2.8957(1776)
K1-O2:	3.0502(832)	K1-O2	2.8957(1776)
K1-O2	3.0502(850)	K1-O4	2.8070(1602)
K1-O2:	3.0502(850)	K1-O4	2.8070(1602)
Average distance	3.0502(297)	Average distance	2.8851(601)
Distortion	0.002 xE-04	Distortion	8.955 xE-04
		K1-O2	3.0969(1813)
		K1-O2	3.0969(1813)
		Average distance	2.9274(545)
		Distortion	15.327 xE-04
Ti1-O1	1.9846(871)	Ti1-O1	1.9805(1718)
Ti1-O1	1.9340(843)	Ti1-O1	1.9490(1146)
Ti1-O1	1.9340(843)	Ti1-O1	1.9490(1146)
Ti1-O2	1.8366(1231)	Ti1-O3	1.7613(1698)
Ti1-O2	2.0290(785)	Ti1-O4	2.0203(1070)
Ti1-O2	2.0290(785)	Ti1-O4	2.0203(1070)
Average distance	1.9579(370)	Average distance	1.9468(547)
Distortion:	11.603 xE-04	Distortion:	20.385 xE-04
		Ti2-O3	1.9937(1091)
		Ti2-O3	1.9937(1091)
		Ti2-O2	1.9902(1908)
		Ti2-O2	1.9193(1093)
		Ti2-O2	1.9193(1093)
		Ti2-O4	1.8214(1670)
		Average distance :	1.9396(558)
		Distortion:	10.287 xE-04

Further to understand the pressure evolution of structure, the unit cell parameters of both ambient and high pressure phases observed at different pressures are compared. The evolutions of unit cell parameters with pressure are shown in Fig.7.8.

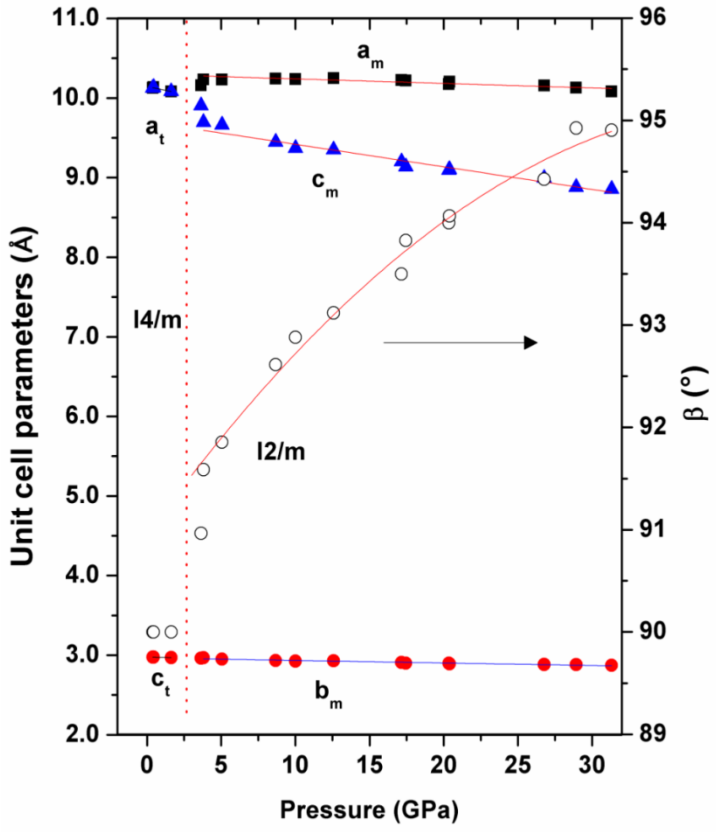

Fig.7.8: Pressure evolution of unit cell parameters of $K_2Fe_2Ti_6O_{16}$

It can be seen that the unit cell parameters decrease monotonically in tetragonal phase. However, the unit cell parameters disperse at the phase transition pressure, viz. expansion along one axis (a_m) in the transformed monoclinic phases. The variation of a-axis of monoclinic phase is observed to be almost invariant up to about 25 GPa and then it shows only a marginal decrease with increasing pressure. The other two axes (b_m and c_m) of the unit cell decrease continuously with increasing pressure. The anisotropic variation is related to the monoclinic distortions (β) which show continuous but non linear increasing trend with pressure. From the linear fits, the axial compressibilities of the ambient and high pressure phases are obtained and they are given in Table 7.5.

Table 7.5: Compressibility EOS parameters and thermal expansion parameters

Tetragonal		**Monoclinic**	
βa (GPa^{-1})	3.33×10^{-3}	βa (GPa^{-1})	0.27×10^{-3}
		βb (GPa^{-1})	1.11×10^{-3}
βc (GPa^{-1})	1.54×10^{-3}	βc (GPa^{-1})	3.8×10^{-3}
β_V (GPa^{-1})	8.16×10^{-3}	β_V (GPa^{-1})	5.15×10^{-3}
V_o ($Å$)^3	306.1(0.3)	V_o ($Å$)^3	303.4(1.8)
B_o (GPa)	122(12)	B_o (GPa)	127(8)
B_o'	4	B_o'	4

A comparison of axial compressibilities ($(\beta_x = -\frac{\partial \ln x}{\partial P})$, where x = unit cell parameters), indicates that the ratio β_a: β_b: β_c is 2.17:2.17:1.00 for tetragonal phase, while the same for monoclinic phase is 1.00:3.99:13.97. Thus the compression behaviors of the ambient and HP phase are different, which can be accounted by the variation of the coordination of K^+ ions in the 2 × 2 tunnel. It may be suggested that the strain introduced in compression of KO_8 is relieved by distorting the lattice and deviating the angle from 90°. The pressure evolution of unit cell volume of $K_2Fe_2Ti_6O_{16}$ (shown in Fig.7.8) indicates an almost smooth variation in unit cell volume with pressure in the complete studied range of pressure. It can be noticed that the decrease in unit cell volume of tetragonal phases is relatively faster compared to the monoclinic phase. However no noticeable volume discontinuity is observed at the transition, which is in accordance with a displacive type phase transition which occurs without much variation in the overall arrangements of ions. In addition on decreasing pressure, the monoclinic phase completely reverts back to tetragonal phase near about the same pressure as in upstroke data. Complete reversal of tetragonal phase is observed in the pressure released sample. The structural data of the pressure released phase is included in Table 7.2.

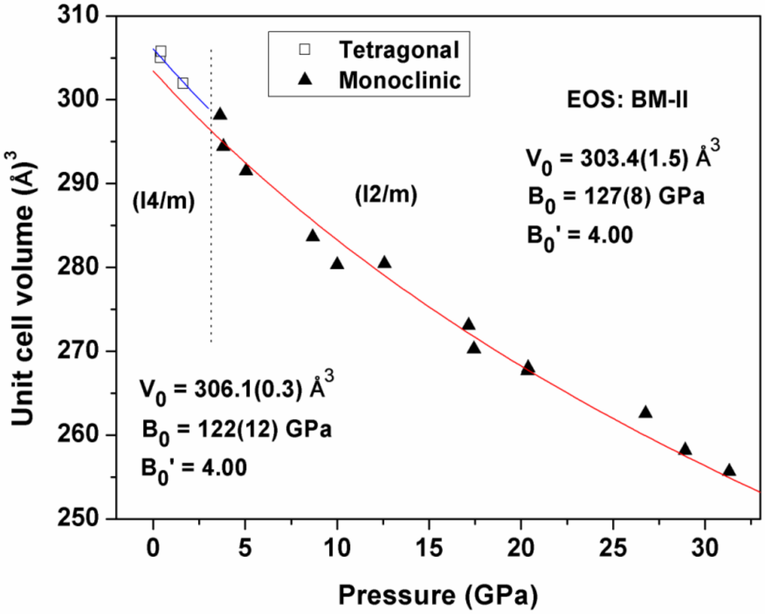

Fig.7.9: Pressure evolutions of unit cell volume of $K_2Fe_2Ti_6O_{16}$

The pressure-volume data was fitted with the 2nd order Birch-Murnaghan (BM) equation of state (EOS) [185]. The obtained EOS parameters for high pressure monoclinic phase are V_0 = 303.4(1.5) Å^3, B_0 = 127 (8) GPa and B_0’ = 4.0. Similarly, from the 2nd order BM EOS, the obtained V_0 and B_0 for the ambient pressure phase are found to be 306.1(0.3) Å^3 and 122(12) GPa, respectively. The increase in bulk modulus is marginal (~ 4 %), which can be attributed to almost similar structural arrangements in both ambient and high pressure phases. Similar marginal increase in bulk modulus in pressure induced displacive phase transitions in $Sr_2ZnGe_2O_7$ (tetragonal, B_0 = 83 GPa to monoclinic, B_0 = 85 GPa [34]) and $BaTe_2O_6$ (orthorhombic, B_0 =123.2 GPa to monoclinic, B_0 =129.3 GPa) have been reported in literature [131a]. Also the changes in unit cell volume at the transition in such materials are only marginal. The change in volume as well as bulk modulus can be attributed to the variation of free volume in the unit cell. The increase in packing is resulted by the displacements of the octahedral units and the increase in coordination number around the K^+ ions. High pressure studies on lead alumino silicate ($Pb_{0.8}Al_{1.6}Si_{2.4}O_8$) prepared at HP-HT conditions (16.5GPa and 1450°C) shows a tetragonal (I4) structure while no monoclinic phase has been observed, which may be attributed to the simultaneous effects of pressure and temperature [186].

Ballaran *et al*. have reported ferroelectric I4/m to I2/m phase transition at around 19 GPa in hollandite type $K_{0.8}Na_{0.2}AlSi_3O_8$, prepared under similar HP-HT conditions (20 GPa and 1700°C) [156c]. The equation of state of the tetragonal and high pressure monoclinic phase obtained by similar BM-II EOS indicates lower bulk modulus for the tetragonal phase (174 GPa) compared to monoclinic phase (198 GPa). It can be mentioned here that the bulk modulus of hollandite type $KAlSi_3O_8$ is about 208 GPa and the tetragonal to monoclinic phase transition occurs at significantly higher pressure, like ~ 23 GPa. It can be mentioned here that the crystal chemistry of hollandite type materials are related to ionic radii of the octahedral (B) and tunnel cation (A). Post *et al*. have proposed the tetragonal to monoclinic structural transition occurs at the limit r_B/r_A ~ 0.48. The r_B/r_A (~ 0.41) for $K_2Fe_2Ti_6O_{16}$ is close to the limiting value compared to the silicates (~ 0.35) [146b]. For $Na_2Fe_2Ti_6O_{16}$, this ratio is ~ 0.52 and thus forms only stable monoclinic lattice. Lower tetragonal to monoclinic transition pressure reported by Ballaran *et al*. for $K_{0.8}Na_{0.2}AlSi_3O_8$ may be related to the incorporation of smaller cation like Na^+ in the sites of K^+ ions. In a similar analogy, $Na_2Fe_2Ti_6O_{16}$ should reversibly transform to tetragonal $K_2Fe_2Ti_6O_{16}$ type structure at higher temperature. Since the octahedral units of such ferrotitanates are relatively rigid, the increase or decrease in the ionic radius of A-site should govern the transition pressure. Since the r_B/r_A of $K_2Fe_2Ti_6O_{16}$ is close to the limiting value and thus a feeble compression in the KO_8 polyhedra reduces the symmetry. Thus it is expected that with increasing pressure, the cations become less labile inside the tunnels and becomes more incompressible. This aspect is further explained while discussing the temperature dependent studies.

7.3.4. Temperature dependent studies

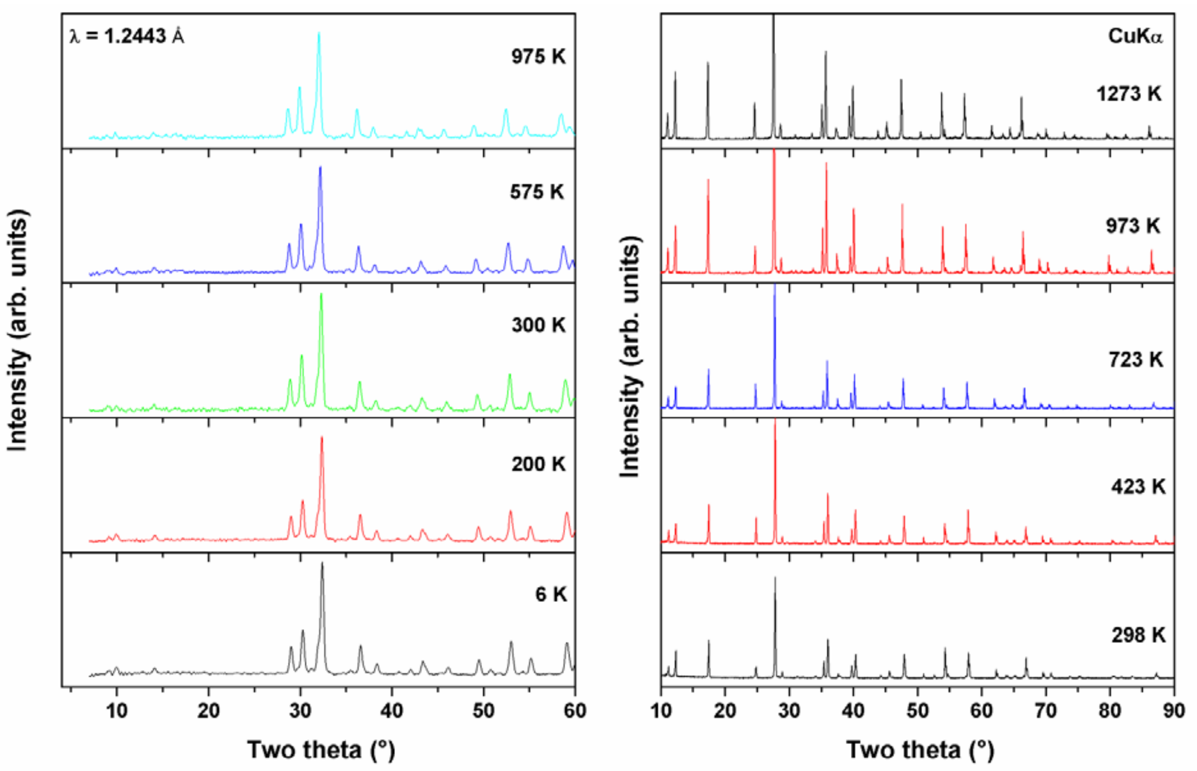

Fig.7.10: Evolution of powder neutron diffraction patterns (λ: 1.2443 Å) and XRD patterns (λ = Cu K_α) with temperature

Thermal stability of $K_2Fe_2Ti_6O_{16}$ with temperature has been investigated by both variable temperature powder neutron diffraction (in between 6K to 975 K) and XRD (in between 298 K to 1273 K). Typical diffraction patterns recorded at different temperature are shown in Fig.7.10.

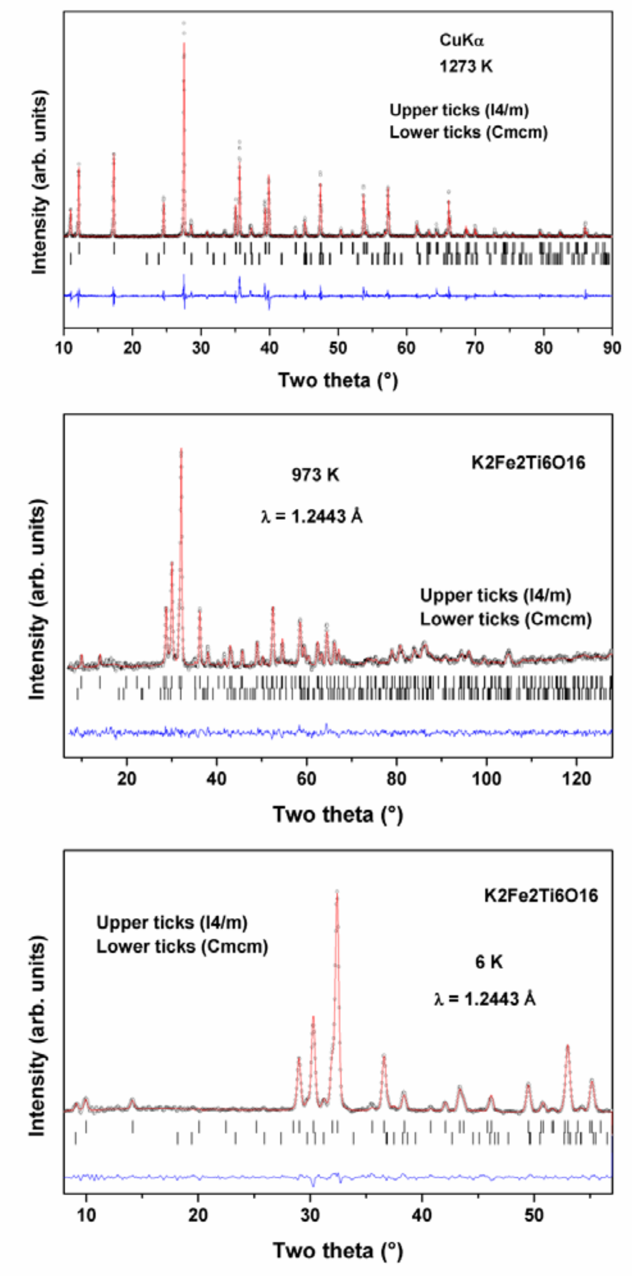

Fig.7.11: Rietveld refinement plots of tetragonal $K_2Fe_2Ti_6O_{16}$ at some representative temperatures. (a) at 6 K (PND), (b) at 975 K (PND), and (c) at 1273 K (XRD)

It can be seen that the PND or XRD patterns recorded at different temperature are closely similar to their respective ambient temperature data, which suggests for absence of any structural transition in the complete range of studies (6 K to 1273 K). The analysis of the PND and XRD data recorded at different temperatures are carried out in a closely similar manner as mentioned earlier. Refined position coordinates and unit cell parameters at 6 K; a = 10.1021(5) Å, c = 2.9728(2) Å, V = 303.38(3) $Å^3$, at 975 K: a = 10.1976(6) Å, c = 3.0030(2) Å, V: 312.29(4) $Å^3$, and at 1273 K; a = 10.2315(2) Å, c = 3.0134(1) Å, V = 315.46(1) $Å^3$. Typical Rietveld refinements plots for these temperatures are shown in Fig.7.11.

The analysis of the refined structural parameters observed at low and high temperature indicates that the octahedral BO_6 remains almost similar and average B-O bonds increases marginally (~ 1.5 %) with temperature. The average M-O bonds of the MO_6 octahedra at 6 and 1273 K are: 1.970(2) and 2.008(3) Å, respectively. Similarly, the distortion in the BO_6 octahedron also does not show appreciable variation (4.15×10^{-4} at 6 K, 3.81×10^{-4} at 975 K (from PND) data and they are significantly lower compared to the distortion introduced by pressure. The variations of unit cell parameters with temperature are shown in Fig.7.12. It is observed that unit cell parameters systematically decreases with decreasing temperature and becomes almost invariant at lower temperature, below 150K. The coefficients of average axial and volume expansion are calculated from the observed unit cell parameters at 6 K and 1273 K. Obtained values are: $\alpha_a = 10.11 \times 10^{-6}$ K^{-1}, $\alpha_c = 10.79 \times 10^{-6}$ K^{-1} and $\alpha_V = 31.42 \times 10^{-6}$ K^{-1}. The variation of unit cell parameters and volume could be fitted by considering the Einstein model, $X_T = X_0 + \varepsilon(e^{\vartheta_\epsilon/T} - 1)^{-1}$; where x is unit cell parameter, ϵ and ϑ_ϵ are Einstein constant and Einstein temperature, respectively [164a, 174a]. The slightly larger expansion along the *c*-axis compared to *a*-axis can be attributed to the packed configuration octahedral units along the *c*-direction.

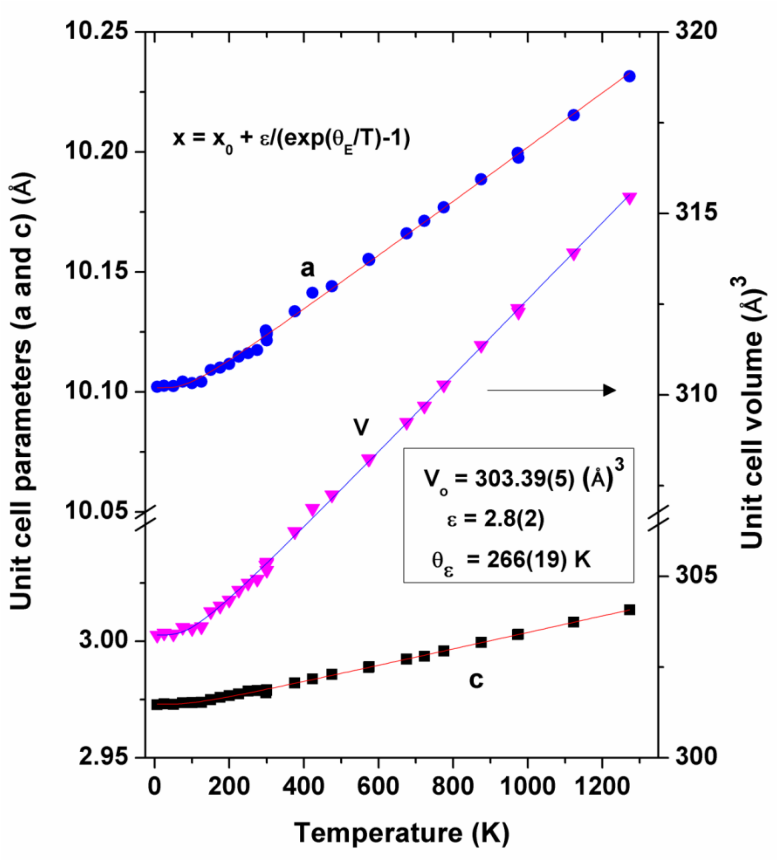

Fig.7.12: Evolutions of unit cell parameters of tetragonal $K_2Fe_2Ti_6O_{16}$ with temperature, fitted with Einstein model

A comparison of the pressure and temperature dependent studies indicates, the *a*-axis is more compressible compared to the *c*-axis in tetragonal hollandite ($\beta a/\beta c$ = 2.17) while a-axis has smaller expansion compared to c-axis (α_a/α_c = 0.94). This fact corroborates with the close packing of octahedral MO_6 units along the *c*-axis, where the expansion and compression are mainly controlled by the expansion of chemical bonds and inter-cation repulsions. In addition it can be mentioned here that the variation of K-O bond lengths with temperature are appreciably higher compared to the (Fe/Ti)-O bond lengths. The average K-O bond lengths at 6 K and 975 K are 2.974 and 3.040 Å, respectively. The (Fe/Ti)-O bond lengths at 6 K and 975 K are 1.970 Å and 1.981 Å, respectively. Thus the coefficients of average thermal expansion of K-O and (Fe/Ti)-O bonds are 22.90×10^{-6} K^{-1} and 5.76×10^{-6} K^{-1}, respectively. This is consistent with the weak nature of the K-O bonds. Thus the larger expansion of K-O bond reduces the ratio of ionic radii of octahedral and tunnel cations and hence favor for tetragonal structure at higher temperature. It also can be noted here that the differences in expansion of bonds is accommodated by the deformation of octahedra. It can also be suggested that the expansion or compressibility of $K_2Fe_2Ti_6O_{16}$ is essentially controlled by the bonding in octahedral in $2 \times \infty$ sheets. Since the inter-cation distance (B^{n+}-B^{n+}) is lower along the *c*-axis compared to the *a*-axis of the tetragonal phase (Fig.7.6), the latter shows larger compression compared to the former. The channels containing the K^+ ions can easily shrink with pressure. However, the expansion of the channel with increasing temperature is restricted by the octahedral units.

Further analysis of the variation of unit cell volume with pressure or temperature indicates that unit cell volume decreases only by 0.6 % by decreasing temperature down to 6 K while the volume drops to about 1.1 % by increasing pressure to 1.6 GPa. The reduction of unit cell volume to about 2.2 % (at around 3.6 GPa) leads to structural instability and hence leads to a phase transition from tetragonal to monoclinic structure. Thus it can be anticipated that the tetragonal structure remains unaffected by lowering temperature. Similar comparison of temperature dependent unit cell parameters indicates that the unit cell volume expand to about 3.3 % up to 1273 K. Earlier thermal expansion studies on tetragonal hollandite type $A_2Al_2Ti_6O_{16}$ (A = monovalent alkali ions) indicated that the anisotropy in axial expansion is sensitive to the nature of cation in the 2×2 tunnel, viz. $\alpha_a < \alpha_c$ for $K_2Al_2Ti_6O_{16}$ while $\alpha_a > \alpha_c$ for A = Rb and Cs. Also the coefficients of volume expansion vary non-monotonously with increasing radii of A^+ ions, viz. α_V (K^{-1}) are 30.4×10^{-6} (for $K_2Al_2Ti_6O_{16}$), 32.8×10^{-6} (for

$Rb_2Al_2Ti_6O_{16}$) and 31.6 × 10^{-6} (for $Cs_2Al_2Ti_6O_{16}$). The anomalous behavior can be due to the larger expansion of A-O bonds in Cs and Rb hollandite.

Knyazev *et al.* have summarized the systematic of thermal expansion with ionic radii of A^+ ions and suggested lower expansion with Na^+ hollandite compared to others [178a] ($Na_2Al_2Ti_6O_{16}$: 24.8 × 10^{-6} K^{-1}; $Na_2Fe_2Ti_6O_{16}$: 27.01 × 10^{-6} K^{-1}) [178a, 187]. However, the results indicate no systematic in α_V for tetragonal $A_2Fe_2Ti_6O_{16}$, A = K^+ (32.85 × 10^{-6} K^{-1}), Rb^+ (29.37 × 10^{-6} K^{-1}) and Cs^+ (34.06 × 10^{-6} K^{-1}) hollandites, but can be suggested that compounds with $A_2B_2Ti_6O_{16}$ type hollandites have larger expansion and they are in the range between 30-34 × 10^{-6} K^{-1}. Xu *et al.* have prepared series of alkali and alkaline earth containing hollandite type materials and indicated that the lowering of unit cell volume to about 1.3 % retains the tetragonal structure. However, the change in symmetry from tetragonal to monoclinic due to lowering of average ionic radius of A site cation has been reported in literature. Carter has pointed out that the stoichiometry of $Ba_xM_8O_{16}$ is governing factor of tetragonal to monoclinic transitions, where the lower concentration of Ba^{2+} favor for tetragonal while at higher concentrations monoclinic structure is favored [177]. Thus the decreases in volume is not the sole criteria for the transition, rather it can be explained by the internal strain in the lattice and in particular in 2 × 2 hollandite type tunnels. Larger distortion favors for monoclinic structure while lower distortion is in favor for tetragonal structure. From the temperature and pressure dependent studies, it can be suggested that the transition from tetragonal to monoclinic phase is related to distortion around the K^+ ions. The spherical surrounding or regular cubical polyhedra around K^+ stabilizes the tetragonal phase. However, the distorted polyhedra around the ions in the tunnel is either due to displacement of octahedral units or local strain arising from smaller ionic radius of the cation, leads to transformation of tetragonal structure to monoclinic structure. Thus the structure transforms to monoclinic structure at appreciably lower pressure. The distorted monoclinic phase is retained up to very high pressure. However, the post hollandite phase cannot be ruled out at higher pressure, but no other transition is expected with temperature. The observed specific heat anomaly at lower temperature observed earlier might be related to electronic transition which may be attributed to change of electronic structure as observed in hollandite type manganese and titanate. Further detailed studies on electronic properties may be able to unravel the electronic structure aspects in hollandite type ferrotitanates.

7.4. Development of ceramic lattice for Cs^+ immobilization

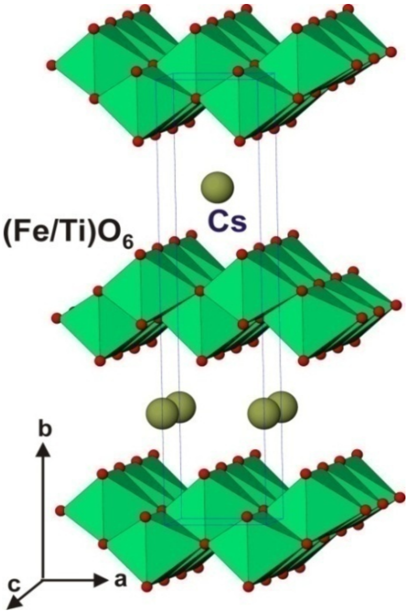

Fig.7.13: Crystal structure of $Cs_2Fe_2Ti_6O_{16}$

In the aim to find suitable host lattice for immobilization of Cs^+, a systematic studies on stabilities of hollandite type titanates with compositions as $A_2Ti_6Fe_2O_{16}$ ($A = Cs^+$) were carried out. $A_2Ti_6Fe_2O_{16}$ ($A = Cs^+$) composition was prepared by solid state reaction. The structural characterization of material at ambient temperature indicted that the structure varies with nature of alkali cation, viz. monoclinic, tetragonal and orthorhombic for Na^+, K^+ and Cs^+ ions, respectively. Analysis of the products obtained after heating at different temperatures indicated that the compositions with K^+ and Na^+ are stable up to 1100°C. The composition with Cs^+ was prepared at 600 to 800°C and found to have an orthorhombic lattice which is retained up to 1000°C. These hollandite type host materials are promising materials for immobilization of Cs^+ ions.

7.5. Conclusions

In summary detailed structural stability of tetragonal hollandite type $K_2Fe_2Ti_6O_{16}$ have been investigated in a wide range of temperature and pressure. These studies indicated high thermal stability of the lattice while an instability of the tetragonal lattice at a moderate pressure (~ 3.6 GPa). Under the influence of pressure, the tetragonal lattice distorts and transforms to a monoclinic lattice with marginal alteration in the structural arrangements. The compressibility and equation of states of both ambient and high pressure phases is only about 4% increase in bulk modulus by the phase transition. The tetragonal hollandite structure of $K_2Fe_2Ti_6O_{16}$ structure shows almost isotropic expansion at higher temperature and almost no change in the unit cell parameters below 150 K. No structural transition is observed in the low temperature diffraction data which suggests that the earlier reported specific heat anomaly is related to possible electronic phenomena in $K_2Fe_2Ti_6O_{16}$. This study supports for the high stability of the hollandite type ferrotitanates at higher pressure and temperature and can account for their existence in lower mantle. Also their stabilities support them as promising materials for usage in geological repository of nuclear wastes.

Chapter 8

Na-birnessite for separation of clinical-grade ^{90}Y from $^{90}Sr/^{90}Y$ mixture

8.1. Introduction

Ion exchange is regarded as a robust technology of great practical importance with many applications for societal benefits [60, 188]. Identification and synthesis of efficient and economical ion exchange materials have been extensively conducted especially, in radiochemical separations of several medically important radioisotopes from their precursors for use in nuclear medicine [189]. Until recently, conventional organic resins were the most widely used ion-exchangers for these applications. Owing to the stringent clinical requirements like extremely high purity and adequate radioactive concentration several inorganic ion exchangers such as nano-structured metal oxides, functionalized silica, etc. [189a, 190] have now emerged as an increasingly important replacement or a complement for separation of radioisotopes from their precursors. These advanced ion exchangers often have the advantages of much greater selectivity for target radioactive metal ions and higher radiation stability compared to conventional organic resins leading to efficient large-scale radiochemical separations for clinical use [191].

Among the radiochemical separations studied thus far, $^{90}Sr/^{90}Y$ separation holds paramount importance in the context of nuclear medicine [192]. The $^{90}Sr/^{90}Y$ system is one of the typical examples of a secular equilibrium with a very long-lived parent (^{90}Sr, $t_{½}$ = 28.8 y) radioisotope and a short-lived daughter (^{90}Y, $t_{½}$ = 64.1 h) radioisotope. By adopting a suitable separation methodology, the daughter radioisotope can be repeatedly separated in a suitable medium for radiopharmaceutical preparation. Radiopharmaceuticals based on ^{90}Y, a pure β-emitter (E_{max} = 2.28 MeV), are clinically well-established and are used for the treatment of cancer as well as in radiation synovectomy [193]. Ideally, there is an unlimited potential availability of ^{90}Y, as its parent ^{90}Sr is one of the major fission products and the annual world production of ^{90}Sr in the nuclear reactors amounts to 600 MCi [192d, 194]. The possible widespread availability of ^{90}Y at a reasonable cost would make it an economical choice for therapeutic use in nuclear medicine clinics world over.

Despite the possibility for abundant availability of ^{90}Y, presently its cost is very high in the international market which makes ^{90}Y-based therapy unaffordable especially in developing countries [192d]. This is primarily because a simple, efficient and inexpensive radiochemical separation methodology has not yet been developed which can routinely be used for large-scale production of ^{90}Y in centralized radiopharmacies for commercial use. Most of the present generation technologies employed for ^{90}Sr/^{90}Y separation involve multiple steps of solvent extraction, ion exchange or extraction chromatography either alone or in combination which makes the overall process very cumbersome [192d]. In view of the radiation and toxicological hazards associated with ^{90}Sr handling [192d], it is essential to execute such complicated procedures in specifically designed hot cells equipped with remotely operable and fully automated radiochemical separation modules. Such sophisticated settings have high operational costs which increase the overall production cost of ^{90}Y for clinical use. Presently, ^{90}Y is separated in few leading industrial setups in the developed countries and supplied as a radiochemical in inorganic form to the radiopharmacies [192d]. Additionally, the relatively short half-life of this radioisotope provides logistic challenges for its supply to distant user sites. In view of the versatility and robustness of ion-exchange technology, it is highly desirable to identify advanced ion-exchange materials for simple, efficient and cost-effective separation of ^{90}Y, which could easily be carried out in centralized radiopharmacies to meet the regional demands of this radioisotope.

Over the past few years, several 'new generation' inorganic ion-exchangers having layered structures with exchangeable interlayer cations have emerged as a promising choice in the nuclear industry [195]. However, most of these materials have been used in radionuclide sequestration and radioactive waste remediation [195a, 195c-e] and their utility in radiochemical separation for nuclear medicine applications is yet to be explored. Among these materials, synthetic birnessite has attracted huge research interest due to their high functionality, stability, environment compatibility, and feasibility for large-scale synthesis at a low cost [196]. Birnessite is a kind of hydrous layered manganese oxide (phyllomanganate) with stacks of MnO_6 octahedral units with large interlayer spacing (~7 Å), which could incorporate many elements like Na, K, Mg, Ni, etc. in cationic form. MnO_6 octahedral units present in the structure are connected to each other by sharing edges, resulting in a uniform MnO_2 layer [196b, c, 197]. The ions present in between the layers are labile in nature, can move into or out of the interlayer region without much structural rearrangements due to the hydrous layered structure of birnessite. Therefore, such materials can be used as promising ion-exchangers for selective separation of radioactive metal ions. In view of similar ionic radii of Sr^{2+} and Na^{+}, synthetic sodium birnessite was viewed as an ideal choice for effective $^{90}Sr/^{90}Y$ radiochemical separation.

Herein, synthesis and structural characterization of sodium birnessite for use as an ion-exchanger in $^{90}Sr/^{90}Y$ separation is elaborated. The parameters for the radiochemical separation were optimized to obtain ^{90}Y with high purity for preparation of radiopharmaceuticals. The reproducibility of the process was demonstrated by performing the radiochemical separation in several batches. As a proof of concept, ^{90}Y obtained after the separation process was utilized in preparation of ^{90}Y-labeled dimeric cyclic RGD peptide derivative, DOTA-E[c(RGDfK)]$_2$ and evaluated in preclinical settings [191].

8.2. Experimental methods

Layered hydrated sodium birnessite was prepared by adopting the synthesis procedure described in earlier sections of the thesis, using oxidation of $MnCl_2.4H_2O$ (99.99 % trace metal basis, Sigma-Aldrich) in presence of excess of NaOH [143].

8.3. Structural characterization

Structural characterization of the material was carried out by X-ray diffraction (XRD) and small-angle X-ray scattering (SAXS) experiment on powder sample. SAXS study has been performed using a laboratory based SAXS facility at Bhabha Atomic Research Centre with Cu-K_α X-ray radiation. Thermogravimetric analysis and FTIR absorption study on the sample were carried out to confirm the stoichiometry of the material followed by morphological studies by using transmission electron microscopy.

8.4. Ion exchange characteristics of synthetic sodium birnessite

In pH−dependent experiments, the pH of the solution was adjusted either by HCl (Suprapur, Merck) solution or NaOH solution. The pH value was measured by a PHS-3C pH meter at the beginning of the ion exchange experiments. All measurements were carried out at 25 °C in triplicate. The distribution ratios (K_d) of Sr^{2+} and Y^{3+} ions for the birnessite matrix were measured at different pH, using ^{85}Sr+^{89}Sr and ^{90}Y as radiotracers. In each experiment, 20 mg of sorbent was suspended in 10 mL solution containing the radioactive metal ions, in a 20 mL vial. The vials were shaken in a wrist arm mechanical shaker for 2 h at 25 °C and then filtered. An aliquot of the solution before and after equilibration were measured in a well type NaI(Tl) counter using appropriate window ranges (400–600 keV for ^{85}Sr+^{89}Sr and 0-500 keV for ^{90}Y). In order to study the time dependence of the sorption of Sr^{2+} ions onto synthetic sodium birnessite, the K_d of ^{85}Sr+^{89}Sr in solution at pH 4 was determined at different time intervals. The attainment of equilibrium was indicated by the constant K_d value after a certain period of time.

The sorption capacity of synthetic sodium birnessite for Sr^{2+} was determined by batch equilibration method. An accurately weighed amount of sorbent (20 mg) was taken in a stoppered glass conical flask and equilibrated with 10 mL of the Sr^{2+} solution of varying concentration (0.025-1 mg of Sr per mL) spiked with ~ 370 kBq (10 μCi) of ^{85}Sr+^{89}Sr for 2 h at pH 4. Subsequently, the contents were filtered and the activity of the filtrate was compared with that of the standard solution taken from the equilibrium mixture before equilibration with birnessite. The ion exchange capacity (q_e) was calculated using the expression, $q_e = \frac{(C_0 - C_e)V}{m}$ where C_o and C_e represent the initial and equilibrium concentrations of Sr^{2+} respectively in terms of mg/mL calculated from activity per mL values, V is the volume (in mL) of solution and m is the mass (in g) of the sorbent. The Sr^{2+} sorption isotherm was analyzed by Langmuir, Freundlich and Dubinin-Radushkevich (D-R) Isotherm models. Dubinin-Radushkevich (D-R) Isotherm model is;

$$\ln q_e = \ln X_m - \beta\varepsilon^2 \qquad (8.1)$$

where, X_m is the maximum sorption capacity, β is the activity coefficient related to the mean sorption energy and ε is the Polanyi potential, which can be written as

$$\varepsilon = RT \ln\left(1 + \frac{1}{C_e}\right) \qquad (8.2)$$

where, R is the universal gas constant [expressed in units of kJ/(mol.K)] and T is the temperature (in K). In all these models, q_e is the amount of Sr^{2+} ions adsorbed on birnessite at equilibrium (expressed in terms of mg/g), C_e is the equilibrium concentration of metal ions (expressed in terms of mg/L). The kinetics for the Sr^{2+} sorption by birnessite, as a function of time at equilibrium has been analyzed by pseudo first order and pseudo second order kinetic models.

8.4.1. Separation of ^{90}Y from ^{90}Sr using synthetic sodium birnessite as ion exchanger

The ^{90}Sr/^{90}Y separation was carried out by batch equilibration method. The ^{90}Sr/^{90}Y equilibrium mixture (in 1 mL solution containing 185 MBq of ^{90}Sr at pH 4) was spiked with ~ 370 kBq (10 μCi) of ^{85}Sr+^{89}Sr. This solution was carefully transferred in a centrifuge tube containing 100 mg of birnessite and the contents were equilibrated under constant shaking in a mechanical shaker operating at room temperature for 2 h. Subsequently, the reaction mixture was centrifuged and the supernatant containing ^{90}Y was carefully withdrawn and passed through 0.22 µm filter and collected in a sterile vial. In order to retrieve ^{90}Sr from synthetic sodium birnessite, 1 mL of 0.1 M HCl was added to the centrifuge tube containing the ion exchanger, vortexed for 15 min and centrifuged. The supernatant containing ^{90}Sr and ^{85}Sr+^{89}Sr was separated and used for separation studies after re-growth of ^{90}Y. The activity of ^{90}Y was measured using a pre-calibrated ‘PTW Curiementor 3’ dose calibrator.

8.5. Quality control of ^{90}Y after radiochemical separation

8.5.1. Radionuclidic purity

The presence of radiostrontium impurities (in the form of ^{85}Sr) in ^{90}Y solution could be determined from the γ-spectrum of ^{90}Y recorded using HPGe detector (Canberra Eurisys, France) coupled to a 4K multichannel analyzer (MCA) system. A ^{152}Eu reference source, obtained from Amersham Inc., USA, was used for energy and efficiency calibration of the HPGe detector. For this purpose, a small aliquot of ^{90}Y solution was withdrawn and the γ-spectrum was recorded after appropriate dilution of the radioactivity so that the dead time of the detector was < 5 %. The characteristic γ-peak (513 keV) corresponding to ^{85}Sr was monitored for determination of the level of radiostrontium impurities. The level of ^{90}Sr impurity in ^{90}Y solution was further validated by extraction paper chromatography (EPC) technique as reported earlier [193].

8.5.2. Radiochemical purity

The radiochemical purity of ^{90}Y solution (in the form of Y^{3+} ions) was determined by paper chromatography assay, as per the reported procedure [198]. For this purpose, 5 μL of radioactive solution was spotted on a paper chromatography strip at 1.5 cm from the bottom. The chromatogram was developed in acetic acid in water (1:1 v/v) medium. Subsequently, the paper chromatography strip was dried and cut into 1 cm pieces and activity of each piece was determined using a NaI (Tl) counter.

8.5.3. Chemical purity

In order to determine the presence of chemical impurities (in the form of Cu, Zn, Co, Ni, Fe, Pb, and Mn ions) in the ^{90}Y solution after radiochemical separation, the samples were allowed to decay for 2 months. The trace levels of the metal ion contamination in the decayed samples were determined by inductively coupled plasma-atomic emission spectroscopy analysis (using ICP-AES JY-238 spectrometer, Emission Horiba Group, France). The calibration curves for these ions were obtained by using standard solutions having known concentration of these ions.

8.5.4. Biological purity

Sterility of the ^{90}Y solution was tested in tryptic soya broth media and fluid thioglycollate media using Himedia Labs sterility test kits [199]. Pyrogenicity of the preparation was checked by point-of-use test system (PTS).

8.6. Simulated study for radiochemical separation of ^{90}Y from Sr carrier added solution, equivalent to 37 GBq of ^{90}Sr

The effects of macroscopic amounts of Sr^{2+} ions on the radiochemical separation of ^{90}Y was investigated by conducting the experiments using a Sr/Y mixture prepared with inactive Sr and Y carrier, spiking it with an equilibrium mixture of ^{90}Sr/^{90}Y containing 37 MBq (1 mCi) of ^{90}Sr as well as 3.7 MBq (100 μCi) of ^{85}Sr+^{89}Sr. The simulated solution was prepared by dissolving 22.5 mg of anhydrous strontium carbonate and 2.32 μg of yttrium oxide in 2 M HCl. After adjusting the pH of the resultant solution to ~ 4, radiochemical separation of ^{90}Y was carried out as per the method described above. The activity content of the recovered ^{90}Y was measured and the level of radioactive strontium impurities present in it was estimated.

8.6.1. Preparation of ^{90}Y-labeled DOTA-E[c(RGDfK)]$_2$

After radiochemical separation of ^{90}Y, it was used for radiolabeling with DOTA-E[c(RGDfK)]$_2$ (> 99% chemically pure, ABX Advanced Biochemical Compounds, Germany) as per the reported procedure [200]. Briefly, a stock solution of the peptide conjugate was prepared in deionized water with a concentration of 1 mg/mL. A 25 μL aliquot of this solution containing 25 μg (14.7 nM) of DOTA-E[c(RGDfK)]$_2$ was taken and 475 μL of 0.1 M ammonium acetate buffer of pH 5.5 and 500 μL aliquot of ^{90}Y solution (74 MBq) was added. The reaction mixture was incubated at 90 °C for 30 min after adjusting the pH to ~ 4. After the completion of the reaction, the mixture was allowed to cool till it reached room temperature, a small aliquot was withdrawn and complexation yield was determined by high performance liquid chromatography (HPLC) technique. The HPLC instrument (JASCO PU 1580, Japan) was equipped with a NaI (Tl) detector. HPLC was carried out using a dual-pump HPLC unit with a C-18 reversed phase HiQ-Sil (5 μm, 25 × 0.46 cm) column. The elution was monitored both by detecting UV signals at 270 nm as well as by radioactivity signal using NaI(Tl) detector. The mobile phase consisted of water (A) and acetonitrile (B) mixtures with 0.1% trifluoroacetic acid and following gradient elution technique was adopted for the separation: 0-4 min 95% A, 4-15 min 95% to 5% A, 15-20 min 5% A, 20-25 min 5% A to 95% A, 25-30 min 95% A. The flow rate was maintained at 1 mL/min. The complexation yield of ^{90}Y-DOTA-E[c(RGDfK)]$_2$ was also rapidly determined by paper chromatography as per the reported procedure using acetonitrile in water (1:1 v/v) as the eluting solvent [191].

8.6.2. Bio-distribution studies

All animal studies were performed under a protocol approved by the Bhabha Atomic Research Centre Institutional Animal Ethics Committee. The biological behavior of ^{90}Y-DOTA-E[c(RGDfK)]$_2$ was studied in C57BL/6 mice bearing melanoma tumors. Melanoma tumors were developed by injecting ~ 1× 10^6 melanoma cells (ATCC-CRL-6475) suspended in 200 μL of phosphate buffered saline (PBS) subcutaneously into the right thigh of each C57/BL6 mouse weighing 20 - 25 g. The animals were observed for visibility of tumors and allowed to grow for about 2 weeks. Animals bearing tumors with a mean diameter of ~ 8 mm (range, 6-9 mm) were used in the bio-distribution experiments.

The ^{90}Y-DOTA-E[c(RGDfK)]$_2$ radiotracer was diluted in PBS medium and 100 µL (3.7 MBq) solution was injected into each animal through a lateral tail vein. The animals were sacrificed by cardiac puncture post-anaesthesia at different times of post-injection (p.i.). Four animals were used at each time point. Various organs, tissues and tumors were excised after sacrifice, washed with PBS, dried and the radioactivity associated with each organ and tissue was determined using a flat-type NaI (Tl) counter. The weight of each organ and tumor was also determined by using an analytical balance. The percentage injected dose (%ID) in various organs, tissues and tumor was calculated from the above data and expressed as percentage injected dose per gram (%ID/g) of organ/tissue.

8.7. Results and discussion

The radiochemical separation of ^{90}Y from ^{90}Sr/^{90}Y secular equilibrium mixture is a convenient method to obtain high specific activity ^{90}Y in a no-carrier-added (NCA) form for preparation of radiopharmaceuticals for targeted therapy [192d]. Over the last 5 decades, there have been enormous research efforts from all over the world toward development of methodologies for radiochemical separation of ^{90}Y from ^{90}Sr/^{90}Y equilibrium mixture [192d]. However, the radiochemical separation of NCA ^{90}Y suitable for clinical use is still a challenging task and the feasibility of adopting a separation methodology suitable for operation in a centralized radiopharmacy has remained an unrealistic proposition. Aim of this study is to develop a facile separation technology amenable for adoption in a centralized radiopharmacy set-up for obtaining clinical-grade NCA ^{90}Y. Attempts were made to explore the possibility of using synthetic sodium birnessite as the ion exchanger for the radiochemical separation and optimized the various process parameters in order to achieve this objective. Yttrium-90 obtained after radiochemical separation was utilized for preparation of ^{90}Y-DOTA-E[c(RGDfK)]$_2$, the biological efficacy of which was evaluated in C57BL/6 mice bearing melanoma tumors. The overall process of radiochemical separation of ^{90}Y and its utilization in preclinical settings is schematically illustrated in Fig.8.1.

8.7.1. Synthesis and structural characterization of sodium birnessite

Naturally occurring birnessite is one of the most common manganese dioxides in the clay size (< 2 µm) fraction of soils [197a]. However, naturally occurring birnessite structures are poor crystalline in nature, due to fine particle sizes and poor ordering [197b].

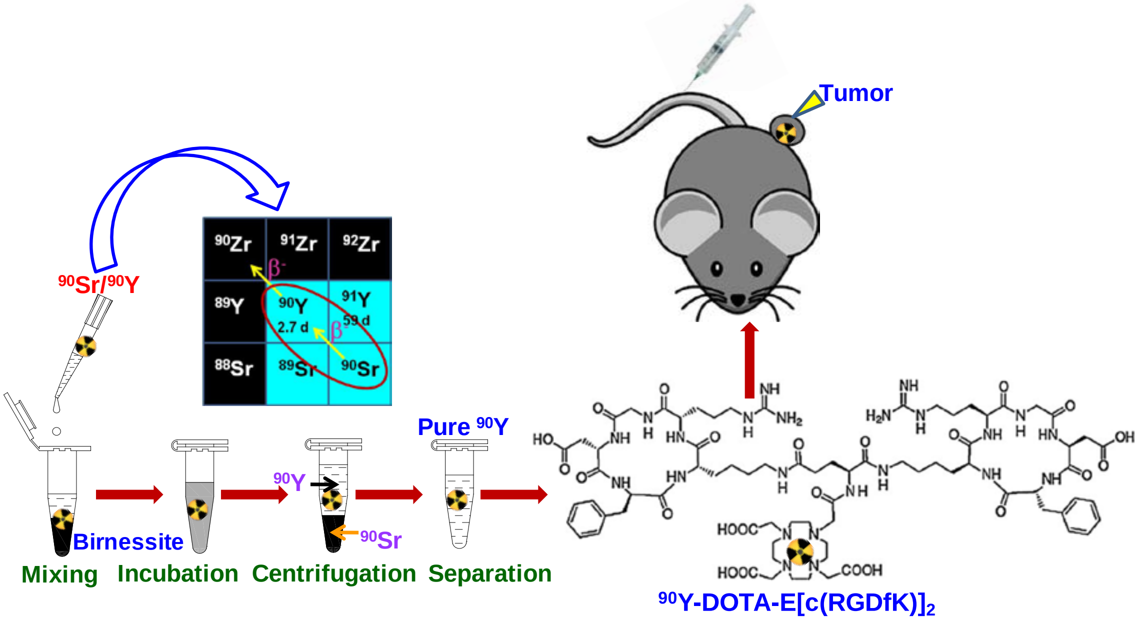

Fig.8.1: Schematic illustration of radiochemical separation of ^{90}Y from ^{90}Sr

In order to achieve rapid, selective and reproducible ion-exchange separation, highly crystalline synthetic sodium birnessite was used in the present study. Sodium birnessite could be easily be synthesized on a multi-gram scale and with high purity by oxidation of

$MnCl_2.4H_2O$ in presence of excess of NaOH. Phase purity and crystalline nature of the synthesized sodium birnessite was confirmed by the XRD studies (Fig.8.2A). Diffraction pattern of the final dried sample is similar to the XRD pattern reported by Cai *et al.* [143] Structure model with composition $Na_{0.55}Mn_2O_4{\cdot}1.5H_2O$ was used as the initial structural model to refine the XRD pattern. The obtained XRD pattern was fitted well with this model, unit cell parameters obtained are a = 5.1896(7) Å, b = 2.8649(4) Å, c = 7.3578(7) Å, β = 103.101(2)°, V = 106.55(2), the sample crystallizes in monoclinic lattice with space group C2/m. Typical Rietveld refinement plot of the synthesized sodium birnessite is shown in Fig.8.2A [191].

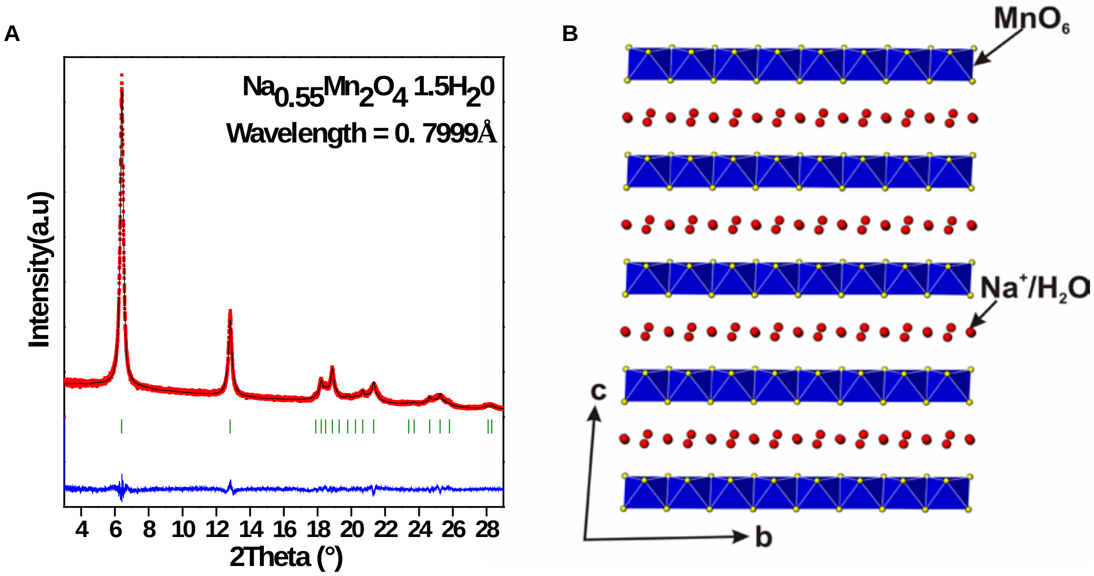

Fig.8.2: (A) Powder XRD pattern of synthetic sodium birnessite. (B) View of the three dimensional crystal structure of synthetic sodium birnessite

Atom coordinates obtained from Rietveld refinement were used to draw the crystal structure of synthetic sodium birnessite as shown in Fig.8.2B. From the crystal structure it is clear that manganese coordinates to six oxygen atoms to form an octahedron, which in turn connected to another manganese octahedron by sharing edge which leads to the formation of sheet along ab-plane leaving two epical oxygen atoms along the c-direction. Charge of these MnO_2 layers is compensated by the presence of Na^+ ions between the MnO_2 layers. Sodium ions between the layers are surrounded by H_2O molecules. Manganese in synthetic birnessite possess both + 3 and + 4 oxidation states, average oxidation state of the synthetic material is 3.5 as reported by Cai *et al.* [143]

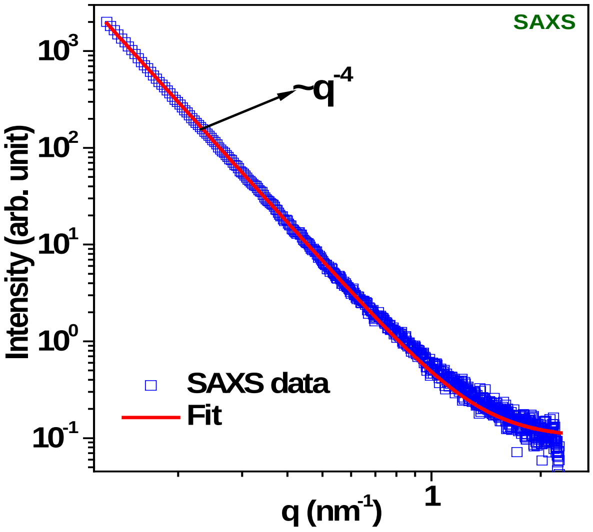

Fig.8.3: The SAXS profile of synthetic sodium birnessite sample

SAXS on synthetic sodium birnessite sample was carried out using a laboratory based SAXS facility. The experimental SAXS profile is shown in Fig.8.3. The scattering wave vector q and the real space dimension in scattering experiment are inversely related, i.e. D = 2π/q, where D is the typical real space dimension. Thus, the length scale probed in the present experiment is 2-50 nm. It is found that experimental profile follows power law behaviour with an exponent value of -4.

$$I(q) = Cq^{-4} + bkg \qquad (8.3)$$

Where, C is the scale factor and bkg is the q-independent background scattering. The power law behaviour of the scattering intensity as represented in equation (8.3) is called Porod's law [201]. The scattering from a smooth surface gives rise to such power law scattering. The fitting of the experimental data to equation (8.3) is quite good (Fig.8.3). This indicates that the pore/particle size in the synthetic sodium birnessite sample is larger than 50 nm and hence only surface scattering was observed in the present q-range of the SAXS measurements. This was further confirmed by light scattering study wherein broad particle size distribution in the range of 0.5-3 µm was observed (Fig.8.4).

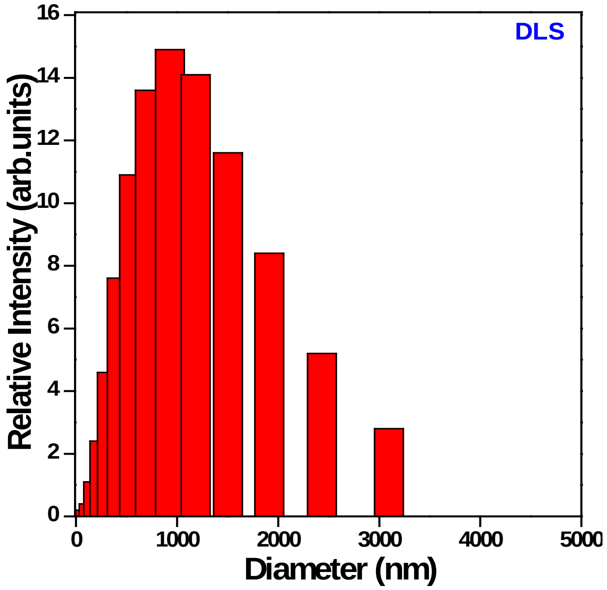

Fig.8.4: Particle size distribution for synthetic Na-birnessite determined by DLS study

The FTIR spectrum of synthetic sodium birnessite is shown in Fig.8.5. The IR bands at 420, 482 and 514 cm^{-1} are due to Mn-O stretching vibrations and are the characteristic bands for birnessite mineral. [202] Bands at 3445 cm^{-1} and 1537, 1645 cm^{-1} are due to stretching and bending vibrations of water molecules present in between the layers of manganese octahedra.

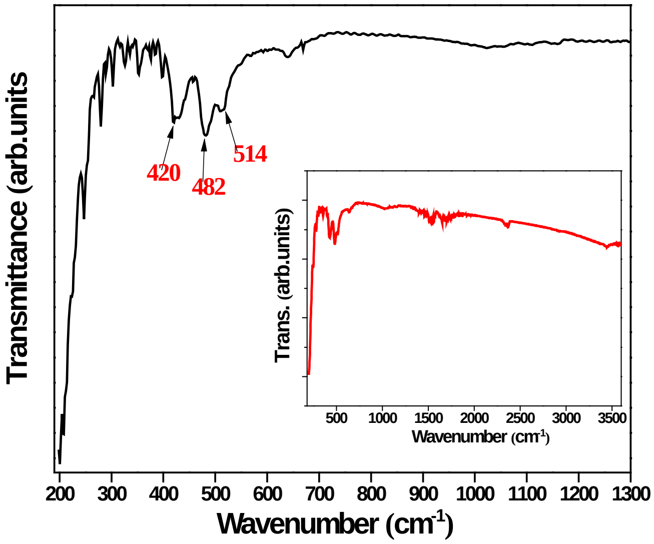

Fig.8.5: Typical IR spectrum of synthetic Na-birnessite

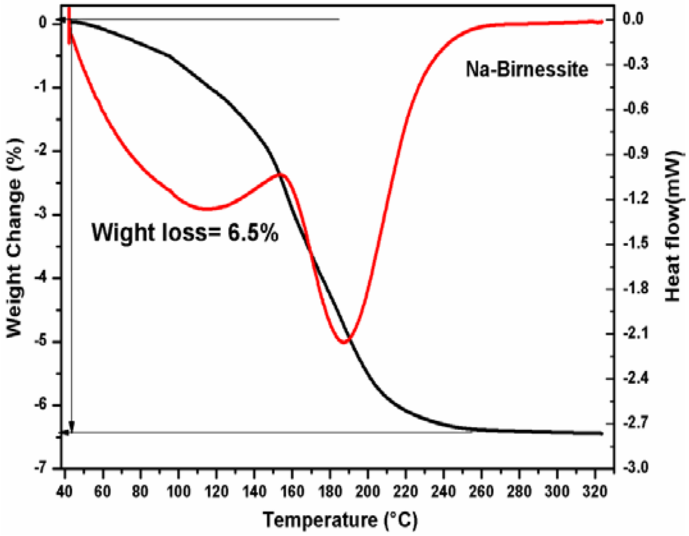

Fig.8.6: Typical thermogravimetric curves of synthetic Na-birnessite in heating cycle

Thermogravimetric plot of the prepared composition recorded while heating from ambient to 350°C is shown in Fig.8.6. From the figure it is prominent that sharp weight loss of the sample is in accordance with presence of water between MnO_2 layers. Cai *et al.* have also reported similar thermogravimetric plot showing weight loss due removal of water [143]. Layered morphology of synthetic sodium birnessite is shown by the TEM images (Fig.8.7

A). The HRTEM image confirms crystalline nature of layers in sodium birnessite structure (Fig.8.7 B). The calculated interlayer distance from the electron diffraction pattern is ~3 Å.

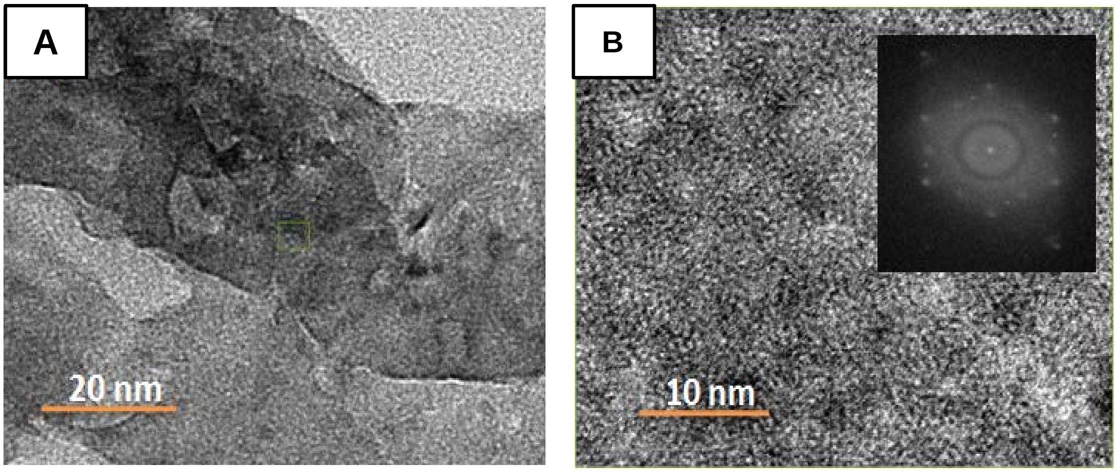

Fig.8.7: (A) TEM image showing the layered morphology of synthetic Na-birnessite. (B) HRTEM image showing the array of MnO_2 layers in synthetic Na-birnessite

8.7.2. Ion exchange characteristics of synthetic sodium birnessite

The K_d value is an important parameter signifying the affinity and selectivity of synthetic sodium birnessite for Sr^{2+} and Y^{3+} ions and helps to arrive at the optimum conditions for their radiochemical separation. The K_d values for Sr^{2+} and Y^{3+} ions were determined at various pH values (Fig.8.8A). The K_d values for both Sr^{2+} and Y^{3+} ions increased with increase in pH and maximum affinity was observed under near neutral conditions. However, the K_d values for Sr^{2+} ions was much higher than that of Y^{3+} ions in the entire pH range studied, indicating higher selectivity and affinity of synthetic sodium birnessite towards Sr^{2+} ions. At pH 4, maximum separation factor (defined by the ratio of K_d values of Sr^{2+} and Y^{3+} ions) of > 2500 could be achieved and therefore this pH was chosen in subsequent studies for quantitative removal of ^{90}Sr from ^{90}Y. After the radiochemical separation process, ^{90}Sr sorbed in synthetic sodium birnessite could be recovered in acidic solution (pH < 2) and preserved for re-growth of ^{90}Y.

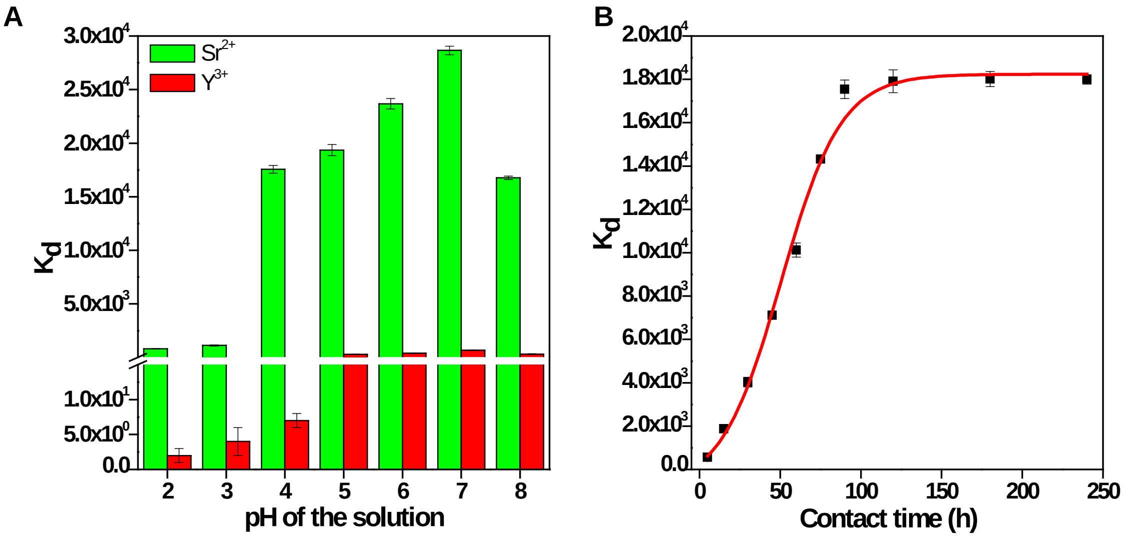

Fig. 8.8: (A) Variation in K_d values of Sr^{2+} and Y^{3+} ions in synthetic sodium birnessite as a function of pH. (B) Variation in K_d values of Sr^{2+} ions in synthetic sodium birnessite at pH 4 as a function of time

In order to determine an optimum contact time required for the complete sorption of the $^{90}Sr^{2+}$ ions in synthetic sodium birnessite, the time course of the sorption process was studied by following the K_d values at different time intervals at room temperature which is an indication of the progress of the sorption process (Fig.8.8 B). The K_d values for Sr^{2+} ions increased rapidly with time at the beginning and remained almost constant after 90 min, indicating that the sorption equilibrium was attained reasonably fast. In all subsequent batch experiments, a contact time of > 90 min was maintained in order to ensure quantitative uptake of ^{90}Sr in synthetic sodium birnessite. A qualitative mechanism of selective Sr^{2+} uptake in synthetic sodium birnessite has been proposed by the analysis of the above XRD, TEM and K_d data (Fig.8.9). Layered sodium birnessite has exchangeable Na^+ ions located in the interlayer. Owing to similar ionic radii and electropositivity of hydrated Na^+ and Sr^{2+} ions, [203] the $^{90}Sr^{2+}$ ions easily migrate and are bound tightly in the interlayers of the layered structure of synthetic sodium birnessite by exchange with Na^+ ions. The less electropositive hydrated Y^{3+} ions are more sluggish in diffusion to the interlayer of sodium birnessite structure and therefore selective uptake of Sr^{2+} ions could be achieved to aid toward $^{90}Sr/^{90}Y$ radiochemical separation.

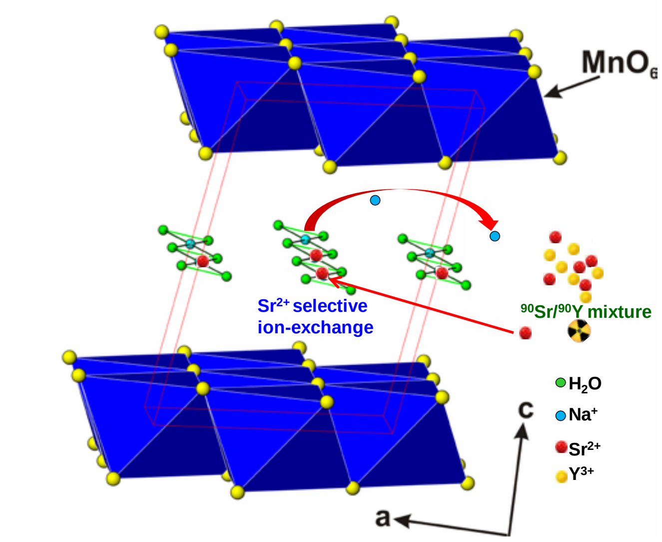

Fig.8.9: Schematic illustrating qualitative mechanism of Sr^{2+} selective ion exchange in synthetic Na-birnessite

To determine the affinity and maximum exchange capacity of synthetic sodium birnessite, equilibrium studies were conducted with various initial concentrations of Sr^{2+} ions (from 0.025-1 mg Sr per mL). The removal capacity q plotted against the initial Sr^{2+} ions concentration is graphed in Fig.8.10. The amount of Sr^{2+} adsorbed increases from 12.6 ± 1.3 mg/g to 99 ± 2 mg/g with the increase in initial concentration from 0.025-1 mg/mL. The Sr^{2+} ion adsorbed is higher when the initial metal ions concentration is high. This is because of the efficient use of the adsorptive capacity of synthetic sodium birnessite due to greater driving force by a higher concentration gradient pressure [204].

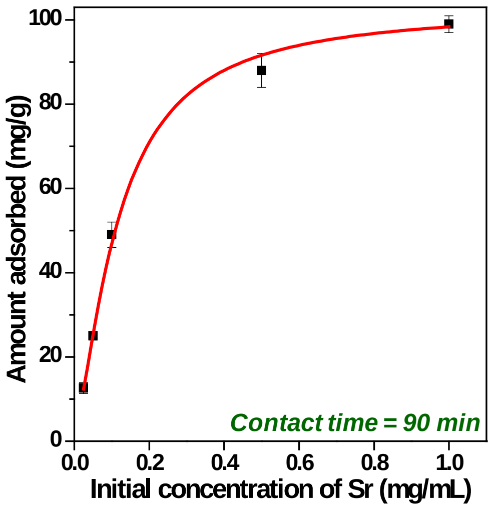

Fig.8.10: Plot of the initial concentration of Sr^{2+} versus the amount adsorbed in synthetic sodium birnessite

Selective uptake of Sr^{2+} ions in synthetic sodium birnessite results from a mass transfer process that occurs at the interface between solid and liquid phases. Equilibrium relationships between the sorbent and the sorbate are described by sorption isotherms, usually as the ratio between the quantity sorbed and that which remains in the solution at a fixed temperature. The selective uptake of metal ions from aqueous solution is influenced by several factors e.g., the type and amount of ion exchange material, pH, time and temperature [204]. Any sorption isotherm is valid for a particular temperature, pH and ionic strength. The Langmuir, Freundlich and D-R isotherms are used to describe the interaction of the synthetic sodium birnessite particles and Sr^{2+} ions (Fig.8.11, Fig.8.12) [195a, 204]. The Langmuir isotherm model assumes that monolayer adsorption takes place on a homogenous surface with uniform energies of adsorption on the surface [205].

It was found that the equilibrium data could be fitted well with Langmuir model with $R^2 = 0.99$, which implied that the adsorption sites in synthetic sodium birnessite were equivalent with each site only adsorbing one Sr^{2+} and the adsorbed Sr^{2+} are localized without transmigration. This indirectly established the observation from the SAXS study where the experimental profile followed power law behaviour implying that x-ray scattering occurred from a smooth and homogenous surface (Fig.8.11).

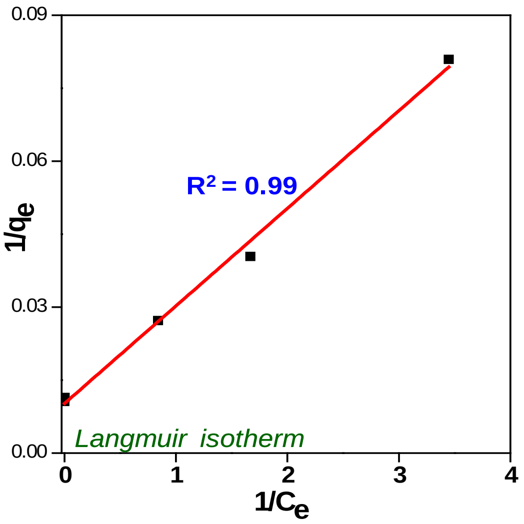

Fig.8.11: Langmuir isotherm plot for the uptake of Sr^{2+} by Na- birnessite at pH 4

The Freundlich model assumes that multilayer adsorption occurs on a heterogeneous surface [205]. However, the equilibrium data could not be fitted well with Freundlich model ($R^2 = 0.72$) indicating that this model is not appropriate for understanding the sorption behavior of synthetic sodium birnessite (Fig.8.12). The sorption data have also been analyzed using the D-R model, to distinguish between physical and chemical adsorption, [204] based on the characteristics of synthetic sodium birnessite.

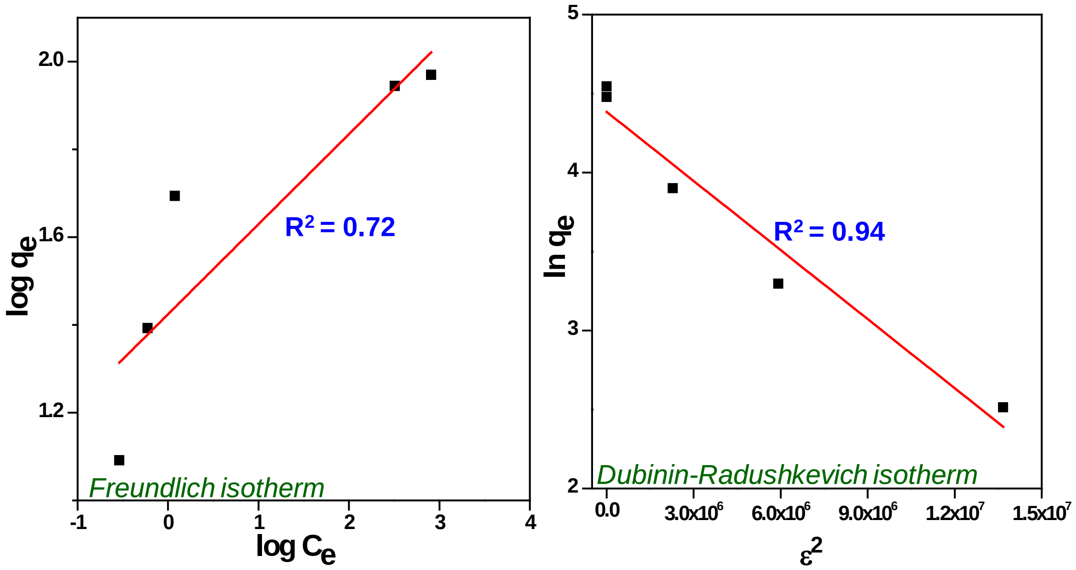

Fig.8.12: Freundlich isotherm and D-R isotherm plot for the uptake of Sr^{2+} by Na-birnessite at pH 4

The plot of ln q_e versus ε^2 (Fig.8.12) gives a straight line ($R^2 = 0.94$) and the values of X_m and β evaluated from the intercept and slope of the graph were determined to be 4.38 ± 0.12 mol/g and 1.45×10^{-7} J^2/mol^2, respectively. The mean sorption energy (E) is a critical parameter for distinguishing between physical and chemical adsorption, [204] and it is given by:

$$E = (\sqrt{2\beta})^{-1} \qquad (8.4)$$

The magnitude of E (1.86 kJ/mol) obtained in the present study indicates that physical adsorption of Sr^{2+} ions takes place in synthetic sodium birnessite [204]. It is due to this fact that ^{90}Sr adsorbed in synthetic sodium birnessite could be retrieved in acidic medium after the radiochemical separation process and reused for subsequent studies after allowing in-growth of ^{90}Y. Thus, the same feed solution of ^{90}Sr could be used multiple times for obtaining ^{90}Y.

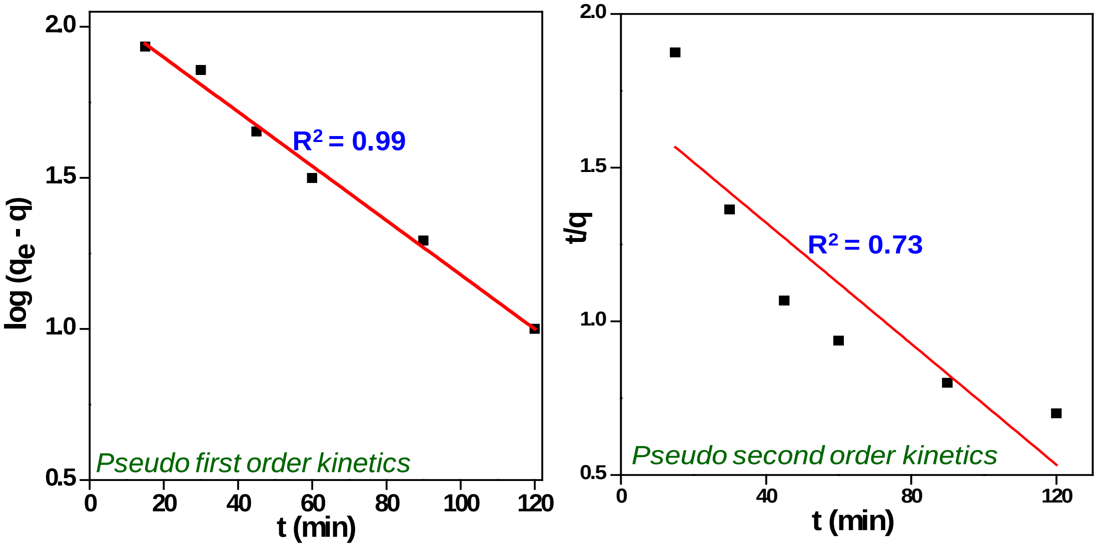

Fig.8.13: Pseudo first-order and Pseudo second-order reaction rate kinetics for the uptake of Sr^{2+} on synthetic sodium birnessite at pH 4

In order to understand the kinetics for the sorption of Sr^{2+} ions by synthetic sodium birnessite under equilibrium conditions at room temperature, two different kinetic models (pseudo-first-order and pseudo-second-order reaction models) were evaluated (Fig.8.13) [204-205]. The correlation coefficient for the linear plot of log (q_e- q) versus time from the pseudo-first-order rate expression was 0.99, which was much greater than the R^2 value (0.73) for the pseudo-second-order kinetics. Hence, the best-fit model for the uptake of Sr^{2+} by synthetic sodium birnessite was pseudo-first-order [191].

8.7.3. Separation of ^{90}Y from ^{90}Sr using synthetic sodium birnessite as ion exchanger

In order to translate the laboratory findings into real conditions, process demonstration runs were carried out using synthetic sodium birnessite as the ion exchanger in 10 different batches and the results are summarized in Table 8.1. In all these batches, same feed solution of ^{90}Sr was used after allowing 15 days time interval for in-growth of ^{90}Y. The overall yield of ^{90}Y after the radiochemical separation was > 80 % and the results are quite reproducible in all the batches.

8.7.4. Quality control of ^{90}Y after radiochemical separation

Since ^{90}Y obtained after radiochemical separation is intended to be used for human clinical investigations, stringent quality control measures are essential. The results of detailed quality control of ^{90}Y are explained below.

Table 8.1: Performance evaluation of the radiochemical separation process in 10 different batches

Batch No.	Activity of ^{90}Sr (MBq)	Activity of ^{90}Y separated (MBq)	Level of ^{90}Sr in ^{90}Y (%)	Radiochemical purity of ^{90}Y in the form of Y^{3+} (%)	Level of chemical impurities in ^{90}Y (µg.mL^{-1})	Radiolabeleing yield of ^{90}Y-DOTA-E[c(RGDfK)]$_2$ (%)
1	185.0	153.6	8×10^{-5}	99.7 ± 0.2	Cu, Zn, Co, Ni, Fe, Pb, Mn individual impurities ≤ 0.1 µg/mL	97.6 ± 1.2
2	184.8	158.9	7×10^{-5}	99.6 ± 0.1		98.1 ± 1.5
3	184.6	151.4	6×10^{-5}	99.8 ± 0.1		98.7 ± 1.4
4	184.4	154.8	8×10^{-5}	99.6 ± 0.2		96.9 ± 0.8
5	184.2	152.2	9×10^{-5}	99.9 ± 0.1		98.4 ± 0.8
6	184.0	153.1	4×10^{-5}	99.5 ± 0.3		98.1 ± 1.7
7	183.8	151.9	5×10^{-5}	99.4 ± 0.3		97.7 ± 1.4
8	183.6	154.5	7×10^{-5}	99.7 ± 0.1		97.1 ± 1.6
9	183.4	155.7	8×10^{-5}	99.8 ± 0.2		98.3 ± 0.5
10	183.2	152.6	6×10^{-5}	99.5 ± 0.2		96.5 ± 0.9

8.7.4.1. Radionuclidic purity

Yttrium-90 used for preparation of radiopharmaceuticals should be of very high radionuclidic purity (> 99.999 %), as the most probable contaminant ^{90}Sr, is a bone seeker. The maximum permissible body burden of ^{90}Sr in the entire lifetime of an individual is only 74 kBq [192d]. This translates the limits of ^{90}Sr to 74 kBq in 37 GBq of ^{90}Y, assuming that a patient may be administered with a maximum of 37 GBq of ^{90}Y in his lifespan [192d]. According to United States Pharmacopeia, ^{90}Sr/^{90}Y activity ratio should not exceed 2×10^{-5} parts (or 2×10^{-3} %) at the time of injection of any ^{90}Y-based radiopharmaceutical [16, 192d]. In view of such a demanding situation, the activity of ^{90}Sr in the ^{90}Y solution should be carefully analyzed to ensure that it is well within the acceptable limits. Radionuclidic purity estimation by making use of the γ-spectrometric analysis showed that the level of ^{90}Sr impurity in ^{90}Y after radiochemical separation was $< 1 \times 10^{-4}$ % in all the batches, which was within the acceptable limits as per the United States Pharmacopeia (Table 8.1, Fig.8.14). The results were further corroborated by extraction paper chromatography assay adopting the reported procedure (Fig.8.15).

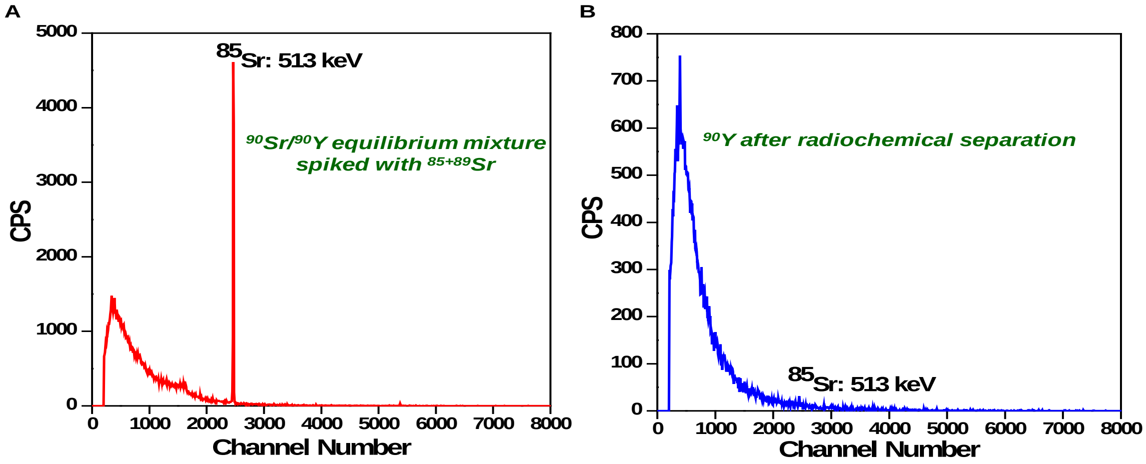

Fig.8.14: Typical γ-spectra of (A) ^{90}Sr/^{90}Y equilibrium mixture spiked with ^{85}Sr+^{89}Sr, (B) ^{90}Y after radiochemical separation

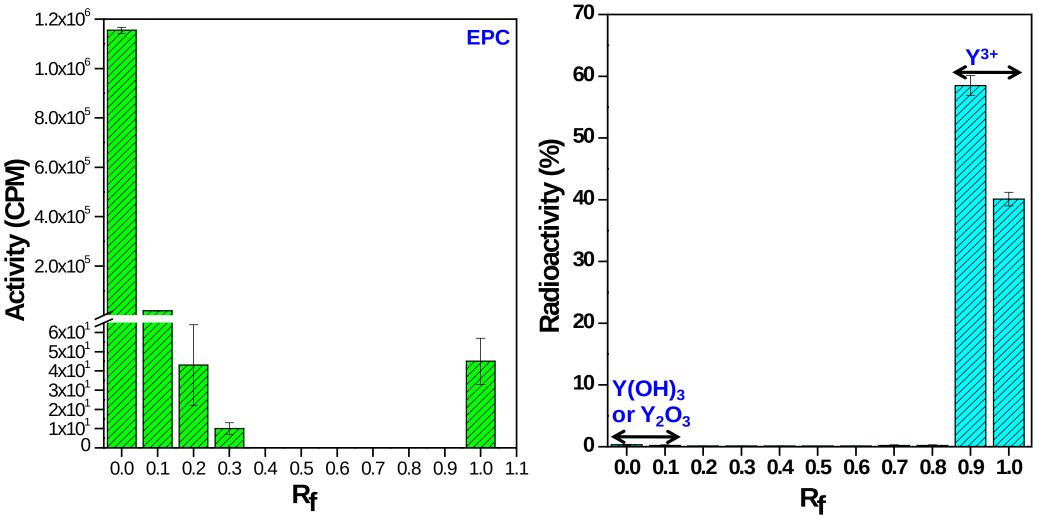

Fig.8.15: Extraction paper chromatography pattern of ^{90}Y obtained after radiochemical separation (left), Paper chromatographic pattern of ^{90}Y developed in acetic acid in water (1:1 v/v) medium (right)

8.7.4.2. Radiochemical purity

The radiochemical purity of ^{90}Y (in the form of Y^{3+} ions) was > 99 % in all the batches (Table 8.1, Fig.8.15), indicating the suitability of ^{90}Y obtained after radiochemical separation process for preparation of radiopharmaceuticals.

8.7.4.3. Chemical purity

The chemical impurities in the form of other metal ions in the ^{90}Y solution obtained after radiochemical separation would compete with Y^{3+} in the complexation process for the preparation of radiopharmaceuticals. ICP-AES analysis of the decayed ^{90}Y samples showed that Cu, Zn, Co, Ni, Fe, Pb, Mn ion impurities were present in the ^{90}Y solution after radiochemical separation (Table 8.1). However the level of each of these metal ion impurities was < 0.1 μg/mL and is not expected to pose any serious issue in the radiopharmaceutical preparation process.

8.7.4.4. Biological purity

After passing through 0.22 μm filter, ^{90}Y solution was found to be sterile. The endotoxins in all the decayed ^{90}Y samples tested were found to be < 5 endotoxin unit (EU)/mL, which is within the permissible limits for clinical use [199].

8.7.5. Simulated study for radiochemical separation of ^{90}Y from Sr carrier added solution, equivalent to 37 GBq of ^{90}Sr

The recovery of ^{90}Y from Sr/Y mixture simulated to represent 37 GBq of ^{90}Sr, was also equally good as in when lower amounts of ^{90}Sr, were used. The overall yields of ^{90}Y in the simulated experiments were 83±4 % and the level of ^{90}Sr impurity present in ^{90}Y was $(5 \pm 3) \times 10^{-5}$ % (n = 3).

8.7.5.1. Preparation of ^{90}Y-labeled DOTA-E[c(RGDfK)]$_2$

Yttrium-90 labeled dimeric cyclic RGD peptide derivative, DOTA-E[c(RGDfK)]$_2$, is an established radiopharmaceutical for targeted therapy of tumors over expressing integrin-$\alpha_v\beta_3$ receptors [200]. The suitability of ^{90}Y obtained after radiochemical separation for biomedical applications could be demonstrated by labeling DOTA-E[c(RGDfK)]$_2$ (in nano-molar concentrations) with ^{90}Y. The radiolabeling of DOTA-E[c(RGDfK)]$_2$ with ^{90}Y is also an indirect test to ascertain the chemical purity of ^{90}Y as very high chemical purity is essential to achieve a good complexation yield of the radiolabeled agent. The radiolabeling yield of ^{90}Y-DOTA-E[c(RGDfK)]$_2$ was determined by paper chromatography using 50% acetonitrile in water as eluent (Fig.8.16).

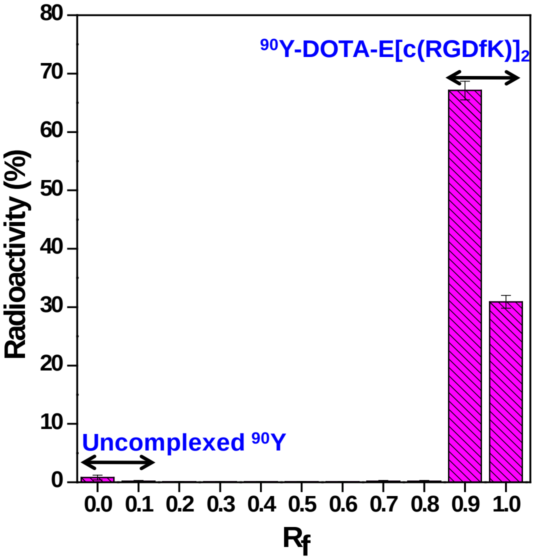

Fig.8.16: Paper chromatographic pattern of ^{90}Y-DOTA-E[c(RGDfK)]$_2$ developed in acetonitrile in water (1:1 v/v) medium

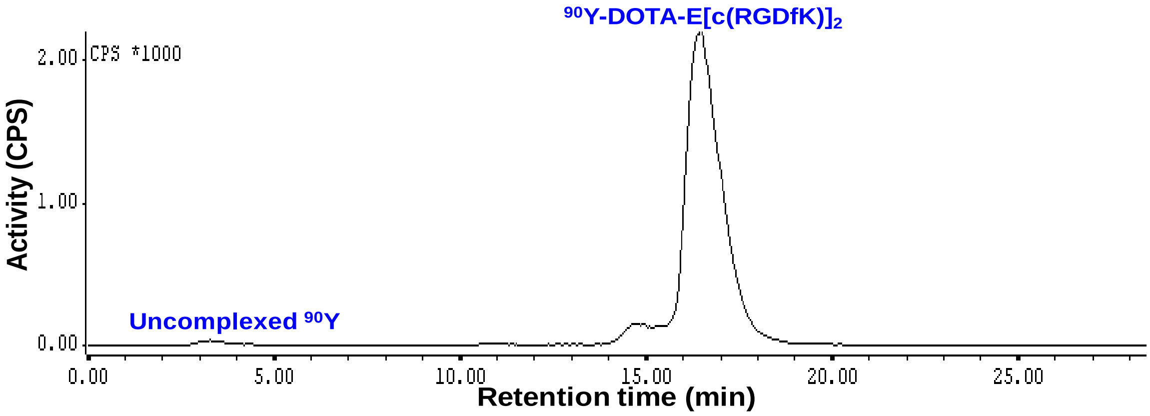

Fig.8.17: Typical HPLC pattern of ^{90}Y-DOTA-E[c(RGDfK)]$_2$

It was observed that ^{90}Y-DOTA-E[c(RGDfK)]$_2$ moved towards the solvent front (R_f = 0.8-0.9), whereas under identical conditions, unlabeled ^{90}Y remained at the point of application (R_f = 0). The radiolabeling yield of ^{90}Y-DOTA-E[c(RGDfK)]$_2$ was also validated by HPLC studies, wherein, the radiolabeled agent demonstrated retention time of 16.8 min while uncomplexed ^{90}Y was eluted out within 3-4 min (Fig.8.17). By both the studies, the radiolabeling yield of ^{90}Y-DOTA-E[c(RGDfK)]$_2$ was determined to be > 95 % and it remained consistent in all the batches (Table 8.1) [191].

8.7.6. Bio-distribution studies

The results of the biodistribution studies revealed significant tumor uptake (5.1 ± 0.6 %ID/g) within 30 min p.i. Accumulation of activity was also observed in various non-target organs such as liver, intestine kidney etc. at 30 min p.i. However, with the progress of time, the accumulated activity in the non-target organs gradually cleared through renal route. The tumor-to-blood and tumor-to-muscle ratios of ^{90}Y-DOTA-E[c(RGDfK)]$_2$ at different time points p.i. are shown in Fig.8.18.

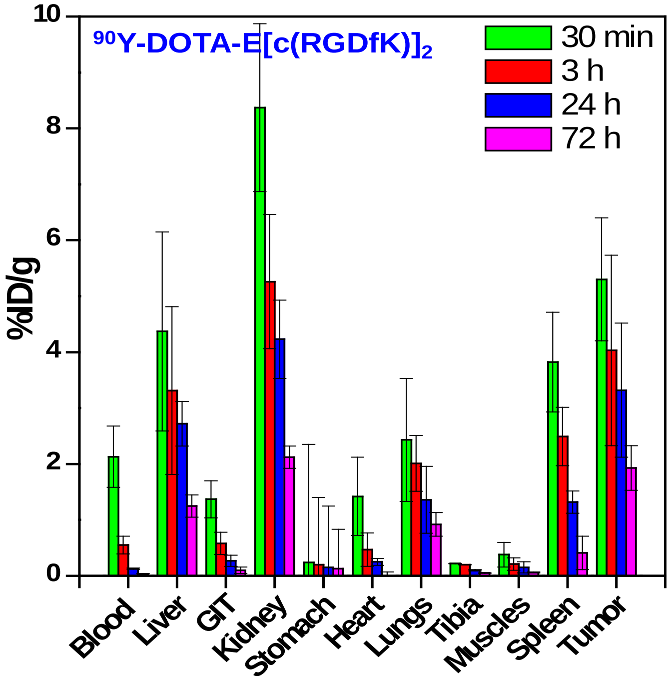

Fig.8.18: Bio-distribution study in C57BL/6 mice bearing melanoma tumors after the administration of ^{90}Y-DOTA-E[c(RGDfK)]$_2$

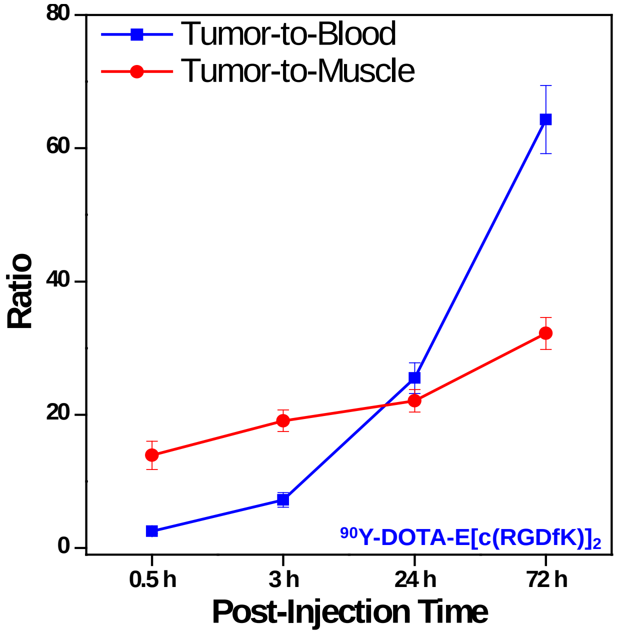

Fig.8.19: The tumor-to-blood and tumor-to-muscle ratios of ^{90}Y-DOTA-E[c(RGDfK)]$_2$ at different time points p.i. of the radiotracer

The tumor-to-blood ratio was observed to increase from 2.5 ± 0.3 at 30 min p.i. to 64.3 ± 5.1 at 72 h p.i. Between the same time points, the tumor-to-muscle ratios increased from 13.9 ± 2.1 to 32.2 ± 2.4 (Fig.8.19). It is evident that ^{90}Y-DOTA-E[c(RGDfK)]$_2$ exhibited favourable tumor to background ratio for used as a radiopharmaceutical for targeted therapy. The bio-distribution pattern ^{90}Y-DOTA-E[c(RGDfK)]$_2$ prepared with ^{90}Y obtained after radiochemical separation using synthetic sodium birnessite as ion exchanger is comparable with the data when the radiotracer was prepared using ^{90}Y separated by conventional methods [200].

8.8. Conclusions

In conclusion, synthetic sodium birnessite has been synthesized and an efficient ion-exchange strategy for radiochemical separation of ^{90}Y from ^{90}Sr/^{90}Y equilibrium mixture is successfully realized. Synthetic sodium birnessite could rapidly capture Sr^{2+} with excellent selectivity, high capacity, and ^{90}Y could be separated with appreciable yield in a form suitable for preparation of radiopharmaceuticals. The reliability and reproducibility of the approach have been amply demonstrated in several batch experiments. The overall process is simple and easily executable in a hot cell facility for large-scale separation and is therefore adaptable for practical use in a centralized radiopharmacy set-up. Wide scale implementation of this facile radiochemical separation strategy would greatly enhance the global availability of ^{90}Y for preparation of a variety of ^{90}Y-based target specific radiopharmaceuticals for use in nuclear medicine. These findings also offer important experimental basis for the understanding and searching of new ion exchangers for radiochemical separation of other medically important radioisotopes.

Chapter 9

Thermophysical properties of relevant phosphates

9.1. Introduction

This chapter is comprised of three independent sections describing ion exchange properties, thermodynamic characteristics and magnetic properties of some other prepared phosphates for aim of the thesis. First part of the chapter deals with synthesis and ion exchange properties of tunnel structured complex phosphates $KLn(PO_3)_4$, Ln=Ce, Eu with potassium ions as exchangeable ions. $KCe(PO_3)_4$ and $KEu(PO_3)_4$ have been synthesized by solid state synthesis process, ion exchangeabilities of the title materials have been investigated by using inactive cesium and strontium. Details of crystal structure and ion exchange properties of these are described in this section. Second part of the chapter comprises of thermodynamic properties of two complex phosphates as $K_3Ln_5(PO_4)_6$, where Ln = Gd and Eu. Synthesis of these materials along with crystal structure is elaborated. Comparison of measured standard molar enthalpy of formation and molar heat capacity of these compounds by high temperature calorimetry has been discussed. Measured standard free energy of formation of the synthesized materials from standard molar enthalpy of formation and heat capacities are useful for predicting the usage of these matrices in the nuclear fuel cycle. Thermodynamic results of the synthesized materials are elaborated in this part. The third part of this chapter deals with the preparation, crystal structure and magnetic properties of complex phosphate $Mn_5(HPO_4)_2(PO_4)_2.4H_2O$ (synthetic Hureaulite mineral). This compound is found to be stable up to 300°C and showed a ferromagnetic like sharp transition at 6K. Synthesis and magnetic properties of this synthetic mineral are elaborated in this part.

9.2. Ion exchange properties of $KLn(PO_3)_4$: Ln = Ce and Eu

9.2.1. Introduction

In the aim to study the potentials of complex phosphates as ion exchangers, two stoichiometric compositions as $KLn(PO_3)_4$ with Ln = Ce and Eu were prepared by solid state reactions and characterized by powder X-ray diffraction method. The Cs^+ and Sr^{2+} exchange properties of both materials were investigated by using standard solutions of Sr^{2+} or Cs^+ in low acidic medium [16, 24].

9.2.2. Experimental techniques

Both the studied compositions have almost similar XRD patterns which suggest their iso-structural nature. All the observed reflections in the powder XRD pattern of both compositions could be assigned to the monoclinic ($P2_1$) phases. The refined unit cell parameters of the $KCe(PO_3)_4$ are: a = 7.2958(1) Å, b = 8.4938(2) Å, c = 8.0525(2) Å, β = 92.066(2) °. V = 498.68(2) $Å^3$ and those of $KEu(PO_3)_4$ are : a = 7.2593(4) Å, b = 8.3655(5) Å, c = 7.9365(4) Å, β = 91.831(5)°, V = 481.71(5) $Å^3$. The smaller unit cell parameters of $KEu(PO_3)_4$ are in accordance with the smaller ionic radii of Eu^{3+} compared to Ce^{3+}.

The crystal structure of $KLn(PO_3)_4$ has infinite chains of PO_4 tetrahedra formed by linking two oxygen atoms of PO_4. These chains are linked by Ln^{3+} containing polyhedra by sharing free oxygen atoms of $(PO_3)_\infty$ chains. The Ln^{3+} ions have nearly regular square antiprismatic coordination polyhedra. The typical arrangements of the $(PO_3)_\infty$ chains and Ln^{3+} ions form one dimensional channels along the long b-axis, which are filled by K^+ ions to maintain the charge neutrality. Though the structure is ionic, the rigid framework like arrangement makes it insoluble in aqueous medium. Since the K^+ ions are ionically bonded to the network of [Ce$(PO_3)_4$]$^-$ ions, they are likely to have higher mobility along the channel direction. Typical crystal structure of KLn$(PO_3)_4$ is shown in Fig.9.1.

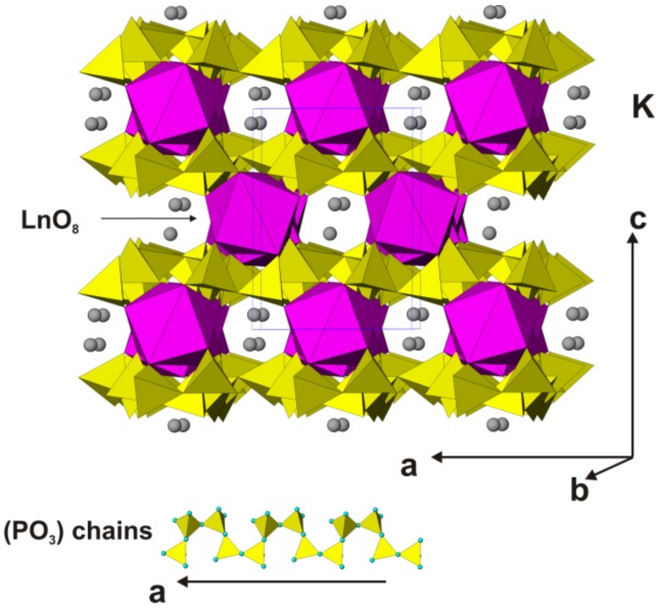

Fig.9.1: Typical crystal structure of KLn$(PO_3)_4$ (Ln=Ce, Eu)

9.2.3. Results and discussion

Ion exchange behavior of KCe$(PO_3)_4$ and KEu$(PO_3)_4$ were investigated for Cs^+ and Sr^{2+} in low acidic medium. Weighed quantity of sample was equilibrated with Sr^{2+} and Cs^+ for 2 h and the solution was analyzed for quantification of K^+, Sr^{2+} and Cs^+. Ion exchangeability of these materials was evaluated by equilibrating the sample with standard concentration of Cs^+, Sr^{2+} solutions separately. After certain equilibration time, supernatant liquid was analyzed using ICP-AES, which showed the decrease in concentration of Cs^+, Sr^{2+} from the feed solution. It is observed that 63% of Cs^+, 77% of Sr^{2+} were exchanged by KCe$(PO_3)_4$ and 73% of Cs^+, 40% of Sr^{2+} were exchanged by KEu$(PO_3)_4$. Typical percentage of ion exchange is shown in Table 9.1.

Table 9.1: Comparison of ion uptake of $KCe(PO_3)_4$ and $KEu(PO_3)_4$

Percentage of exchange	Cs^+ (10mg)	Sr^{2+} (10mg)	Cs^+ (100mg)	Sr^{2+} (100mg)
$KCe(PO_3)_4$	63	71	59	75
$KEu(PO_3)_4$	73	5	72.5	40

The presence of K^+ ions in the equilibrated solution confirmed the exchange of Sr^{2+} or Cs^+ with K^+ ions. Comparison of uptake of Cs^+, Sr^{2+} by both $KCe(PO_3)_4$ and $KEu(PO_3)_4$ materials is shown in Fig.9.2.

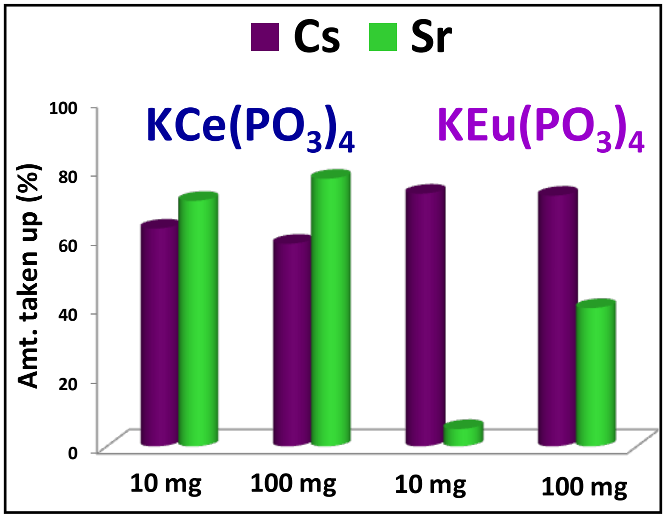

Fig.9.2: Comparison of ion uptake of $KCe(PO_3)_4$ and $KEu(PO_3)_4$

9.3. Thermodynamic investigations on $K_3Ln_5(PO_4)_6$, Ln = Eu, Gd compounds

9.3.1. Introduction

Thermodynamic properties of two complex phosphates $K_3Ln_5(PO_4)_6$, where Ln = Eu and Gd were investigated in order to verify the suitability of the materials towards immobilization of radionuclides. Both the materials are iso-structural and have monoclinic

(C2/c) lattice. Obtained unit cell volumes of $K_3Gd_5(PO_4)_6$ and $K_3Eu_5(PO_4)_6$ are in accordance with the lanthanide contraction. The standard molar enthalpy of formation and molar heat capacity of these compounds has been measured using high temperature calorimeter. The average enthalpy of dissolution of $K_3Gd_5(PO_4)_6$ (s) and $K_3Eu_5(PO_4)_6$ (s) at 298K are 555.5 ± 9.2 $K.J.mol^{-1}$ and 613.3±2.8 $K.J.mol^{-1}$ respectively. Standard molar enthalpy of formation ($\Delta_f H^o_{298}$) has been obatined using thermochemical cycle and the obtained values are -12234.8 ± 61.5 $K.J.mol^{-1}$ and -11790.9 ± 58.2 $K.J.mol^{-1}$ for $K_3Gd_5(PO_4)_6$ and $K_3Eu_5(PO_4)_6$, respectively. From the enthalpy increment, obtained heat capacities for $K_3Gd_5(PO_4)_6$ and $K_3Eu_5(PO_4)_6$ at 298 K are 675.9 J K^{-1} mol^{-1} and 722.35 J K^{-1} mol^{-1}, respectively. Further the standard free energy of formation $(\Delta_f G^0_T)$ and their temperature dependencies were obtained from enthalpy increments. The obtained thermodynamic functions and stabilities of the compounds can be useful for predicting their usage as matrix for nuclear waste immobilization as well as for other high temperature applications [206].

9.3.2. Experimental techniques

The title samples were synthesized by solid state reaction between KH_2PO_4, $NH_4H_2PO_4$ and Ln_2O_3 (Ln=Gd and Eu) by the procedure reported earlier for the synthesis of $K_3Gd_5(PO_4)_6$ [207]. The final sintered $K_3Ln_5(PO_4)_6$ (Ln= Eu and Gd) samples were characterized by powder X-ray diffraction.

9.3.3 High temperature calorimetry studies

A high temperature Calvet calorimeter (Model HT-1000, M/s. Setaram, France) was employed for all the calorimetric experiments. The standard molar enthalpies of dissolution of $K_3Ln_5(PO_4)_6$ (Ln = Gd and Eu) compounds and their binary constituent oxides viz.,

Gd_2O_3(s), Eu_2O_3(s), K_2O(s) and P_2O_5(s) in liquid Na_2O + MoO_3 (3:4 molar ratio) solvent at 985 K were investigated. The enthalpy calibration was carried out by comparing measured enthalpy increments of synthetic sapphire [NIST SRM-720] with its literature values [208]. The details of the calorimeter and experimental procedure have been described in literature [209]. The synthesis and characterization of Na_2O + MoO_3 (3:4 molar ratio) solvent were carried out as per the reported literature [210]. The Na_2O + MoO_3 (3:4 molar ratio) solvent was characterized by SEM chemical analysis and XRD techniques. The atom % of Mo, Na and O obtained from the chemical analysis of the solvent were found to be 15.9 ± 0.2, 24.3 ± 0.3 and 59.8 ± 0.4, respectively which are in agreement with the expected values 16, 24 and 60 atom percent. No other chemical impurity was observed in the elemental analysis of the solvent. Sample powder from the same lot was used for all the enthalpy measurements.

About 6g of Na_2O + MoO_3 solvent was taken in two identical platinum tubes (protective liner) having outer diameter matching exactly with the alumina reaction cell and this ensured proper thermal contact with the reaction cell. The reaction cell assembly was slowly introduced into the calorimeter maintained at 985 ± 0.05 K. The alumina reaction tubes were equilibrated with the calorimeter till a steady heat flux signal was obtained. Heat effects due to loss of any volatile components was same in the sample and reference cells hence got nullified in the resulting signal, a steady base line of the differential heat flow signal (slope nearly zero) is obtained. Reactants in the form of tiny pellets (about few milligrams) were dropped from room temperature to the reaction cell containing liquid solvent maintained at 985 K and the corresponding enthalpy change was determined by integrating the heat flow signal with respect to time. For each dissolution experiment, reaction time was determined by recording the heat flow signal (J/g) for different time intervals. Steady base line in the heat flow signal was observed after 3600 seconds of sample dropping beyond which no significant change in the heat flow values could be noticed.

The heat flow signals were recorded for same time period for all the experiments. For each experiment, fresh solvent was loaded in order to maintain similar dilution condition. Amount of the sample dropped into solvent was chosen in such a manner that the condition of infinite dilution is always maintained. After each measurement, the sample was slowly withdrawn from the calorimeter chamber and allowed to cool to room temperature. The SEM-EDS analysis of the dissolved samples was carried out in order to confirm uniform distribution of solute particles in the solvent [206].

9.3.4. Heat capacity measurements

The enthalpy increments (H_T–H_{298}) of the $K_3Ln_5(PO_4)_6$ (Ln = Gd and Eu) compounds were measured in between the temperature range 325 K to 936 K using a high temperature Calvet calorimeter following the drop technique. The sample pellets were first annealed in air at 1173 K for 24 h and brought into room temperature under the flow of argon gas. Tiny pellets were maintained at 298 K and dropped into the sample cell equilibrated at constant desired temperature. The heat flow signal accompanying the sample drop was recorded under isothermal condition and calculated to obtain its enthalpy increments.

9.3.5. Results and discussion

9.3.5.1. Ambient temperature structural studies

Observed XRD patterns of $K_3Gd_5(PO_4)_6$ and $K_3Eu_5(PO_4)_6$ are found to agree well with that of X-ray diffraction pattern reported earlier for $K_3Gd_5(PO_4)_6$[158]. The powder XRD patterns of both were analyzed with the model structures based on the structural data reported earlier for $K_3Gd_5(PO_4)_6$ (monoclinic, Space Group: C2/c) [207]. The observed unit cell parameters for $K_3Gd_5(PO_4)_6$ are: a = 17.4686(9) Å, b = 6.9283(4) Å, c = 18.1087(1) Å and β = 114.415(4)°, V = 1995.68(2) Å^3 and those for $K_3Eu_5(PO_4)_6$ are: a = 17.4978(1) Å, b = 6.9482(5) Å, c = 18.1489(1) Å and β = 114.483(5)°, V = 2008.10(2) Å^3. Typical Rietveld refinement plots for $K_3Gd_5(PO_4)_6$ and $K_3Eu_5(PO_4)_6$, are shown in Fig.9.3.

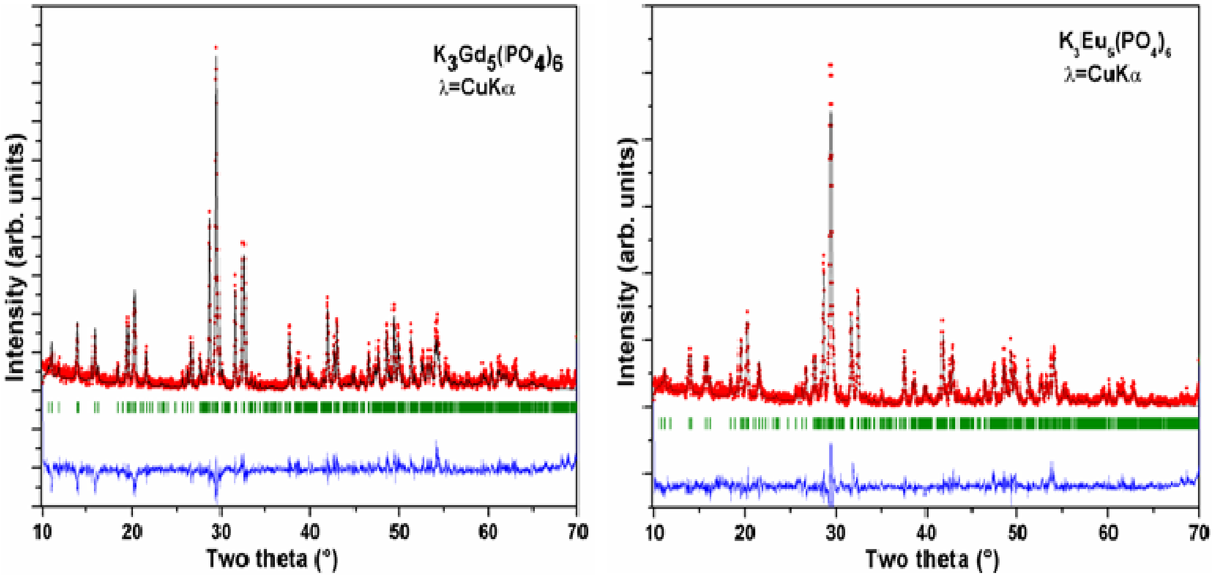

Fig.9.3: Rietveld refinement plot of the $K_3Gd_5(PO_4)_6$ and $K_3Eu_5(PO_4)_6$

The crystal structure of $K_3Ln_5(PO_4)_6$ (Ln = Gd and Eu) can be envisaged as three dimensional array of $Ln_5(PO_4)_6^{3-}$ clusters and K^+ ions. The LnO_8 and LnO_9 polyhedra in the present structure are similar to those in zircon and monazite type structures respectively. The three dimensional arrangement of arrangement of LnO_8, LnO_9 and PO_4 units in the structure of $K_3Ln_5(PO_4)_6$ is shown in Fig. 9.5.

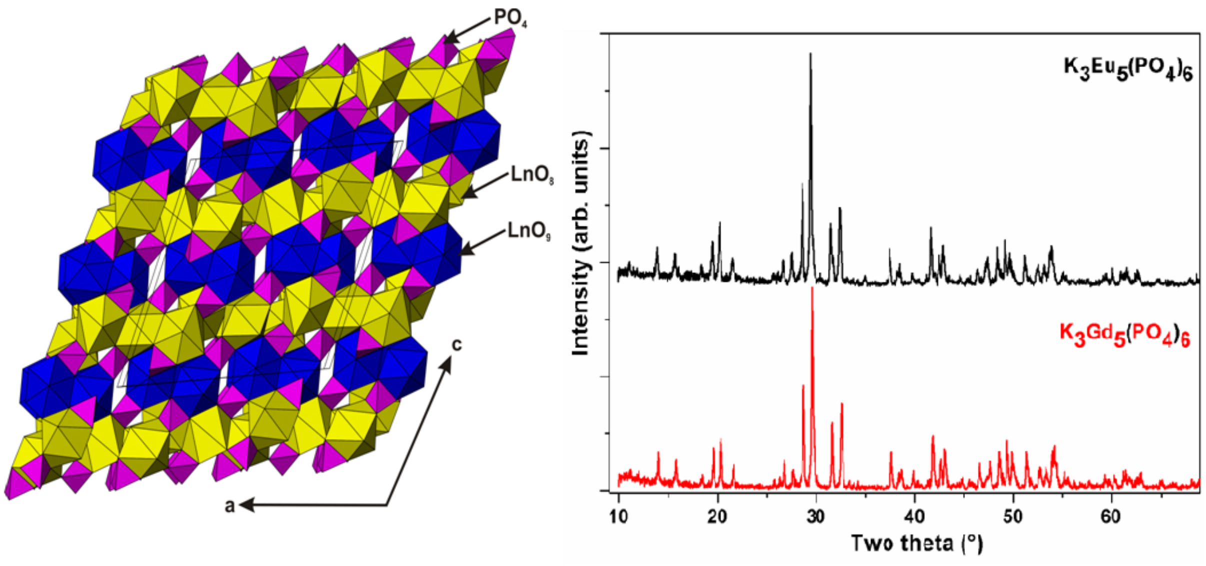

Fig.9.4: Arrangement of LnO_n and PO_4 polyhedra and XRD pattern of $K_3Ln_5(PO_4)_6$

9.3.5.2. Standard molar enthalpy of formation of $K_3Ln_5(PO_4)_6$ (Ln = Gd and Eu)

The standard molar enthalpies of formation of $K_3Ln_5(PO_4)_6$ (Ln = Gd and Eu) compounds were determined from their heat of dissolution data and molar heat of dissolution values of constituent binary compounds Gd_2O_3(s), Eu_2O_3(s), K_2CO_3(s) and P_2O_5(s) in liquid Na_2O + MoO_3 (3:4 molar ratio) solvent at 985 K. As K_2O is difficult to handle in air, K_2CO_3(s) was chosen instead of K_2O to determine the heat of dissolution of K_2CO_3(s).

Heat flow signals for the dissolution of $K_3Ln_5(PO_4)_6$ (Ln = Gd and Eu), Gd_2O_3(s), Eu_2O_3(s) and K_2CO_3(s) in Na_2O + MoO_3 solvent (3:4 molar mixture) at 985 K are presented in Fig.9.5. Dissolution of $K_3Ln_5(PO_4)_6$ (Ln = Gd and Eu) and K_2CO_3(s) compounds resulted in endothermic signals, whereas for Gd_2O_3(s) and Eu_2O_3(s) net exothermic signals were observed. The observed heat flow signals could be attributed to the sum of the heat effects due to (i) heating of sample from 298 to 985 K (ii) lattice dissociation (iii) enthalpy change due to chemical interactions. The signals due to chemical interactions are generally exothermic in nature, whereas first two effects are endothermic in nature. Depending upon the magnitude of these heat effects the net heat flow signal can be exothermic or endothermic.

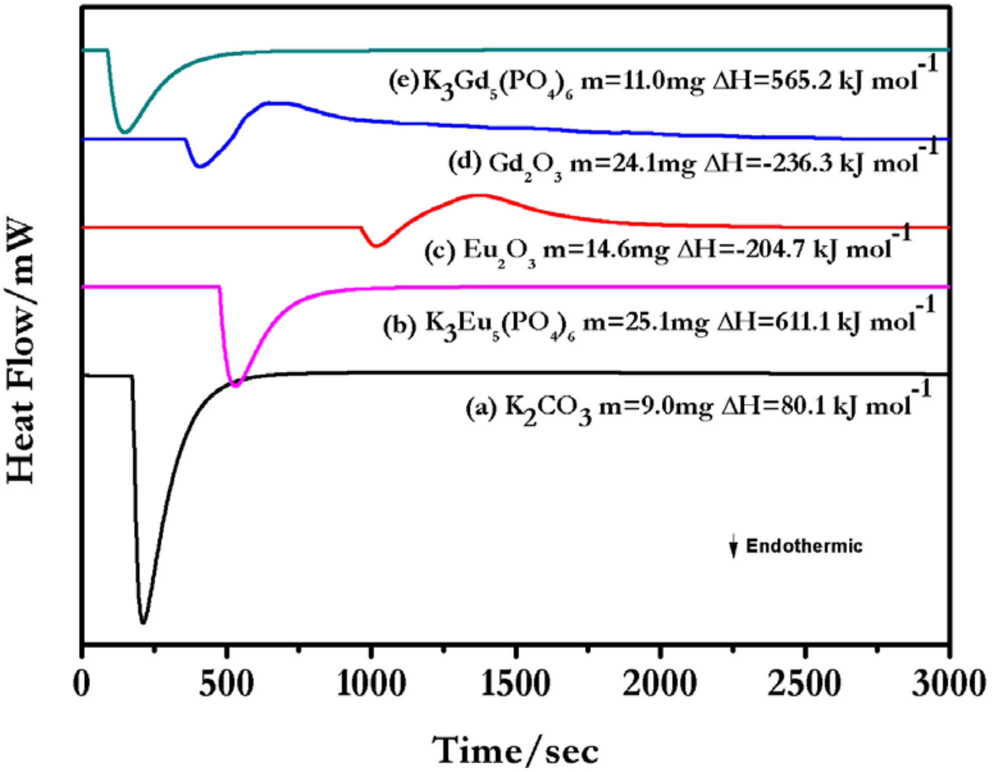

Fig.9.5: Typical heat flow signal after dropping the sample into Na_2O-MoO_3 melt with time

The endothermic signals for $K_3Ln_5(PO_4)_6$ (Ln = Gd and Eu) indicate that the lattice dissociation energy predominates over the heat effects due to chemical interactions. The net exothermic heat effect observed in case of Gd_2O_3(s), Eu_2O_3(s) could be due to the interaction of these oxides with the solvent (solute-solvent interaction) resulting in the formation of some intermediate products. The overall heat effect for dissolution was calculated employing the SETSOFT software supplied along with the instrument [211].

DTA analysis of the sample containing 100 mg of solvent and 20 mg of the $K_3Ln_5(PO_4)_6$ (Ln = Gd and Eu) recorded from room temperature to 1273 K (Fig.9.6) results several endothermic/exothermic peaks below 950 K. The appearance of endothermic/exothermic peaks after melting of solvent (812 K) is indicative of multi stage solvent solute interactions which are not observed beyond 950 K. XRD analysis of DTA residue did not show any peak due $K_3Gd_5(PO_4)_6$ or $K_3Eu_5(PO_4)_6$.

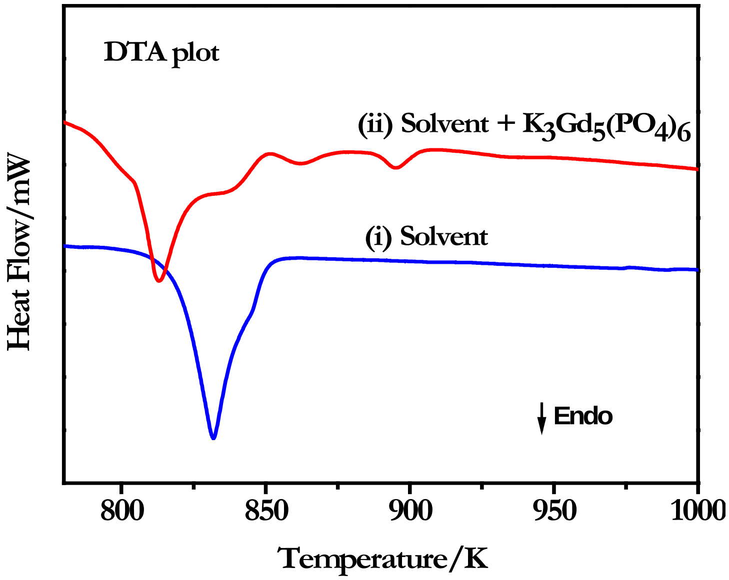

Fig.9.6: DTA plot of (i) solvent (ii) solvent + $K_3Gd_5(PO_4)_6$ compound

The uniform distribution of elements and complete disintegration of the compounds in the solvent were further confirmed by the SEM-EDS analysis. About 50 mg sample was equilibrated with 1 g of solvent at 973 K for 2 h and solidified products were characterized by SEM-EDS. Uniform distribution of elements in the solvent matrix is concluded by mapping the emitted X-rays in EDS studies (Fig.9.7). Presence of $K_3Ln_5(PO_4)_6$ (Ln = Gd and Eu) phase was not observed in the solvent after equilibration and hence complete interaction of solute with solvent forming different products is concluded [206].

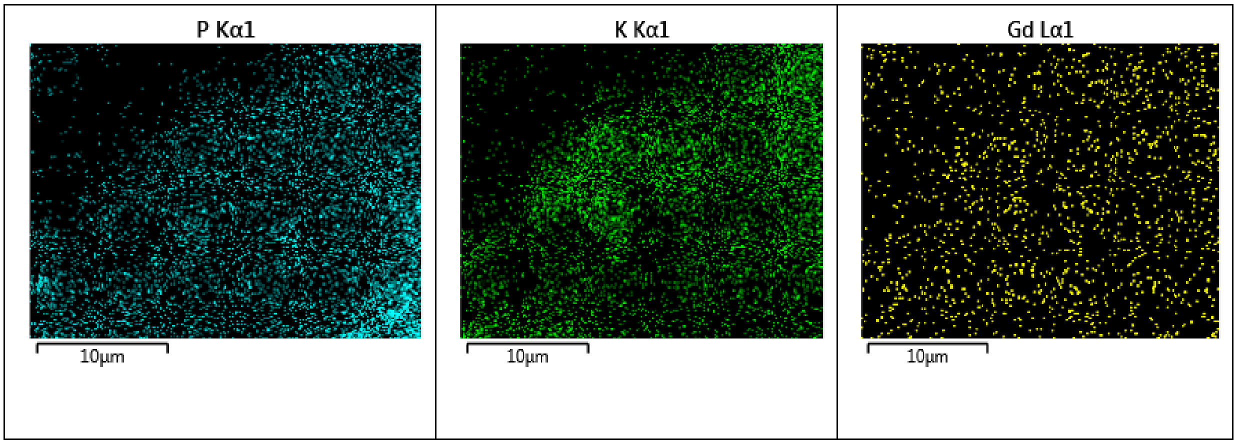

Fig.9.7: Elemental X-ray map of the samples equilibrated in the solvent at 985K showing uniform distribution of K, Gd and P ions

The molar heat of dissolution for $K_3Ln_5(PO_4)_6$ (M = Gd and Eu), Gd_2O_3(s), Eu_2O_3(s) and K_2CO_3(s) at T = 985 K plotted against their respective molar concentration resulted in a constant enthalpy value. In the present study, the average of four measurements for each sample was considered. The average enthalpy of dissolution for $K_3Gd_5(PO_4)_6$ and $K_3Eu_5(PO_4)_6$ are 555.5 ± 9.2 kJ mol^{-1} and 613.3 ± 2.8 kJ mol^{-1} respectively. For Gd_2O_3(s), Eu_2O_3(s) and K_2CO_3(s) enthalpy of dissolution were found to be -238.0 ± 2.0 kJ mol^{-1}, -201.5 ± 3.3 kJ mol^{-1} and 80.0 ± 0.3 kJ mol^{-1}, respectively. Since P_2O_5(s) is a highly hygroscopic and reactive material, the value of molar enthalpy of dissolution of P_2O_5(s) was therefore obtained from the heat of dissolution of $Ca_3(PO_4)_2$(s) and CaO(s) measured under exactly similar conditions. The average enthalpy of dissolution for CaO(s) and $Ca_3(PO_4)_2$(s) were found to be -92.88 ± 0.27 kJ.mol^{-1} and 262.97 ± 3.33 kJ.mol^{-1}, respectively**.** The details of the experimental measurements are similar to the that reported in literature [212]. The thermo-chemical cycle for derivation of standard molar enthalpies of dissolution of P_2O_5 (s, 298K) is given in Table 9.2.

Table 9.2: Thermo-chemical cycles for derivation of standard molar enthalpies of dissolution of P_2O_5(s, 298K) MO_x(sln) = dilute solution of species MO_x in 6g liquid Na_2O+MO_3 (3:4 molar ratio) solvent maintained at T = 985 K and P = 101.325 kPa, where, ΔH is the molar enthalpy. $\Delta_{ds}H^o_{298}(P_2O_5) = \Delta H_1 + \Delta H_2 - 3\Delta H_3 - 3\Delta H_4 - \Delta H_5$

Reactions	ΔH_i	ΔH kJ·mol^{-1}
$Ca_3(PO_4)_2$(s,298K) + (sln) = 3CaO(sln) + P_2O_5(sln)	ΔH_1	358.9±0.8
3Ca(s,298K) + 2P(s,298K) + 4O_2(g, 298K) = $Ca_3(PO_4)_2$(s,298K)	ΔH_2	-4120.8±11.6
CaO(s,298K) + (sln) = CaO(sln)	ΔH_3	-8.35±0.06
Ca(s,298K) + 0.5O_2(g,298K) = CaO(s,298K)	ΔH_4	-634.29±1.67
2P(s,298K) + 2.5O_2(g,298K) = P_2O_5(s,298K)	ΔH_5	-1504.9±0.5
P_2O_5(s,298K) + (sln) = P_2O_5(sln)	$\Delta_{ds}H^o_{298}$	-329.1±11.8

The standard molar enthalpies of formation of $K_3Ln_5(PO_4)_6$ (Ln = Gd and Eu) were derived using the thermo chemical cycles given in Table 9.3. The values for molar enthalpies of dissolution (ΔH_{disso}) of $K_3Ln_5(PO_4)_6$ (Ln = Gd and Eu), Gd_2O_3(s), Eu_2O_3(s), K_2CO_3(s), P_2O_5(s) were combined together with other auxiliary data such as standard molar enthalpies of formation of Gd_2O_3(s), Eu_2O_3(s), K_2CO_3(s) and P_2O_5(s) from the literature[213] to derive standard molar enthalpy of formation of $K_3Ln_5(PO_4)_6$ (Ln = Gd and Eu) at 298K. The standard molar enthalpy of formation of $K_3Ln_5(PO_4)_6$ (Ln = Gd and Eu) at 298K are found to be -11754.4, -11310.5 kJ mol^{-1}, respectively. $\Delta_f H°_{298\ K}$ of $K_3Ln_5(PO_4)_6$ (Ln = Gd, Eu) = $-\Delta H_{1M} + \frac{3}{2}\Delta H_2 + \frac{5}{2}\Delta H_3 + 3\,\Delta H_4 - \frac{3}{2}\Delta H_5 + \frac{3}{2}\Delta H_6 + \frac{5}{2}\Delta H_7 + 3\Delta H_8$. Where ΔH_{1M} is standard molar enthalpy of dissolution of $K_3M_5(PO_4)_6$ at 298 K, ΔH_{7M} is standard molar enthalpy of formation of M_2O_3 at 298 K, $\Delta_fH^o_{298\ K,M}$ is standard molar enthalpy of formation of $K_3M_5(PO_4)_6$ at 298 K

Table 9.3: Thermo chemical cycle for derivation of standard molar enthalpies of formation of $K_3M_5(PO_4)_6$ (M = Gd and Eu) compounds; MO_x(sln) = dilute solution of species MO_x in 6g Na_2O + MoO_3 3:4 molar solvent maintained at 985 K

Reactions	ΔH_i	ΔH (kJ mol^{-1})
$K_3M_5(PO_4)_6$ (s, 298K) + (sln) = $\frac{3}{2}$ K_2O(sln) + $\frac{5}{2}$ M_2O_3(sln) + 3 P_2O_5(sln)	ΔH_{1Gd}	555.5 ± 9.2
	ΔH_{1Eu}	613.3 ± 2.8
K_2CO_3(s, 298K) + (sln) = K_2O(sln) + CO_2 (g, 298 K)	ΔH_2	80.0 ± 0.3
M_2O_3(s, 298K) + (sln) = M_2O_3(sln)	ΔH_{3Gd}	-238.0 ± 2.0
	ΔH_{3Eu}	-201.5 ± 3.3
P_2O_5(s, 298K) + (sln) = P_2O_5(sln)	ΔH_4	-329.1±11.8
C (s, 298 K) + O_2(g, 298 K) = CO_2 (g, 298 K)	ΔH_5	-393.5 ± 3.9
2 K (s, 298 K) + C (s, 298 K) + $\frac{3}{2}$ O_2(g, 298 K) = K_2CO_3 (s, 298K)	ΔH_6	-1150.2 ± 11.5
2 M (s, 298K) + $\frac{3}{2}$ O_2(g, 298 K) = M_2O_3(s, 298 K)	ΔH_{7Gd}	-1826.9 ± 18.3
	ΔH_{7Eu}	-1662.7 ± 16.6
2 P (s, 298K) + $\frac{5}{2}$ O_2(g, 298 K) = P_2O_5(s, 298 K)	ΔH_8	-1504.9 ± 0.5
3 K (s, 298K) + 5 (s, 298K) + 6 P (s, 298K) + 12 O_2 (g, 298 K) = $K_3M_5(PO_4)_6$ (s, 298K)	$\Delta_fH^o_{298\ K,Gd}$	-12234.8 ± 61.5
	$\Delta_fH^o_{298\ K,Eu}$	-11790.9 ± 58.2

9.3.5.3. Enthalpy increment and heat capacity

The enthalpy increment (H_T–H_{298}) values for $K_3Ln_5(PO_4)_6$(s) (Ln= Gd and Eu) obtained at different temperatures are given in Table 9.4. The values of enthalpy increment were found to be reproducible within ± 0.05%. The measured enthalpy increment values were fitted into a 4-term polynomial function of temperature using Shomate's method [214]. The expressions of H_T–H_{298} for $K_3Gd_5(PO_4)_6$(s) and $K_3Eu_5(PO_4)_6$(s) can be given as:

$$\mathrm{H_T - H_{298}}(K_3Gd_5(PO_4)_6, \mathrm{s}) = 468.5\ \mathrm{T} + 0.2412T^2 - \frac{5.648*10^6}{\mathrm{T}} - 142187.8 \tag{9.1}$$

$$\mathrm{H_T - H_{298}}(K_3Eu_5(PO_4)_6, \mathrm{s}) = 651.9\ \mathrm{T} + 0.1998T^2 + \frac{4.330*10^6}{\mathrm{T}} - 226643.9 \tag{9.2}$$

Table 9.4: Enthalpy increment (H_T–H_{298}) values for $K_3Gd_5(PO_4)_6$(s) and $K_3Eu_5(PO_4)_6$(s)

T/K	**$K_3Gd_5(PO_4)_6$**			**$K_3Eu_5(PO_4)_6$**		
	H_T-H_{298} (Measured Value) ($J.mol^{-1}$)	**H_T-H_{298}** (Fit Value) ($J.mol^{-1}$)	**% Error**	**H_T-H_{298}** (Measured Value) ($J.mol^{-1}$)	**H_T-H_{298}** (Fit Value) ($J.mol^{-1}$)	**% Error**
324.9	19448.5	18113.0	6.87	19570.3	19573.2	-0.01
350.2	37128.9	35410.9	4.63	41665.3	38516.7	7.56
375.5	57314.1	52711.7	8.03	64450.5	57922.9	10.13
400.1	73521.2	70391.8	4.26	82725.4	77614.4	6.18
426.5	96653.1	88271.3	8.67	108770.7	97807.9	10.08
477.2	135255.4	124484.5	7.96	152130.5	139017.0	8.62
528.2	162954.7	161890.5	0.65	183405.2	181635.2	0.97
579.4	194484.8	200503.1	-3.09	219794.9	225447.5	-2.57
630.2	238980.6	239833.5	-0.36	268880.2	270505.7	-0.60
681.3	276698.9	280610.9	-1.41	311260.4	316515.7	-1.69
732	319131.9	322387.8	-1.02	359050.3	363539.2	-1.25
783.3	365985.1	365596.2	0.11	411720.5	412034.7	-0.08
834.3	413132.9	409831.7	0.80	464780.4	461527.7	0.70
885.3	452913.9	455180.9	-0.50	509540.5	512103.6	-0.50
935.9	503745.2	501552.3	0.44	566754.2	563143.4	0.64

The heat capacities of $K_3Ln_5(PO_4)_6$(s) (Ln= Gd and Eu) at 298 K ($C^0_{p,298}$) were estimated from the values of $C^0_{p,298}$ of K_3PO_4 (s) and $LnPO_4$ (s) (Ln= Gd and Eu) [213b, 215] by applying Neuman-Kopp's molar additive rule. The standard molar heat capacity (Cp°) values of these compounds derived by differentiating the above enthalpy increment expressions with respect to temperature and the obtained values for $K_3Gd_5(PO_4)_6$(s) and $K_3Gd_5(PO_4)_6$(s) are 675.9 $J.mol^{-1}.K^{-1}$ and 722.3 $J.mol^{-1}.K^{-1}$ respectively [206].

9.3.5.4. Construction of thermodynamic tables for $K_3M_5(PO_4)_6$(s) (M= Gd and Eu)

The standard molar enthalpy of formation ($\Delta_f H^0_{298}$) of $K_3Gd_5(PO_4)_6$(s) and $K_3Gd_5(PO_4)_6$(s) are determined using high temperature calorimeter. The standard molar heat capacity Cp° of the compounds was derived from the measured enthalpy increment data. The standard molar entropy (S^0_{298}) of $K_3Gd_5(PO_4)_6$(s) and $K_3Gd_5(PO_4)_6$(s) have been estimated by adding the standard molar entropies (S^0_{298}) of component phosphates in their respective molar ratio from the literature [213b]. The values of the standard molar enthalpy and entropy for $K_3Ln_5(PO_4)_6$(s) (Ln= Gd and Eu) as a function of temperature are listed in Tables 9.5 and Table 9.6. The Gibbs energy of the compound at any temperature T was calculated from the combined values of standard molar enthalpy and standard molar entropy for the compound using the relation:

9.3.5.5. Standard Gibbs energy of formation of $K_3Ln_5(PO_4)_6$(s) (Ln= Gd and Eu)

Gibbs energy of formation of $K_3Ln_5(PO_4)_6$(s) (Ln= Gd and Eu) were derived using the standard enthalpies of formation data of the compound together with their respective standard heat capacity change ΔCp^0 and estimated entropy change ΔS^0_{298} for the formation reaction using the relation:

$$\Delta_f G^0_T = \Delta_f H^0_{298} + \int_{298}^{T} \Delta_f\, Cp^0 dT - T \times \left[\Delta_f S^0_{298} + \int_{298}^{T} \frac{\Delta_f Cp^0}{T} dT\right] \qquad (9.3)$$

$\Delta_f Cp^0$ for $K_3Ln_5(PO_4)_6$(s) (Ln= Gd and Eu) were estimated considering the formation reactions 3K (s) + 5Ln(s) + 6P(s,l) + $12O_2$ (g) = $K_3Ln_5(PO_4)_6$(s) (Ln= Gd and Eu)

Table 9.5: Thermodynamic data for $K_3Gd_5(PO_4)_6$

T/K	Cp°_m (J.mol^{-1}.K^{-1})	S°_T (J.mol^{-1}.K^{-1})	$-H^\circ_T$ (kJ.mol^{-1})	$-G^\circ_T$ (kJ.mol^{-1})	$-\frac{(G^\circ_T - H^\circ_{298})}{T}$ (J.mol^{-1}.K^{-1})	$-\Delta_f H^\circ_m$ (kJ.mol^{-1})	$-\Delta_f S^\circ_m$ (J.mol^{-1})	$-\Delta_f G^\circ_m$ (kJ.mol^{-1})
300	675.9	838.7	12233.5	12485.2	834.6	12235.0	2407.9	11512.6
400	696.6	1035.5	12165.1	12579.3	861.3	12242.7	2430.2	11270.6
500	732.1	1194.6	12093.8	12691.0	912.5	12247.5	2441.3	11026.9
600	773.4	1331.6	12018.5	12817.5	971.1	12249.4	2444.8	10782.6
700	817.4	1454.1	11939.0	12956.9	1031.5	12248.2	2443.0	10538.1
800	862.9	1566.2	11855.0	13108.0	1091.5	12243.9	2437.2	10294.1
900	909.3	1670.6	11766.4	13269.9	1150.1	12236.4	2428.4	10050.8
1000	956.2	1768.8	11673.1	13441.9	1207.1	12225.7	2417.2	9808.5

The heat capacity of $K_3Ln_5(PO_4)_6$(s) (Ln= Gd and Eu) have been measured in this work by drop calorimetric method, whereas the heat capacities of the constituent elements have been taken from the literature [210, 212]. Similarly the $\Delta_f S^0_{298}$ of $K_3Ln_5(PO_4)_6$(s) (Ln= Gd and Eu) were calculated from the estimated S^0_{298}values for the compound together with S^0_{298}values for the constituent elements. The estimated standard molar entropy of formation

$\Delta_f S^0_{298}$ of ($K_3Ln_5(PO_4)_6$(s) (Ln= Gd and Eu) were found to be -2407.4 $\mathrm{J.mol^{-1}.K^{-1}}$, -2493.6 $\mathrm{J.mol^{-1}.K^{-1}}$ respectively. The standard molar free energy of formation ($\Delta_f G^0_T$) of $K_3Ln_5(PO_4)_6$(s) (Ln= Gd and Eu) calculated using standard molar enthalpy of formation ($\Delta_f H^0_{298}$), estimated standard molar entropy of formation ($\Delta_f S^0_{298}$) and the calculated standard molar heat capacity change for the formation ($\Delta_f Cp^0$) of compounds are listed in Table 9.5 and Table 9.6 [206].

Table 9.6: Thermodynamic data for $K_3Eu_5(PO_4)_6$

T/K	Cp°_m (J.mol^{-1}.K^{-1})	S°_T (J.mol^{-1}.K^{-1})	-H°$_T$ (kJ.mol^{-1})	-G°$_T$ (kJ.mol^{-1})	$\frac{-(G^\circ_T - H^\circ_{298})}{T}$ (J.mol^{-1}.K^{-1})	$-\Delta_f H^\circ_m$ (kJ.mol^{-1})	$-\Delta_f S^\circ_m$ (J.mol^{-1})	$-\Delta_f G^\circ_m$ (kJ.mol^{-1})
300	723.7	802.2	11789.6	12030.2	797.7	11790.8	2493.2	11042.8
400	784.7	1019.2	11714.0	12121.7	826.9	11780.6	2473.8	10791.1
500	834.4	1199.7	11633.0	12232.8	883.9	11764.8	2455.8	10536.9
600	879.7	1355.9	11547.2	12360.8	949.8	11743.8	2437.6	10281.3
700	922.9	1494.8	11457.1	12503.5	1017.9	11717.8	2419.0	10024.5
800	964.9	1620.8	11362.7	12659.3	1085.5	11686.9	2400.0	9766.9
900	1006.3	1736.8	11264.1	12827.3	1151.5	11651.2	2380.6	9508.7
1000	1047.3	1845.0	11161.5	13006.4	1215.5	11610.7	2360.8	9249.9

9.3.6. Conclusions

Structural and thermodynamic properties of two complex phosphates (viz., $K_3Gd_5(PO_4)_6$(s) and $K_3Eu_5(PO_4)_6$(s)), have been determined from X-ray diffraction and calorimetric investigations. The standard molar heat capacity of these compounds derived from enthalpy increment data could be expressed as:

$$C^\circ_{p,m}(K_3Gd_5(PO_4)_6, \mathrm{s}) = 468.5 + 0.482\mathrm{T} + \frac{5.645*10^6}{\mathrm{T}^2} \text{ and}$$

$$C^{\circ}_{p,m}(K_3Eu_5(PO_4)_6, s) = 651.9 + 0.400T + \frac{4.330 * 10^6}{T^2}.$$

The standard molar enthalpies of formation of $K_3Ln_5(PO_4)_6$(s) (Ln= Gd and Eu) at 298 K were found to be -12234.8 ± 61.5 and -11790.9 ± 58.2 kJ mol^{-1}, respectively. The information on thermodynamic properties of $K_3Ln_5(PO_4)_6$(s) (Ln= Gd and Eu) will be useful for optimization of conditions and predicting their behavior during nuclear waste immobilization as well as in usage of these materials at higher temperature.

9.4. Preparation, thermal and magnetic properties of $Mn_5(HPO_4)_2(PO_4)_2$ $4H_2O$

9.4.1. Introduction

Framework metal phosphates, in particular open framework materials of transition metal ions have been of research interest due to their wide spectrum of technological applications, like absorbents, ion exchangers, and catalysts as well as basic crystal-chemistry and fundamental molecular magnetic materials [216]. In view of this, a number of framework materials, metal oxide framework and organic-inorganic hybrid materials are being investigated due to their tunable structural features. Often the properties of such materials are governed by the clusters of the magnetic ions. Depending on the nature of magnetic ions and interaction of intra and inter-cluster interactions, the magnetic property are diversified and varies with the strength of external parameters, like electrical or magnetic field as well as electromagnetic radiations. Often the magnetic properties of such materials are governed by the clusters of the magnetic ions. $Mn_5(HPO_4)_2(PO_4)_2$ $4H_2O$ [here after named as MnHPO] is one such phosphate mineral which occurs in nature with a wide varieties magnetic and nonmagnetic divalent cations [217]. Though the mineral has been investigated for its crystal structure, the magnetic properties have been explored recently by Li *et al.* [218] A complex antiferromagnetic behavior with non-vanishing magnetic moment has been reported for this material. In order to understand the fundamental properties of complex phosphates, the title complex phosphate (MnHPO) was prepared and investigated its stability and magnetic properties and they are explained in the following sections.

9.4.2. Experimental

An appropriate amount of ammonium dihydrogen phosphate was added slowly to the saturate solution of $MnCl_2.4H_2O$ at 60˚C while stirring the solution constantly. The precipitate was filtered out and washed several times with distilled water and then dried at ambient temperature followed by heating at 100°C in air. The obtained product was characterized by powder X-ray diffraction data recorded on a powder X-ray diffractometer (Rigaku, Japan) using monochromatic Cu Kα radiation. Thermal stability of the sample was studied by thermogravimetry using Setaram thermobalance by heating the sample from ambient to 600°C in air. Magnetic properties of the samples were investigated (between 1 to 300K) by using physical property measurement system (9T PPMS; Quantum Design).

9.4.3. Result and discussion

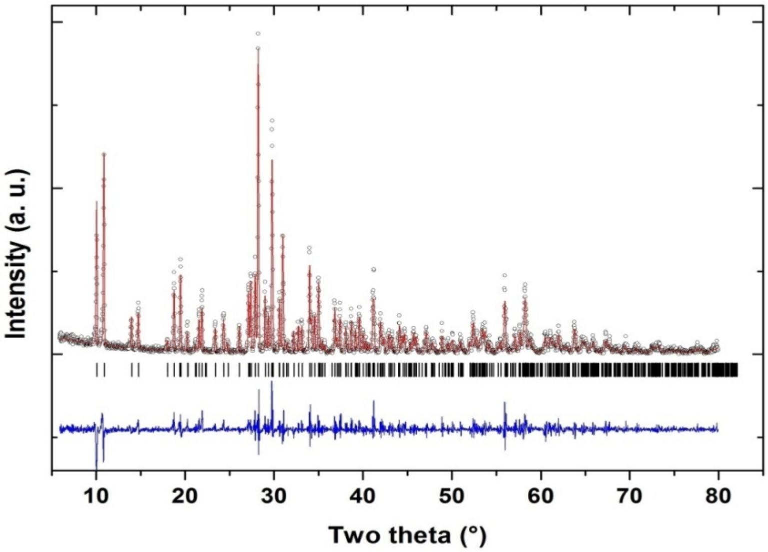

Fig.9.8: Powder XRD pattern of $Mn_5(HPO_4)_2(PO_4)_2$ $4H_2O$

The typical powder XRD pattern of the light pink colored precipitate is shown in Fig.9.8. Rietveld analysis of the powder XRD pattern was carried and the refined unit cell parameters are a = 17.6093(7) Å, b = 9.1376(4) Å, c = 9.4999(4) Å, β = 96.605(4)°; V = 1518.4(1) Å^3, Monoclinic, space group C2/c. These values are in good agreement with those reported in literature [217].

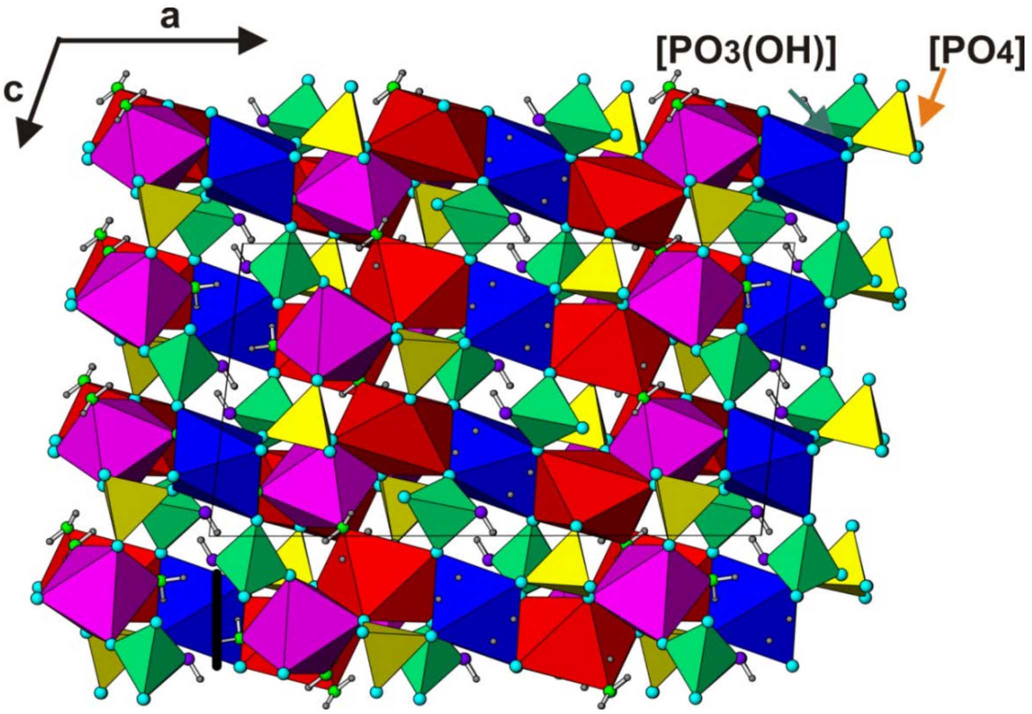

Fig.9.9: Crystal structure of $Mn_5(HPO_4)_2(PO_4)_2\ 4H_2O$

The crystal structure of the MnHPO is formed by a complex arrangement of five edge shared MnO_6 octahedra. The clusters of these octahedra are linked with each other by phosphate groups through corner sharing of one of the octahedra. In such arrangements, all the Mn^{2+} ions have strong interactions due shorter Mn^{2+}-Mn^{2+} distances (3.35-3.80Å). However the square and tetrahedral sub-lattices of Mn^{2+} ions are likely to have a unique feature in their magnetic properties. Typical crystal structure of MnHPO is shown in fig.9.9.

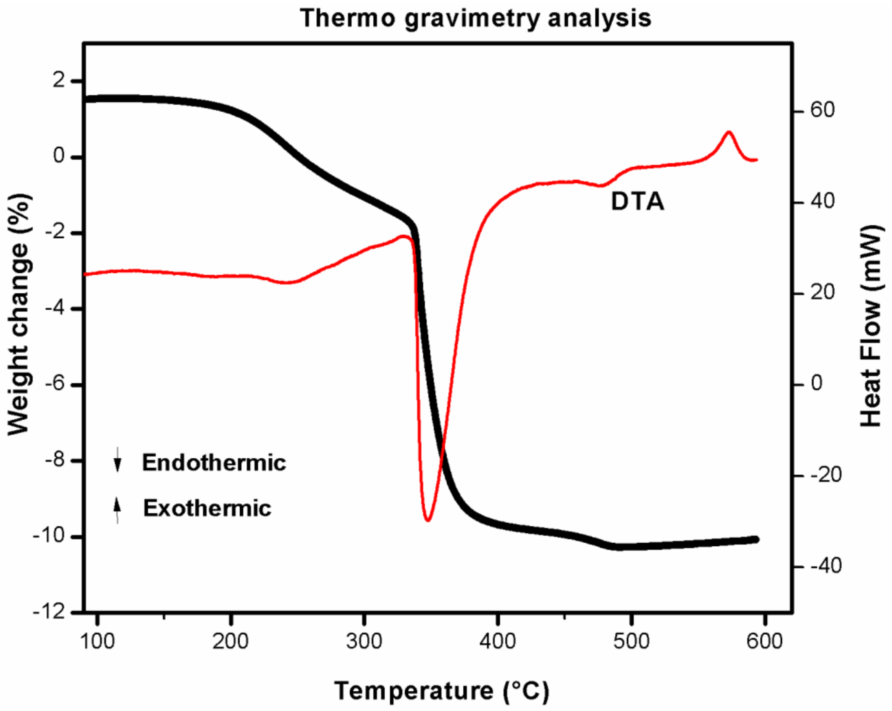

Fig.9.10: TG-DTA traces of MnHPO

Typical TG-DTA traces recorded from ambient temperature to 600°C are shown in Fig.9.10. A total mass loss of about 12.0 % is observed in three steps equivalent for the loss of 5 water molecules in the sample (12.3 %). The XRD analysis of the TG residue indicate the formation of $Mn_2P_2O_7$ and $Mn_3(PO_4)_3$ along with small amounts of an unidentified phase. It can be seen from the DTA traces, three weight loss steps of the sample are accompanied as endothermic peaks in DTA. However, a weak exothermic peak around 580°C without any appreciable weight change might be due to a partial oxidation of the Mn^{2+}.

The temperature dependent magnetization in between 2 to 300 K measured in field cooled (FC) and zero field cooled (ZFC) conditions are shown in Fig.9.11. A sharp increase in magnetization in both FC and ZFC is observed around 6.0 K, while no visual anomaly in between 6 to 300 K is noticed in both the curves. The observed transition is slightly lower than that reported by Li *et al*. (~ 7.4 K) [218]. The observed magnetic behavior is not exactly similar to that observed by Li *et al*. They have not observed saturations in the magnetization and rather observed sharp decrease in ZFC and FC magnetization at lower temperature.

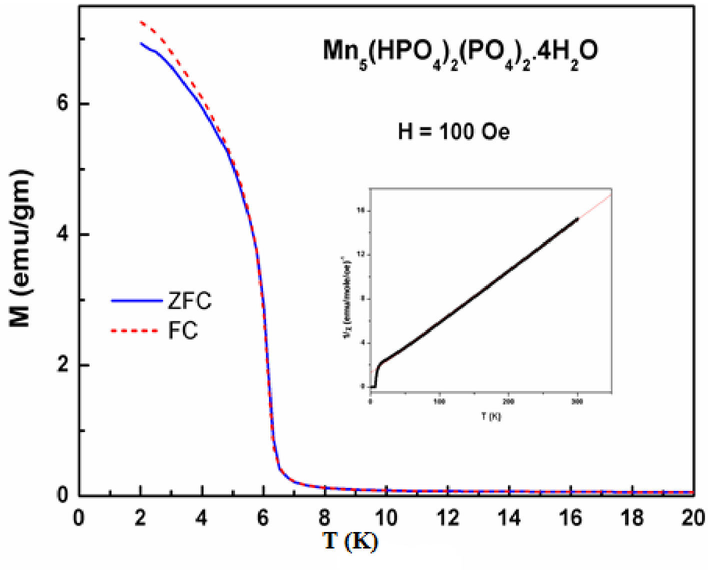

Fig.9.11: Magnetization variation with temperature of MnHPO

The effective magnetic moment (μ_{eff}) of the Mn^{2+} and Weiss constant (θ) obtained are 2.62 μ_B and -26.5K, respectively. The observed θ/Tc (~ 4.2) is similar to non-frustrated ferromagnetic type ordering [219]. Thus the system is likely to have coexisting ferromagnetic and antiferromagnetic interactions. The negative value of Weiss constant and appreciably lower values of magnetic moment suggests dominating antiferromagnetic interaction among the Mn^{2+} ions. From the structural analysis of the studied compounds shorter Mn-Mn separation can lead to such antiferromagnetic interactions. However, the inter cluster (through the apex oxygen) interaction can be ferromagnetic due to larger separations. Thus the magnetic properties are expected to be governed by these two competing anti-ferro and ferromagnetic interactions.

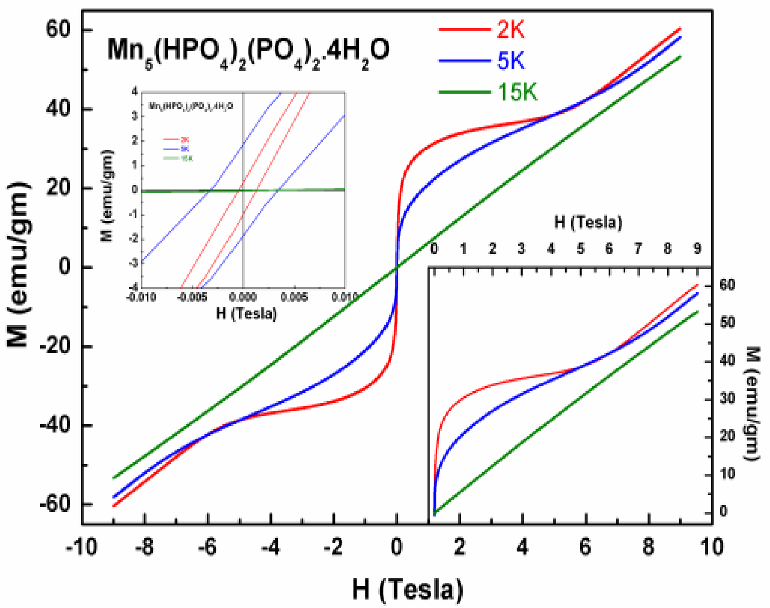

Fig.9.12: Magnetization variation of MnHPO with magnetic field

The field dependent magnetizations at several temperatures have been recorded and they are shown in Fig. 9.12. No hysteresis loop is observed at 15 K, which is similar to any paramagnetic materials. However, at lower temperature the magnetization increases sharply with a small field and tends to saturate within field of 2T. Beyond 2T, the magnetization rises linearly due to the antiferromagnetic interactions. A small coercive fields of ~ 40 Oe arises from ferromagnetic ordering in the clusters. Once the FM saturation occurs, the signature of AFM is clearly observed in this complex magnetically ordered system.

9.4.4. Conclusions

A complex phosphate $Mn_5(HPO_4)_2(PO_4)_2$ $4H_2O$ was prepared and thermal stability, crystal structure have been concluded. A ferromagnetic like transition with low coercive field is observed in $Mn_5(HPO_4)_2(PO_4)_2$ $4H_2O$ around 6 K. Interplay of ferromagnetic and antiferromagnetic interactions govern its magnetic behavior.

Chapter 10

Summary and future scope

10.1. Summary of the present thesis

Aim of the present thesis is to design various inorganic framework materials for selective separation of radionuclides from nuclear waste and lattices for immobilization of radionuclides. Crystal structure of a material plays an important role in designing materials in achieving desired property. In view of this, framework connected phosphates with different structures and properties, titanates with flexible structure and porous manganates were synthesized. Aim of synthesizing varieties of inorganic materials was solely for the nuclear back end applications.

$K_2Ce(PO_4)_2$ is a novel framework compound with cerium in +IV oxidation state. +IV oxidation state of cerium is not common in phosphate matrix and very few reports are available in literature. Potassium ions present along the tunnels get exchanged in presence of Sr^{2+} in solution. Characterization of Sr loaded samples revealed that Sr^{2+} ions are uniformly distributed throughout the lattice thus supporting the ion exchange mechanism. $K_2Zr(PO_4)_2$ belong to similar class of framework connected phosphates with layered structure. Ion exchange properties of this material are better than that of $K_2Ce(PO_4)_2$ because of layered structure of the material. $K_2Ce(PO_4)_2$ and $K_2Zr(PO_4)_2$ are promising materials for separation of ^{90}Sr from nuclear waste solutions and also convert into stable apatite or NZP type lattices by generating minimum secondary waste volume. To follow the high temperature stability of $K_2Ce(PO_4)_2$, *in-situ* variable temperature XRD studies have been carried out, which revealed that ambient temperature monoclinic phase remains unchanged at lower temperature while it transforms to a tetragonal structure at higher temperature. Observed phase transition is also confirmed by Raman spectroscopy as well as *ab initio* density functional theory (DFT) calculations. The high temperature tetragonal phase reverts to ambient monoclinic phase on cooling. Detailed structural analyses of the ambient and high temperature phases suggest a reconstructive 1st order type phase transition. Highly open and loosely packed structure of HT tetragonal phase shows anisotropic thermal expansion. High temperature behaviour of virgin $K_2Ce(PO_4)_2$ and Sr- $K_2Ce(PO_4)_2$ samples are different. The observed ion exchange characteristics and high temperature results reveal that $K_2Ce(PO_4)_2$ could be a promising material for separation and immobilization of ^{90}Sr from nuclear waste.

Manganese oxide minerals have been explored for separation of fission products from nuclear waste. Birnessite minerals with sodium and potassium ions as exchangeable ions have shown selectivity for separation of ^{90}Sr in presence of various other metal ions. Birnessite minerals are known for separation of heavy metal pollutants, but no reports are available for their stability in nuclear waste conditions. Na, K-birnessite minerals were characterized before and after ion exchange, which revealed that uniform distribution of Sr^{2+} ions throughout the lattice. Na-birnessite has shown high distribution constants compared to K-birnessite because of well defined crystal structure along with easy exchange of Na^+ ions in presence of Sr^{2+} ions. Na-birnessite mineral is further studied for separation of ^{90}Y from ^{90}Sr-^{90}Y equilibrium mixture to use as a radiopharmaceutical. Detailed ion-exchange experiments with $^{90}Sr/^{90}Y$ equilibrium mixture confirmed the high selectivity of synthetic sodium birnessite for Sr^{2+} ions. The conditions were optimized for efficient $^{90}Sr/^{90}Y$ radiochemical separation and ^{90}Y could be obtained with > 80 % separation yield. The quality of ^{90}Y obtained after the radiochemical separation met all the pharmaceutical requirements for clinical use. As a proof of concept, ^{90}Y-labeled dimeric cyclic RGD peptide derivative, DOTA-E[c(RGDfK)]$_2$ was formulated and its biological efficacy was established in C57/BL6 mice bearing melanoma tumors. This strategy may well be extended for radiochemical separation of other medically important radioisotopes.

Complex $K_3Gd_5(PO_4)_6$ has been synthesized expecting better ion exchangeability compared to $K_2Ce(PO_4)_2$ owing to high potassium content in the material. Potassium ions present in $K_3Gd_5(PO_4)_6$ are labile in nature, present for charge neutrality of the lattice. $K_3Gd_5(PO_4)_6$ but did not show appreciable exchange of K^+ ions with Sr^{2+} because movement of ions is not favorable due to helical arrangement K^+ ions in the tunnels. $K_3Gd_5(PO_4)_6$ is further investigated for its high temperature stability by *in-situ* variable temperature XRD studies in a wider temperature range from 20 to 1073K. The material is found to be stable in the studied temperature range and evolution of the unit cell parameters is anisotropic in nature. Thermal expansion and its anisotropy are largely controlled by the temperature effect on the GdO_n polyhedra and their linkages, temperature dependent Raman spectroscopic studies also indicated no structural change in the studied temperature range. The temperature and field dependent magnetic measurements indicated no long range magnetic ordering down to 2K. The field dependent magnetization and saturation at lower temperature suggests the superparamagnetic nature of the sample. Hollandite type $K_2Fe_2Ti_6O_{16}$ has been synthesized for nuclear back end applications, this lattice is found to be stable at high temperatures and pressures and a promising material for immobilization of nuclear waste. Several hollandite type titanates with composition $A_2Ti_6Fe_2O_{16}$ (A = Na, K and Cs) have been prepared and characterized. The structural characterization of materials at ambient temperature indicted that the structure varies with nature of alkali cation. High temperature stability of the Na and K analogous composition shows stability at higher temperature. Under high pressure the tetragonal $K_2Ti_6Fe_2O_{16}$ undergoes a phase transition at relatively lower pressure (~ 3.6 GPa).

The orthorhombic $Cs_2Ti_6Fe_2O_{16}$ is found to be stable up to 1000°C. These are the promising materials for immobilization of ^{137}Cs.

Many other phosphates like $KLn(PO_3)_4$, Ln=Ce, Eu have been investigated for their ion exchange characteristics in low acidic medium. Though the initial results were promising for the uptake of Cs^+ and Sr^{2+}, phosphate group leaches out into the solution and thus further studies were not carried out. Thermodynamic properties of $K_3Gd_5(PO_4)_6$ and its europium analogue $K_3Eu_5(PO_4)_6$ were investigated and the standard molar heat capacity have been derived from enthalpy increment data. The standard molar enthalpies of formation of $K_3Ln_5(PO_4)_6(s)$ (Ln= Gd and Eu) at 298 K were found to be -12234.8 ± 61.5 and -11790.9 ± 58.2 kJ mol^{-1} respectively. Thermodynamic properties of $K_3Ln_5(PO_4)_6(s)$ (Ln= Gd and Eu) will be useful for optimization of conditions during nuclear waste immobilization. A complex phosphate, $Mn_5(HPO_4)_2(PO_4)_2\ 4H_2O$ (Hureaulite mineral) was prepared and its thermal stability, crystal structure and magnetic properties were investigated. A ferromagnetic like transition with low coercive field is observed in $Mn_5(HPO_4)_2(PO_4)_2\ 4H_2O$ around 6 K. Due to complex crystal structure of the synthesized material, sorption behavior of this synthetic mineral was not observed.

10.2. Future scope of the thesis

Though several interesting conclusions as mentioned above have been inferred from the present study, more explorations are still required to further understand the mechanism of the title study and to bring these materials into real large scale practice. The scope for the extension of this thesis work can be based on the two aspects like selective separation of radionuclides and reusability of the synthesized material.

- Radionuclides separated from nuclear waste are used as radiopharmaceuticals of high radiochemical purity. Presence of many interfering ions in the nuclear waste inhibits the selective uptake of radionuclides and thus a multistep separation procedure or newer exchangers should be explored.
- Further improvements in the design of framework inorganic material can be carried out with organic ligands where the functionality can be controlled by controlling the properties of organic ligands.
- Elution of radionuclides from inorganic ion exchangers after reprocessing of nuclear waste is a difficult task. Metal organic framework materials are the upcoming materials with tailored crystal structure and they can be explored for better elution.
- Silicotitanates, tungstates, silicates are promising materials for nuclear backend applications, and these systems can also be investigated for such applications.
- More explorations should be made to improve performance of the Na-birnessite minerals by making polymer beads.

References

References

1. Bhardwaj, S., Indian nuclear power programme–Past, present and future. *Sadhana* **2013,** *38* (5), 775-794.

2. (a) Raj, B.; MUDALI, U. K. In *1National Institute of Advanced Studies, Bengaluru 560 012, India 2Corrosion Science and Technology Group, Indira Gandhi Centre for Atomic Research, Kalpakkam 603 102, India*, Proc Indian Natn Sci Acad, 2015; pp 801-826; (b) Kaushik, C.; Mishra, R.; Sengupta, P.; Kumar, A.; Das, D.; Kale, G.; Raj, K., Barium borosilicate glass–a potential matrix for immobilization of sulfate bearing high-level radioactive liquid waste. *Journal of nuclear materials* **2006,** *358* (2-3), 129-138.

3. Nash, K. L.; Lumetta, G. J., *Advanced separation techniques for nuclear fuel reprocessing and radioactive waste treatment*. Elsevier: 2011.

4. Qureshi, M.; Varshney, K., *Inorganic ion exchangers in chemical analysis*. CRC press: 1991.

5. (a) Sengupta, P.; Kaushik, C.; Dey, G., Immobilization of high level nuclear wastes: the Indian Scenario. In *On a Sustainable Future of the Earth's Natural Resources*, Springer: 2013; pp 25-51; (b) Scheetz, B.; Agrawal, D.; Breval, E.; Roy, R., Sodium zirconium phosphate (NZP) as a host structure for nuclear waste immobilization: a review. *Waste Management* **1994,** *14* (6), 489-505; (c) Raj, K.; Kaushik, C. In *Glass matrices for vitrification of radioactive waste–an Update on R & D Efforts*, IOP Conference Series: Materials Science and Engineering, IOP Publishing: 2009; p 012002; (d) Kuno, M.; Hamada, M., Radioactive Waste Treatment and Disposal Technique. In *Earthquake Engineering for Nuclear Facilities*, Springer: 2017; pp 211-228.

6. Reusswig, F.; Komendantova, N.; Battaglini, A., New Governance Challenges and Conflicts of the Energy Transition: Renewable Electricity Generation and Transmission as Contested Socio-technical Options. In *The Geopolitics of Renewables*, Springer: 2018; pp 231-256.

7. Collins, E.; Del Cul, G.; Moyer, B., Advanced reprocessing for fission product separation and extraction. In *Advanced Separation Techniques for Nuclear Fuel Reprocessing and Radioactive Waste Treatment*, Elsevier: 2011; pp 201-228.

8. Garamszeghy, M., Nuclear fuel waste projections in Canada–2015 update. *Nuclear Waste Management Organization December* **2015**.

9. Glatz, J.-P.; Souček, P.; Malmbeck, R., Key challenges in advanced reprocessing of spent nuclear fuels. In *Reprocessing and Recycling of Spent Nuclear Fuel*, Elsevier: 2015; pp 49-62.

10. Mckay, H., The PUREX process. In *Science and technology of tribuytl phosphate*, 1990.

11. (a) Gupta, A., India's nuclear energy programme: prospects and challenges. *Strategic Analysis* **2011,** *35* (3), 373-380; (b) Bruno, J.; Ewing, R. C., Spent nuclear fuel. *Elements* **2006,** *2* (6), 343-349.

12. Ojovan, M. I.; Lee, W. E., *An introduction to nuclear waste immobilisation*. Newnes: 2013.

13. Conner, J. R., ChemicalFixation and Solidificationof Hazardous Wastes. *Van Nostrand Reinhold, New York* **1990,** *692* (1990), 335.

14. (a) Weber, W.; Ewing, R.; Catlow, C.; De La Rubia, T. D.; Hobbs, L.; Kinoshita, C.; Matzke, H.; Motta, A.; Nastasi, M.; Salje, E., Radiation effects in crystalline ceramics for the immobilization of high-level nuclear waste and plutonium. *Journal of Materials Research* **1998,** *13* (6), 1434-1484; (b) Linge, I.; Vedernikova, M.; Savkin, M.; Samoilov, A., Special Radwaste Management Prospects. *Atomic Energy* **2017,** *122* (6), 396-399.

15. Ozawa, M.; Nemoto, S.; Togashi, A.; Kawata, T.; Onishi, K., Partitioning of actinides and fission products in highly-active raffin ate from purex process by mixer-settlers. *Solvent Extraction and Ion Exchange* **1992,** *10* (5), 829-846.

16. Lee, W.; Ojovan, M.; Stennett, M.; Hyatt, N., Immobilisation of radioactive waste in glasses, glass composite materials and ceramics. *Advances in Applied Ceramics* **2006,** *105* (1), 3-12.

References

17. (a) Harjula, R.; Lehto, J.; Paajanen, A.; Tusa, E.; Yarnell, P., Use inorganic ion exchange materials as precoat filters for nuclear waste effluent treatment. *Reactive and Functional Polymers* **2004,** *60*, 85-95; (b) Al Attar, L.; Safia, B., Sorption of 226Ra from oil effluents onto synthetic cation exchangers. *Journal of environmental management* **2013,** *124*, 156-164.

18. Fiskum, S.; Arm, S.; Fountain, M.; Steele, M.; Blanchard Jr, D., Spherical Resorcinol-Formaldehyde Resin Testing for 137Cs Removal from Simulated and Actual Hanford Waste Tank 241-AP-101 Diluted Feed (Envelope A) Using Small Column Ion Exchange. *Pacific Northwest National Laboratory report, WTP-RPT-134, Rev 0* **2006**.

19. Yekta, S.; Sadeghi, M., Investigation of the Sr2+ Ions Removal from Contaminated Drinking Water Using Novel CaO NPs@ MOF-5 Composite Adsorbent. *Journal of Inorganic and Organometallic Polymers and Materials* **2017**, 1-16.

20. Horwitz, E. P.; Dietz, M. L.; Chiarizia, R.; Diamond, H.; Maxwell III, S. L.; Nelson, M. R., Separation and preconcentration of actinides by extraction chromatography using a supported liquid anion exchanger: application to the characterization of high-level nuclear waste solutions. *Analytica chimica acta* **1995,** *310* (1), 63-78.

21. Ringwood, A.; Kesson, S.; Ware, N.; Hibberson, W.; Major, A., Immobilisation of high level nuclear reactor wastes in SYNROC. *Nature* **1979,** *278* (5701), 219.

22. Routson, R.; Jansen, G.; Robinson, A., 241Am, 237Np, and 99Tc sorption on two United States subsoils from differing weathering intensity areas. *Health Physics* **1977,** *33* (4), 311-317.

23. Raj, K.; Prasad, K.; Bansal, N., Radioactive waste management practices in India. *Nuclear Engineering and Design* **2006,** *236* (7-8), 914-930.

24. Al-Attar, L.; Dyer, A.; Paajanen, A.; Harjula, R., Purification of nuclear wastes by novel inorganic ion exchangers. *Journal of Materials Chemistry* **2003,** *13* (12), 2969-2974.

25. (a) Sales, B.; Boatner, L., Lead phosphate glass as a stable medium for the immobilization and disposal of high-level nuclear waste. *Materials letters* **1984,** *2* (4), 301-304; (b) Sales, B.;

Boatner, L., Lead-iron phosphate glass: a stable storage medium for high-level nuclear waste. *Science* **1984,** *226* (4670), 45-48.

26. (a) Sharma, J.; Ruhela, R.; Harindaran, K.; Mishra, S.; Tangri, S.; Suri, A., Separation studies of uranium and thorium using tetra (2-ethylhexyl) diglycolamide (TEHDGA) as an extractant. *Journal of radioanalytical and nuclear chemistry* **2008,** *278* (1), 173-177; (b) Deepika, P.; Sabharwal, K.; Srinivasan, T.; Vasudeva Rao, P., Studies on the use of N, N, N, N-tetra (2-ethylhexyl) diglycolamide (TEHDGA) for actinide partitioning. I: Investigation on third-phase formation and extraction behavior. *Solvent Extraction and Ion Exchange* **2010,** *28* (2), 184-201.

27. Park, Y.; Lee, Y.-C.; Shin, W. S.; Choi, S.-J., Removal of cobalt, strontium and cesium from radioactive laundry wastewater by ammonium molybdophosphate–polyacrylonitrile (AMP–PAN). *Chemical Engineering Journal* **2010,** *162* (2), 685-695.

28. (a) Clearfield, A.; Stynes, J., The preparation of crystalline zirconium phosphate and some observations on its ion exchange behaviour. *Journal of Inorganic and Nuclear Chemistry* **1964,** *26* (1), 117-129; (b) Clearfield, A.; Smith, G. D., Crystallography and structure of. alpha.-zirconium bis (monohydrogen orthophosphate) monohydrate. *Inorganic chemistry* **1969,** *8* (3), 431-436.

29. (a) Al-Attar, L.; Dyer, A., Ion exchange in birnessite. *Land Contamination & Reclamation* **2007,** *15* (4), 427-436; (b) Al-Attar, L.; Dyer, A., Sorption behaviour of uranium on birnessite, a layered manganese oxide. *Journal of Materials Chemistry* **2002,** *12* (5), 1381-1386.

30. Tranter, T.; Herbst, R.; Todd, T.; Olson, A.; Eldredge, H., Evaluation of ammonium molybdophosphate-polyacrylonitrile (AMP-PAN) as a cesium selective sorbent for the removal of 137Cs from acidic nuclear waste solutions. *Advances in Environmental Research* **2002,** *6* (2), 107-121.

31. Reisman, R. E.; Mauriello, P. M.; Davis, G. B.; Georgitis, J. W.; DeMasi, J. M., A double-blind study of the effectiveness of a high-efficiency particulate air (HEPA) filter in the treatment of

patients with perennial allergic rhinitis and asthma. *Journal of Allergy and Clinical Immunology* **1990,** *85* (6), 1050-1057.

32. Gorby, Y. A.; Lovley, D. R., Enzymic uranium precipitation. *Environmental Science & Technology* **1992,** *26* (1), 205-207.

33. (a) Marinin, D. V.; Brown, G. N., Studies of sorbent/ion-exchange materials for the removal of radioactive strontium from liquid radioactive waste and high hardness groundwaters. *Waste Management* **2000,** *20* (7), 545-553; (b) Duff, M. C.; Coughlin, J. U.; Hunter, D. B., Uranium co-precipitation with iron oxide minerals. *Geochimica et Cosmochimica Acta* **2002,** *66* (20), 3533-3547.

34. (a) Faucon, P.; Adenot, F.; Jacquinot, J.; Petit, J.; Cabrillac, R.; Jorda, M., Long-term behaviour of cement pastes used for nuclear waste disposal: review of physico-chemical mechanisms of water degradation. *Cement and Concrete Research* **1998,** *28* (6), 847-857; (b) Blasius, E.; Klein, W.; Schön, U., Separation of strontium from nuclear waste solutions by solvent extraction with crown ethers. *Journal of radioanalytical and nuclear chemistry* **1985,** *89* (2), 389-398.

35. Rao, M. R.; Hari, K.; Devanna, N.; Chandrasekhar, K., Derivative spectrophotometric determination of uranium (VI) using 2-hydroxy-3-methoxybenzaldehydeisonicotinoylhydrazone reagent. *Asian journal of chemistry* **2008,** *20* (2), 1402.

36. Baes Jr, C.; Zingaro, R. A.; Coleman, C., The extraction of uranium (VI) from acid perchlorate solutions by Di-(2-ethyl-hexyl)-phosphoric acid in n-hexane. *The Journal of Physical Chemistry* **1958,** *62* (2), 129-136.

37. Stary, J.; Irving, H., The solvent extraction of metal chelates. **1964**.

38. Mohapatra, P.; Ansari, S.; Sarkar, A.; Bhattacharyya, A.; Manchanda, V., Evaluation of calix-crown ionophores for selective separation of radio-cesium from acidic nuclear waste solution. *Analytica chimica acta* **2006,** *571* (2), 308-314.

39. Clearfield, A.; Thomas, J., The solubility of α-zirconium phosphate and hafnium phosphate in strong phosphoric acid. *Inorganic and Nuclear Chemistry Letters* **1969,** *5* (9), 775-779.

40. El-Naggar, I. M.; Abou-Mesalam, M. M., Novel inorganic ion exchange materials based on silicates; synthesis, structure and analytical applications of magneso-silicate and magnesium alumino-silicate sorbents. *Journal of hazardous materials* **2007,** *149* (3), 686-692.

41. Cheetham, A. K.; Férey, G.; Loiseau, T., Open-framework inorganic materials. *Angewandte Chemie International Edition* **1999,** *38* (22), 3268-3292.

42. (a) Spokoyny, A. M.; Kim, D.; Sumrein, A.; Mirkin, C. A., Infinite coordination polymer nano-and microparticle structures. *Chemical Society Reviews* **2009,** *38* (5), 1218-1227; (b) Goodenough, J.; Hong, H.-P.; Kafalas, J., Fast Na+-ion transport in skeleton structures. *Materials Research Bulletin* **1976,** *11* (2), 203-220.

43. (a) Kastrissios, T.; Stephenson, M.; Turner, P. S.; White, T. J., Hydrothermal dissolution of perovskite: Implications for Synroc formulation. *Journal of the American Ceramic Society* **1987,** *70* (7); (b) Dosch, R.; Headley, T.; Hlava, P., Crystalline titanate ceramic nuclear waste forms: processing and microstructure. *Journal of the American Ceramic Society* **1984,** *67* (5), 354-361.

44. (a) Clearfield, A., Inorganic ion exchangers, past, present, and future. *Solvent Extraction and Ion Exchange* **2000,** *18* (4), 655-678; (b) Siddiqi, Z. M.; Pathania, D., Titanium (IV) tungstosilicate and titanium (IV) tungstophosphate: two new inorganic ion exchangers. *Journal of Chromatography A* **2003,** *987* (1-2), 147-158; (c) Lehto, J.; Harjula, R., Selective separation of radionuclides from nuclear waste solutions with inorganic ion exchangers. *Radiochimica Acta* **1999,** *86* (1-2), 65-70.

45. El-Kamash, A.; El-Gammal, B.; El-Sayed, A., Preparation and evaluation of cerium (IV) tungstate powder as inorganic exchanger in sorption of cobalt and europium ions from aqueous solutions. *Journal of hazardous materials* **2007,** *141* (3), 719-728.

46. Dosch, R.; Borwn, N.; Stephens, H.; Anthony, R. *Treatment of liquid nuclear wastes with advanced forms of titanate ion exchangers*; Sandia National Labs., Albuquerque, NM (United States): 1993.

47. (a) Singh, S.; Thorat, V.; Kaushik, C.; Raj, K.; Eapen, S.; D'Souza, S., Potential of Chromolaena odorata for phytoremediation of 137Cs from solution and low level nuclear waste. *Journal of hazardous materials* **2009,** *162* (2-3), 743-745; (b) Singh, S.; Eapen, S.; Thorat, V.; Kaushik, C.; Raj, K.; D'souza, S., Phytoremediation of 137cesium and 90strontium from solutions and low-level nuclear waste by Vetiveria zizanoides. *Ecotoxicology and environmental safety* **2008,** *69* (2), 306-311.

48. Vellingiri, K.; Kim, K.-H.; Pournara, A.; Deep, A., Towards high-efficiency sorptive capture of radionuclides in solution and gas. *Progress in Materials Science* **2018**.

49. Haushalter, R. C.; Mundi, L. A., Reduced molybdenum phosphates: octahedral-tetrahedral framework solids with tunnels, cages, and micropores. *Chemistry of materials* **1992,** *4* (1), 31-48.

50. (a) Yang, C.; Srinivasan, S.; Bocarsly, A.; Tulyani, S.; Benziger, J., A comparison of physical properties and fuel cell performance of Nafion and zirconium phosphate/Nafion composite membranes. *Journal of Membrane Science* **2004,** *237* (1-2), 145-161; (b) Henry, J. V.; Bonner, D. M., Acetylornithinase of Escherichia coli: partial purification and some properties. *J. biol. Chem.* **1956,** *218*, 97-106; (c) Dale, T. J.; Rebek, J., Fluorescent sensors for organophosphorus nerve agent mimics. *Journal of the American Chemical Society* **2006,** *128* (14), 4500-4501; (d) Aono, H.; Sugimoto, E.; Sadaoka, Y.; Imanaka, N.; Adachi, G. y., Ionic conductivity of solid electrolytes based on lithium titanium phosphate. *Journal of the electrochemical society* **1990,** *137* (4), 1023-1027.

51. (a) Troup, J.; Clearfield, A., Mechanism of ion exchange in zirconium phosphates. 20. Refinement of the crystal structure of. alpha.-zirconium phosphate. *Inorganic chemistry* **1977,** *16* (12), 3311-3314; (b) Costantino, U.; Gasperoni, A., Crystalline insoluble acid salts of tetravalent metals: XI. Synthesis and ion-exchange properties of tin (IV) phosphate and tin (IV) arsenate. *Journal of Chromatography A* **1970,** *51*, 289-296.

52. Clearfield, A.; Landis, A.; Medina, A.; Troup, J., More on crystalline zirconium phosphates. *Journal of Inorganic and Nuclear Chemistry* **1973,** *35* (4), 1099-1108.

53. Achary, S.; Bevara, S.; Tyagi, A., Recent progress on synthesis and structural aspects of rare-earth phosphates. *Coordination Chemistry Reviews* **2017,** *340*, 266-297.

54. (a) Lehto, J.; Clearfield, A., The ion exchange of strontium on sodium titanate Na4Ti9O20. xH2O. *Journal of radioanalytical and nuclear chemistry* **1987,** *118* (1), 1-13; (b) Izawa, H.; Kikkawa, S.; Koizumi, M., Ion exchange and dehydration of layered [sodium and potassium] titanates, Na2Ti3O7 and K2Ti4O9. *The Journal of Physical Chemistry* **1982,** *86* (25), 5023-5026.

55. Cherry, B. R.; Nyman, M.; Alam, T. M., Investigation of cation environment and framework changes in silicotitanate exchange materials using solid-state 23Na, 29Si, and 133Cs MAS NMR. *Journal of Solid State Chemistry* **2004,** *177* (6), 2079-2093.

56. (a) El-Naggar, I.; Mowafy, E.; Abdel-Galil, E., Diffusion mechanism of certain fission products in the particles of silico (IV) titanate. *Colloids and Surfaces A: Physicochemical and Engineering Aspects* **2007,** *307* (1-3), 77-82; (b) Anthony, R. G.; Dosch, R. G.; Philip, C. V., Method of using novel silico-titanates. Google Patents: 2000.

57. Lefkowitz, J. P.; Rouff, A. A.; Elzinga, E. J., Influence of pH on the reductive transformation of birnessite by aqueous Mn (II). *Environmental Science & Technology* **2013,** *47* (18), 10364-10371.

58. Iyer, A.; Del-Pilar, J.; King'ondu, C. K.; Kissel, E.; Garces, H. F.; Huang, H.; El-Sawy, A. M.; Dutta, P. K.; Suib, S. L., Water oxidation catalysis using amorphous manganese oxides, octahedral molecular sieves (OMS-2), and octahedral layered (OL-1) manganese oxide structures. *The Journal of Physical Chemistry C* **2012,** *116* (10), 6474-6483.

59. Kanungo, S. B.; Tripathy, S. S.; Rajeev, Adsorption of Co, Ni, Cu, and Zn on hydrous manganese dioxide from complex electrolyte solutions resembling sea water in major ion content. *Journal of Colloid and Interface Science* **2004,** *269* (1), 1-10.

60. Clearfield, A., Role of ion exchange in solid-state chemistry. *Chemical Reviews* **1988,** *88* (1), 125-148.

References

61. Houde-Walter, S. N.; Inman, J. M.; Dent, A.; Greaves, G. N., Sodium and silver environments and ion-exchange processes in silicate and aluminosilicate glasses. *The Journal of Physical Chemistry* **1993,** *97* (37), 9330-9336.

62. Calvin, C., Alumino silicate cation exchangers. Google Patents: 1950.

63. Choi, Y.-G.; Sakai, G.; Shimanoe, K.; Miura, N.; Yamazoe, N., Preparation of aqueous sols of tungsten oxide dihydrate from sodium tungstate by an ion-exchange method. *Sensors and Actuators B: Chemical* **2002,** *87* (1), 63-72.

64. Teiga, B. C., Síntese e caracterização do sistema vítreo (1-x) NaPO 3–(x) WO 3. **2009**.

65. Collins, F. C.; Kimball, G. E., Diffusion-controlled reaction rates. *Journal of colloid science* **1949,** *4* (4), 425-437.

66. (a) Uhlmann, D., *Introduction to ceramics*. John Wiley and Sons, New York, NY: 1976; (b) Jayakumar, O.; Tyagi, A., 5 Spintronic Materials, Synthesis, Processing and Applications. *Functional Materials: Preparation, Processing and Applications* **2011**, 193.

67. Higashi, K.; Sonoda, K.; Ono, H.; Sameshima, S.; Hirata, Y., Synthesis and sintering of rare-earth-doped ceria powder by the oxalate coprecipitation method. *Journal of Materials Research* **1999,** *14* (3), 957-967.

68. Bevara, S.; Achary, S.; Babu, P.; Tyagi, A. In *Preparation, thermal and magnetic properties of Mn5 (HPO4) 2 (PO4) 2 4H2O*, AIP Conference Proceedings, AIP Publishing: 2015; p 030021.

69. Cullity, B. D., Elements of X-ray Diffraction. **2001**.

70. Klug, H. P.; Alexander, L. E., X-ray diffraction procedures: for polycrystalline and amorphous materials. *X-Ray Diffraction Procedures: For Polycrystalline and Amorphous Materials, 2nd Edition, by Harold P. Klug, Leroy E. Alexander, pp. 992. ISBN 0-471-49369-4. Wiley-VCH, May 1974.* **1974**, 992.

71. Toby, B. H., R factors in Rietveld analysis: how good is good enough? *Powder diffraction* **2006,** *21* (1), 67-70.

72. Norrish, K.; Chappell, B. W., X-ray fluorescence spectrometry. **1977**.

73. Bambynek, W.; Crasemann, B.; Fink, R.; Freund, H.-U.; Mark, H.; Swift, C.; Price, R.; Rao, P. V., X-ray fluorescence yields, Auger, and Coster-Kronig transition probabilities. *Reviews of modern physics* **1972,** *44* (4), 716.

74. Chastain, J.; King, R. C.; Moulder, J., *Handbook of X-ray photoelectron spectroscopy: a reference book of standard spectra for identification and interpretation of XPS data*. Physical Electronics Division, Perkin-Elmer Corporation Eden Prairie, Minnesota: 1992.

75. Koningsberger, D.; Prins, R., X-ray absorption: principles, applications, techniques of EXAFS, SEXAFS, and XANES. **1988**.

76. Kubicki, J. D.; Paul, K. W.; Kabalan, L.; Zhu, Q.; Mrozik, M. K.; Aryanpour, M.; Pierre-Louis, A.-M.; Strongin, D. R., ATR–FTIR and density functional theory study of the structures, energetics, and vibrational spectra of phosphate adsorbed onto goethite. *Langmuir* **2012,** *28* (41), 14573-14587.

77. Schrader, B., *Infrared and Raman spectroscopy: methods and applications*. John Wiley & Sons: 2008.

78. (a) Long, D. A., The Raman effect: a unified treatment of the theory of Raman scattering by molecules. *West Sussex* **2002**; (b) Herzberg, G., *Infrared and Raman spectra of polyatomic molecules*. D. Van Nostrand Company.; New York: 1945.

79. Garn, P. D. *Thermoanalytical methods of investigation*; Academic Press: 1965.

80. (a) Doyle, C., Estimating thermal stability of experimental polymers by empirical thermogravimetric analysis. *Analytical Chemistry* **1961,** *33* (1), 77-79; (b) Coats, A.; Redfern, J., Thermogravimetric analysis. A review. *Analyst* **1963,** *88* (1053), 906-924.

81. (a) Khursheed, A., Scanning electron microscope. Google Patents: 2007; (b) Horisberger, M., Colloidal gold: a cytochemical marker for light and fluorescent microscopy and for transmission and scanning electron microscopy. *Scanning electron microscopy* **1981,** (Pt 2), 9-31.

References

82. De Graef, M., *Introduction to conventional transmission electron microscopy*. Cambridge University Press: 2003.

83. Clarke, J.; Braginski, A. I., *The SQUID handbook: Applications of SQUIDs and SQUID systems*. John Wiley & Sons: 2006.

84. (a) Maclntyre, I., Flame photometry. In *Advances in clinical chemistry*, Elsevier: 1961; Vol. 4, pp 1-28; (b) Barnes, R. B.; Richardson, D.; Berry, J. W.; Hood, R. L., Flame photometry a rapid analytical procedure. *Industrial & Engineering Chemistry Analytical Edition* **1945,** *17* (10), 605-611.

85. (a) Azizian, S., Kinetic models of sorption: a theoretical analysis. *Journal of Colloid and Interface Science* **2004,** *276* (1), 47-52; (b) Jin, S.; Sen, A.; Sandvik, A. W., Ashkin-Teller criticality and pseudo-first-order behavior in a frustrated Ising model on the square lattice. *Physical review letters* **2012,** *108* (4), 045702.

86. (a) Ho, Y.-S.; Ofomaja, A. E., Pseudo-second-order model for lead ion sorption from aqueous solutions onto palm kernel fiber. *Journal of hazardous materials* **2006,** *129* (1-3), 137-142; (b) Ho, Y.-S.; McKay, G., Pseudo-second order model for sorption processes. *Process biochemistry* **1999,** *34* (5), 451-465.

87. Weisz, P.; Swegler, E., Effect of Intra-particle Diffusion on the Kinetics of Catalytic Dehydrogenation. of Cyclohexane. *The Journal of Physical Chemistry* **1955,** *59* (9), 823-826.

88. (a) LeVan, M. D.; Vermeulen, T., Binary Langmuir and Freundlich isotherms for ideal adsorbed solutions. *The Journal of Physical Chemistry* **1981,** *85* (22), 3247-3250; (b) Dada, A.; Olalekan, A.; Olatunya, A.; Dada, O., Langmuir, Freundlich, Temkin and Dubinin–Radushkevich isotherms studies of equilibrium sorption of Zn2+ unto phosphoric acid modified rice husk. *IOSR Journal of Applied Chemistry* **2012,** *3* (1), 38-45.

89. Sheindorf, C.; Rebhun, M.; Sheintuch, M., A Freundlich-type multicomponent isotherm. *Journal of Colloid and Interface Science* **1981,** *79* (1), 136-142.

90. (a) Sellaoui, L.; Soetaredjo, F. E.; Ismadji, S.; Lima, É. C.; Dotto, G. L.; Lamine, A. B.; Erto, A., New insights into single-compound and binary adsorption of copper and lead ions on a treated sea mango shell: experimental and theoretical studies. *Physical Chemistry Chemical Physics* **2017,** *19* (38), 25927-25937; (b) Sellaoui, L.; Franco, D. S. P.; Dotto, G. L.; Lima, É. C.; Lamine, A. B., Single and binary adsorption of cobalt and methylene blue on modified chitin: Application of the Hill and exclusive extended Hill models. *Journal of Molecular Liquids* **2017,** *233*, 543-550; (c) Sellaoui, L.; Dotto, G. L.; Lamine, A. B.; Erto, A., Interpretation of single and competitive adsorption of cadmium and zinc on activated carbon using monolayer and exclusive extended monolayer models. *Environmental Science and Pollution Research* **2017,** *24* (24), 19902-19908.

91. Manos, M. J.; Kanatzidis, M. G., Metal sulfide ion exchangers: superior sorbents for the capture of toxic and nuclear waste-related metal ions. *Chemical Science* **2016,** *7* (8), 4804-4824.

92. (a) Varshney, K.; Tayal, N.; Gupta, U., Acrylonitrile based cerium (IV) phosphate as a new mercury selective fibrous ion-exchanger: synthesis, characterization and analytical applications. *Colloids and Surfaces A: Physicochemical and Engineering Aspects* **1998,** *145* (1-3), 71-81; (b) Metwally, S.; El-Gammal, B.; Aly, H.; Abo-El-Enein, S., Removal and separation of some radionuclides by poly-acrylamide based Ce (IV) phosphate from radioactive waste solutions. *Separation Science and Technology* **2011,** *46* (11), 1808-1821; (c) Clearfield, A., Ion exchange and adsorption in layered phosphates. *Materials chemistry and physics* **1993,** *35* (3-4), 257-263.

93. (a) Yan, L.-g.; Yang, K.; Shan, R.-r.; Yan, T.; Wei, J.; Yu, S.-j.; Yu, H.-q.; Du, B., Kinetic, isotherm and thermodynamic investigations of phosphate adsorption onto core–shell Fe3O4@ LDHs composites with easy magnetic separation assistance. *Journal of Colloid and Interface Science* **2015,** *448*, 508-516; (b) Mckay, G.; Blair, H.; Gardner, J., Adsorption of dyes on chitin. I. Equilibrium studies. *Journal of applied polymer science* **1982,** *27* (8), 3043-3057; (c) Fan, Y.-H.; Zhang, S.-W.; Qin, S.-B.; Li, X.-S.; Qi, S.-H., An enhanced adsorption of organic dyes onto NH2 functionalization titanium-based metal-organic frameworks and the mechanism investigation. *Microporous and*

Mesoporous Materials **2018,** *263*, 120-127; (d) Chegrouche, S.; Mellah, A.; Barkat, M., Removal of strontium from aqueous solutions by adsorption onto activated carbon: kinetic and thermodynamic studies. *Desalination* **2009,** *235* (1-3), 306-318.

94. Bevara, S.; Achary, S. N.; Patwe, S. J.; Sinha, A. K.; Tyagi, A. K., Preparation and crystal structure of K 2 Ce (PO 4) 2: a new complex phosphate of Ce (iv) having structure with one-dimensional channels. *Dalton Transactions* **2016,** *45* (3), 980-991.

95. Doerffel, M.; Liebertz, J., Crystal growth and structure determination of potassium zirconium phosphate K2Zr (PO4) 2. *Zeitschrift für Kristallographie-Crystalline Materials* **1990,** *193* (1-4), 155-160.

96. Rodriguez-Carvajal, J., FULLPROF. 2k: Rietveld, profile matching and integrated intensity refinement of X-ray and neutron data. *A computer program* **2000**.

97. (a) Park, S.; Cho, S.; Ahn, W.; Kim, W., Adsorption characteristics of divalent cation-exchanged ETS-4s pretreated at different temperature. *Microporous and Mesoporous Materials* **2011,** *145* (1-3), 200-204; (b) Hong, H.-J.; Jeong, H. S.; Kim, B.-G.; Hong, J.; Park, I.-S.; Ryu, T.; Chung, K.-S.; Kim, H.; Ryu, J., Highly stable and magnetically separable alginate/Fe3O4 composite for the removal of strontium (Sr) from seawater. *Chemosphere* **2016,** *165*, 231-238.

98. Thanh, L. H.; Liu, J., Flotation separation of strontium via phosphate precipitation. *Water Science and Technology* **2017,** *75* (11), 2520-2526.

99. Clearfield, A.; Tindwa, R., Exchange of large cations and charged complexes with amine intercalates of zirconium phosphates. *Inorganic and Nuclear Chemistry Letters* **1979,** *15* (5-6), 251-254.

100. Bevara, S.; Achary, S.; Patwe, S.; Sinha, A.; Mishra, R.; Kumar, A.; Kaushik, C.; Tyagi, A. In *Crystal structure and cation exchanging properties of a novel open framework phosphate of Ce (IV)*, AIP Conference Proceedings, AIP Publishing: 2016; p 140040.

101. (a) Varshney, K.; Tayal, N.; Khan, A.; Niwas, R., Synthesis, characterization and analytical applications of lead (II) selective polyacrylonitrile thorium (IV) phosphate: a novel fibrous ion exchanger. *Colloids and Surfaces A: Physicochemical and Engineering Aspects* **2001,** *181* (1-3), 123-129; (b) Gray, M. J.; Malati, M. A., Adsorption from aqueous solution by δ-manganese dioxide I. Adsorption of the alkaline-earth cations. *Journal of Chemical Technology and Biotechnology* **1979,** *29* (3), 127-134.

102. (a) Shrivastava, O.; Chourasia, R., Crystal chemistry of sodium zirconium phosphate based simulated ceramic waste forms of effluent cations (Ba2+, Sn4+, Fe3+, Cr3+, Ni2+ and Si4+) from light water reactor fuel reprocessing plants. *Journal of hazardous materials* **2008,** *153* (1-2), 285-292; (b) Raicevic, S.; Kaludjerovic-Radoicic, T.; Zouboulis, A., In situ stabilization of toxic metals in polluted soils using phosphates: theoretical prediction and experimental verification. *Journal of hazardous materials* **2005,** *117* (1), 41-53.

103. Tarte, P.; Rulmont, A.; Merckaert-Ansay, C., Vibrational spectrum of nasicon-like, rhombohedral orthophosphates MIMIV2 (PO4) 3. *Spectrochimica Acta Part A: Molecular Spectroscopy* **1986,** *42* (9), 1009-1016.

104. (a) Pavel, C. C.; Popa, K., Investigations on the ion exchange process of Cs+ and Sr2+ cations by ETS materials. *Chemical Engineering Journal* **2014,** *245*, 288-294; (b) Nikolova, R.; Shivachev, B.; Ferdov, S., Crystal structures of Mg2+, Ba2+ and Cs+ exchanged K–Na–ETS-4. *Microporous and Mesoporous Materials* **2013,** *165*, 121-126.

105. Bregiroux, D.; Popa, K.; Jardin, R.; Raison, P.; Wallez, G.; Quarton, M.; Brunelli, M.; Ferrero, C.; Caciuffo, R., Crystal structure and thermal expansion of the low-and high-temperature forms of BaM IV (PO 4) 2 compounds (M= Ti, Zr, Hf and Sn). *Journal of Solid State Chemistry* **2009,** *182* (5), 1115-1120.

106. Bregiroux, D.; Popa, K.; Wallez, G., Crystal chemistry of MIIM′ IV (PO4) 2 double monophosphates. *Journal of Solid State Chemistry* **2015,** *230*, 26-33.

References

107. Popa, K.; Konings, R.; Wiss, T.; Leiste, H., Hydrothermal alteration of BaxMIVxCe2− 2 x (PO4) 2 [MIV= Zr, Hf] as hosts for minor actinides. *Journal of radioanalytical and nuclear chemistry* **2007,** *273* (3), 563-567.

108. Trobajo, C.; Rodríguez, M. L.; Suárez, M.; García, J. R.; Rodríguez, J.; Parra, J. B.; Salvadó, M. A.; Pertierra, P.; García-Granda, S., Layered mixed tin-titanium phosphates. *Journal of Materials Research* **1998,** *13* (3), 754-759.

109. Parreu, I.; Carvajal, J.; Solans, X.; Díaz, F.; Aguiló, M., Crystal structure and optical characterization of pure and Nd-substituted type III KGd (PO3) 4. *Chemistry of materials* **2006,** *18* (1), 221-228.

110. (a) Salvadó, M. A.; Pertierra, P.; Trobajo, C.; García, J. R., Crystal structure of a Cerium (IV) bis (phosphate) derivative. *Journal of the American Chemical Society* **2007,** *129* (36), 10970-10971; (b) Nazaraly, M.; Wallez, G.; Chanéac, C.; Tronc, E.; Ribot, F.; Quarton, M.; Jolivet, J. P., The First Structure of a Cerium (IV) Phosphate: Ab Initio Rietveld Analysis of CeIV (PO4)(HPO4) 0.5 (H2O) 0.5. *Angewandte Chemie International Edition* **2005,** *44* (35), 5691-5694; (c) Nazaraly, M.; Wallez, G.; Chanéac, C.; Tronc, E.; Ribot, F.; Quarton, M.; Jolivet, J.-P., Synthesis and characterization of CeIV (PO4)(HPO4) 0.5 (H2O) 0.5. *Journal of Physics and Chemistry of Solids* **2006,** *67* (5-6), 1075-1078; (d) Lai, Y.-H.; Chang, Y.-C.; Wong, T.-F.; Tai, W.-J.; Chang, W.-J.; Lii, K.-H., High-temperature, high-pressure hydrothermal synthesis, crystal structures, and spectroscopic studies of a uranium (IV) phosphate (Na10U2P6O24) and the isotypic cerium (IV) phosphate (Na10Ce2P6O24). *Inorganic chemistry* **2013,** *52* (23), 13639-13643.

111. (a) Wallez, G.; Raison, P. E.; Dacheux, N.; Clavier, N.; Bykov, D.; Delevoye, L.; Popa, K.; Bregiroux, D.; Fitch, A. N.; Konings, R. J., Triclinic–Cubic phase transition and negative expansion in the actinide IV (Th, U, Np, Pu) diphosphates. *Inorganic chemistry* **2012,** *51* (7), 4314-4322; (b) Wallez, G.; Bregiroux, D.; Popa, K.; Raison, P. E.; Apostolidis, C.; Lindqvist-Reis, P.; Konings, R. J.; Popa, A. F., BaAnIV (PO4) 2 (AnIV= Th, Np)–a new family of layered double phosphates. *European*

Journal of Inorganic Chemistry **2011,** *2011* (1), 110-115; (c) Popa, K.; Wallez, G.; Raison, P. E.; Bregiroux, D.; Apostolidis, C.; Lindqvist-Reis, P.; Konings, R. J., SrNp (PO4) 2: An original ordered modification of cheralite. *Inorganic chemistry* **2010,** *49* (15), 6904-6908; (d) Popa, K.; Wallez, G.; Bregiroux, D.; Loiseau, P., M II Ge (PO 4) 2 (M= Ca, Sr, Ba): Crystal structure, phase transitions and thermal expansion. *Journal of Solid State Chemistry* **2011,** *184* (10), 2629-2634.

112. Xu, Y.; Feng, S.; Pang, W.; Pang, G., Hydrothermal synthesis and characterization of (NH4) Ce (PO4) 2· H2O. *Chemical Communications* **1996,** (11), 1305-1306.

113. Xu, Y.; Feng, S.; Pang, W., Hydrothermal synthesis and characterization of K2Ce (PO4) 2· H2O. *Materials letters* **1996,** *28* (4-6), 499-502.

114. Salvadó, M. A.; Pertierra, P.; Bortun, A. I.; Trobajo, C.; Garcia, J. R., Phosphorous acid and urea: Valuable sources of phosphorus and nitrogen in the hydrothermal synthesis of ammonium-thorium phosphates. *Inorganic chemistry* **2008,** *47* (16), 7207-7210.

115. Ogorodnyk, I. V.; Zatovsky, I. V.; Baumer, V. N.; Slobodyanik, N. S.; Shishkin, O. V., A disordered cerium (IV) phosphate with a tunnel structure, K4CeZr (PO4) 4. *Acta Crystallographica Section C: Crystal Structure Communications* **2006,** *62* (12), i100-i102.

116. (a) Le, M.-V.; Tsai, D.-S.; Yang, C.-Y.; Chung, W.-H.; Lee, H.-Y., Proton conductors of cerium pyrophosphate for intermediate temperature fuel cell. *Electrochimica Acta* **2011,** *56* (19), 6654-6660; (b) Cross, J. N.; Villa, E. M.; Wang, S.; Diwu, J.; Polinski, M. J.; Albrecht-Schmitt, T. E., Syntheses, structures, and spectroscopic properties of plutonium and americium phosphites and the redetermination of the ionic radii of Pu (III) and Am (III). *Inorganic chemistry* **2012,** *51* (15), 8419-8424; (c) Borhan, A.; APETRĂCHIOAEI, B.; Karin, P., ON THE EXISTENCE OF CERIUM (IV) ORTHOPHOSPHATE,“Ce3 (PO4) 4”. *Rev. Roum. Chim* **2010,** *55* (7), 389-393; (d) Bevara, S.; Achary, S. N.; Tyagi, A. K., K2Ce (PO4) 2: A new complex phosphate of Ce (IV). *Foundations of Crystallography* **2017,** *70* (C844), C844.

References

117. Hammersley, A.; Svensson, S.; Hanfland, M.; Fitch, A.; Hausermann, D., Two-dimensional detector software: from real detector to idealised image or two-theta scan. *International Journal of High Pressure Research* **1996,** *14* (4-6), 235-248.

118. Blöchl, P. E., Projector augmented-wave method. *Physical review B* **1994,** *50* (24), 17953.

119. Perdew, J. P.; Burke, K.; Ernzerhof, M., Generalized gradient approximation made simple. *Physical review letters* **1996,** *77* (18), 3865.

120. Perdew, J. P.; Chevary, J.; Vosko, S.; Jackson, K. A.; Pederson, M. R.; Singh, D.; Fiolhais, C., Erratum: Atoms, molecules, solids, and surfaces: Applications of the generalized gradient approximation for exchange and correlation. *Physical Review B* **1993,** *48* (7), 4978.

121. Monkhorst, H. J.; Pack, J. D., Special points for Brillouin-zone integrations. *Physical Review B* **1976,** *13* (12), 5188.

122. Mujica, A.; Rubio, A.; Munoz, A.; Needs, R., High-pressure phases of group-IV, III–V, and II–VI compounds. *Reviews of modern physics* **2003,** *75* (3), 863.

123. Szczygiel, I., Investigations of new binary phosphate K4Ce2P4O15. *Thermochimica acta* **2004,** *417* (1), 75-78.

124. Galešić, N.; Matković, B.; Topić, M.; Coffou, E.; Šljukić, M., The Crystal Structure of Disodium Thorium Bisphosphate, Na2Th (PQ4) 2. *Croatica Chemica Acta* **1984,** *57* (4), 597-608.

125. Yu, N.; Klepov, V. V.; Modolo, G.; Bosbach, D.; Suleimanov, E. V.; Gesing, T. M.; Robben, L.; Alekseev, E. V., Morphotropy and Temperature-Driven Polymorphism in A2Th (AsO4) 2 (A= Li, Na, K, Rb, Cs) Series. *Inorganic chemistry* **2014,** *53* (20), 11231-11241.

126. (a) Bevara, S.; Patwe, S.; Achary, S.; Tyagi, A.; Mishra, K.; Ravindran, T.; Gupta, M.; MittaI, R.; Sinha, A. K. In *Structural and phase transition studies on K 2 Ce (PO 4) 2*, Proceedings of the sixth DAE-BRNS interdisciplinary symposium on materials chemistry, 2016; (b) Mishra, K. K.; Bevara, S.; Ravindran, T.; Patwe, S.; Gupta, M. K.; Mittal, R.; Krishnan, R. V.; Achary, S.; Tyagi, A.,

High pressure behavior of complex phosphate K2Ce [PO4] 2: Grüneisen parameter and anharmonicity properties. *Journal of Solid State Chemistry* **2018,** *258*, 845-853.

127. Bevara, S.; Mishra, K. K.; Patwe, S. J.; Ravindran, T.; Gupta, M. K.; Mittal, R.; Krishna, P. S. R.; Sinha, A. K.; Achary, S. N.; Tyagi, A. K., Phase transformation, vibrational and electronic properties of K2Ce (PO4) 2: a combined experimental and theoretical study. *Inorganic chemistry* **2017,** *56* (6), 3335-3348.

128. (a) Woodcock, D.; Lightfoot, P., Comparison of the structural behaviour of the low thermal expansion NZP phases MTi 2 (PO 4) 3 (M= Li, Na, K). *Journal of Materials Chemistry* **1999,** *9* (11), 2907-2911; (b) Kamali, K.; Ravindran, T.; Shekar, N. C.; Pandey, K.; Sharma, S., Pressure induced phase transformations in NaZr2 (PO4) 3 studied by X-ray diffraction and Raman spectroscopy. *Journal of Solid State Chemistry* **2015,** *221*, 285-290.

129. Lacomba-Perales, R.; Errandonea, D.; Meng, Y.; Bettinelli, M., High-pressure stability and compressibility of A PO 4 (A= La, Nd, Eu, Gd, Er, and Y) orthophosphates: An x-ray diffraction study using synchrotron radiation. *Physical Review B* **2010,** *81* (6), 064113.

130. Tyagi, A. K.; Achary, S. N., Diffraction and Thermal Expansion of Solids. *Thermodynamic Properties of Solids* **2010**, 197-267.

131. (a) Mishra, K. K.; Achary, S. N.; Chandra, S.; Ravindran, T.; Sinha, A. K.; Singh, M. N.; Tyagi, A. K., Structural and Thermal Properties of BaTe2O6: Combined Variable-Temperature Synchrotron X-ray Diffraction, Raman Spectroscopy, and ab Initio Calculations. *Inorganic chemistry* **2016,** *55* (17), 8994-9005; (b) Mishra, K.; Arora, A.; Tripathy, S.; Pradhan, D., Dielectric and polarized Raman spectroscopic studies on 0.85 Pb (Zn1/3Nb2/3) O3-0.15 PbTiO3 single crystal. *Journal of Applied Physics* **2012,** *112* (7), 073521.

132. Fatteley, W.; Dollish, F.; McDevitt, N.; Bentley, F., Infrared and Raman selection rules for molecular and lattice vibrations. Wiley, New York: 1972.

References

133. Mishra, K.; Sivasubramanian, V.; Arora, A., Low-temperature Raman spectroscopic studies in NaNbO3. *Journal of Raman Spectroscopy* **2011,** *42* (3), 517-521.

134. Balkanski, M.; Wallis, R.; Haro, E., Anharmonic effects in light scattering due to optical phonons in silicon. *Physical Review B* **1983,** *28* (4), 1928.

135. (a) Bevara, S.; Giri, P.; Achary, S. N.; Bhallerao, G.; Mishra, R. K.; Kumar, A.; Kaushik, C. P.; Tyagi, A. K., Synthetic Na/K-birnessite for efficient management of Sr (II) from nuclear waste. *Journal of Environmental Chemical Engineering* **2018**; (b) Morrey, J.; Swanson, J., A Primer on Hanford Defense Tank Wastes and Prospects for Advanced Chemical Separations. *Pacific Northwest Laboratory report* **1991**.

136. Pekarek, V.; Veselý, V., Synthetic inorganic ion exchangers—II: salts of heteropolyacids, insoluble ferrocyanides, synthetic aluminosilicates and miscellaneous exchangers. *Talanta* **1972,** *19* (11), 1245-1283.

137. Paulus, W. J.; Komarneni, S.; Roy, R., Bulk synthesis and selective exchange of strontium ions in Na4Mg6Al4Si4O20F4 mica. *Nature* **1992,** *357* (6379), 571.

138. Ryu, J.; Kim, S.; Hong, H.-J.; Hong, J.; Kim, M.; Ryu, T.; Park, I.-S.; Chung, K.-S.; Jang, J. S.; Kim, B.-G., Strontium ion (Sr2+) separation from seawater by hydrothermally structured titanate nanotubes: Removal vs. recovery. *Chemical Engineering Journal* **2016,** *304*, 503-510.

139. (a) Zhang, L.; Wei, J.; Zhao, X.; Li, F.; Jiang, F.; Zhang, M.; Cheng, X., Removal of strontium (II) and cobalt (II) from acidic solution by manganese antimonate. *Chemical Engineering Journal* **2016,** *302*, 733-743; (b) Zhang, L.; Wei, J.; Zhao, X.; Li, F.; Jiang, F.; Zhang, M.; Cheng, X., Competitive adsorption of strontium and cobalt onto tin antimonate. *Chemical Engineering Journal* **2016,** *285*, 679-689; (c) Zhang, L.; Wei, J.; Zhao, X.; Li, F.; Jiang, F., Adsorption characteristics of strontium on synthesized antimony silicate. *Chemical Engineering Journal* **2015,** *277*, 378-387.

140. (a) Mishra, S. P., Removal behavior of hydrous manganese oxide and hydrous stannic oxide for Cs (I) ions from aqueous solutions. *Separation and purification technology* **2007,** *54* (1), 10-17;

(b) Ghaly, M.; El-Dars, F. M.; Hegazy, M.; Rahman, R. A., Evaluation of synthetic Birnessite utilization as a sorbent for cobalt and strontium removal from aqueous solution. *Chemical Engineering Journal* **2016,** *284*, 1373-1385.

141. Kanungo, S. B.; Tripathy, S. S., Adsorption of Co, Ni, Cu, and Zn on hydrous manganese dioxide from complex electrolyte solutions resembling sea water in major ion content. *Journal of Colloid and Interface Science* **2004,** *269* (1), 1-10.

142. (a) Bevara, S.; Giri, P.; Achary, S. N.; Bhallerao, G.; Mishra, R. K.; Kumar, A.; Kaushik, C. P.; Tyagi, A. K., Synthetic Na/K-birnessite for efficient management of Sr (II) from nuclear waste. *Journal of Environmental Chemical Engineering* **2018,** *6* (6), 7200-7213; (b) Anirudhan, T.; Radhakrishnan, P., Kinetic and equilibrium modelling of Cadmium (II) ions sorption onto polymerized tamarind fruit shell. *Desalination* **2009,** *249* (3), 1298-1307.

143. Cai, J.; Liu, J.; Suib, S. L., Preparative parameters and framework dopant effects in the synthesis of layer-structure birnessite by air oxidation. *Chemistry of materials* **2002,** *14* (5), 2071-2077.

144. Qin, Z.; Xiang, Q.; Liu, F.; Xiong, J.; Koopal, L. K.; Zheng, L.; Ginder-Vogel, M.; Wang, M.; Feng, X.; Tan, W., Local structure of Cu2+ in Cu-doped hexagonal turbostratic birnessite and Cu2+ stability under acid treatment. *Chemical Geology* **2017,** *466*, 512-523.

145. Ling, F. T.; Post, J. E.; Heaney, P. J.; Kubicki, J. D.; Santelli, C. M., Fourier-transform infrared spectroscopy (FTIR) analysis of triclinic and hexagonal birnessites. *Spectrochimica Acta Part A: Molecular and Biomolecular Spectroscopy* **2017,** *178*, 32-46.

146. (a) Shen, Y.; Zerger, R.; DeGuzman, R.; Suib, S.; McCurdy, L.; Potter, D.; O'young, C., Manganese oxide octahedral molecular sieves: preparation, characterization, and applications. *Science* **1993,** *260* (5107), 511-515; (b) Post, J. E., Manganese oxide minerals: Crystal structures and economic and environmental significance. *Proceedings of the National Academy of Sciences* **1999,** *96* (7), 3447-3454.

147. Parc, S.; Nahon, D.; Tardy, Y.; Vieillard, P., Estimated solubility products and fields of stability for cryptomelane, nsutite, birnessite, and lithiophorite based on natural lateritic weathering sequences. *American Mineralogist* **1989,** *74* (3-4), 466-475.

148. Tournassat, C.; Charlet, L.; Bosbach, D.; Manceau, A., Arsenic (III) oxidation by birnessite and precipitation of manganese (II) arsenate. *Environmental Science & Technology* **2002,** *36* (3), 493-500.

149. Della Puppa, L.; Komárek, M.; Bordas, F.; Bollinger, J.-C.; Joussein, E., Adsorption of copper, cadmium, lead and zinc onto a synthetic manganese oxide. *Journal of Colloid and Interface Science* **2013,** *399*, 99-106.

150. Wang, J.; Li, D.; Li, P.; Zhang, P.; Xu, Q.; Yu, J., Layered manganese oxides for formaldehyde-oxidation at room temperature: the effect of interlayer cations. *Rsc Advances* **2015,** *5* (122), 100434-100442.

151. (a) Sadeghi, M.; Yekta, S.; Ghaedi, H.; Babanezhad, E., MnO2 NPs-AgX zeolite composite as adsorbent for removal of strontium-90 (90Sr) from water samples: Kinetics and thermodynamic reactions study. *Materials chemistry and physics* **2017,** *197*, 113-122; (b) Boumaiza, H.; Coustel, R.; Despas, C.; Ruby, C.; Bergaoui, L., Interaction of ammonium with birnessite: Evidence of a chemical and structural transformation in alkaline aqueous medium. *Journal of Solid State Chemistry* **2018,** *258*, 543-550.

152. Bevara, S.; Giri, P.; Patwe, S. J.; Achary, S. N.; Mishra, R. K.; Kumar, A.; Sinha, A. K.; Kaushik, C. P.; Tyagi, A. K., Separation of 90Sr from nuclear waste by crystalline complex phosphates of Ce (IV) and Zr (IV). *Journal of Environmental Chemical Engineering* **2018,** *6* (2), 2248-2261.

153. Horchani-Naifer, K.; Férid, M., Structure and ionic conductivity of NaCeP2O7. *Solid State Ionics* **2005,** *176* (23-24), 1949-1953.

154. Huang, H.; Chen, G.; Zhang, Y., Two Bi-based phosphate photocatalysts: Crystal structure, optical property and photocatalytic activity. *Inorganic Chemistry Communications* **2014,** *44*, 46-49.

155. (a) Clavier, N.; Dacheux, N.; Podor, R., Synthesis, characterization, sintering, and leaching of β-TUPD/monazite radwaste matrices. *Inorganic chemistry* **2006,** *45* (1), 220-229; (b) Chen, S.; Wang, Y.; Zhang, J.; Zhao, L.; Wang, Q.; Han, L., Luminescent properties of novel K3R (PO4) 2: Tb3+ (R= Y and Gd) phosphors for displays and lightings. *Journal of Luminescence* **2014,** *150*, 46-49; (c) Arunkumar, P.; Jayajothi, C.; Jeyakumar, D.; Lakshminarasimhan, N., Structure–property relations in hexagonal and monoclinic BiPO 4: Eu 3+ nanoparticles synthesized by polyol-mediated method. *Rsc Advances* **2012,** *2* (4), 1477-1485.

156. (a) Clavier, N.; Dacheux, N.; Wallez, G.; Quarton, M., Improvement of the preparation of sintered pellets of thorium phosphate-diphosphate and associated solid solutions from crystallized precursors. *Journal of nuclear materials* **2006,** *352* (1-3), 209-216; (b) Boatner, L. A., Synthesis, structure, and properties of monazite, pretulite, and xenotime. *Reviews in mineralogy and geochemistry* **2002,** *48* (1), 87-121; (c) Beall, G.; Boatner, L.; Mullica, D.; Milligan, W., The structure of cerium orthophosphate, a synthetic analogue of monazite. *Journal of Inorganic and Nuclear Chemistry* **1981,** *43* (1), 101-105.

157. Arakcheeva, A.; Chapuis, G.; Petříček, V.; Dušek, M.; Schoenleber, A., The incommensurate structure of K3In (PO4) 2. *Acta Crystallographica Section B: Structural Science* **2003,** *59* (1), 17-27.

158. Zhu, J.; Cheng, W.-D.; Wu, D.-S.; Zhang, H.; Gong, Y.-J.; Tong, H.-N.; Zhao, D., Potassium gadolinium phosphate with a tunnel structure: Synthesis, structure, and optical properties of K3Gd5 (PO4) 6. *Crystal growth & design* **2006,** *6* (7), 1649-1652.

159. Terebilenko, K. V.; Zatovsky, I. V.; Slobodyanik, N. S.; Domasevitch, K. V.; Pushkin, D. V.; Baumer, V. N.; Sudavtsova, V. S., Phase relations in the system K2MoO4–KPO3–MoO3–Bi2O3: A new phosphate K3Bi5 (PO4) 6. *Journal of Solid State Chemistry* **2007,** *180* (12), 3351-3359.

References

160. Hizhnyi, Y. A.; Nedilko, S.; Chornii, V.; Slobodyanik, M.; Zatovsky, I.; Terebilenko, K., Electronic structures and origin of intrinsic luminescence in Bi-containing oxide crystals BiPO4, K3Bi5 (PO4) 6, K2Bi (PO4)(MoO4), K2Bi (PO4)(WO4) and K5Bi (MoO4) 4. *Journal of alloys and compounds* **2014,** *614*, 420-435.

161. Meng, F.; Zhang, H.; Chen, C.; Kim, S. I.; Seo, H. J.; Zhang, X., A study of luminescence from Eu3+, Ce3+, Tb3+ and Ce3+/Tb3+ in new potassium gadolinium phosphate K3Gd5 (PO4) 6. *Journal of Alloys and Compounds* **2016,** *671*, 150-156.

162. (a) Achary, S.; Errandonea, D.; Muñoz, A.; Rodríguez-Hernández, P.; Manjón, F.; Krishna, P.; Patwe, S.; Grover, V.; Tyagi, A., Experimental and theoretical investigations on the polymorphism and metastability of BiPO 4. *Dalton Transactions* **2013,** *42* (42), 14999-15015; (b) Vergeer, P.; Vlugt, T.; Kox, M.; Den Hertog, M.; Van der Eerden, J.; Meijerink, A., Quantum cutting by cooperative energy transfer in Yb x Y 1− x P O 4: Tb 3+. *Physical Review B* **2005,** *71* (1), 014119.

163. Patwe, S.; Achary, S.; Tyagi, A., Lattice thermal expansion of zircon-type LuPO4 and LuVO4: A comparative study. *American Mineralogist* **2009,** *94* (1), 98-104.

164. (a) Chatterji, T.; Hansen, T. C., Magnetoelastic effects in Jahn–Teller distorted CrF2 and CuF2 studied by neutron powder diffraction. *Journal of Physics: Condensed Matter* **2011,** *23* (27), 276007; (b) Fei, Y., Thermal expansion. *Mineral physics & crystallography: a handbook of physical constants* **1995,** *2*, 29-44.

165. (a) Bevara, S.; Achary, S.; Tyagi, A.; Mishra, K.; Ravindran, T.; Sinha, A.; Sastry, P. In *Structural investigation on K 3 Gd 5 (PO 4) 6 in between 20 K to 1073 K*, Proceedings of the sixth DAE-BRNS interdisciplinary symposium on materials chemistry, 2016; (b) Bevara, S.; Achary, S.; Tyagi, A.; Sinha, A.; Sastry, P. In *X-ray diffraction studies on K 3 Gd 5 (PO 4) 6 between 20K to 1073 K*, Proceedings of the DAE-BRNS symposium on condensed matter physics under extreme conditions: book of abstracts, 2016.

166. Achary, S. N.; Errandonea, D.; Santamaria-Perez, D.; Gomis, O.; Patwe, S. J.; Manjón, F. J.; Hernandez, P. R.; Munoz, A.; Tyagi, A. K., Experimental and Theoretical Investigations on Structural and Vibrational Properties of Melilite-Type Sr2ZnGe2O7 at High Pressure and Delineation of a High-Pressure Monoclinic Phase. *Inorganic chemistry* **2015,** *54* (13), 6594-6605.

167. Fately, W. G., Infrared and Raman Selection Rules for Molecular and Lattice Vibrations by William G. Fateley. **1972**.

168. Szczygieł, I.; Macalik, L.; Znamierowska, T.; Hanuza, J., Electronic absorption and vibrational IR and Raman studies of binary phosphate β-K4Ce2P4O15. *Journal of Alloys and Compounds* **2004,** *380* (1-2), 274-278.

169. Mishra, K.; Ghosh, S.; Ravindran, T.; Amirthapandian, S.; Kamruddin, M., Thermal conductivity and pressure-dependent Raman studies of vertical graphene nanosheets. *The Journal of Physical Chemistry C* **2016,** *120* (43), 25092-25100.

170. Ravindran, T.; Sivasubramanian, V.; Arora, A. K., Low temperature Raman spectroscopic study of scandium molybdate. *Journal of Physics: Condensed Matter* **2004,** *17* (2), 277.

171. Palacios, E.; Rodríguez-Velamazán, J.; Evangelisti, M.; McIntyre, G.; Lorusso, G.; Visser, D.; de Jongh, L. J.; Boatner, L. A., Magnetic structure and magnetocalorics of GdPO 4. *Physical Review B* **2014,** *90* (21), 214423.

172. Ni, Y.; Hughes, J. M.; Mariano, A. N., Crystal chemistry of the monazite and xenotime structures. *American Mineralogist* **1995,** *80* (1-2), 21-26.

173. (a) Chen, Y.-C.; Prokleška, J.; Xu, W.-J.; Liu, J.-L.; Liu, J.; Zhang, W.-X.; Jia, J.-H.; Sechovský, V.; Tong, M.-L., A brilliant cryogenic magnetic coolant: magnetic and magnetocaloric study of ferromagnetically coupled GdF 3. *Journal of Materials Chemistry C* **2015,** *3* (47), 12206-12211; (b) Evangelisti, M.; Sorop, T. G.; Bakharev, O. N.; Visser, D.; Hillier, A. D.; Alonso, J. J.; Haase, M.; Boatner, L. A.; De Jongh, L. J., Size-dependent magnetic ordering and spin dynamics in DyPO 4 and GdPO 4 nanoparticles. *Physical Review B* **2011,** *84* (9), 094408.

174. (a) Bevara, S.; Achary, S. N.; Garg, N.; Chitnis, A.; Sastry, P.; Shinde, A.; Krishna, P. S. R.; Tyagi, A. K., Pressure and Temperature Dependent Structural Studies on Hollandite Type Ferrotitanate and Crystal Structure of a High Pressure Phase. *Inorganic chemistry* **2018,** *57* (4), 2157-2168; (b) Ishii, T.; Kojitani, H.; Akaogi, M., High-pressure phase transitions and subduction behavior of continental crust at pressure–temperature conditions up to the upper part of the lower mantle. *Earth and Planetary Science Letters* **2012,** *357*, 31-41.

175. Tumurugoti, P.; Clark, B.; Edwards, D.; Amoroso, J.; Sundaram, S., Cesium incorporation in hollandite-rich multiphasic ceramic waste forms. *Journal of Solid State Chemistry* **2017,** *246*, 107-112.

176. (a) Cheary, R., A structural analysis of potassium, rubidium and caesium substitution in barium hollandite. *Acta Crystallographica Section B: Structural Science* **1987,** *43* (1), 28-34; (b) Cheary, R. W., An analysis of the structural characteristics of hollandite compounds. *Acta Crystallographica Section B: Structural Science* **1986,** *42* (3), 229-236.

177. Carter, M., Tetragonal to monoclinic phase transformation at room temperature in BaxFe2xTi8− 2xO16 hollandite due to increased Ba occupancy. *Materials research bulletin* **2004,** *39* (7-8), 1075-1081.

178. (a) Knyazev, A.; Mączka, M.; Ladenkov, I.; Bulanov, E.; Ptak, M., Crystal structure, spectroscopy, and thermal expansion of compounds in MI2O–Al2O3–TiO2 system. *Journal of Solid State Chemistry* **2012,** *196*, 110-118; (b) Michiue, Y., Phase relations in NaxCrxTi8− xO16 at 1350° C and crystal structure of hollandite-like Na2Cr2Ti6O16. *Journal of Solid State Chemistry* **2006,** *179* (8), 2578-2583.

179. Akaogi, M.; Kamii, N.; Kishi, A.; Kojitani, H., Calorimetric study on high-pressure transitions in KAlSi 3 O 8. *Physics and chemistry of minerals* **2004,** *31* (2), 85-91.

180. (a) He, Y.; Sun, Y.; Lu, X.; Gao, J.; Li, H.; Li, H., First-principles prediction of fast migration channels of potassium ions in KAlSi3O8 hollandite: Implications for high conductivity anomalies in

subduction zones. *Geophysical Research Letters* **2016,** *43* (12), 6228-6233; (b) Kawai, K.; Tsuchiya, T., First-principles study on the high-pressure phase transition and elasticity of KAlSi3O8 hollandite. *American Mineralogist* **2013,** *98* (1), 207-218.

181. (a) Dewaele, A.; Loubeyre, P.; Mezouar, M., Equations of state of six metals above 94 GPa. *Physical Review B* **2004,** *70* (9), 094112; (b) Krogh Andersen, A. M.; Carlson, S., High-pressure structures of α-and δ-ZrMo2O8. *Acta Crystallographica Section B: Structural Science* **2001,** *57* (1), 20-26; (c) Pandey, K.; Poswal, H.; Mishra, A.; Dwivedi, A.; Vasanthi, R.; Garg, N.; Sharma, S. M., Energy-dispersive X-ray diffraction beamline at Indus-2 synchrotron source. *Pramana* **2013,** *80* (4), 607-619.

182. Endo, T.; Nagayama, H.; Sato, T.; Shimada, M., Crystal growth of potassium titanates in the system K2O-Fe2O3-TiO2. *Journal of crystal growth* **1986,** *78* (3), 423-430.

183. Grey, I.; Li, C.; Madsen, I.; Watts, J., The stability and structure of Csx [Ti2− x4□ x4] O4, 0.61< x< 0.65. *Journal of Solid State Chemistry* **1987,** *66* (1), 7-19.

184. Ishiwata, S.; Bos, J.; Huang, Q.; Cava, R., Structure and magnetic properties of hollandite Ba1. 2Mn8O16. *Journal of Physics: Condensed Matter* **2006,** *18* (15), 3745.

185. Birch, F., Finite strain isotherm and velocities for single-crystal and polycrystalline NaCl at high pressures and 300 K. *Journal of Geophysical Research: Solid Earth* **1978,** *83* (B3), 1257-1268.

186. Downs, R. T.; Hazen, R. M.; Finger, L. W.; Gasparik, T., Crystal chemistry of lead aluminosilicate hollandite: A new high-pressure synthetic phase with octahedral Si. *American Mineralogist* **1995,** *80* (9-10), 937-940.

187. Knyazev, A.; Chernorukov, N.; Ladenkov, I.; Belopol'skaya, S., Synthesis, structure, and thermal expansion of M 2 Fe 2 Ti 6 O 16 and MFeTiO 4 compounds. *Inorganic Materials* **2011,** *47* (9), 999.

188. (a) Alexandratos, S. D., Ion-Exchange Resins: A Retrospective from Industrial and Engineering Chemistry Research. *Industrial & Engineering Chemistry Research* **2009,** *48* (1), 388-

398; (b) Wheaton, R. M.; Anderson, R. E., Industrial applications of ion exchange resins. *Journal of Chemical Education* **1958,** *35* (2), 59; (c) Jiang, S.; Ladewig, B. P., High Ion-Exchange Capacity Semihomogeneous Cation Exchange Membranes Prepared via a Novel Polymerization and Sulfonation Approach in Porous Polypropylene. *ACS Applied Materials & Interfaces* **2017,** *9* (44), 38612-38620.

189. (a) Mushtaq, A., Inorganic ion-exchangers: Their role in chromatographic radionuclide generators for the decade 1993-2002. *Journal of Radioanalytical and Nuclear Chemistry* **2004,** *262* (3), 797-810; (b) Dash, A.; Chakravarty, R., Pivotal role of separation chemistry in the development of radionuclide generators to meet clinical demands. *RSC Advances* **2014,** *4* (81), 42779-42803; (c) Dash, A.; Knapp Jr, F. F., An overview of radioisotope separation technologies for development of 188W/188Re radionuclide generators providing 188Re to meet future research and clinical demands. *RSC Advances* **2015,** *5* (49), 39012-39036.

190. (a) Chakravarty, R.; Shukla, R.; Ram, R.; Venkatesh, M.; Tyagi, A. K.; Dash, A., Exploitation of Nano Alumina for the Chromatographic Separation of Clinical Grade 188Re from 188W: A Renaissance of the 188W/188Re Generator Technology. *Analytical Chemistry* **2011,** *83* (16), 6342-6348; (b) Chakravarty, R.; Ram, R.; Mishra, R.; Sen, D.; Mazumder, S.; Pillai, M. R. A.; Dash, A., Mesoporous Alumina (MA) Based Double Column Approach for Development of a Clinical Scale 99Mo/99mTc Generator Using (n,γ)99Mo: An Enticing Application of Nanomaterial. *Industrial & Engineering Chemistry Research* **2013,** *52* (33), 11673-11684; (c) Chakravarty, R.; Shukla, R.; Ram, R.; Venkatesh, M.; Dash, A.; Tyagi, A. K., Nanoceria-PAN Composite-Based Advanced Sorbent Material: A Major Step Forward in the Field of Clinical-Grade 68Ge/68Ga Generator. *ACS Applied Materials & Interfaces* **2010,** *2* (7), 2069-2075; (d) Chakravarty, R.; Chakraborty, S.; Shukla, R.; Bahadur, J.; Ram, R.; Mazumder, S.; Dev Sarma, H.; Tyagi, A. K.; Dash, A., Mechanochemical synthesis of mesoporous tin oxide: a new generation nanosorbent for 68Ge/68Ga generator technology. *Dalton Transactions* **2016,** *45* (34), 13361-13372; (e) Amor-

Coarasa, A.; Schoendorf, M.; Meckel, M.; Vallabhajosula, S.; Babich, J. W., Comprehensive Quality Control of the ITG 68Ge/68Ga Generator and Synthesis of 68Ga-DOTATOC and 68Ga-PSMA-HBED-CC for Clinical Imaging. *Journal of nuclear medicine : official publication, Society of Nuclear Medicine* **2016,** *57* (9), 1402-5.

191. Chakravarty, R.; Bevara, S.; Bahadur, J.; Chakraborty, S.; Dev Sarma, H.; Achary, S. N.; Dash, A.; Tyagi, A. K., Birnessite: A New-Generation and Cost Effective Ion Exchange Material for Separation of Clinical-Grade 90Y from 90Sr/90Y Mixture. *ChemistrySelect* **2018,** *3* (38), 10670-10676.

192. (a) Chakravarty, R.; Chakraborty, S.; Dash, A., A systematic comparative evaluation of 90Y-labeled bifunctional chelators for their use in targeted therapy. *Journal of labelled compounds & radiopharmaceuticals* **2014,** *57* (2), 65-74; (b) Chakravarty, R.; Chakraborty, S.; Dash, A., Formulation and purification of therapeutic dose of (90)Y-labeled peptides: Some interesting radiochemistry aspects. *Applied radiation and isotopes : including data, instrumentation and methods for use in agriculture, industry and medicine* **2017,** *121*, 1-5; (c) Saxena, S. K.; Pandey, U.; Kumar, Y.; Chakravarty, R.; Sarma, H. D.; Dash, A., On the application of Nafion membrane for the preparation of (90)Y skin patches, quality control, and biological evaluation for treatment of superficial tumors. *Cancer biotherapy & radiopharmaceuticals* **2014,** *29* (5), 200-9; (d) Chakravarty, R.; Dash, A.; Pillai, M. R., Availability of yttrium-90 from strontium-90: a nuclear medicine perspective. *Cancer biotherapy & radiopharmaceuticals* **2012,** *27* (10), 621-41; (e) Montana, R. L.; Gonzalez, I. H.; Ramirez, A. A.; Garaboldi, L.; Chinol, M., Yttrium-90 -- current status, expected availability and applications of a high beta energy emitter. *Current radiopharmaceuticals* **2012,** *5* (3), 253-63.

193. Chakravarty, R.; Pandey, U.; Manolkar, R. B.; Dash, A.; Venkatesh, M.; Pillai, M. R., Development of an electrochemical 90 Sr-90 Y generator for separation of 90 Y suitable for targeted therapy. *Nuclear medicine and biology* **2008,** *35* (2), 245-53.

References

194. Wester, D. W.; Steele, R. T.; Rinehart, D. E.; DesChane, J. R.; Carson, K. J.; Rapko, B. M.; Tenforde, T. S., Large-scale purification of 90Sr from nuclear waste materials for production of 90Y, a therapeutic medical radioisotope. *Applied radiation and isotopes : including data, instrumentation and methods for use in agriculture, industry and medicine* **2003,** *59* (1), 35-41.

195. (a) Yang, H.; Luo, M.; Luo, L.; Wang, H.; Hu, D.; Lin, J.; Wang, X.; Wang, Y.; Wang, S.; Bu, X.; Feng, P.; Wu, T., Highly Selective and Rapid Uptake of Radionuclide Cesium Based on Robust Zeolitic Chalcogenide via Stepwise Ion-Exchange Strategy. *Chemistry of Materials* **2016,** *28* (23), 8774-8780; (b) Li, J.; Zhang, P.; Wang, J.; Wang, M., Birnessite-Type Manganese Oxide on Granular Activated Carbon for Formaldehyde Removal at Room Temperature. *The Journal of Physical Chemistry C* **2016,** *120* (42), 24121-24129; (c) Li, N.; Zhang, L.; Chen, Y.; Fang, M.; Zhang, J.; Wang, H., Highly Efficient, Irreversible and Selective Ion Exchange Property of Layered Titanate Nanostructures. *Advanced Functional Materials* **2012,** *22* (4), 835-841; (d) Ishikawa, Y.; Tsukimoto, S.; Nakayama, K. S.; Asao, N., Ultrafine Sodium Titanate Nanowires with Extraordinary Sr Ion-Exchange Properties. *Nano Letters* **2015,** *15* (5), 2980-2984; (e) Manos, M. J.; Ding, N.; Kanatzidis, M. G., Layered metal sulfides: Exceptionally selective agents for radioactive strontium removal. *Proceedings of the National Academy of Sciences* **2008,** *105* (10), 3696.

196. (a) Birkner, N.; Navrotsky, A., Thermodynamics of manganese oxides: Sodium, potassium, and calcium birnessite and cryptomelane. *Proceedings of the National Academy of Sciences of the United States of America* **2017,** *114* (7), E1046-e1053; (b) Ghaly, M.; El-Dars, F. M. S. E.; Hegazy, M. M.; Abdel Rahman, R. O., Evaluation of synthetic Birnessite utilization as a sorbent for cobalt and strontium removal from aqueous solution. *Chemical Engineering Journal* **2016,** *284*, 1373-1385; (c) Yin, H.; Liu, F.; Feng, X.; Liu, M.; Tan, W.; Qiu, G., Co2+-exchange mechanism of birnessite and its application for the removal of Pb2+ and As(III). *Journal of hazardous materials* **2011,** *196*, 318-26.

197. (a) Lopano Christina, L.; Heaney Peter, J.; Post Jeffrey, E., Cs-exchange in birnessite: Reaction mechanisms inferred from time-resolved X-ray diffraction and transmission electron

microscopy. In *American Mineralogist*, 2009; Vol. 94, p 816; (b) Post Jeffrey, E.; Veblen David, R., Crystal structure determinations of synthetic sodium, magnesium, and potassium birnessite using TEM and the Rietveld metho. *American Mineralogist* **1990,** *75*, 477-489.

198. Chakravarty, R.; Chakraborty, S.; Khan, M. S.; Ram, R.; Sarma, H. D.; Dash, A., An electrochemical approach for removal of radionuclidic contaminants of Eu from (153)Sm for effective use in metastatic bone pain palliation. *Nuclear medicine and biology* **2017,** *58*, 8-19.

199. Chakravarty, R.; Chakraborty, S.; Radhakrishnan, E. R.; Kamaleshwaran, K.; Shinto, A.; Dash, A., Clinical (68)Ga-PET: Is radiosynthesis module an absolute necessity? *Nuclear medicine and biology* **2017,** *46*, 1-11.

200. Chakraborty, S.; Chakravarty, R.; Sarma, H. D.; Pillai Maroor Raghavan, A.; Ashutosh, D., Utilization of a novel electrochemical 90Sr/90Y generator for the preparation of 90Y-labeled RGD peptide dimer in clinically relevant dose. In *Radiochimica Acta*, 2014; Vol. 102, p 523.

201. Boldon, L.; Laliberte, F.; Liu, L., Review of the fundamental theories behind small angle X-ray scattering, molecular dynamics simulations, and relevant integrated application. *Nano reviews* **2015,** *6*, 25661.

202. Ling, F. T.; Post, J. E.; Heaney, P. J.; Kubicki, J. D.; Santelli, C. M., Fourier-transform infrared spectroscopy (FTIR) analysis of triclinic and hexagonal birnessites. *Spectrochimica acta. Part A, Molecular and biomolecular spectroscopy* **2017,** *178*, 32-46.

203. (a) Persson, I., Hydrated metal ions in aqueous solution: How regular are their structures? In *Pure and Applied Chemistry*, 2010; Vol. 82, p 1901; (b) Marcus, Y., Ionic radii in aqueous solutions. *Chemical Reviews* **1988,** *88* (8), 1475-1498.

204. Saxena, S.; Prasad, M.; D'Souza, S. F., Radionuclide Sorption onto Low-Cost Mineral Adsorbent. *Industrial & Engineering Chemistry Research* **2006,** *45* (26), 9122-9128.

205. Zhang, Y.; Lin, X.; Hu, S.; Zhang, X.; Luo, X., Core-shell zeolite@Alg-Ca particles for removal of strontium from aqueous solutions. *RSC Advances* **2016,** *6* (78), 73959-73973.

References

206. Dawar, R.; Bevara, S.; Achary, S. N.; Babu, P.; Mishra, R.; Tyagi, A. K., Thermodynamic investigations on K3Ln5 (PO4) 6 (Ln= Eu and Gd) compounds. *Journal of Alloys and Compounds* **2019,** *771*, 936-943.

207. Bevara, S.; Achary, S. N.; Mishra, K. K.; Ravindran, T.; Sinha, A. K.; Sastry, P.; Tyagi, A. K., Temperature dependent structural, vibrational and magnetic properties of K 3 Gd 5 (PO 4) 6. *Physical Chemistry Chemical Physics* **2017,** *19* (8), 6030-6041.

208. Kubaschewski, O.; Alcock, C. B.; Spencer, P., Materials Thermochemistry. Revised. *Pergamon Press Ltd, Headington Hill Hall, Oxford OX 3 0 BW, UK, 1993. 363* **1993**.

209. Phapale, S.; Mishra, R.; Das, D., Standard enthalpy of formation of compounds of the Cd–Zr system. *Journal of nuclear materials* **2008,** *375* (2), 259-262.

210. Jafar, M.; Phapale, S. B.; Achary, S. N.; Mishra, R.; Tyagi, A. K., High temperature crystallographic and thermodynamic investigations on synthetic calzirtite (Ca2Zr5Ti2O16). *Journal of Alloys and Compounds* **2016,** *682*, 284-293.

211. Zaman, F.; Beezer, A.; Mitchell, J.; Clarkson, Q.; Elliot, J.; Davis, A.; Willson, R., The stability of benzoyl peroxide by isothermal microcalorimetry. *International journal of pharmaceutics* **2001,** *227* (1-2), 133-137.

212. Rawat, D.; Phapale, S.; Mishra, R.; Dash, S., Thermodynamic studies on charge-coupled substituted synthetic monazite. *Journal of nuclear materials* **2017,** *487*, 406-417.

213. (a) Robie, R. A.; Hemingway, B. S., Thermodynamic properties of minerals and related substances at 298.15 K and 1 bar (10^5 pascals) pressure and at higher temperatures. **1995**; (b) Barin, I.; Platzki, G., *Thermochemical data of pure substances*. Wiley Online Library: 1989; Vol. 304.

214. Shomate, C. H., A Method for Evaluating and Correlating Thermodynamic Da ta. *The Journal of Physical Chemistry* **1954,** *58* (4), 368-372.

215. Popa, K.; Konings, R., High-temperature heat capacities of EuPO4 and SmPO4 synthetic monazites. *Thermochimica acta* **2006,** *445* (1), 49-52.

216. (a) Xing, H.; Yang, W.; Su, T.; Li, Y.; Xu, J.; Nakano, T.; Yu, J.; Xu, R., Ionothermal Synthesis of Extra-Large-Pore Open-Framework Nickel Phosphite 5 H3O·[Ni8 (HPO3) 9Cl3]· 1.5 H2O: Magnetic Anisotropy of the Antiferromagnetism. *Angewandte Chemie International Edition* **2010,** *49* (13), 2328-2331; (b) Umeyama, D.; Horike, S.; Inukai, M.; Itakura, T.; Kitagawa, S., Inherent proton conduction in a 2D coordination framework. *Journal of the American Chemical Society* **2012,** *134* (30), 12780-12785.

217. Moore, P.; Araki, T., HUREAULITE, MN52+ (H2O) 4 [PO3 (OH)] 2 [PO4] 2-ITS ATOMIC ARRANGEMENT. *American Mineralogist* **1973,** *58* (3-4), 302-307.

218. Li, B.; Jiang, N.; Tian, J.; Li, T.; Hou, G.; Zhang, J., Exploration of the slow relaxation behavior in the manganese phosphate network. *Dalton Transactions* **2014,** *43* (24), 9267-9270.

219. Greedan, J. E., Geometrically frustrated magnetic materialsBasis of a presentation given at Materials Discussion No. 3, 26–29 September, 2000, University of Cambridge, UK. *Journal of Materials Chemistry* **2001,** *11* (1), 37-53.